Plasma Physics Reports, Vol. 26, No. 5, 2000, pp. 375–378. Translated from Fizika Plazmy, Vol. 26, No. 5, 2000, pp. 403–406.

TOKAMAKS

Suppression of Neoclassical Tearing Modes by a Magnetic Well in Shear-Optimized Discharges

A. B. Mikhaĭlovskiĭ[1], B. N. Kuvshinov[1], V. D. Pustovitov[1], and S. E. Sharapov[1, 2]

[1]*Institute of Nuclear Fusion, Russian Research Centre Kurchatov Institute, pl. Kurchatova 1, Moscow, 123182 Russia*

[2]*JET Joint Undertaking, Abingdon, Oxfordshire, OX14 3EA, UK*

Received April 27, 1999; in final form, October 13, 1999

Abstract—The idea is suggested that the neoclassical tearing modes in shear-optimized discharges in tokamaks can be suppressed by a magnetic well. It is noted that this effect can be strengthened by shaping magnetic surfaces due to the combined influence of ellipticity and triangularity. *© 2000 MAIK "Nauka/Interperiodica".*

1. It is known that shear-optimized discharges are one of the most prospective variants of long confinement of high-temperature plasma in tokamaks [1, 2]. It is also known that one of the basic obstacles for achieving sufficiently high β are neoclassical tearing modes (NTMs) leading to the formation of magnetic islands [3–6]. In this connection, the problem of the suppression of NTMs in the shear-optimized discharges becomes urgent. In this work, the idea is proposed that, under the specified conditions, NTMs can be suppressed by a magnetic well. The precondition for this is the fact that, in the region of the internal transport barrier (ITB) arising in the discharges of the specified type, the shear is small, the ion temperature is larger than the electron temperature, and the gradient of the ion temperature is larger than the density gradient [2]. This strengthens the effect of a magnetic well, which, in usual discharges, is small in comparison with the effect of the bootstrap current, which is responsible for the formation of magnetic islands [7, 8]. The effect of a magnetic well can be reinforced even more due to the noncircular shape (ellipticity and triangularity) of the magnetic surfaces.

2. Let us generalize the equation for stationary islands derived in [9] by taking account of the magnetic well. We will cite the formulas of [9] as (I…). We start from the known equation for the stationary magnetic island of the form (I.5.1) (see also [10] and Appendix):

$$\sum_{\sigma_\chi}\int_{-1}^{\infty} d\Omega \oint \frac{J_\parallel \cos\xi}{\sqrt{\Omega + \cos\xi}} d\xi = \frac{c}{8\sqrt{2}} S\Delta' \frac{wB_0}{R_0 q}. \quad (1)$$

Here, w is the island width; Δ' is the standard parameter of the theory of tearing modes, which is assumed to be negative (for instance, $\Delta' = -2m/r$ for $m \gg 1$, m being the poloidal mode number); B_0 is the toroidal magnetic field; Ω is the surface function of the island explained in [9] (see also Appendix); ξ is the angle variable of the island; χ is the poloidal magnetic flux; $\sigma_\chi = \mathrm{sgn}(\chi - \chi_s)$, χ_s is the "centering" magnetic flux of the island; $S = rq'/q$ is the shear; q is the safety factor; r is the average radius of the corresponding equilibrium magnetic surface; the prime denotes the derivative over r; R_0 is the major radius of the torus; c is the speed of light; and $J_\parallel$ is the parallel current, equal to

$$J_\parallel = J_{bs} + \tilde{J}_\parallel. \quad (2)$$

Here, J_{bs} is the bootstrap current and $\tilde{J}_\parallel$ is the part of $J_\parallel$ dependent on ξ and satisfying the condition $\langle \tilde{J}_\parallel \rangle_\xi = 0$, where $\langle \ldots \rangle_\xi$ stands for the averaging over the island magnetic surface (see [9] for details).

It is assumed that, in the considered region of the plasma column, the banana regime is realized; i.e., $\nu < \epsilon^{3/2} v_T / qR_0$, where ν is the characteristic particle collisional frequency, v_T is the particle thermal velocity, and $\epsilon = r/R_0$. In addition, similar to [10], it is assumed that $\epsilon \ll 1$.

We assume that the current $\tilde{J}_\parallel$ arising due to the curvature of the magnetic field lines satisfies the equation

$$(\nabla_\parallel)_\theta \tilde{J}_\parallel + (\nabla \cdot \mathbf{j}_\perp)_\theta = 0, \quad (3)$$

where

$$\mathbf{j}_\perp = \frac{c}{\mathbf{B}^2}[\mathbf{B} \times \nabla p]. \quad (4)$$

Here, $\mathbf{B}$ and p are the total magnetic field and the total plasma pressure, respectively (the sums of the equilibrium and perturbed parts). The operation $(\ldots)_\theta$ means the averaging over the poloidal coordinate θ at constant ξ. Correspondingly, equation (1) can be represented in the form [cf. (I.5.3)]

$$\Delta'/4 + \Delta_{bs} + \Delta_U = 0, \quad (5)$$

where Δ_{bs} is the contribution of the bootstrap current and Δ_U is due to the magnetic curvature effect.

1063-780X/00/2605-0375$20.00

The value Δ_{bs} was calculated in [9]. According to (I.5.51), it is equal to

$$\Delta_{bs} = \frac{2c_{bs}}{w}K_{bs}. \tag{6}$$

Here, K_{bs} and c_{bs} are given by the formulas

$$K_{bs} = -1.23\epsilon^{1/2}\beta_{pe}\frac{r}{S}\left[(1+\tau_i)\frac{n_0'}{n_0} + 0.40\frac{T_e'}{T_e} - 0.17\tau_i\frac{T_i'}{T_i}\right], \tag{7}$$

$$c_{bs} = -\frac{1}{4}\int_1^\infty d\Omega\frac{k}{E(k)}\langle(\Omega+\cos\xi)^{1/2}\rangle_\xi \times\oint\frac{\cos\xi d\xi}{(\Omega+\cos\xi)^{1/2}} = 0.79, \tag{8}$$

where $k = [2/(\Omega+1)]^{1/2}$; $E(k)$ is the complete elliptical integral of the second kind; $\beta_{pe} = 8\pi n_0 T_e/B_\theta^2$, B_θ is the poloidal magnetic field; $\tau_i = T_i/T_e$; and n_0, T_e, and T_i are the equilibrium plasma density and electron and ion temperatures, respectively.

According to (1), (2), and (5), we have

$$\Delta_U = -\frac{2\sqrt{2}R_0 q}{cSw}\sum_{\sigma_\chi}\int_{-1}^\infty d\Omega\oint\frac{\tilde{J}_\parallel\cos\xi}{\sqrt{\Omega+\cos\xi}}d\xi. \tag{9}$$

It follows from [9] that

$$(\nabla_\parallel)_\theta = k_\parallel\frac{\partial}{\partial\xi}, \tag{10}$$

where

$$k_\parallel = -\frac{mSw\sigma_\chi}{\sqrt{2}R_0 qr}(\Omega+\cos\xi)^{1/2}. \tag{11}$$

Using (4), we find that, in terms of the variables ξ and θ,

$$\nabla\cdot\mathbf{j}_\perp = \frac{cw'}{B_0^3 r}\frac{\partial p}{\partial\theta}, \tag{12}$$

where

$$w' \equiv \frac{d}{dr}\langle\mathbf{B}_0^2 + 8\pi p_0\rangle. \tag{13}$$

Here, p_0 is the equilibrium plasma pressure and $\langle\ldots\rangle$ stands for the averaging over the equilibrium magnetic surfaces.

It follows from [9] that the total plasma pressure is a function of the island magnetic surface; i.e., $p = p(\Omega)$. Then, in terms of ξ, θ, and Ω, we have

$$\left(\left(\frac{\partial p}{\partial\theta}\right)_r\right)_\theta = m\frac{\partial p}{\partial\Omega}\sin\xi, \tag{14}$$

where subscript r denotes that differentiation is performed at a constant r. Then, from (12) we obtain

$$(\nabla\cdot\mathbf{j}_\perp)_\theta = \frac{cw'm}{B_0^3 r}\frac{\partial p}{\partial\Omega}\sin\xi. \tag{15}$$

Using (10), (11), and (15), we represent (3) in the form

$$\frac{\partial\tilde{J}_\parallel}{\partial\xi} = \frac{\sqrt{2}cw'\sigma_\chi}{wSB_0^3}\frac{\sin\xi}{(\Omega+\cos\xi)^{1/2}}\frac{\partial p}{\partial\Omega}. \tag{16}$$

Hence,

$$\tilde{J}_\parallel = -\frac{2\sqrt{2}cw'\sigma_\chi}{wSB_0^3}[(\Omega+\cos\xi)^{1/2} - \langle(\Omega+\cos\xi)^{1/2}\rangle_\xi]\frac{\partial p}{\partial\Omega}. \tag{17}$$

Then, (9) takes the form

$$\Delta_U = -\frac{8R_0^2 q^2 w'}{S^2 w^2 B_0^4}\sum_{\sigma_\chi}\sigma_\chi\int_{-1}^\infty d\Omega\frac{\partial p}{\partial\Omega}\langle(\Omega+\cos\xi)^{1/2}\rangle_\xi \times\oint\frac{\cos\xi d\xi}{(\Omega+\cos\xi)^{1/2}}. \tag{18}$$

One can obtain from [9] that

$$p = p_0(\chi_s) + \frac{1}{R_0 B_\theta}\frac{dp_0}{dr}h(\Omega), \tag{19}$$

where $h(\Omega)$ is the function explained in [9]. Then, we obtain

$$\frac{\partial p}{\partial\Omega} = \frac{1}{R_0 B_\theta}\frac{dp_0}{dr}\frac{dh}{d\Omega}. \tag{20}$$

According to (I.2.20) and (I.5.50), we have

$$\frac{dh}{d\Omega} = \frac{\pi}{8}\sigma_\chi w R_0 B_\theta\frac{k}{E(k)}. \tag{21}$$

It follows from (8), (18), (20), and (21) that

$$\Delta_U = -\frac{2c_{bs}}{w}U_0 \equiv -\frac{1.58}{w}U_0, \tag{22}$$

where

$$U_0 = -\frac{4\pi p_0' w' q^2 R_0^2}{S^2 B_0^4}. \tag{23}$$

Substituting (6) and (22) into (5), we obtain

$$\frac{\Delta'}{4} + \frac{1.58}{w}(K_{bs} - U_0) = 0. \tag{24}$$

It follows from (24) that, for $\Delta' < 0$, the stationary magnetic island is absent if

$$U_0 \geq K_{bs}. \tag{25}$$

This inequality is the criterion for suppression of neoclassical magnetic islands by a magnetic well.

According to formula (2.79) of [11], the vacuum value of w' in a noncircular tokamak can be represented as

$$w' = -\frac{2B_\theta^2}{r}[1 - q^2(1 + 6e\tau/\epsilon)], \tag{26}$$

where e is the ellipticity and τ is the triangularity of the magnetic surfaces. These values are determined in such a way that the equation for a magnetic surface of average radius r has the form

$$\rho^2(1 + e\cos 2\theta + 2\tau\cos 3\theta) = r^2, \tag{27}$$

where ρ and θ are the polar coordinates related to the center of this surface. Using (23) and (26), we find

$$U_0 = -\frac{\epsilon^2\beta_{pe}r}{S^2}\left[(1+\tau_i)\frac{n_0'}{n_0} + \frac{T_e'}{T_e} + \tau_i\frac{T_i'}{T_i}\right] \times\left(1 - \frac{1}{q^2} + 6e\tau/\epsilon\right). \tag{28}$$

3. Criterion (25) can be represented in the form

$$f(r) \geq 1, \tag{29}$$

where

$$f(r) = U_0/K_{bs}. \tag{30}$$

Substituting (7) and (28) into (30), we obtain

$$f(r) = 0.81\frac{\epsilon^{3/2}}{S}\frac{1 + \tau_i + \eta_e + \tau_i\eta_i}{1 + \tau_i + 0.40\eta_e - 0.17\tau_i\eta_i} \times\left(1 - \frac{1}{q^2} + 6e\tau/\epsilon\right), \tag{31}$$

where $\eta_\alpha = \partial\ln T_\alpha/\partial\ln n_0$, $\alpha = e, i$.

The standard discharges are characterized by $S \simeq 1$, $T_i \simeq T_e$, $\eta_e \simeq \eta_i \simeq 1$, and $6e\tau/\epsilon < 1$. Then, we have

$$f(r) \simeq \epsilon^{3/2} \ll 1. \tag{32}$$

Therefore, the magnetic well is of minor importance for NTMs in such discharges.

On the other hand, in the ITB region, in the shear-optimized discharges [2], we have $S \ll 1$, $T_i > T_e$, and $\eta_i > 1$. If, in addition, the magnetic surfaces are noncircular so that $6e\tau/\epsilon > 1$, the criterion for NTM stabilization (29) may be satisfied.

ACKNOWLEDGMENTS

This work was supported in part by the Russian Foundation for Basic Research, project no. 96-15-96815 (under the program "Leading Scientific Schools").

APPENDIX

In the presence of a magnetic island, the total magnetic field $\mathbf{B}$ takes the form (see [9] for details)

$$\mathbf{B} = \mathbf{B}_0 + \tilde{\mathbf{B}}, \tag{A.1}$$

where $\mathbf{B}_0$ and $\tilde{\mathbf{B}}$ are the equilibrium and perturbed magnetic fields, respectively, defined by

$$\mathbf{B}_0 = RB_\phi\nabla\phi + rB_\theta\nabla\theta, \tag{A.2}$$

$$\tilde{\mathbf{B}} = \nabla\phi\times\nabla\psi. \tag{A.3}$$

Here, R is the major radius, ψ is the perturbed magnetic flux equal to

$$\psi = \tilde{\psi}\cos\xi, \tag{A.4}$$

ϕ and θ are the toroidal and poloidal angles, B_ϕ and B_θ are the toroidal and poloidal components of the magnetic field $\mathbf{B}_0$, and $\tilde{\psi}$ is a positive constant. In terms of the island width w, we have

$$\tilde{\psi} = w^2R_0B_\theta S/16r_s. \tag{A.5}$$

According to Ampére's law, the parallel current $J_\parallel \equiv \mathbf{b}\cdot\mathbf{j}$ (where $\mathbf{b} = \mathbf{B}_0/B_0$ and $\mathbf{j}$ is the current density) associated with magnetic field $\mathbf{B}$ is equal to

$$J_\parallel = c\mathbf{b}\cdot\nabla\times\mathbf{B}/4\pi. \tag{A.6}$$

Introducing $x \equiv r - r_s$, we integrate (A.6) weighted with $\cos\xi$ over x within an interval much wider than the island and over ξ within the interval $-\pi \leq \xi \leq \pi$ and use the matching condition

$$\left.\frac{d\ln\psi}{dx}\right|_{-\infty}^{\infty} = \Delta' \tag{A.7}$$

to obtain

$$\int_{-\infty}^{\infty}dx\int_{-\pi}^{\pi}d\xi\cos\xi J_\parallel = c\tilde{\psi}\Delta'/4R_0. \tag{A.8}$$

In addition, according to [9], we have

$$\Omega = SR_0B_\theta x^2/(2r_s\tilde{\psi}) - \cos\xi, \tag{A.9}$$

so that

$$dx = \sigma_\chi\left(\frac{r_s\tilde{\psi}}{2SR_0B_\theta}\right)^{1/2}\frac{d\Omega}{(\Omega + \cos\xi)^{1/2}}. \tag{A.10}$$

Then, (A.8) takes the form

$$\sum_{\sigma_\chi}\int_{-1}^{\infty}d\Omega\oint\frac{J_\parallel\cos\xi}{(\Omega + \cos\xi)^{1/2}}d\xi = \frac{c}{4}\Delta'\left(\frac{2S\tilde{\psi}B_\theta}{r_sR_0}\right)^{1/2}. \tag{A.11}$$

Substituting $\tilde{\psi}$ from (A.5) and taking into account that, in the case of a weak deviation of the magnetic surfaces from the circular ones, $B_\theta = \epsilon B_0/q$, in which we are interested here, we arrive at (1).

It worth noting a discrepancy in [9, 10]: in the initial formulas of these papers, as well as in our formula (1), w denotes the width of the magnetic island, whereas in some other equations in [9, 10], w denotes the half-width of the island.

REFERENCES

1. The JET Team, Plasma Phys. Controlled Fusion **39**, B353 (1997).
2. A. C. C. Sips, Y. Baranov, C. D. Challis, *et al.*, Plasma Phys. Controlled Fusion **40**, 1171 (1998).
3. W. X. Qu and J. D. Callen, Report no. UWPR 85-5 (University of Wisconsin, 1985).
4. R. Carrera, R. D. Hazeltine, and M. Kotschenreuther, Phys. Fluids **29**, 899 (1986).
5. Z. Chang, J. D. Callen, E. D. Fredrickson, *et al.*, Phys. Rev. Lett. **74**, 4663 (1995).
6. H. R. Wilson, M. Alexander, J. W. Connor, *et al.*, Plasma Phys. Controlled Fusion **38**, 149 (1996).
7. M. Kotschenreuther, R. D. Hazeltine, and P. J. Morrison, Phys. Fluids **28**, 294 (1985).
8. B. N. Kuvshinov, V. P. Lakhin, A. B. Mikhaĭlovskiĭ, *et al.*, Fiz. Plazmy **15**, 1160 (1989) [Sov. J. Plasma Phys. **15**, 671 (1989)].
9. B. N. Kuvshinov and A. B. Mikhaĭlovskiĭ, Fiz. Plazmy **24**, 275 (1998) [Plasma Phys. Rep. **24**, 245 (1998)].
10. H. R. Wilson, J. W. Connor, R. J. Hastie, and C. C. Hegna, Phys. Plasmas **3**, 248 (1996).
11. A. B. Mikhaĭlovskiĭ, *Instabilities in a Confined Plasma* (Institute of Physics, Bristol, 1998).

Translated by the authors

Plasma Physics Reports, Vol. 26, No. 5, 2000, pp. 379–387. Translated from Fizika Plazmy, Vol. 26, No. 5, 2000, pp. 407–415.

MAGNETIC CONFINEMENT SYSTEMS

Numerical Study of a DRAKON-type Closed Magnetic Configuration with a Spatial Axis

V. V. Kondakov, S. F. Perelygin, and V. M. Smirnov

Moscow Engineering Physics Institute (Technical University), Kashirskoe sh. 31, Moscow, 115409 Russia

Received June 25, 1999

Abstract—Results are presented from numerical studies of the magnetic field lines and the charged-particle trajectories in the magnetic system of the DRAKON device and of its curvilinear element—the KREL with magnetic mirrors. For the KREL, mirror ratio values are found that do not worsen the particle-drift compensation. The dimensions of the input region for the electrons injected into the KREL to create the beam–plasma discharge are calculated. Calculations show that, in the paraxial approximation, after multiple passes around the device, the magnetic field lines and trajectories of individual transit particles form a system of embedded toroidal surfaces with circular cross sections. When symmetrically changing the current distributions in the coils of the device, these surfaces shift with respect to their previous positions, but their shape remains the same. For the DRAKON device with helical KRELs, the shift of the drift surfaces with respect to the magnetic surfaces, as well as the flow of the longitudinal diamagnetic currents from the KRELs into the rectilinear regions, is found as a function of the pitch angle θ of the KREL helix. © *2000 MAIK "Nauka/Interperiodica"*.

1. INTRODUCTION

The long equilibrium stellarator configuration DRAKON, which was proposed in 1981, consists of two separate equilibrium parts: two rectilinear regions with a uniform magnetic field and two curvilinear elements (KRELs) that close the system [1]. Equilibrium of the system elements means that the diamagnetic plasma currents do not go beyond its boundary. This property of the magnetic configuration can be experimentally verified only in a closed magnetic confinement system. However, according to theoretical estimates [1], the knowledge of the toroidal drift trajectories of individual particles in a curvilinear magnetic field allows us to evaluate the behavior of the diamagnetic plasma currents. If the KRELs are such that, after passing through the curvilinear region, the Larmor center of the particle comes into the vicinity of the same magnetic field line on which it was at the input to the KREL (drift compensation), then the flow of the longitudinal diamagnetic currents from the KREL into the rectilinear regions will be small even in a closed magnetic confinement system. The degree of compensation is determined by the residual drift—the distance between the Larmor center and the initial magnetic line at the output of the curvilinear element.

In this paper, we study numerically the properties of the DRAKON closed magnetic confinement system for different types of curvilinear elements. In Section 3, we consider the effect of the magnetic mirrors on the electron-drift compensation in an individual geodesic KREL. Section 4 describes the influence of various current distributions in the system windings on the position and shape of the magnetic and drift surfaces in the DRAKON with KRELs consisting of three half-tori. In Section 5, we optimize the DRAKON-1 system with helical KRELs with respect to the pitch angle θ of the helix in order to decrease both the flow of the longitudinal diamagnetic current from the KRELs into the rectilinear regions and the departure of the drift surfaces from the magnetic ones.

2. CALCULATION OF THE MAGNETIC FIELD LINES AND ELECTRON TRAJECTORIES

As a model for the vacuum magnetic field, we used the field of a system of thin current coils with radius a. The winding current J was chosen so that the value of the magnetic field B satisfied the proposed projects [2]. The magnetic field of an individual coil was calculated by the Biot–Savart formula. The calculation algorithm is described in more detail in the Appendix.

The magnetic field lines were calculated from the equations

$$\frac{d\mathbf{x}}{dl} = \frac{\mathbf{B}}{B}, \tag{1}$$

by the third-order Runge–Kutta method with an automatic step selection. Here, the total field $\mathbf{B}$ of the solenoid is the superposition of the fields of N coils, $\mathbf{B} = \sum_{k=1}^{N} \mathbf{B}_k$, and l is the length of the field line.

The equations of motion of a charged particle in the magnetic field are

1063-780X/00/2605-0379$20.00

$$\frac{d\mathbf{x}}{dt} = \mathbf{v},$$
$$\frac{d\mathbf{v}}{dt} = \frac{e}{mc}[\mathbf{B}, \mathbf{v}], \quad (2)$$

where $\mathbf{v}$ is the particle velocity, e and m are the particle charge and mass, and c is the speed of light. In the magnetic field, the energy of the charge particle is constant (v = const); then, by using the relations $dl_p = vdt$ and $\frac{d\mathbf{x}}{dt} = v\boldsymbol{\tau}$ (where l_p is the length of the trajectory and $\boldsymbol{\tau}$ is the tangent vector), the set (2) can be presented in the form

$$\frac{d\mathbf{x}}{dl_p} = \boldsymbol{\tau},$$
$$\frac{d\boldsymbol{\tau}}{dl_p} = \frac{e}{mvc}[\mathbf{B}, \boldsymbol{\tau}]. \quad (3)$$

The simultaneous solution of equations (1) and (3) gives the particle trajectory and the field line, along which the particle begins to move. Its drift D with respect to the "starting" field line in the plane of a certain current coil is determined as the distance between the points of intersections of the field line and the trajectory of the particle Larmor center with the coil plane.

3. NUMERICAL INVESTIGATION OF THE MAGNETIC FIELD STRUCTURE AND THE CHARGED-PARTICLE DRIFT IN THE KREL DEVICE WITH MAGNETIC MIRRORS

The closing of the KREL currents can be provided by the appropriate choice of the configuration of the KREL spatial axis. The simplest version is a 3/2-T KREL, which consists of three half-tori rotated 120° with respect to each other in the joining regions [3]. Another version, the geodesic KREL, has been constructed at the Moscow Engineering Physics Institute (MEPI) [4, 5]. This KREL consists of two periods of the five-period helical torus whose spatial axis is the geodesic line on the surface of a torus with a 40-cm major radius and 12-cm minor radius. It is shown experimentally that this KREL contains an equilibrium region (~1.5 periods long), where the electron drift is almost completely compensated [4, 5]. The KREL device can be supplemented with magnetic mirrors [in the end regions (0.25 periods long), the axis is rectified and the current in the coils is increased]. The rectified axis behind the ends of the equilibrium region models the magnetic mirrors attached to the KREL and allows investigation of their influence on the particle-drift compensation. The magnetic mirrors are also required in order to produce a plasma with a beam–plasma discharge (BPD) inside the KREL. In this connection, it is necessary to find such values of the mirror ratio R that do not cause a loss of equilibrium and an additional excursion of both the magnetic field lines and particle trajectories on the chamber wall.

Calculations were performed for a KREL with magnetic mirrors. The model included 40 thin current coils with radius a = 7.5 cm, which were equidistantly positioned along a 178-cm-long system; the distance between the coils was $d = 0.6a$. In [4, 5], it was shown that the equilibrium region in the geodesic KREL covered the region from fourth to 36th coil. In the KREL with magnetic mirrors, additional end coils of the geodesic KREL (from first to fourth and from 37th to 40th) were positioned along the straight line whose direction was determined by the normal to the planes of the fourth and 36th coils, respectively; the current in these coils was varied. We calculated the drift trajectories of electrons starting from the plane of the fourth coil at a distance $r < 0.1a$ from the geometrical axis. The longitudinal Larmor radius of these electrons, which was calculated by the total velocity, was $\rho^* = m_e v_e c/eB = 0.03a$–$0.16a$; the electron energy was W = 100–2400 eV; and the magnetic field on the axis of the equilibrium region was $B \approx 140$ G.

The rectified axis behind the ends of the equilibrium region causes a decrease in the rotational transformation. As a result, the drift compensation somewhat worsens; i.e., the residual drift D_r defined as the distance between the Larmor center of an electron and the starting field line at the output of the equilibrium region increases (Fig. 1). In the geodesic KREL, we have $D_r < 0.15D_{max}$, where D_{max} is the maximum electron drift (in the center of the KREL). When the rectilinear regions are included, D_r increases to $0.25D_{max}$. With the rectified axis and decreased current in the rectified coils (which corresponds to the simulation of the DRAKON device), when the average field value in the KREL is higher than the average field in the rectilinear region, the electron-drift compensation worsens: for $R = B_1/B_0 = 0.3$, D_r increases to $0.4D_{max}$ (here, B_1 is the magnetic field on the axis of the fourth coil and B_0 is the field on the axis of the 20th coil). As R increases, the residual drift decreases and reaches its minimum at a certain value R_{opt}. Then, the residual drift increases as the mirror ratio increases to R_{max}, when the electrons start to leave for the chamber wall. The values of R_{opt} and R_{max} depend on the position of the particle starting point, the particle energy, and the direction of the starting velocity. In this case, in the range of R from 1 to 3, D_r does not exceed $0.25D_{max}$. Figure 2a shows the influence of the mirror ratio R on the value of D_r/D_{max} for different starting points of electrons with the energy W = 100 eV that begin to move along the field lines (Fig. 3). In Fig. 2, n and b are the coordinates (in cm) in the directions of the normal and binormal to the geometrical axis in the plane of the starting coil. It is seen from the figure that the values of R_{opt} and R_{max} depend strongly on the position of the particle starting point: R_{opt} varies from 0.9 to 2.7 and R_{max} varies from 3 to 5.8.

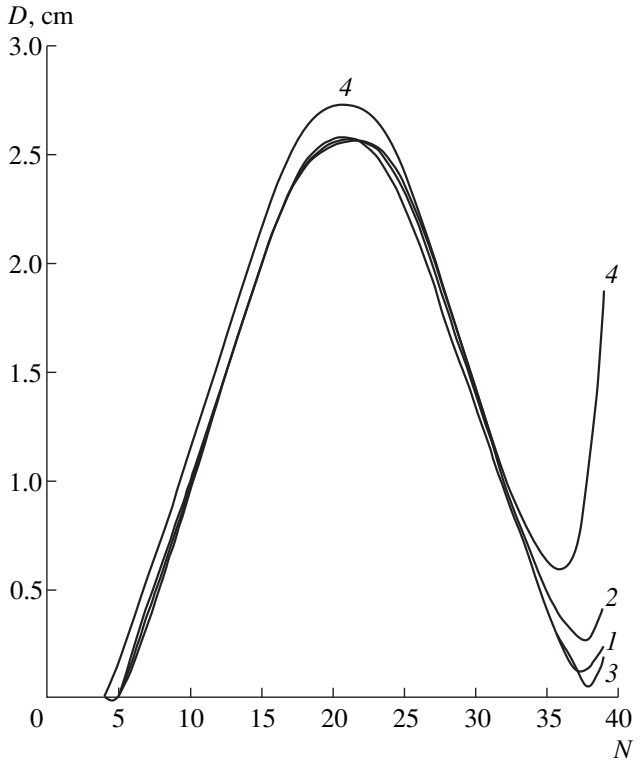

Fig. 1. Shift D of the electrons with energy W = 800 eV coming out of the center of the fourth coil along the magnetic field lines as a function of the coil number N in (*1*) the geodesic KREL and (*2*–*4*) KREL with the axis rectified behind the ends of the equilibrium region for R = (*2*) 0.9, (*3*) R_{opt}, and (*4*) 0.3.

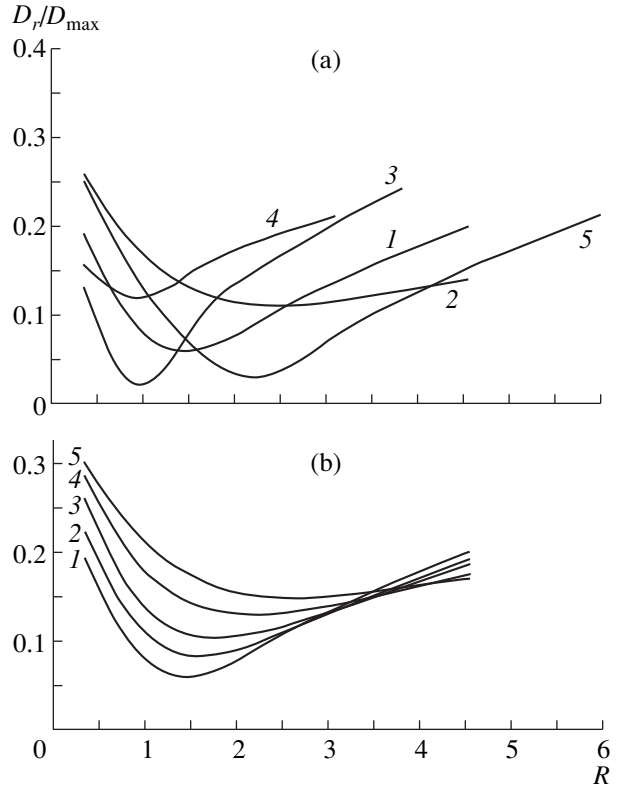

Fig. 2. D_r/D_{max} as a function of the mirror ratio R for different values of the electron energy W and different positions of the starting point (n = 0, ±1, and b = 0, ±1): (a) for W = 100 eV at (*1*) n = 0 and b = 0, (*2*) n = 1 and b = 0, (*3*) n = –1 and b = 0, (*4*) n = 0 and b = 1, and (*5*) n = 0 and b = –1; (b) for n =0 and b = 0 at W = (*1*) 100, (*2*) 400, (*3*) 800, (*4*) 1600, and (*5*) 2400 eV.

The effect of R on the value of D_r/D_{max} as a function of the particle energy is shown in Fig. 2b for the electrons starting along the magnetic field lines from the point n = 0 and b = 0. It is seen that the increase in the electron energy shifts R_{opt} toward larger R, whereas R_{max} does not change. Calculations show that the change in the angle between the direction of the starting velocity of an electron and the magnetic field direction, as well as the rotation of the velocity vector around the vector **B**, has no effect on the values of R_{opt} and R_{max}. Thus, the increase in the current in the transient regions (when the average field is higher than the average field in both the magnetic mirror devices and the KREL) improves the particle-drift compensation. However, the increase in the current in the additional coils leads to the perturbation of the magnetic field in the KREL by the additional magnetic fluxes emerging from the mirrors. The shift of the field lines decreases the amount of electrons that are able to pass along the KREL without contact with the chamber wall. The reason is that some field lines emerge from the chamber, thus carrying the drifting particles onto the wall. We calculated the regions S_1 and S_2 in the input section of the chamber (Fig. 3) such that the field lines starting from S_1 and electrons with $\rho^* \approx 0.09a$ starting from S_2 stay in the KREL over its entire length. The figure shows the boundaries of these regions calculated for eight azimuthal directions. The regions are symmetric about the direction making an angle of 45° with the direction of the binormal to the geometrical axis of the KREL in the plane of the fourth coil. As is seen from Fig. 3, the regions shift only slightly in the fourth quadrant, where the proximity to the curvature center provides a higher field. The strongest shifting takes place in the second quadrant, where the average magnetic field is lower. When the plasma is produced with a BPD, it is necessary to take into account the electron loss on the chamber wall and, for the chosen mirror ratio, place the electron gun inside the calculated region.

For the KREL with the magnetic mirrors, we recommend the mirror ratio R = 1–3. In this case, for the electrons with the longitudinal Larmor radius in the range $0.03a < \rho^* < 0.16a$ that enter the KREL at a distance $r < 0.1a$ from the geometrical axis, the residual drift increases only slightly (at most to $0.25D_{max}$) and the electrons do not fall on the chamber wall.

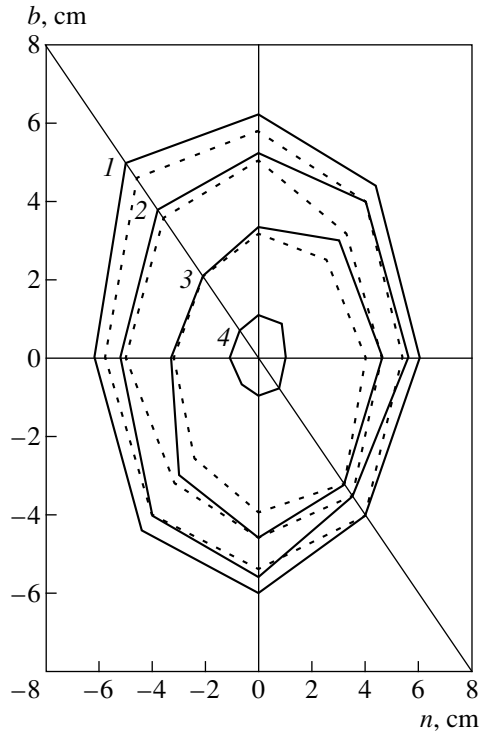

Fig. 3. Domains S_1 for the magnetic field lines in the input cross section of the KREL (solid line) and S_2 for the trajectories of the electrons with the energy W = 800 eV (dashed line) that do not fall on the wall for different values of the mirror ratio R = (*1*) 0.9, (*2*) 1.6, (*3*) and 3.3; (*4*) domain S_3 in the plane of the central coil of the rectilinear region of a DRAKON with a 3/2-T KREL for the trajectories of the electrons with energy W = 50 keV that do not fall on the chamber wall after a single passage around the system.

4. CALCULATION OF THE MAGNETIC FIELD STRUCTURE AND THE CHARGED-PARTICLE MOTION IN A DRAKON WITH A 3/2-T KREL

The development of the first experimental DRAKON magnetic confinement device [2] required the calculation of its vacuum magnetic field structure and analysis of the motion of the individual charged particles in it (single-particle approximation). For analysis, we chose a DRAKON with 3/2-T KRELs. In the mathematical model, 180 thin coils were positioned along the 144-cm-long system. Each KREL consists of 60 coils, and each of the rectilinear regions consists of 30 coils. The radius of the current-carrying coils in the rectilinear regions was a = 4 cm and that in the KREL was 0.6a. The current in the coils of the rectilinear regions was J = 600 A, and, in the KREL, it was 3J. The distance between coils was d = 0.2a. The average magnetic field was 1 kG in the rectilinear region and 3 kG in the KREL. We studied the motion of electrons with an energy of W = 50 keV ($\rho^* \approx 0.2a$) starting from the plane of the central coil of the rectilinear region at a distance $r < 0.1a$ from the axis along the magnetic field line. The size of the model system was chosen to be small so as to save on computation time. The results of calculations carried out with the use of a 12-m-long full-scale model with 450 coils (with radius a = 10 cm and the distance between coils $d \approx 0.2a$) are in agreement with those of the small-scale model. Computation time is saved because, in the small-scale model, the number of coils is less by a factor of 2.5, the relative distance between coils being the same. Moreover, in the small-scale model, the ratio of ρ^* to the axis length is increased approximately by a factor of 8; as a result, the trajectory becomes smoother, which additionally reduces computation time.

The key problem of closed magnetic confinement systems is the problem of the existence of the magnetic surfaces. To find the magnetic surface, we traced the magnetic field line over 100 passages along the system, whereas the closed spur of the surface in the plane of the central coil of the rectilinear region was formed already after 20–30 passages. After a single passage, the calculation error did not exceed 10^{-4} cm. The surfaces were calculated for the distance from the axis $r < 0.25a$. These surfaces are circular in shape, and their axis (magnetic axis) is shifted with respect to the geometrical axis. The deviation of the magnetic axis from the geometrical one in the rectilinear region results from the fact that, when the magnetic field lines enter the magnetic mirror devices from the KRELs, they cannot instantly "forget" about their curvature. In the center of the rectilinear region, this shift can attain a maximum value of 0.03a for a length of the magnetic mirror device of L = 6a.

The drift surfaces were sought by analogy with the magnetic surfaces: the trajectory of a transit electron with energy W = 50 keV was calculated instead of the magnetic field line. After the electron trajectory made a single passage around the device, the calculation error also did not exceed 10^{-4} cm. The surfaces were calculated for the distance $r < 0.25a$ from the axis. The cross sections of the drift surfaces are circular in shape, and their axis is shifted with respect to both the geometrical and magnetic axes. The shift of the axis of drift surfaces with respect to the magnetic axis is proportional to ρ^*.

In order to examine the stability of the system of the magnetic and drift surfaces with respect to the symmetric change in the distribution of the currents J_k in the DRAKON coils, we investigated two regimes.

In the first regime, the current in the coils (from second to 18th) of the central half-tori of both KRELs was increased to 4J. Electrons that start near the axis in the magnetic mirror device pass through the region with a reduced magnetic field ($\Delta B/B$ = 21–38%) in the central region of the KREL. The increase in the current of the coils in the central half-tori reduces the ratio $\Delta B/B$ by more than one-half; this results in a decrease in the number of particles trapped in this magnetic well when the plasma is produced near the axis of the magnetic mirror device.

In the second regime, the current was increased in both the coils of the central half-tori (to 4*J*) and in the five coils of the rectilinear regions near the KREL (to 3*J*). As before, in this case, $\Delta B/B = 10–18\%$ and the magnetic field at the ends of the magnetic mirror devices is equal to the average field in the KREL. The increase in the magnetic field at the boundaries of the rectilinear region results in a double decrease in the number of particles that are confined by the magnetic mirror but, at the same time, penetrate into the curvilinear magnetic field of the KREL, where they experience the uncompensated drift and leave the device.

Calculations show that, when the current in the coils of the central half-tori is increased, the magnetic field lines (including the magnetic axis) in the magnetic mirror device turn out to be shifted (Fig. 4, regime *1*) because of the perturbations of the magnetic field in the rectilinear regions by the magnetic fluxes coming out of the KREL. With the simultaneous increase in the current of the boundary coils of the magnetic mirror devices, this shift should decrease, which was observed in calculations (Fig. 4, regime *2*). When J_k changes, the axis of the drift surfaces shifts following the magnetic axis. In both regimes, the shape of both the magnetic and drift surfaces remains the same. Thus, calculations show that the system of the magnetic and drift surfaces is stable against the symmetric change in J_k in the DRAKON coils. This is evidence for the possibility of varying the current distribution in the device in question.

We also calculated the region S_3 of radius ~0.25*a* in the plane of the central coil in the rectilinear region such that, if the passing electrons with $\rho^* \approx 0.2a$ come out of this region, they stay in the DRAKON over its entire length (we take the radius of the KREL coil for the chamber radius). Particles starting outside the S_3 region fall on the chamber wall during the first passage around the system because of the drift with respect to the magnetic field lines (Fig. 3, region *4*). Thus, we determined the boundary of the domain where the plasma can be produced in the rectilinear region of the DRAKON device.

5. NUMERICAL INVESTIGATION OF THE MAGNETIC FIELD STRUCTURE AND THE CHARGED-PARTICLE MOTION IN THE DRAKON-1 DEVICE

The design of the DRAKON-1 device for investigating the properties of the magnetic confinement system has been proposed by MEPI. In this device, the geometrical axis of each KREL consists of one turn of a helix with additional regions of a quarter of a circle at the ends. These end regions have the same curvature and same direction of the normal to the solenoid axis at the point of connection as the helix. The basic advantage of this system is the absence of the jump in the curvature of the KREL axis, which can assist in plasma confinement. The main parameters of the DRAKON-1 device are presented in Table 1.

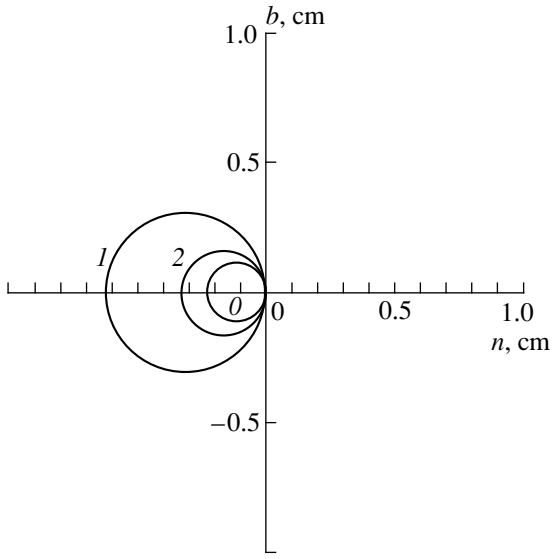

Fig. 4. Cross sections of the magnetic surfaces by the plane of the central coil of the rectilinear region in a DRAKON with 3/2-T KREL: (*0*) unperturbed regime, (*1*) the current in the central regions of the KRELs is increased, and (*2*) the current is increased in both the central regions of the KRELs and the ends of the rectilinear regions.

The device field was modeled by the field produced by 282 thin coils. To reduce the computation time, the length of the model axis was taken to be 15-fold shorter than that of the real device, but the ratio of the distance between coils to the coil diameter in the rectilinear region was the same. In addition, cone-shaped transient regions were introduced between the magnetic mirror devices and KRELs and the coil radius in the KREL was chosen such that the magnetic fluxes in the KREL and in the rectilinear region were equal to each other. The parameters of the numerical model of the DRAKON-1 device are presented in Table 2.

We studied the influence of the pitch angle θ of the KREL helix on the flow of the diamagnetic currents into the rectilinear regions and the departure of the drift surfaces from the magnetic ones.

Figure 5 presents the normalized shift d/ρ^* of the electron drift surfaces with respect to the magnetic ones in the center of the rectilinear region as a function of θ. The curves correspond to the starting points of the particle Larmor center and the magnetic field line located at the distances $R_1 = a/8$ (curves *1*, *2*) and $R_2 = a/2$ (curves *3*, *4*) from the geometrical axis of the magnetic mirror device for two values of ρ^*: $\rho^* \approx 0.015a$ (curves *1*, *3*) and $\rho^* \approx 0.05a$ (curves *2*, *4*). For small *R*, there is a plateau between $\theta = 41°$ and $\theta = 42°$ in the $\frac{d}{\rho^*}(\theta)$ curves. For $R_2 = a/2$, the $\frac{d}{\rho^*}(\theta)$ curves have minima at $\theta = 42°$. According to the general features of drift

Table 1. Basic parameters of the DRAKON-1 device

	Rectilinear region	KREL
Length along the axis, cm	300	300
Vacuum chamber diameter, cm	20	20
Diameter of the solenoid coil, cm:		
inner	25	15
outer	35	35
Coil thickness, cm	0.4	0.4
Number of coils	200	300
Winding pitch, cm	1.5	1
Coil current, kA	1.2	2.4
Magnetic field on the axis, kG	1	3

Table 2. Parameters of the DRAKON-1 model device

	Rectilinear region	KREL	Transient region
Length along the axis, cm	18	20.3	0.9
Radius of the solenoid coil, cm	$a = 4$	2.3	
Number of coils	44	89	4
Winding pitch, cm	0.4	0.23	0.23
Magnetic field on the axis, kG	1	3	

motion, electrons with higher energy have larger deviation $d \sim \sqrt{W}$, where W is the particle energy.

Figure 6 shows $\tan\alpha$ (α is the angle between the "starting coil of the Pfirsh–Schluter currents" and the plane perpendicular to the geometrical axis at the center of the rectilinear region) as a function of θ. The starting coil of the Pfirsh–Schluter currents is defined as a set of points on the magnetic surface such that the integral $U = \int \frac{dl}{B}$ has the same value along all of the magnetic-field-line segments that originate at this coil and arrive at the same coil after a single passage around the system.

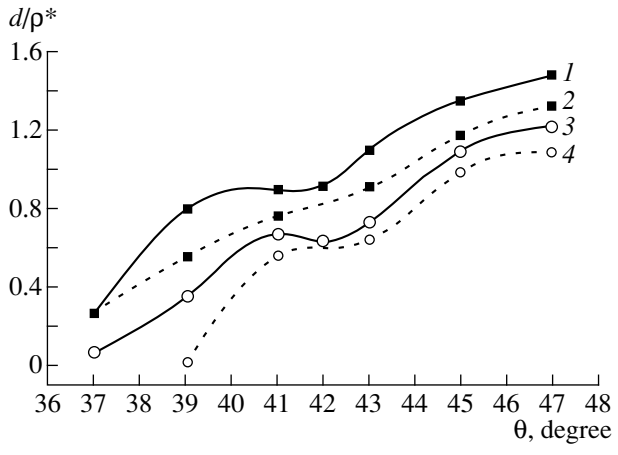

Fig. 5. Normalized shift d/ρ^* of the electron drift surfaces with respect to the magnetic ones in the center of the rectilinear region as a function of θ for (*1*) $R_1 = a/8$ and $\rho^* \approx 0.015a$, (*2*) $R_1 = a/8$ and $\rho^* \approx 0.05a$, (*3*) $R_2 = a/2$ and $\rho^* \approx 0.015a$, and (*4*) $R_2 = a/2$ and $\rho^* \approx 0.05a$.

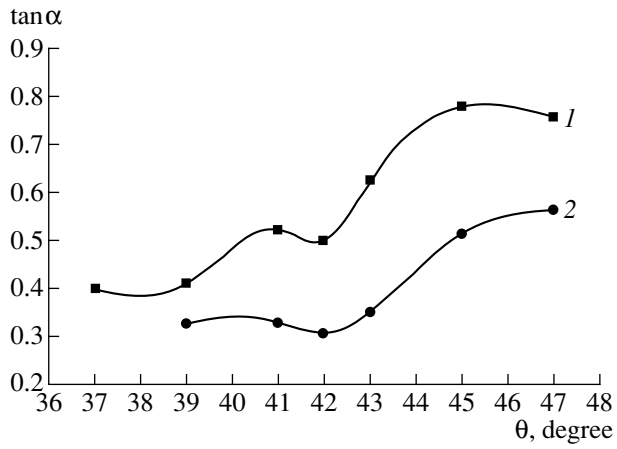

Fig. 6. The value of $\tan\alpha$ as a function of θ for the starting coils of the Pfirsh–Schluter currents on the magnetic surfaces with (*1*) $R_1 = a/8$ and (*2*) $R_2 = a/2$.

This condition results from the following simple considerations. Let there be two close magnetic surfaces with a circular cross section. Let their radii be r_1 and r_2 and the plasma pressure be p_1 and p_2. Then, the relation

$$\nabla p = \frac{1}{c}[\mathbf{j}, \mathbf{B}] \tag{4}$$

for the current flowing through the area bounded by the field-line segments with length l on both boundaries and the segments with length $(r_2 - r_1)$ perpendicular to the magnetic surfaces yields

$$\begin{aligned} J &= \int_0^l dl \int_{r_1}^{r_2} j_\perp dr = \int_0^l dl \int_{r_1}^{r_2} \frac{c\nabla p}{B} dr \\ &\approx \int_0^l (p_2 - p_1)\frac{c}{B} dl = c(p_2 - p_1)\int_0^l \frac{dl}{B}. \end{aligned} \tag{5}$$

From here, we have

$$\int_0^l \frac{dl}{B} = \frac{J}{c(p_2 - p_1)} = \text{const}. \tag{6}$$

If we find the starting coil of the Pfirsh–Schluter currents using the above procedure and place the Pfirsh–Schluter-current coils along the magnetic field lines at the fixed distances $l = l_2 - l_1$ such that

$$\delta U = \int_{l_1}^{l_2} \frac{dl}{B} = \text{const}, \tag{7}$$

then we can specify the closed currents $\mathbf{j}$ flowing along these coils. The tilting angle α of the coils with respect to the magnetic field lines determines the current components $j_\parallel = j\sin\alpha$ and $j_\perp = j\cos\alpha$. By determining the component

$$j_\perp = \frac{c(p_2 - p_1)}{(r_2 - r_1)B}, \tag{8}$$

we find

$$j = \frac{j_\perp}{\cos\alpha} \tag{9}$$

at each point of the magnetic surface. Since the currents between two coils flow in the layer between the magnetic surfaces, such that the closing condition

$$J \sim \int \frac{dl}{B} = \text{const} \tag{10}$$

holds, we found the steady-state current distribution satisfying the conditions

$$\begin{aligned} \operatorname{div} \mathbf{j} &= 0, \\ \nabla p &= \frac{1}{c}[\mathbf{j}, \mathbf{B}], \end{aligned} \tag{11}$$

which correspond to the plasma equilibrium.

The dependences presented in Fig. 6 (curves *1* and *2* plot $\tan\alpha$ for the starting coil of the Pfirsh–Schluter currents on the magnetic surfaces with $R_1 = a/8$ and $R_2 = a/2$, respectively) show the minimum for the Pfirsh–Schluter currents at $\theta = 42°$ in both the paraxial and peripheral regions. Thus, the optimization of the device by varying the parameter θ in order to bring together the drift and magnetic surfaces gives $\theta = 41$–$42°$; the optimization carried out to reduce the Pfirsh–Schluter currents in the rectilinear regions gives approximately the same value. Therefore, the minimization of the shift of the drift surfaces with respect to the magnetic ones is almost equivalent to the minimization of the longitudinal diamagnetic currents.

6. CONCLUSION

Calculations of the magnetic field lines and charged-particle trajectories in the KREL with magnetic mirrors showed that rectifying the axis behind the ends of the equilibrium region and decreasing the current in the rectified coils (i.e., modeling the DRAKON device) lead to an increase in the residual electron drift. As the mirror ratio R increases, the residual drift first decreases and reaches its minimum at a certain value R_{opt}. Then, the residual drift increases as the mirror ratio increases to R_{max}, when the particles begin to fall on the chamber wall. The values of R_{opt} and R_{max} are functions of the starting point and energy of the particle. For a KREL with magnetic mirrors, we can recommend the use of the mirror ratio $R = 1$–3. In this case, first, the residual drift of the particles with $\rho^* < 0.09a$ increases insignificantly (at most to $0.25D_{max}$) and, second, the electrons with $\rho^* < 0.09a$, which start from the region with the radius $r < 0.4a$ with respect to the geometrical axis in the input section of the KREL chamber, do not fall on the wall. Thus, we determined the region appropriate for plasma production with a BPD.

In the paraxial approximation, the magnetic field configuration of the DRAKON closed magnetic confinement device with 3/2-T KRELs is a system of embedded toroidal magnetic surfaces with circular cross sections. After multiple passages around the device, the transit-particle trajectories form a system of embedded surfaces. Thus, the small drift that remains after the particle passes through the KREL is mainly azimuthal rather than radial and does not lead to particle loss. The electrons that come into motion near the axis in the magnetic mirror device, in the central region of KREL, pass through the region with a reduced mag-

netic field ($\Delta B/B$ = 21–38%). If the current distribution in the system coils is such that it halves this ratio and reduces the penetration of electrons trapped in the rectilinear regions into the KREL, then the magnetic and drift surfaces turn out to be shifted with respect to their previous positions, but their shape remains unchanged. In the plane of the central coil of the rectilinear region, we found an area with the radius ~0.25a such that, if the passing electrons with $\rho^* \approx 0.2a$ emerge from it, they stay in the DRAKON over its entire length. This gives an estimate for the region in which the plasma can be produced.

The numerical studies of the DRAKON-1 model device with transient regions show that the optimum pitch angle of the helix is $\theta = 42°$. Such a magnetic configuration provides the minimum (with respect to θ) flow of the Pfirsh–Schluter currents into the rectilinear regions, as well as the almost minimum departure of the drift surfaces from the magnetic ones. Thus, the results of single-particle calculations give an idea of the behavior of the diamagnetic current in the system.

APPENDIX

Calculation of the Magnetic Field

The magnetic field of a single coil with the radius a and current J was calculated by the Biot–Savart formula [6]

$$\mathbf{B}(\mathbf{r}) = \frac{J}{c}\oint\frac{[d\mathbf{l}_k, \mathbf{R}]}{R^3}, \tag{A.1}$$

where $d\mathbf{l}_k$ is the element of the coil length, $\mathbf{R} = \mathbf{r} - \mathbf{r}^*$, and $\mathbf{r}^*$ is the radius vector of the point in the coil; integration is carried out over the coil contour. If we introduce the coil coordinate system

$$\begin{aligned} z_k &= (\mathbf{R}', \boldsymbol{\tau}_k), \\ \mathbf{r}_k &= \mathbf{R}' - z_k\boldsymbol{\tau}_k, \\ (r_k)^2 + (z_k)^2 &= (R')^2, \\ \mathbf{R}' &= \mathbf{r} - \mathbf{r}_{0k}, \end{aligned} \tag{A.2}$$

where $\boldsymbol{\tau}_k$ is the unit vector of the coil axis and $\mathbf{r}_{0k}$ is the radius vector of the coil center, then, denoting $r = r_k$ and $z = z_k$, the corresponding magnetic field components B_r and B_z (A.1) can be represented in the form

$$B_r = \frac{2J}{c}\frac{z}{r\sqrt{(a+r)^2+z^2}}\left(-K(m) + \frac{a^2+r^2+z^2}{(a-r)^2+z^2}E(m)\right),$$

$$B_z = \frac{2J}{c}\frac{1}{\sqrt{(a+r)^2+z^2}}\left(K(m) + \frac{a^2-r^2-z^2}{(a-r)^2+z^2}E(m)\right),$$

$$m = \frac{4ar}{(a+r)^2+z^2}, \tag{A.3}$$

$$K(m) = \int_0^{\frac{\pi}{2}}\frac{d\varphi}{\sqrt{1-m\sin^2\varphi}},$$

$$E(m) = \int_0^{\frac{\pi}{2}} d\varphi\sqrt{1-m\sin^2\varphi}.$$

To save on computation time, the complete elliptic integrals $K(m)$ and $E(m)$ for $m < m^* = 0.1$ were approximated by a series in terms of m, which results in the representation of B_r and B_z in the form (here, J is in A and B is in G)

$$B_r = \frac{\pi J}{10}\frac{3maz}{4((a+r)^2+z^2)^{3/2}}f(m),$$

$$B_z = \frac{\pi J}{10}\frac{1}{((a+r)^2+z^2)^{1/2}}\left[\frac{2a^2E_1(m)}{(a-r)^2+z^2} - \frac{3m^2}{16}f(m)\right],$$

$$\begin{aligned} f(m) &= \left(1 + \sum_{n=1} a_{fn}\right)\frac{1}{1-m}, \\ a_{f0} &= 1, \quad a_{fn} = a_{f(n-1)}\frac{(4n^2-1)m}{4n(n+2)}, \end{aligned} \tag{A.4}$$

$$\begin{aligned} E_1(m) &= 1 + \sum_{n=1} a_{en}, \\ a_{e0} &= 1, \quad a_{en} = a_{e(n-1)}\frac{(2n-1)(2n-3)m}{(2n)^2}. \end{aligned}$$

For $m > m^*$, $K(m)$ and $E(m)$ were calculated by the method of the arithmetical–geometrical mean, which, for B_r and B_z, yields

$$B_r = \frac{\pi J}{10}\frac{z}{r\sqrt{(a+r)^2+z^2}}\left(-K_1(m) + \frac{1-m/2}{1-m}E_1(m)\right),$$

$$B_z = \frac{\pi J}{10}\frac{1}{\sqrt{(a+r)^2+z^2}}\left(K_1(m) + \frac{a^2-r^2-z^2}{(a-r)^2+z^2}E_1(m)\right),$$

$$\begin{aligned} K_1(m) &= \frac{1}{a_N}, \\ E_1(m) &= K_1(m)\left(1 - \frac{1}{2}\sum_{n=0}^{N} 2^n C_n^2\right), \\ a_0 &= 1, \quad a_n = \frac{a_{n-1}+b_{n-1}}{2}, \\ b_0 &= \sqrt{1-m}, \quad b_n = \sqrt{a_{n-1}b_{n-1}}, \\ C_0 &= \sqrt{m}, \quad C_n = \frac{a_{n-1}-b_{n-1}}{2}, \quad C_N = 0. \end{aligned} \tag{A.5}$$

REFERENCES

1. V. M. Glagolev, B. B. Kadomtsev, V. D. Shafranov, and B. A. Trubnikov, in *Proceedings of 10th European Conference on Controlled Fusion and Plasma Physics, Moscow, 1981*, Vol. 1, paper E-8.
2. S. F. Perelygin, Preprint No. 021, MEPI (Moscow Engineering Physics Institute, Moscow, 1996).
3. V. V. Arsenin, V. M. Glagolev, B. B. Kadomtsev, *et al.*, in *Proceedings of 9th IAEA Conference on Plasma Physics and Controlled Nuclear Fusion Research, Baltimore, 1982* [Nucl. Fusion Suppl. **3**, 159 (1983)].
4. S. F. Perelygin and V. M. Smirnov, Fiz. Plazmy **17**, 945 (1991) [Sov. J. Plasma Phys. **17**, 551 (1991)].
5. S. F. Perelygin and V. M. Smirnov, Nucl. Fusion **33**, 354 (1993).
6. L. D. Landau and E. M. Lifshitz, *Electrodynamics of Continuous Media* (Nauka, Moscow, 1970; Pergamon, Oxford, 1960).

Translated by A. D. Smirnova[†]

[†] Deceased.

Plasma Physics Reports, Vol. 26, No. 5, 2000, pp. 388–396. Translated from Fizika Plazmy, Vol. 26, No. 5, 2000, pp. 416–425.

PLASMA DYNAMICS

Radial Structure of the Wakefield Excited during the Self-Modulation of a Laser Pulse in a Plasma

N. E. Andreev*, V. I. Kirsanov*, and A. S. Sakharov**

**High Energy Density Research Center, Associated Institute for High Temperatures, Russian Academy of Sciences, Izhorskaya ul. 13/19, Moscow, 127412 Russia*

***Institute of General Physics, Russian Academy of Sciences, ul. Vavilova 38, Moscow, 117942 Russia*

Received October 21, 1999

Abstract—A study is made of the structure of the wakefield excited in the linear stage of the self-modulation of a high-power laser pulse in a homogeneous underdense plasma. It is shown that the fronts of the wake wave are curved and the profile of the wakefield amplitude differs strongly from the intensity profile of the laser pulse. The diffraction effects are found to play a key role in the formation of the transverse profile of the wakefield. © *2000 MAIK "Nauka/Interperiodica".*

1. INTRODUCTION

In recent years, much attention has been devoted to the problem of the interaction of high-power laser pulses with underdense plasmas. The increased interest in this problem is associated, in particular, with the development of laser schemes for particle acceleration by the plasma wakefield generated by laser pulses [1–3]. One of the most important problems in this line of research is that of investigating the structure of the wakefield, which can be essentially non-one-dimensional under the strong focusing conditions of laser light.

One of the ways of generating a large-amplitude wakefield is to create conditions for the onset of an instability that gives rise to the self-modulation of a short ($t_0 \le 1$ ps) laser pulse propagating in an underdense plasma, such that $\omega \gg \omega_p$, where ω is the carrier frequency of the pulse and $\omega_p \equiv (4\pi e^2 n_{e0}/m_e)^{1/2}$ is the electron plasma frequency. This method for generating plasma waves was first proposed in [4–6] and then was implemented in experiments [7–9]. The instability causes the pulse to become modulated (with the characteristic longitudinal wavenumber $k_p \equiv \omega_p/v_g \approx \omega_p/c$, where $v_g = kc^2/\omega \approx c$ is the group velocity of a laser pulse) due to the redistribution of the laser energy in either the longitudinal [10] or transverse [2, 11–14] direction. In order to accelerate electrons to energies of about 1 GeV and higher, the laser pulse should be strongly focused and the plasma density should be sufficiently low, in which case the transverse redistribution of laser energy is expected to be the main cause of the instability.

In the conventional simplified analytic approach to describing the effects associated with the transverse redistribution of laser energy in the course of laser–plasma interaction, the radial profiles of the electromagnetic field phase and perturbed plasma permittivity are assumed to be parabolic (the aberration-free approximation [15]). In the aberration-free approximation, the initially Gaussian transverse profile of the laser pulse intensity will always remain Gaussian, in which case the equations for the electromagnetic field reduce to the equation for the field amplitude on the axis (or to the equation for the laser spot size).

The aberration-free approximation is justified for moderate-power laser pulses guided with preformed plasma density channels [16] under conditions such that the amplitudes of the instability-driven perturbations of the plasma permittivity $\delta\varepsilon$ are much smaller than the radial variations of the plasma permittivity in the channel, $\delta\varepsilon_0$. For laser pulses guided in initially homogeneous ($\delta\varepsilon_0 = 0$) nonlinear media (in particular, in plasmas), retaining the lowest order terms in the expansion of the perturbed plasma permittivity in powers of r^2 is justified only in the axial region. Below, the aberration-free approximation applied to the processes near the pulse axis will be referred to as the paraxial approximation. We will show that the paraxial approximation can be used to describe satisfactorily how the amplitude of the excited plasma wave grows on the pulse axis. On the other hand, the solutions obtained in the paraxial approximation are not completely self-consistent, so that this approximation is inapplicable for describing the evolution of both the radial structure of an electromagnetic field and the perturbed electron density during the self-modulation of a laser pulse in a plasma.

Our purpose here is to investigate the radial structure of the wakefield excited during the self-modulation of a laser pulse. The linear stage of the instability is

1063-780X/00/2605-0388$20.00 © 2000 MAIK "Nauka/Interperiodica"

analyzed using the self-consistent set of equations describing the interaction between a weakly relativistic laser pulse and an underdense plasma [4–6, 17] without any *a priori* assumptions regarding the shape of the transverse profiles of the amplitudes of the excited perturbations. We show that the radial profile of the wakefield amplitude differs strongly from the transverse profile of the laser pulse and that the fronts of the wake wave are substantially curved.

2. BASIC EQUATIONS

We consider a laser pulse with an axisymmetric distribution of the electric field amplitude $E_0(z, r, t)$ propagating in an initially homogeneous (n_{e0} = const) underdense ($\omega \gg \omega_p$) plasma along the z-axis. We assume that the pulse is not too intense, $v_E/c = eE_0/m_e c\omega \ll 1$.

We describe the evolution of the electric field amplitude and electron density using the self-consistent set of equations [17]

$$\left(2i\omega\frac{\partial}{\partial t} + c^2\Delta_\perp + \frac{\omega_p^2}{\omega^2}\frac{\partial^2}{\partial\xi^2} + 2c\frac{\partial^2}{\partial\xi\partial t}\right)a = \omega_p^2\left(N - \frac{1}{4}|a|^2\right)a, \quad (1)$$

$$\left(\frac{\partial^2}{\partial\xi^2} + k_p^2\right)N = \frac{1}{4}\Delta|a|^2. \quad (2)$$

Here, $\xi = z - v_g t$, a is a slowly varying ($|\partial \ln a/\partial t| \ll \omega$) dimensionless complex electric-field amplitude related to the electric field E of the pulse by

$$\frac{eE}{m_e c\omega} \equiv \frac{1}{2}(a(\xi, r, t)\exp(ikz - i\omega t) + \text{c.c.}), \quad (3)$$

$N \equiv \delta n_e/n_{e0} \ll 1$ is the dimensionless perturbed electron density, $\Delta_\perp \equiv (1/r)\partial/\partial r(r\partial/\partial r)$, and $\Delta \equiv \partial^2/\partial\xi^2 + \Delta_\perp$. Equation (2) is written in the quasisteady approximation (without the terms $c^{-2}\partial^2/\partial t^2$ and $2c^{-1}\partial^2/\partial\xi\partial t$ in parentheses on the left-hand side); i.e., the perturbations are assumed to grow on characteristic time scales longer than the pulse duration t_0.

We consider the self-modulation of a sufficiently long ($\omega_p t_0 \gg 1$) laser pulse whose initial intensity obeys a Gaussian transverse profile

$$a_0(\xi, r) = a_m(\xi)\exp(-r^2/r_0^2), \quad (4)$$

where $r_0 \gg k_p^{-1}$.

We assume that the intensity $a_m(\xi)$ varies gradually in the region $\xi < 0$ ($d\ln a_m/d\xi \ll k_p$) and decreases rather sharply (on a scale length shorter than or comparable with k_p^{-1}) inside the pulse front (in the region $\xi > 0$). In this case, the plasma wave generated by the pulse front gives rise to the initial perturbations of the electron density (see, e.g., [18, 19]):

$$N|_{t=0} = N_f\exp(-r^2/r_0^2)\cos k_p\xi. \quad (5)$$

Note that the shape of the front has an insignificant impact on the dynamics of the laser-pulse–plasma interaction and governs exclusively the initial amplitude of the excited plasma wave. For simplicity, we assume that the wave amplitude undergoes a jump at the pulse front ($k_p L_f \ll 1$), in which case the initial amplitude of the plasma wave excited by the front is $N_f = (1/4)a_m^2$ ($\xi = 0$).[1]

Below, we will be interested in the case such that

$$1 \ll k_p^2 r_0^2 \ll \frac{16\omega^2}{\omega_p^2}, \quad 1 \ll \frac{\omega_p W}{P_c} \ll \frac{\omega^2}{\omega_p^2}, \quad (6)$$

where $W = c^{-1}\int P d\xi$ is the pulse energy, $P = \frac{c}{4}\left(\frac{m_e c\omega}{e}\right)^2\int_0^\infty |a|^2 r dr \approx 0.55k^2 r_0^2 a_m^2$ GW is the pulse power, and $P_c \approx 17\omega^2/\omega_p^2$ GW [20, 21] is the threshold power for relativistic self-focusing ($P/P_c \approx 0.032k_p^2 r_0^2 a_m^2$). Under conditions (6), the self-modulation of the pulse occurs primarily due to the transverse energy redistribution [11] (the third and fourth terms in parentheses on the left-hand side of equation (1) are small in comparison with the second term) and develops on time scales much shorter than the Rayleigh time $t_R \equiv kr_0^2/2c$ (the characteristic time for the diffractive spreading of the pulse).

From equations (1) and (2), we can immediately see that, when the transverse redistribution of the pulse energy dominates, the radial profiles of the electron density that form during the self-modulation process should differ greatly from the transverse profile of a_0^2. In fact, using the relationship $\int_0^\infty |a^2| r dr = \text{const}$, which is valid in the case at hand, we integrate equation (2) over r with allowance for the boundary condition at the sharp front to obtain

$$\int_0^\infty N(\xi, r, t) r dr = \frac{1}{4}N_f r_0^2\cos(k_p\xi). \quad (7)$$

[1] The perturbations of the electron density, N_{pond}, associated with the displacement of electrons from the region occupied by the pulse in the transverse direction via the high-frequency potential are relatively small ($N_{\text{pond}} \sim a_0^2 k_p^{-2} r_0^{-2} \ll N_f$) and can be neglected.

This indicates that, when the instability is well developed (i.e., the amplification coefficient $K \equiv |N/N_f|_{r=0}$ for the seed perturbations is much larger than unity), either the perturbation N at the fixed longitudinal coordinate should be an alternating-sign function of r or the width of the radial profile of N should decrease substantially (to about $r_0 K^{-1/2}$).

3. PARAXIAL APPROXIMATION

Here, we consider the radial structure of the electron density perturbations excited during the self-modulation of a laser pulse within the paraxial approximation.

In this approximation, which is widely used in simplified analyses of the evolution of the transverse profiles of laser beams and pulses, the complex amplitude a of the laser field and the perturbed electron density N are represented as [15]

$$a = \frac{a_m}{f(\xi, t)} \exp\left(-\frac{r^2}{f^2(\xi, t) r_0^2}\right) \times \exp(i\psi_0(\xi, t) + i\psi_2(\xi, t) r^2), \quad (8)$$

$$N = N_0(\xi, t) + N_2(\xi, t)\frac{r^2}{r_0^2}. \quad (9)$$

In other words, we expand the perturbed density and the phase of the pulse in powers of r, retaining terms up to the second order, and assume that the transverse profile of the laser field amplitude remains Gaussian (with the transverse dimension $r_0 f$). Then, we substitute (8) and (9) into (1) and (2) and linearize the resulting equations in $\delta f \equiv f - 1$.

We represent N as $N = (1/2)[\tilde{N}\exp(ik_p\xi) + \text{c.c.}]$, where $\tilde{N} = \tilde{N}_0 + \tilde{N}_2 r^2/r_0^2$, and introduce the dimensionless variables

$$\zeta = (cW)^{-1}\int_{\infty}^{\xi} P d\xi, \quad \rho = \frac{r}{r_0}, \quad \tau = \frac{1}{\sqrt{\beta}}\frac{t}{t_R}, \quad (10)$$

where the small parameter

$$\beta \equiv \left(\frac{1}{8}\int a_m^2(\xi) k_p^3 r_0^2 d\xi\right)^{-1} \approx (3.9\omega_p W/P_c)^{-1} \ll 1 \quad (11)$$

is equal in order of magnitude to the squared ratio of the characteristic rise time of the self-modulational instability to the characteristic time t_R for the diffractive spreading of the pulse.

As a result, for a pulse with the initial radial profile (4) and a sharp front, equations (1) and (2) reduce to the following equation for the envelope of the electron density perturbations on the axis $\tilde{N}_0$ (see [11–14]):

$$\frac{\partial^2}{\partial\tau^2}\frac{\partial}{\partial\zeta}\tilde{N}_0 = -2i\left(\tilde{N}_0 - \frac{N_f}{2}\right) \quad (12)$$

with the initial and boundary (at $\zeta = 0$) conditions

$$\tilde{N}_0|_{\tau=0} = \tilde{N}_0|_{\zeta=0} = N_f, \quad \left.\frac{\partial\tilde{N}_0}{\partial\tau}\right|_{\tau=0} = 0. \quad (13)$$

The quantities $\tilde{N}_2$ and $\tilde{N}_0$ are related by $\tilde{N}_2 = 2N_f - 4\tilde{N}_0$; i.e., in the axial region, the envelope of the electron density perturbations is

$$\tilde{N} = \tilde{N}_0 - (4\tilde{N}_0 - 2N_f)\frac{r^2}{r_0^2}. \quad (14)$$

The solution to equation (12) has the form [12, 13]

$$\tilde{N}_0 = N_f\left(1 + \frac{1}{2}\sum_{n=1}^{\infty}\frac{1}{n!(2n)!}(-2i\xi\tau^2)^n\right). \quad (15)$$

We define the characteristic size of the electron density perturbations in the transverse direction as

$$R_N \equiv [-2|\tilde{N}|/(\partial^2|\tilde{N}|/\partial r^2)|_{r=0}]^{1/2}. \quad (16)$$

Then, with allowance for (14), we obtain

$$R_N \equiv \frac{1}{2}\left[1 - \text{Re}\left(\frac{N_f}{2\tilde{N}_0}\right)\right]^{-1/2} r_0. \quad (17)$$

We can see that, in the paraxial approximation, the characteristic width R_N of the wake near the axis, which is equal to $R_N = r_0/\sqrt{2}$ at $t = 0$, decreases to $r_0/2$ in the initial stage of instability and then (for $K \gg 1$) remains unchanged.

Representing $\tilde{N}$ in the form $\tilde{N} = |\tilde{N}|\exp(i\varphi)$ and using (14), we can find the radius of curvature R_c of the front of the electron density perturbations, which is defined as $\varphi(r, \xi) + k_p\xi = \text{const}$. In the axial region, we have

$$R_c^{-1} = -\text{Im}\left(\frac{1}{\tilde{N}_0}\frac{\partial^2\tilde{N}}{\partial r^2}\right)k_p^{-1} = -4\,\text{Im}\left(\frac{N_f}{\tilde{N}_0}\right)k_p^{-1} r_0^{-2}, \quad (18)$$

where we adopted $R_c > 0$ for a concave front. This expression shows that, in the initial stage of instability ($K \geq 1$), the originally planar fronts of a wake wave become curved ($R_c^{-1} \sim k_p^{-1} r_0^{-2}$); however, in the stage of well-developed instability ($K \gg 1$), the front curvature R_c^{-1} rapidly falls to zero according to the law $\sim 1/K(t)$. Therefore, a theoretical approach based on the paraxial approximation for a homogeneous plasma predicts neither a substantial increase in the transverse inhomoge-

neity of the wake nor the curvature of the fronts of a wake wave in the stage of well-developed self-modulational instability. Also, within this approach (by virtue of the basic assumptions underlying the paraxial approximation), we fail to describe the formation of nonmonotonic transverse profiles of the wake.

4. SELF-CONSISTENT RADIAL PROFILES OF THE PERTURBATIONS

Now, we consider a linear approximation that gives a better insight into the transverse structure of the perturbations produced during the self-modulation of a laser pulse. We represent a in the form

$$a = A\exp(i\psi), \tag{19}$$

where A and ψ are the real amplitude and real phase of the pulse. In contrast to the paraxial approximation, we do not make any assumptions regarding the shape of the transverse profile of A and do not expand ψ and N in powers of r^2.

We analyze how the self-modulation of the pulse perturbs the laser field on time scales $t \ll t_R$, on which the diffractive spreading of an unmodulated pulse can be neglected. We linearize equations (1) and (2) in small quasi-periodic (with a longitudinal wavenumber close to k_p) deviations of the amplitude and phase, δA and $\delta\psi$, from the unperturbed state (in which the wave fronts of a laser pulse are planar, $\psi_0 = 0$).

Representing δA, $\delta\psi$, and N in the form

$$\{\delta A, \delta\psi, N\} = \frac{1}{2}(\{\delta\tilde{A}, \delta\tilde{\psi}, \tilde{N}\}\exp(ik_p\xi) + \text{c.c.}) \tag{20}$$

and assuming that $|\Delta_\perp| \ll |\partial^2/\partial\xi^2| \approx k_p^2$, we obtain from (1) and (2) the following expressions for the slowly varying ($\partial\ln\{\delta\tilde{A}, \delta\tilde{\psi}, \tilde{N}\}/\partial\xi \ll k_p$) complex amplitudes of the perturbations in the region occupied by the pulse, $-L < \xi < 0$:

$$\frac{\partial}{\partial t}\delta\tilde{\psi} = -\frac{\omega_p^2}{2\omega}\tilde{N} + \frac{\omega_p^2}{4\omega}a_0\delta\tilde{A} + \frac{c^2}{2\omega}\frac{1}{a_0^2 r}\frac{\partial}{\partial r}a_0^2 r\frac{\partial}{\partial r}\frac{1}{a_0}\delta\tilde{A}, \tag{21}$$

$$a_0\frac{\partial}{\partial t}\delta\tilde{A} = -\frac{c^2}{2\omega}\frac{1}{r}\frac{\partial}{\partial r}a_0^2 r\frac{\partial}{\partial r}\delta\tilde{\psi}, \tag{22}$$

$$\frac{\partial}{\partial\xi}\tilde{N} = \frac{1}{4}ik_p a_0\delta\tilde{A}. \tag{23}$$

Note that the terms on the right-hand side of (21) describe, respectively, the refraction by electron density perturbations, relativistic self-focusing, and diffraction.

Equations (21)–(23) can be reduced to the following equation for $\tilde{N}$:

$$\left(\frac{\partial^2}{\partial t^2} + \frac{1}{4}\frac{c^4}{\omega^2}\frac{1}{r}\frac{\partial}{\partial r}ra_0^2\frac{\partial}{\partial r}\frac{1}{a_0^2 r}\frac{\partial}{\partial r}a_0^2 r\frac{\partial}{\partial r}\frac{1}{a_0^2}\right)\frac{\partial}{\partial\xi}\tilde{N} = \frac{i}{16}k_p\omega_p^2\frac{c^2}{\omega^2}\frac{1}{r}\frac{\partial}{\partial r}a_0^2 r\frac{\partial}{\partial r}\tilde{N}, \tag{24}$$

where we keep the term accounting for the diffraction of the perturbed laser field (the second term in parentheses on the left-hand side). Note that, for perturbations with characteristic transverse scale sizes of about the transverse dimension r_0 of the pulse, this term is small in comparison with the first term on time scales $t \ll t_R$. The second derivative with respect to r on the right-hand side of (24) results in a more rapid growth of perturbations with shorter transverse scale sizes. As a result, the role of the diffraction term in (24) (which is proportional to the fourth derivative with respect to r) increases. When this term becomes on the order of the first term, the growth rate of the small-scale transverse perturbations decreases. Consequently, it is very important to take into account diffraction effects, because they lower the anomalously high growth rates of perturbations with characteristic transverse scale sizes much shorter than the transverse dimension of the pulse.

Switching to the dimensionless variables (10) and introducing the notation

$$\hat{Q}_r\tilde{N} \equiv \frac{1}{4\rho}\frac{\partial}{\partial\rho}\exp(-2\rho^2)\rho\frac{\partial}{\partial\rho}\tilde{N}, \tag{25}$$

$$\hat{Q}_d\tilde{N} \equiv \frac{1}{16\rho}\frac{\partial}{\partial\rho}\exp(-2\rho^2)\rho\frac{\partial}{\partial\rho}\exp(2\rho^2)\frac{1}{\rho}\frac{\partial}{\partial\rho} \times \exp(-2\rho^2)\rho\frac{\partial}{\partial\rho}\exp(2\rho^2)\tilde{N}, \tag{26}$$

we obtain from (24) the following equation for a pulse with the initial radial profile (4) and a sharp front:

$$\left(\frac{\partial^2}{\partial^2\tau} + \beta\hat{Q}_d\right)\frac{\partial}{\partial\zeta}\tilde{N} = \frac{i}{2}\hat{Q}_r\tilde{N}, \tag{27}$$

which contains a small dimensionless parameter β.

If the seed wave of the electron density perturbations is generated by the pulse front [see (5)], then the initial and boundary (at $\zeta = 0$) conditions for $\tilde{N}$ have the form

$$\tilde{N}\big|_{\tau=0} = \tilde{N}\big|_{\zeta=0} = N_f\exp(-2\rho^2), \quad \left.\frac{\partial\tilde{N}}{\partial\tau}\right|_{\tau=0} = 0. \tag{28}$$

In (27), the operators $\hat{Q}_r$ and $\hat{Q}_d$ account for the effects of refraction of the laser field by the excited electron-density wave and the diffraction of the perturbed laser

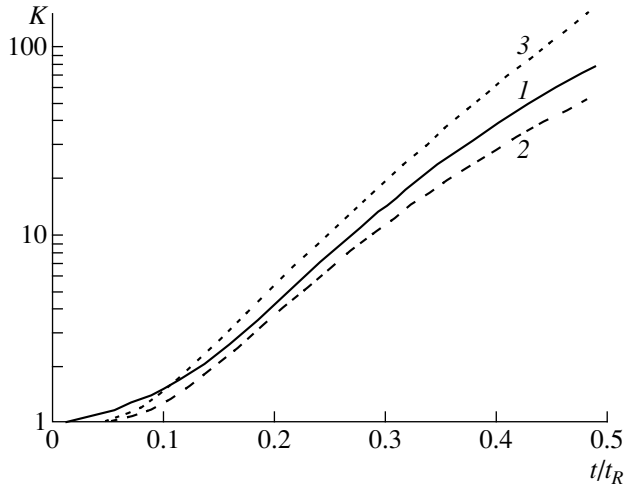

Fig. 1. Time evolutions of the amplification coefficient K of the seed perturbations of the electron density on the axis behind the pulse for $\omega/\omega_p = 45$, $a_{max} = 0.15$, $k_p r_0 = 28$, $k_p L = 100$, $k_p L_1 = 6$, and $k_p L_2 = 15$ (which corresponds to $\beta = 1/256$). The evolutions were traced by numerically solving equations (1) and (2) (curve *1*), equation (27) (curve *2*), and equation (12) in the paraxial approximation (curve *3*).

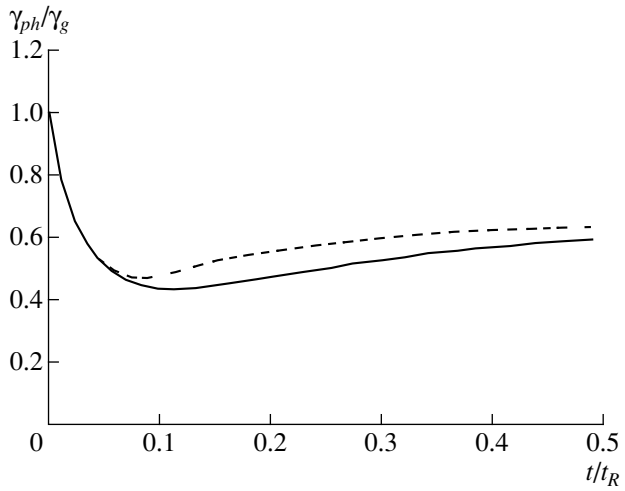

Fig. 2. Time evolutions of the relativistic factor γ_{ph} computed from the phase velocity of the wake wave on the pulse axis for the same plasma and pulse parameters as in Fig. 1. The solid curve illustrates the solution to equation (27), and the dashed curve was obtained in the paraxial approximation.

field, respectively. In the paraxial approximation, equation (12) is an analogue of equation (27).

5. NUMERICAL RESULTS

Numerical analysis of the linear stage of self-modulation showed that, in the parameter range (6), the solution to equations (1) and (2) is well approximated by the solution to the reduced one-parameter equation (27). Figure 1 presents time evolutions of the amplification coefficient K of the seed perturbations of the electron density on the axis behind the pulse. The evolutions were traced by numerically solving equations (1) and (2) (curve *1*), equation (27) (curve *2*), and equation (12) in the paraxial approximation (curve *3*). The longitudinal profile of the pulse $a_m(\xi)$ was specified as

$$a_m(\xi) = \begin{cases} a_{\max}\exp\left(-\dfrac{\xi^4}{L_1^4}\right) \text{ for } \xi > 0 \text{ (front)}, \\ a_{\max} \text{ for } -L < \xi < 0 \text{ (top)}, \\ a_{\max}\exp\left[-\dfrac{(\xi - L)^4}{L_2^4}\right] \text{ for } \xi < -L \text{ (trailing edge)}. \end{cases} \quad (29)$$

Computations were carried out for the following parameters of the plasma and laser pulse: $\omega/\omega_p = 45$, $a_{max} = 0.15$, $k_p r_0 = 28$ (which corresponds to $P/P_c \approx 0.57$ at the top of the pulse), $k_p L = 100$, $k_p L_2 = 15$, and $k_p L_1 = 6$. For these parameter values, formula (11) gives $\beta \approx 1/256$.

We can see that the time evolution $K(t)$ computed from (27) is close to that obtained by solving equations (1) and (2) numerically and that the growth of the electron density perturbations on the whole is well described by the paraxial approximation, although the amplification coefficient is somewhat overestimated.

As the amplitude of the wake wave grows, its phase velocity decreases [11–14]. Figure 2 shows time evolutions of the ratio of the relativistic factor $\gamma_{ph} = (1 - v_{ph}^2/c^2)^{-1/2}$ computed from the phase velocity $v_{ph} = (1 - \omega_p^{-1}\partial\varphi/\partial t)v_g$ of the wake wave on the pulse axis to $\gamma_g = (1 - v_g^2/c^2)^{-1/2}$. The solid curve illustrates the solution to equation (27), and the dashed curve was obtained in the paraxial approximation. The time evolutions of γ_{ph}/γ_g calculated using these approximate approaches are seen to be in close agreement.

Hence, the numerical results shown in Figs. 1 and 2 allow us to conclude that, in the above parameter range, the paraxial approximation satisfactorily describes both the amplitude and phase parameters of a wake wave on the pulse axis.

Now, we examine the transverse structure of the wake wave excited during the self-modulation of a laser pulse. Figure 3 shows the contours of N in the trailing part of the pulse at $t = 0.45t_R$ for the same plasma and pulse parameters as in Fig. 1. The perturbed electron density is normalized to the maximum perturbed density N in the trailing part of the pulse. One can see that the wake wave structure reconstructed from the solution to the reduced one-parameter equation (27) (Fig. 3b) agrees well with that obtained using equations

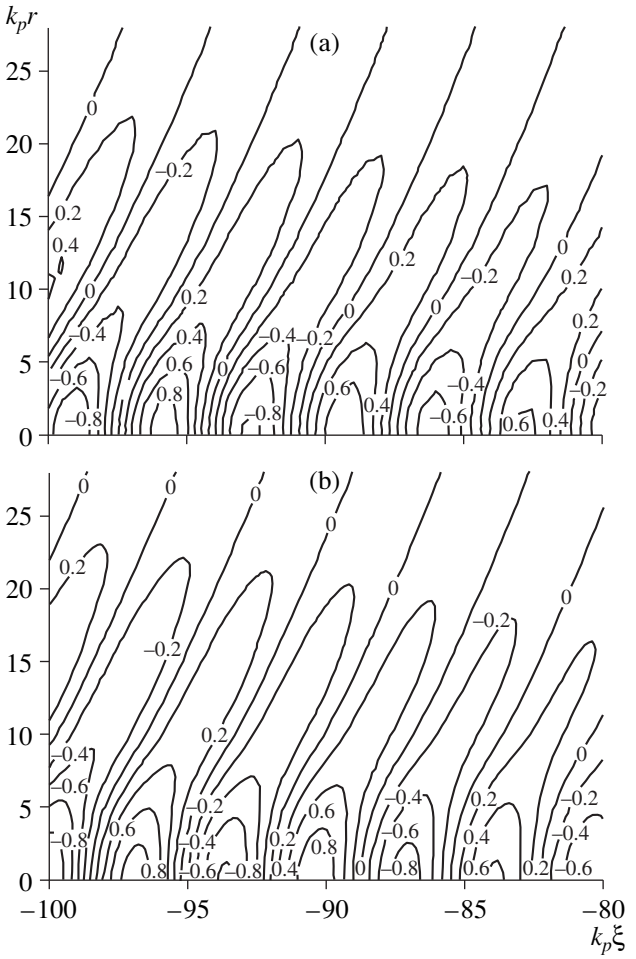

Fig. 3. Structure of the electron density perturbations in the trailing part of the pulse at $t = 0.45t_R$ for the same plasma and pulse parameters as in Fig. 1: (a) solution to equations (1) and (2) and (b) solution to equation (27).

(1) and (2) (Fig. 3a). The fronts of the plasma wave are seen to be highly concave; in the axial region, the front curvature R_c^{-1} is about $20k_p^{-1}r_0^{-2}$.

Figure 4 illustrates the evolution of the profile of the wake wave behind the pulse ($\zeta = -1$) for the same plasma and pulse parameters as in Fig. 1. The curves in Fig. 4 are obtained for a fixed longitudinal coordinate such that the perturbed electron density N is maximum on the axis. The solid curves correspond to the radial profiles of the perturbations $N = (1/2)[\tilde{N}\exp(ik_p\xi) + \text{c.c.}]$ at the initial time $t = 0$ (curve *1*) and at the time $t = 0.45t_R$ ($\tau \approx 7.2$), at which $K \approx 60$. Curve *2* illustrates the solution to equations (1) and (2), curve *3* reflects the solution to equation (27), and curve *4* refers to the paraxial approximation. The dashed curves show the perturbation amplitudes $|\tilde{N}|$ (the envelope of the electron density perturbations N) computed from the solutions to equations (1) and (2) (curve *2*') and to equation (27) (curve *3*'). The electron density is normalized to the

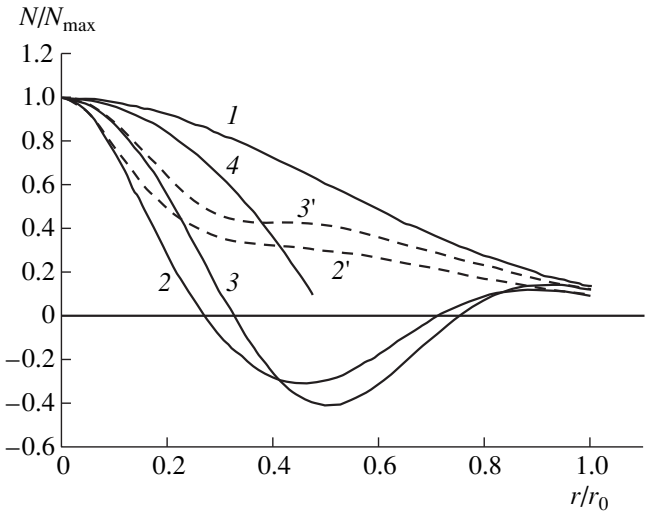

Fig. 4. Time evolution of the plasma wave behind the pulse for the same plasma and pulse parameters as in Fig. 1. The curves are obtained at the fixed longitudinal coordinate ξ at which the perturbed electron density N is maximum on the axis. The solid curves correspond to the radial profiles of the perturbed electron density N at the initial time $t = 0$ (curve *1*) and at the time $t = 0.45t_R$. Curve *2* illustrates the solution to equations (1) and (2), curve *3* refers to the solution to equation (27), and curve *4* refers to the paraxial approximation. The dashed curves show the amplitudes of the electron density perturbations (the envelope of the perturbations N) computed from the solutions to equations (1) and (2) (curve *2*') and to equation (27) (curve *3*'). The electron density is normalized to the maximum perturbed density in the plasma wave.

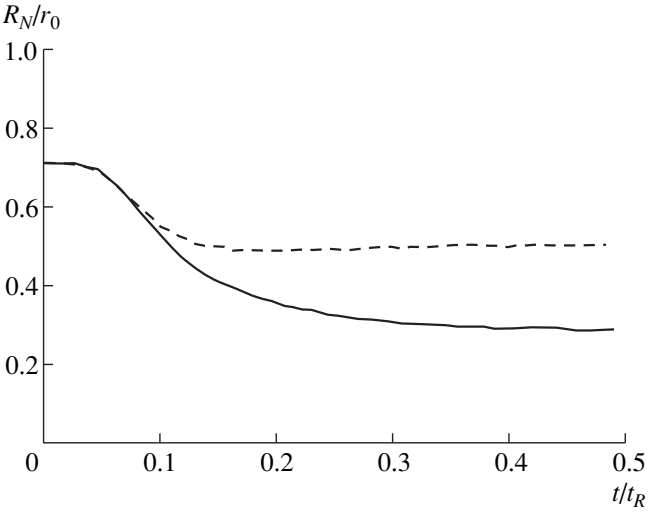

Fig. 5. Time evolutions of the characteristic transverse scale size R_N of the electron density perturbations in the axial region for the same plasma and pulse parameters as in Fig. 1. The solid curve is calculated using equation (27), and the dashed curve refers to the paraxial approximation.

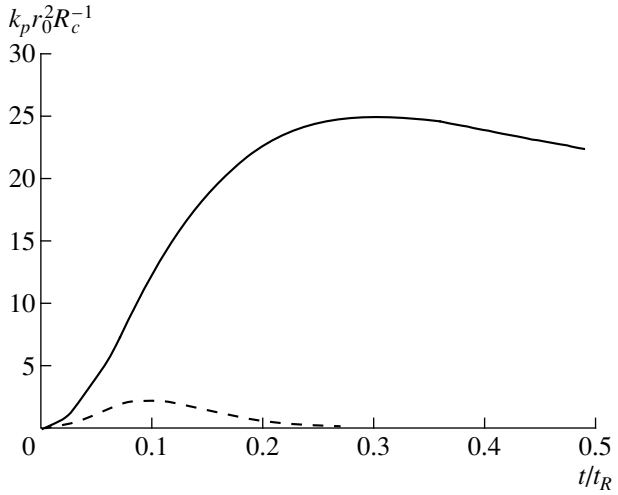

Fig. 6. Time evolution of the curvature of the wake wave fronts in the axial region for the same plasma and pulse parameters as in Fig. 1. The solid curve is calculated from equation (27), and the dashed curve is obtained in the paraxial approximation.

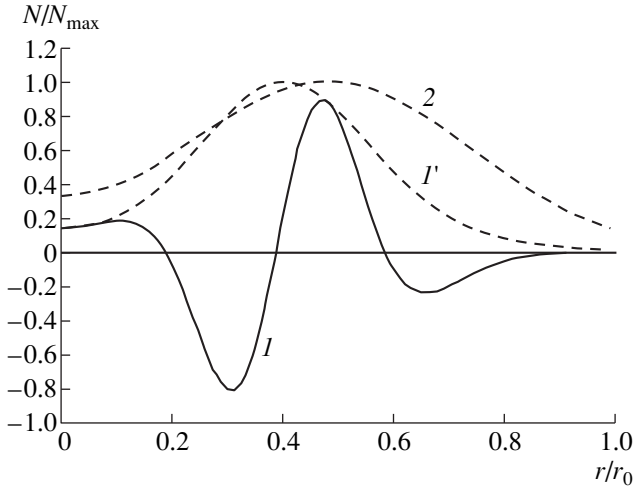

Fig. 7. Radial profile of the plasma wave amplitude behind the pulse without allowance for the diffraction of laser field perturbations at $\tau = 6.3$: curve *1* is the profile of N at a fixed ξ at which N is maximum (in ξ) along the pulse axis, and curve *1'* is the profile of the perturbation amplitude $|\tilde{N}|$. Curve *2* is the profile of the wake amplitude calculated by solving equations (1) and (2) numerically for a long pulse with $k_p L = 600$ (the remaining parameters are the same as in Fig. 1). The solutions are normalized to the maximum perturbed electron density in the plasma wave.

maximum perturbed density in the plasma wave. The profiles computed from the solutions to equation (27) and to equations (1) and (2) are very similar and differ markedly from the profile obtained in the paraxial approximation in that they have a narrow peak near the pulse axis.

Figure 5 shows time evolutions of the characteristic transverse scale size R_N of the electron density perturbations in the axial region [see (16)]. The solid curve is calculated using equation (27), and the dashed curve illustrates the paraxial approximation. We can see that, in accordance with (17), the wake of the laser pulse in the paraxial approximation narrows only to $R_N = r_0/2$, whereas, in the stage of well-developed instability, the self-consistent profile turns out to be significantly narrower ($R_N \approx 0.3 r_0$).

Note that the curves illustrating the profiles of N at a fixed ξ change sign, which is a manifestation of the curvature of the wake wave fronts. Figure 6 demonstrates the time evolution of the curvature of the wake wave fronts in the axial region. The solid curve is calculated from the solution to equation (27), and the dashed curve is obtained in the paraxial approximation. One can see that, in accordance with formula (18), which refers to the paraxial approximation, the wave fronts are slightly curved only in the initial stage of instability; at later times, they again become planar. In contrast, according to the solution to equation (27), the wave fronts rapidly become substantially curved (the front curvature reaches its maximum $R_c^{-1} \approx 25 k_p^{-1} r_0^{-2}$ at $t \approx 0.3 t_R$) and then the front curvature slowly weakens. Numerical analysis shows that, in the range $50 < \beta^{-1} < 1000$, the maximum curvature is approximately equal to $R_c^{-1} \sim 1.5 k_p^{-1} r_0^{-2} \beta^{-1/2}$.

Here, we must point out the following circumstance. In [22–24], the deformation of the wake wave fronts was governed either by the nonlinear character of the excited plasma wave or by the radial plasma nonuniformity induced by a laser pulse guided in a plasma channel. In contrast, in our problem, the deformation of the fronts of a *linear* wake plasma wave excited in an underdense *homogeneous* plasma by a sufficiently wide quasi-one-dimensional laser pulse ($k_p r_0 \gg 1$) is governed exclusively by the specific features of the self-modulational instability itself.

Now, we analyze the role of diffraction effects in more detail. To do that, we neglect the diffraction of the laser field perturbations (the term with β), in which case the solution to equation (27) can be represented as a series:

$$\tilde{N} = \sum_{m=0}^{\infty} \frac{N_f}{m!(2m)!} (2i\tau^2\zeta)^m (\hat{Q}_r)^m \exp(-2\rho^2). \quad (30)$$

Figure 7 illustrates the radial profile of the plasma wave amplitude behind the pulse ($\zeta = -1$) computed without allowance for the diffraction of laser field perturbations at $\tau = 6.3$, which corresponds to $t \approx 0.4 t_R$ for the above case $\beta \approx 1/256$. Curve *1* is the profile of N at a fixed radial coordinate at which N is maximum (in ξ) along the pulse axis, and curve *1'* is the profile of the perturbation amplitude $|\tilde{N}|$. The solution is normalized to the

maximum perturbed electron density in the plasma wave. We can see that neglecting diffraction radically changes the radial structure of the perturbations: a local dip at the axis appears in the profile of the wake amplitude. Periodic variations of the perturbation amplitude in the radial direction at a fixed ξ provide evidence for an even stronger deformation of the fronts of the excited wake wave if the diffraction effects are ignored.

Hence, a comparison between Figs. 4 and 7 shows that, although β is small (in the case at hand, we have $\beta \approx 1/256$), the diffraction effects play a decisive role in the formation of the radial structure of perturbations.

Clearly, at a prescribed amplification coefficient of the seed perturbations, the smaller the β value (which corresponds to longer pulses at a given power), the lesser the role of the diffraction term (the instability develops on time scales short enough for the diffraction of the laser field perturbations not to come into play). This indicates that, below a certain value of β, we may expect the formation of the profiles of the wake amplitude with a dip at the axis. The results of solving the one-parameter equation (27) numerically show that, for the range of amplification coefficients under study ($K \leq 100$), a dip (instead of a narrow peak) forms in the profiles of the wake amplitude in the axial region at β values of about 10^{-3} or lower. For $\beta \ll 10^{-3}$, the diffractive term in equation (27) is small and the self-modulation proceeds in the same manner as in the absence of diffraction. Curve *2* in Fig. 7 illustrates the profile of the wake amplitude computed by solving equations (1) and (2) numerically for a long pulse with $k_pL = 600$ (the remaining parameters being the same as in Fig. 1)[2] at $t = 0.17t_R$ (which corresponds to $\tau \approx 0.63$). In this case, the parameter β is approximately equal to 1/1360. We can see that, as in the absence of diffraction (curve *1'*), a dip appears in the profile of the wake amplitude in the axial region.

6. CONCLUSION

(i) Our investigation of the radial structure of the wakefield generated during the self-modulation of a moderately intense ($I \leq 10^{17}$ W/cm^3) laser pulse shows that the radial profile of the wake amplitude changes strongly in the course of instability and that, in the parameter range (6) (in which the self-modulation is associated primarily with the transverse energy redistribution), the evolution of this profile can be described by only one dimensionless parameter $\beta \approx (4\omega_p W/P_c)^{-1} \ll 1$, which is proportional to the squared ratio of the rise time of the self-modulational instability to the time for the diffractive spreading of the pulse. During the instability, the characteristic radial scale size of the perturbations decreases, so that the diffraction effects become more important. For $\beta > 10^{-3}$ and in the range of amplification coefficients $K \leq 100$, diffraction has a significant impact on the formation of the profiles of the perturbation amplitude, in which case the profiles of the wake amplitude have a narrow peak in the axial region.

(ii) We have shown that the fronts of the wake wave generated during the self-modulation of the pulse are highly concave. This phenomenon is of interest in connection with the problem of effective resonant wakefield acceleration of relativistic charged particles. On the one hand, such a curvature acts to increase the longitudinal size $\Delta\xi$ of the region in which the wakefield simultaneously accelerates and focuses charged particles injected into the axial region [$k_p\Delta\xi = \pi - \operatorname{arccot}(k_pR_N^2/2R_c)$]. On the other hand, as the transverse scale sizes of the inhomogeneity of the wake wave increase, the effect of the radial component of the electric field on the acceleration of the particles injected into the off-axis plasma region grows, which may lead to an unfavorable increase in the transverse momentum of the accelerated particles. Note that the expansion of the region where the accelerating and focusing phases of the electric field of a wake wave overlap due to the curvature of its fronts was discussed previously in connection with other mechanisms for the deformation of wake wave fronts, such as the nonlinearity of an excited plasma wave [23] and the radial plasma inhomogeneity when a laser pulse is guided in a plasma channel [24, 25]. Here, we have shown that the fronts of a wake wave become curved even in the linear stage of the self-modulation of a laser pulse propagating in a homogeneous plasma.

(iii) In our analysis, we neglected the change in the plasma frequency due to the displacement of plasma ions from the axial region under the action of ponderomotive forces. The deformation of the plasma wave fronts due to a decrease in the plasma frequency near the pulse axis $\delta\omega_p$ is insignificant in the range $(R_c^*)^{-1} < R_c^{-1}$, where $(R_c^*)^{-1} \approx k_p^{-1}c^{-1}\int|\partial^2\delta\omega_p/\partial r^2|d\xi$ is the front curvature associated with the change in the plasma frequency. Our estimates show that, for the above parameters of the plasma and laser pulse and for the pulse durations $t_0 \leq 100\,\omega_p^{-1}$, the change in the plasma frequency $\delta\omega_p$ can be legitimately ignored.

(iv) Recent experiments on wakefield excitation during the self-modulation of laser pulses [7–9] were carried out with a relatively dense plasma ($\omega/\omega_p \sim 10$) and with very strong laser fields ($v_E/c \sim 1$) far above the threshold for relativistic self-focusing ($P/P_c \gg 1$). Under the conditions of those experiments, the excited plasma wave is strongly nonlinear. For this reason, we cannot directly compare our results with the data

[2] For a neodymium laser ($\lambda \approx 1$ μm), these parameters correspond to the pulse duration $t_0 \approx 15$ ps, which substantially exceeds the pulse duration in the proposed schemes for laser acceleration based on the self-modulation mechanism for generating wake plasma waves ($t_0 \leq 1$ ps). The results of computations with these parameter values are presented merely to illustrate the effect of the diffraction of the laser field perturbations.

obtained in experiments aimed at achieving the highest possible rates of laser acceleration of particles. On the other hand, most attention is now focused on attempts to accelerate electrons to unsurpassed energies (of about 1 GeV and higher) by a wakefield excited by a laser pulse in plasma. In this way, it is necessary to operate with a lower density plasma [3], in which case laser pulse focusing should be much weaker than that in the cited experiments. Thus, if we consider a laser pulse with the parameters $\lambda_0 = 1$ μm, $P = 10$ TW, and $t_0 = 1$ ps, which are close to those in the experiments of [7–9], but assume that the pulse is focused to a lesser extent ($r_0 \approx 100$ μm, which corresponds to $a_m \approx 0.2$) in a lower density plasma ($n_e/n_c \approx 10^{-3}$), then we obtain $k_pL \approx 60$ and $P/P_c \approx 0.6$. In this case, the resonant acceleration length [1] coincides with the Rayleigh length and the electrons may be accelerated to energies of about 1 GeV. In this example, the plasma and pulse parameters correspond to $\beta \approx 0.006$. Based on the results obtained, we may expect that the profile of the amplitude of the generated plasma wave will become narrower and the wave fronts will become strongly curved even in the linear stage of the self-modulational instability.

(v) Finally, we can say that, since the radial scale sizes of the laser field perturbations excited during the self-modulation of a laser pulse are much smaller than the characteristic width of the pulse, the features of the radial structure of the wakefield that we have discussed here should lead to a broadening of the angular spectrum of the forward-scattered radiation.

ACKNOWLEDGMENTS

This work was supported in part by the Russian Foundation for Basic Research, project nos. 98-02-17455 and 98-02-16263.

REFERENCES

1. T. Tajima and J. M. Dawson, Phys. Rev. Lett. **43**, 267 (1979).
2. E. Esarey, P. Sprangle, J. Krall, and A. Ting, IEEE Trans. Plasma Sci. **24**, 252 (1996).
3. N. E. Andreev and L. M. Gorbunov, Usp. Fiz. Nauk **169**, 53 (1999).
4. N. E. Andreev, L. M. Gorbunov, V. I. Kirsanov, *et al.*, Pis'ma Zh. Éksp. Teor. Fiz. **55**, 551 (1992) [JETP Lett. **55**, 571 (1992)].
5. P. Sprangle, E. Esarey, J. Krall, and G. Joyce, Phys. Rev. Lett. **69**, 2200 (1992); E. Esarey, P. Sprangle, J. Krall, *et al.*, Phys. Fluids B **5**, 2690 (1993); E. Esarey, J. Krall, and P. Sprangle, Phys. Rev. Lett. **72**, 2887 (1994).
6. T. M. Antonsen, Jr. and P. Mora, Phys. Rev. Lett. **69**, 2204 (1992); T. M. Antonsen, Jr. and P. Mora, Phys. Fluids B **5**, 1440 (1993).
7. K. Nakajima, D. Fisher, Y. Kawakubo, *et al.*, Phys. Rev. Lett. **74**, 4428 (1995).
8. A. Modena, Z. Najmudin, A. E. Dangor, *et al.*, Nature **377**, 606 (1995); IEEE Trans. Plasma Sci. **24**, 289 (1996).
9. D. Umstadter, S.-Y. Chen, A. Maksimchuk, *et al.*, Science **273**, 472 (1996).
10. W. B. Mori, C. D. Decker, D. E. Hinkel, and T. Katsouleas, Phys. Rev. Lett. **72**, 1482 (1994); C. D. Decker, W. B. Mori, K.-C. Tzeng, and T. C. Katsouleas, IEEE Trans. Plasma Sci. **24**, 379 (1996).
11. N. E. Andreev, L. M. Gorbunov, V. I. Kirsanov, *et al.*, Fiz. Plazmy **22**, 419 (1996) [Plasma Phys. Rep. **22**, 379 (1996)].
12. N. E. Andreev, V. I. Kirsanov, A. S. Sakharov, *et al.*, Phys. Plasmas **3**, 3121 (1996).
13. N. E. Andreev, L. M. Gorbunov, V. I. Kirsanov, and A. S. Sakharov, IEEE Trans. Plasma Sci. **24**, 363 (1996).
14. N. E. Andreev, L. M. Gorbunov, V. I. Kirsanov, and A. S. Sakharov, in *Proceedings of Symposium on New Modes of Particle Acceleration: Techniques and Sources, Santa Barbara, CA, 1996* [AIP Conf. Proc. **396**, 61 (1997)].
15. M. B. Vinogradova, O. V. Rudenko, and A. P. Sukhorukov, *Theory of Waves* (Nauka, Moscow, 1990), Chap. 11.
16. J. N. McMulin, C. E. Capjack, and C. R. James, Phys. Fluids **21**, 1828 (1978).
17. N. E. Andreev, L. M. Gorbunov, V. I. Kirsanov, *et al.*, Physica Scripta **49**, 101 (1994).
18. L. M. Gorbunov and V. I. Kirsanov, Zh. Éksp. Teor. Fiz. **93**, 509 (1987) [Sov. Phys. JETP **66**, 290 (1987)]; L. M. Gorbunov and V. I. Kirsanov, Tr. FIAN **219**, 3 (1992).
19. S. V. Bulanov, V. I. Kirsanov, and A. S. Sakharov, Fiz. Plazmy **16**, 935 (1990) [Sov. J. Plasma Phys. **16**, 543 (1990)].
20. A. G. Litvak, Zh. Éksp. Teor. Fiz. **30**, 344 (1969) [Sov. Phys. JETP **30**, 344 (1969)].
21. Y. R. Shen, *The Principles of Nonlinear Optics* (Wiley-Interscience, New York, 1984; Nauka, Moscow, 1989), Chap. 17.
22. S. V. Bulanov, F. Pegoraro, A. M. Pukhov, and A. S. Sakharov, Phys. Rev. Lett. **78**, 4205 (1997).
23. N. E. Andreev, L. M. Gorbunov, and R. R. Ramazashvili, Fiz. Plazmy **23**, 303 (1997) [Plasma Phys. Rep. **23**, 277 (1997)].
24. N. E. Andreev, L. M. Gorbunov, V. I. Kirsanov, *et al.*, Phys. Plasmas **4**, 1145 (1997).
25. N. E. Andreev, E. V. Chizhonkov, A. A. Frolov, and L. M. Gorbunov, Nucl. Instrum. Methods Phys. Res. A **410**, 469 (1998).

Translated by O. E. Khadin

Plasma Physics Reports, Vol. 26, No. 5, 2000, pp. 397–404. Translated from Fizika Plazmy, Vol. 26, No. 5, 2000, pp. 426–433.

PLASMA DYNAMICS

Two-Dimensional Modeling of a Transverse Collisionless Shock Wave

S. F. Garanin, A. I. Golubev, and N. A. Ismailova

All-Russia Research Institute of Experimental Physics, Russian Federal Nuclear Center, Sarov, Nizhni Novgorod oblast, 607190 Russia

Received June 11, 1999

Abstract—Transverse collisionless shock waves in a plasma in which the initial β value is equal to zero for electrons and is small but nonzero for ions are studied in the two-dimensional approximation with allowance for anomalous resistivity. A hybrid model is applied such that the ions are treated in the kinetic approximation and the electrons are described in the hydrodynamic approximation. A collisionless shock wave is generated using a piston with a small two-dimensional perturbation. The ion distribution downstream of the shock front and the effect of electron and ion heating are analyzed. It is shown that, for Alfvén–Mach numbers $M_A > 2$, ion heating is attributed primarily to the ions that have experienced a reflection from the shock front and whose velocities downstream of the front are very high. This conclusion agrees with the results of one-dimensional calculations. Solving the problem as formulated shows that two-dimensional effects are insignificant in the range of low Alfvén–Mach numbers ($M_A \le 5$): the direction of the magnetic field is always close to its initial direction, the ions acquire low velocities along the magnetic field, and the quantitative parameters of the plasma downstream of the shock front are close to those obtained from the one-dimensional model. In the range of higher Alfvén–Mach numbers, two-dimensional effects are more pronounced and the ion distribution function is less anisotropic. © *2000 MAIK "Nauka/Interperiodica".*

1. INTRODUCTION

Hybrid numerical methods are widely used to study collisionless shock waves (CSWs) in the one-dimensional approximation (in which all of the quantities depend only on the coordinate transverse to the shock front) [1–6] as well as in the two- and three-dimensional approximations [7] with allowance for particular physical processes. In most shock experiments, current instabilities (primarily, the ion acoustic instability) should develop at the shock front, giving rise to anomalous plasma resistivity, which serves, together with ion gyration, as the main mechanism for the formation of the CSW structure. Anomalous resistivity was taken into account in the one-dimensional simulations of CSWs carried out in [3, 6]. Note that, according to the results of one-dimensional modeling, the ion distribution downstream of the shock front turns out to be unstable [8, 9]; consequently, the CSW itself is also unstable and is distorted on a spatial scale of about $\sim c/\omega_{pi}$. This was demonstrated by Thomas [7] for CSWs with high Mach numbers. However, he neglected plasma resistance, because it should play an insignificant role in the range of high Mach numbers but requires to resolve relatively short spatial scales.

In [6], we showed that the structure of CSWs with moderate Mach numbers should be investigated with allowance for plasma resistance and Joule heat release and that the latter appears to make the main contribution to the plasma thermal energy in the range $M_A < 8$. Here, we study CSWs in the two-dimensional approximation with allowance for anomalous resistivity. We formulate the problem for a plasma in which the initial β value is equal to zero for electrons and is small but nonzero for ions.

Since the plasma downstream of the shock front relaxes to an equilibrium state on a time scale of about the collision time, which can be sufficiently long in shock experiments, we can assume that, in some cases, the plasma state downstream of the front is quasi-equilibrium. For this reason, it is important to know the plasma characteristics, specifically, the energy expended on electron and ion heating and the ion distribution downstream of the front. Here, we will be concerned with just these plasma characteristics. In the case of a magnetohydrodynamic flow, we can make the following assumptions: the ion distribution function keeps its shape and changes adiabatically with the plasma density on time scales shorter than the characteristic ion–ion collision time (after the relaxation of an instability associated with the anisotropy of the distribution function), the ratio of the relative fractions of the energy spent on electron and ion heating is constant on time scales shorter than the time required for the equalization of the electron and ion temperatures, and the electron and ion energies change adiabatically according to the change in the plasma density. The issues of the ion distribution function and the ratio of the relative fractions of the energy expended on electron and ion heating are also important for plasma devices in which the plasma is heated by CSWs (see, e.g., [10]), because

1063-780X/00/2605-0397$20.00

plasma diagnostics implemented in such devices are based on measurements of the spectra of fusion neutrons [11] and deal just with ion spectra (especially, their high-energy parts).

2. PHYSICAL MODEL

We consider a two-dimensional plasma flow under the following assumptions: a CSW propagates along the x-axis, the initial magnetic field is directed along the z-axis, and all of the quantities are functions of x and z because of the presence of perturbations in the z-direction. All three components of the magnetic field and particle velocities may be nonzero.

We describe the electrons by hydrodynamic parameters: the density n, the velocity $\mathbf{v}_e$, the temperature T_e, and the pressure p_e, assuming that the pressure is $p_e = nT_e$ and the adiabatic power-law index is $\gamma = 5/3$. In contrast, we treat the ions in the kinetic approximation, denoting their velocities by $\mathbf{v}$ and their averaged (over the distribution function) density and velocity by n_i and $\mathbf{U}$, respectively. We also assume that the plasma is quasineutral, $n = n_i$.

The equations of ion motion have the form

$$m_i \frac{d\mathbf{v}}{dt} = e\left(\mathbf{E} + \frac{1}{c}[\mathbf{v}\mathbf{B}]\right) - e\eta\mathbf{j}, \tag{1}$$

where m_i is the mass of an ion, $\mathbf{j} = en(\mathbf{U} - \mathbf{v}_e)$ is the current density, and η is the plasma resistivity. We neglect electron inertia in comparison with electron friction against the ions and write the equation of electron motion as

$$-en\left(\mathbf{E} + \frac{1}{c}[\mathbf{v}_e\mathbf{B}]\right) - \nabla p_e + en\eta\mathbf{j} = 0, \tag{2}$$

in which case the electron energy equation has the form

$$\frac{\partial\left(\frac{3}{2}p_e\right)}{\partial t} = \operatorname{div}\left(-\frac{3}{2}\mathbf{v}_e p_e + \chi\nabla T_e\right) - p_e \operatorname{div}\mathbf{v}_e + (1-\alpha)\eta j^2, \tag{3}$$

where χ is the electron thermal conductivity. We also reduce the Joule heating of plasma electrons, because, under the assumption that the plasma resistivity is anomalous due to ion-acoustic turbulence, a small fraction of the Joule heating power is deposited in the ions. We denote this fraction by α and incorporate the Joule heating of plasma ions by supplementing the right-hand side of equation (1) with the term

$$m_i \frac{\alpha\eta j^2}{2nT_i}(\mathbf{v} - \mathbf{U}), \tag{4}$$

where T_i is the averaged (over the distribution function) local ion energy.

The Maxwell equations have the form

$$\operatorname{curl}\mathbf{B} = -\frac{4\pi}{c}\mathbf{j}, \tag{5}$$

$$\frac{\partial\mathbf{B}}{\partial t} = -c\operatorname{curl}\mathbf{E}. \tag{6}$$

In equations (1)–(6), which underlie our model, the quantities η, χ, and α are regarded as phenomenological parameters. We assume that, if the quantities η and χ, which mainly govern the width of the resistive front, are sufficiently small, then neither their magnitudes nor their specific forms will affect the main parameters of a CSW. Consequently, in calculations, we put $\eta = \text{const}$ and assume that χ is related to the magnetic diffusion coefficient $\kappa = \frac{c^2}{4\pi}\eta$ by

$$\chi = 1.5n\beta_e\kappa,$$

where $\beta_e = \frac{8\pi p_e}{B^2}$. We represent the anomalous resistivity in the same approximate form that we used in the one-dimensional simulations [6]:

$$\kappa \sim ac_A\frac{c}{\omega_{pi}},$$

where c_A is the Alfvén velocity and a is a small dimensionless coefficient, which is on the order of the factor α accounting for ion heating due to the induced scattering of ion acoustic oscillations by the ions. Our two-dimensional simulations were carried out with $a = 0.2$ and $\alpha = 0.1$ [6].

3. FORMULATION OF THE PROBLEM

We treat the problem of a CSW in a time-dependent formulation and assume that there is an ideally conducting rigid piston at $x = 0$ and that the velocity of the flow of an initially homogeneous plasma onto the piston surface is $-u$. The perturbation is assumed to be produced by the ions, which are reflected from the piston as if from an inclined surface:

$$\frac{dx}{dz} = 0.05\sin\frac{\pi z}{2z_0},$$

where $2z_0$ is the width of the computation region in the z-direction. In simulations, the boundaries $z = z_0$ and $z = -z_0$ are related through the periodicity conditions. By virtue of the nonlinear and unstable character of the problem, the perturbation, which was initially specified as a single mode, generates numerous shorter wavelength perturbation modes in the course of a run.

We express the density in units of the initial plasma density n_0, the magnetic field in units of the initial magnetic field B_0, the velocity in units of the initial Alfvén velocity, the time in units of the reciprocal initial ion

cyclotron frequency, and the coordinates in units of c/ω_{pi} (where ω_{pi} is the initial ion plasma frequency). At the initial time, the plasma is assumed to be cold, so that $\beta_{e0} = 0$ and $\beta_{i0} = 0.01$. Because of the plasma heating, the β values clearly become much higher than β_{i0} over the course of a run. The initial β_{i0} value is set to be nonzero merely in order to specify the initial Maxwellian ion distribution function, which should remain Maxwellian when the ion heating is described only by (4). The computations were performed for both subcritical ($u = 1$) and supercritical ($u = 3, 6$) CSWs.

We modeled CSWs using the familiar methods for solving equations (1)–(6) [12]. Thus, the behavior of the plasma ions was modeled using the particle-in-cell technique: the averaged plasma parameters were computed by linearly weighing the contributions of particles to the mesh parameter values. Equation (3) was solved using an alternative direction implicit (ADI) method. The magnetic field components $B_{x,z}$ were defined through the A_y-component of the vector potential,

$$\mathbf{B} = \mathrm{curl}\,\mathbf{A}_y.$$

According to (6), this component satisfies the equation

$$\frac{1}{c}\frac{\partial A_y}{\partial t} + E_y = 0,$$

which was solved with the help of the ADI method [12].

The main difficulty in simulations is that of capturing the effects occurring on short spatial scales near the shock front. In [6], we showed that the spatial step Δx of the mesh on which the averaged plasma parameters (density, velocity, temperature, etc.) are to be computed should satisfy the condition $\Delta x \le 0.5\frac{a}{u}$ (written in the above normalized units). In the two-dimensional model, this condition appears to be too restrictive, so that we sometimes used less stringent conditions. However, the results of two-dimensional simulations carried out with different meshes were found to differ insignificantly from each other. Presumably, the reason is that the two-dimensional fronts of CSWs are inclined with respect to the incident plasma flow, so that the effective velocity of the plasma flow onto the shock front is lower than M_A.

4. NUMERICAL RESULTS

According to our simulations, two-dimensional effects can be neglected for CSWs with $u = 1$ and $M_A \simeq 2$, so that the results of one-dimensional modeling [6] are valid in the range of subcritical Mach numbers.

Two-dimensional effects become more pronounced for flow velocities above $u = 3$. As an example, Fig. 1 shows reliefs of the magnetic field component B_z and plasma density n at the time $t = 15$ and Fig. 2 displays the x-profiles of the following parameters: the z-averaged magnetic field component B_z and plasma density, their maximum and minimum values along the z-axis, and the maximum values of the magnetic field components $B_{x,y}$ along the z-axis (in the problem as formulated, these components are odd functions of z and their maxima coincide in absolute value with their minima) for the same time. The results illustrated in Figs. 1 and 2 were obtained from simulations performed with $z_0 = 5$, the spatial steps of the mesh being $\Delta x = 0.05$ and $\Delta z = 0.1$. We can see that the magnetic field oscillations excited downstream of the shock front are characterized by amplitudes $\delta B_x \sim \delta B_y \sim 0.2$, while the oscillations of δB_z along the x-direction have approximately the same wavelength as those in the one-dimensional case [6] and a somewhat smaller amplitude.

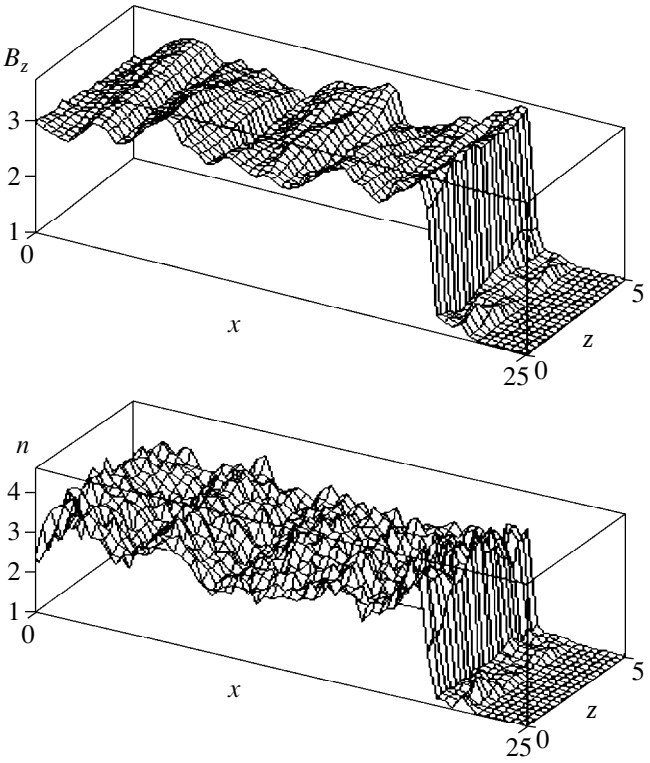

Fig. 1. Reliefs of the magnetic field component B_z and plasma density n for a CSW with $u = 3$ at the time $t = 15$.

The amplitudes of the modes of the magnetic field oscillations excited downstream of the front in the z-direction are illustrated in Fig. 3a, which indicates that the most intense oscillations of the magnetic field components B_x and B_y are those with the wavenumbers $k \sim 1$. A quasilinear analysis of the evolution of noises downstream of the shock front shows that the peak in the noise spectral density is displaced from the initial wavenumber (which corresponds to the maximum growth rate [9]) toward smaller wavenumbers k; this result agrees qualitatively with the results in Fig. 3a. The characteristic mode amplitudes of the magnetic field oscillations in the x- and y-directions differ by a

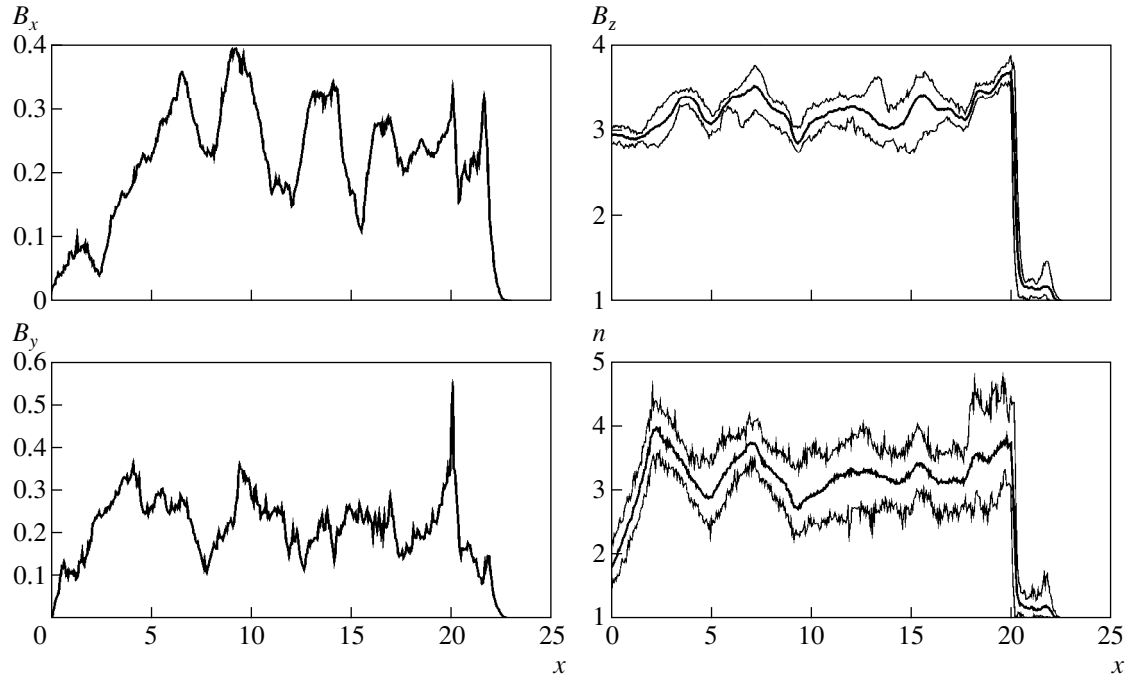

Fig. 2. The x-profiles of the maximum (along the z-axis) values of the magnetic field components $B_{x,y}$ and the maximum and minimum (along the z-axis) values of the B_z-component and plasma density n, as well as of their z-averaged values, for a CSW with $u = 3$ at the time $t = 15$.

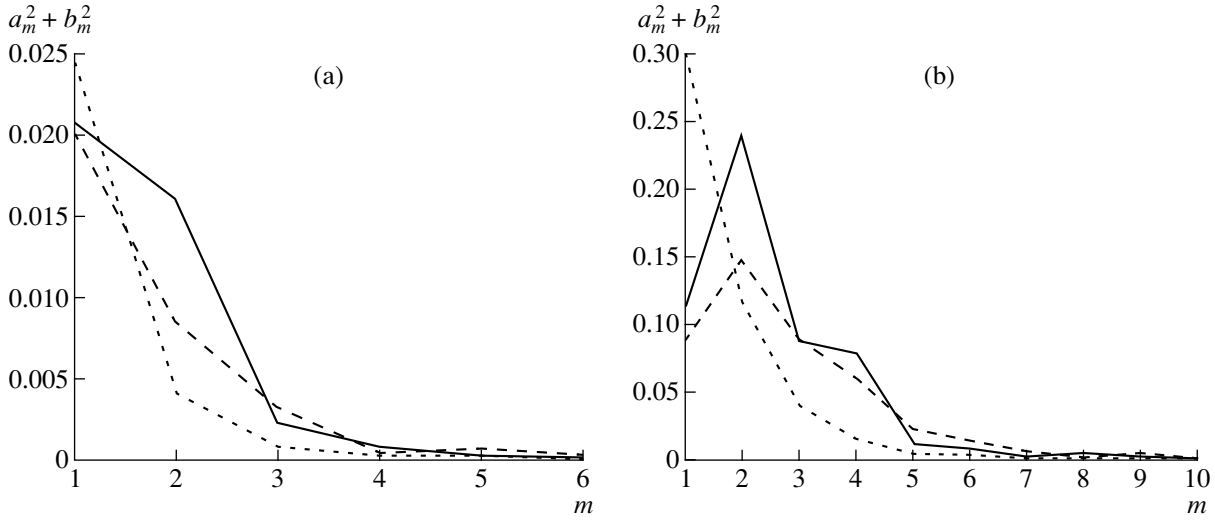

Fig. 3. Squared amplitudes of the modes of the magnetic field oscillations excited downstream of the shock front for CSWs with u = (a) 3 and (b) 6 at the time $t = 15$. Solid, dashed, and dotted curves show the squared amplitudes of B_x, B_y, and B_z, respectively.

factor of less than two. In this sense, the oscillations in the x- and y-directions downstream of the shock front are isotropic.

The ion distributions in the phase planes (x–v_x) and (x–v_y) (Fig. 4) are oscillatory in nature and provide evidence for the presence of ions reflected from the shock front. The ion distribution in the phase plane (x–v_z) is seen to broaden farther away from the front: the noises downstream of the front cause the ion distribution function to become more isotropic (such "isotropization" was studied in [8, 9]). On the whole, the overall two-dimensional picture of the propagation of a supercritical CSW for $u = 3$ agrees qualitatively with the one-dimensional picture [6]: as in one-dimensional simulations, the ions reflected from the shock front are mani-

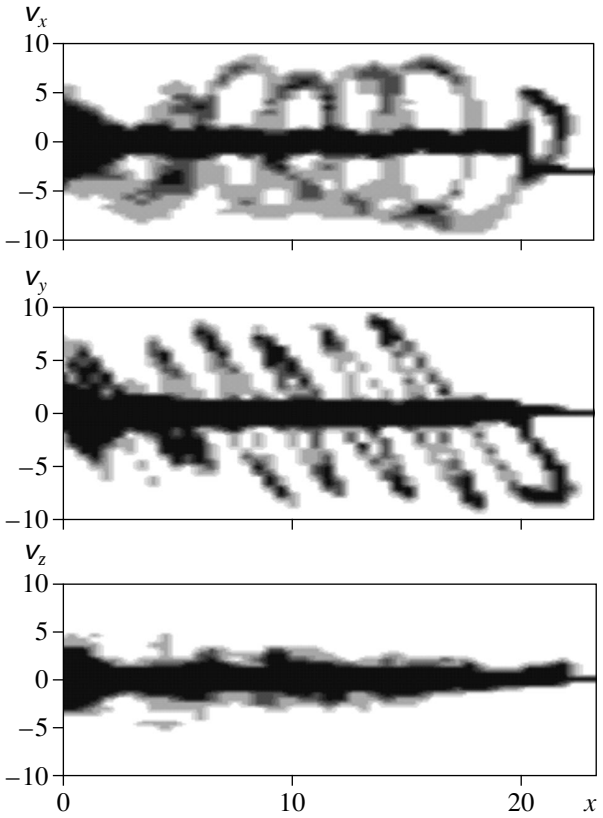

Fig. 4. Ion distributions in the phase planes (x, v_x), (x, v_y), and (x, v_z) for a CSW with $u = 3$ at the time $t = 15$.

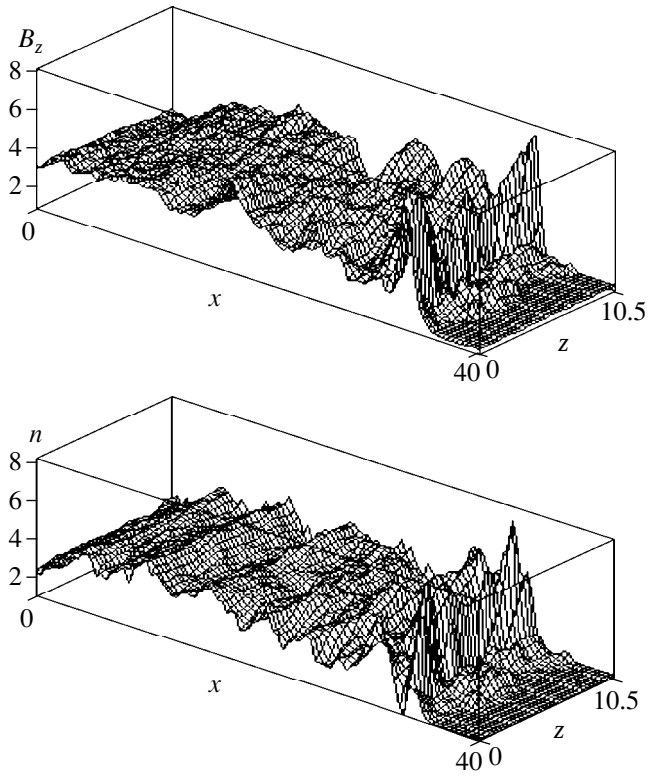

Fig. 5. Reliefs of the magnetic field component B_z and plasma density n for a CSW with $u = 6$ at the time $t = 15$.

fested by the presence of foots and overshoots on the profiles of the magnetic field $B_z(x)$ and plasma density $n(x)$, as well as on the ion distribution in the phase plane. Both two-dimensional and one-dimensional computations present evidence for the unsteady and pulsating character of CSW propagation.

In the case of a CSW with $u = 6$, two-dimensional effects become more pronounced. The reliefs of the magnetic field component B_z and plasma density (Fig. 5) that were computed for $z_0 = 10.5$, $\Delta x = 0.06$, and $\Delta z = 0.3$ illustrate an essentially two-dimensional CSW structure, which is especially distorted in the front region and is similar to the wave structure calculated by Thomas [7] for $M_A \sim 13$, $\beta_{e0} = 4$, and $\beta_{i0} = 0.5$ without allowance for plasma resistance. In Fig. 6, the magnetic field components B_k and the plasma density are illustrated by the profiles of their maximum and minimum values along the z-axis as well as their z-averaged values. We can see that the magnetic field oscillations excited at the shock front have the characteristic amplitudes $\delta B_x \sim \delta B_y \sim 3$ and a somewhat larger amplitude δB_z (the amplitude of the density perturbations δn is also somewhat larger). This is associated with both the nonuniformity (along the z-axis) of the overshoots that appear in the profiles of the magnetic field component B_z and density as a result of reflection of the incident ion flow from the CSW front and with the distortion of the front shape. Downstream of the front, the magnetic field oscillations are damped, so that their amplitudes are relatively small: $\delta B_x \sim \delta B_y \sim \delta B_z \sim 0.8$. Figures 5 and 6 illustrate the damping of oscillations with distance from the shock front.

The amplitudes of the modes of the magnetic field oscillations excited downstream of the front in the z-direction are illustrated in Fig. 3b. One can see that the characteristic wavenumbers $k \sim 0.9$ are somewhat smaller than those in the case of a CSW with $u = 3$, while the oscillations of the components B_x and B_y are isotropic for both CSWs, i.e., with $u = 3$ and 6.

The ion distributions in the phase planes (x, v_x) and (x, v_y) in the case of a CSW with $u = 6$ (Fig. 7) are seen to be more smeared in comparison with the cases of a one-dimensional shock wave [6] and a CSW with $u = 3$ (Fig. 4): the reflected ion flows become less pronounced with distance from the shock front, because the two-dimensional effects are more significant than those in the case of a CSW with $u = 3$ and there are no correlations among the magnetic field oscillations in different regions along the z-axis. The width of the ion distribution in the phase plane (x, v_z) essentially does not change with increasing distance from the shock front (i.e., the velocities v_z acquired by the reflected

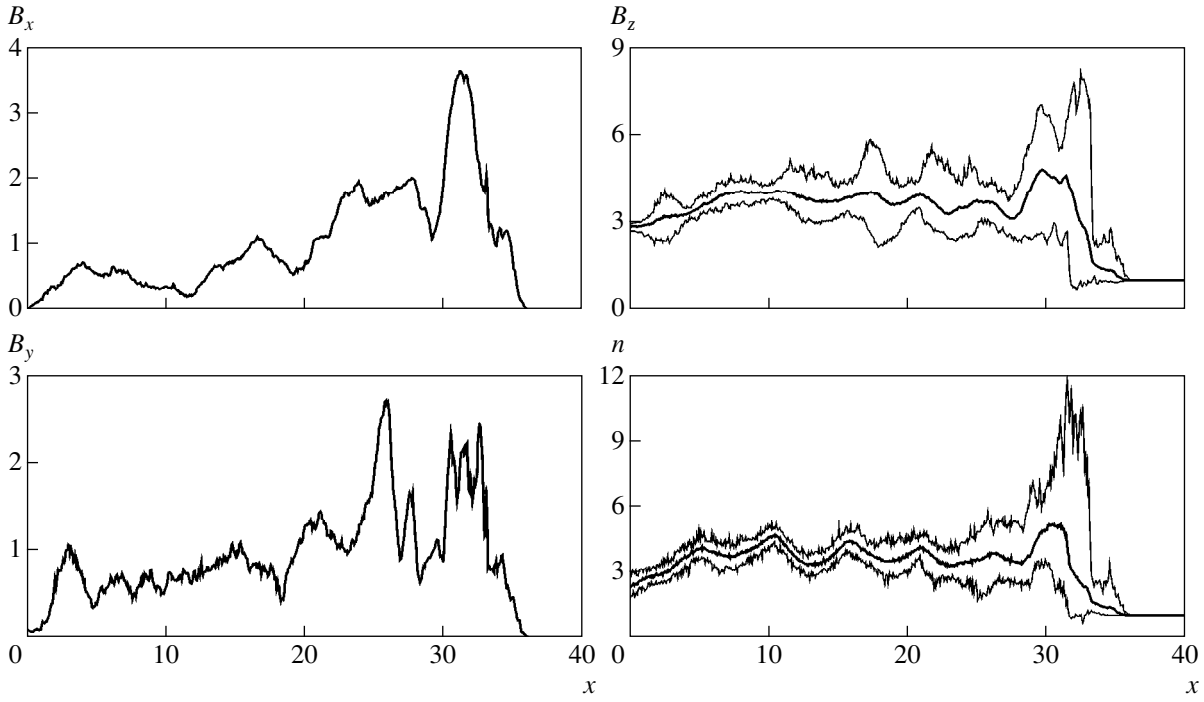

Fig. 6. The x-profiles of the maximum (along the z-axis) values of the magnetic field components $B_{x,y}$ and the maximum and minimum (along the z-axis) values of the B_z-component and plasma density n, as well as of their z-averaged values, for a CSW with $u = 6$ at the time $t = 15$.

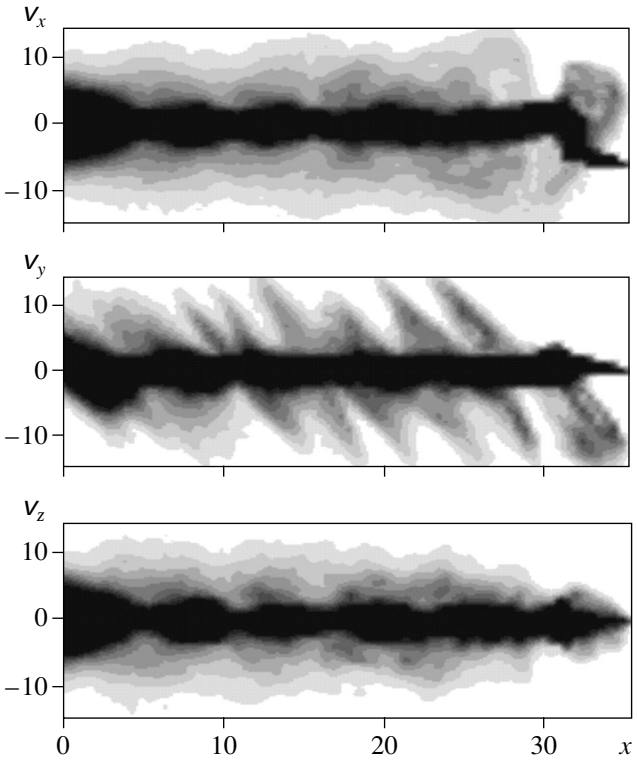

Fig. 7. Ion distributions in the phase planes (x, v_x), (x, v_y), and (x, v_z) for a CSW with $u = 6$ at the time $t = 15$.

ions near the front change insignificantly as the distance from the front increases).

Figure 8 shows the ion distributions downstream of the front computed for the two CSWs under discussion at the time $t = 15$, from which it can also be established whether there are ions reflected from the shock front. In order to eliminate the effect of the zones near the piston and the shock front, the distribution functions were calculated in the region $x_1 = 0.1x_F < x < 0.9x_F = x_2$, where x_F is the coordinate of the CSW front. Since the velocity components v_x and v_y are equalized by the ion cyclotron gyration, Fig. 8 presents the ion distribution functions over the absolute values of the total ion velocity, $f(v)$, and of the velocity component v_z, so that the number of ions in the velocity intervals dv and $d|v_z|$ is equal to $f(v)dv$ and $f(v_z)dv_z$, respectively. Along with the ion distribution functions, Fig. 8 shows the profiles of the quantities $v^2 f(v)$ and $v_z^2 f(v_z)$, characterizing the velocity distribution of the ion kinetic energy. We can see that, as in the case of a one-dimensional CSW, the velocities of the ions reflected from the shock front are very high and the main contribution to the ion thermal energy comes from the reflected ions, although their relative fraction is small. However, in the case of a CSW with $u = 6$, the reflected ions cause the profile of $v^2 f(v)$ to be peaked at a somewhat lower velocity v in comparison with the case of a one-dimensional CSW [6] presumably because of the two-dimensional modu-

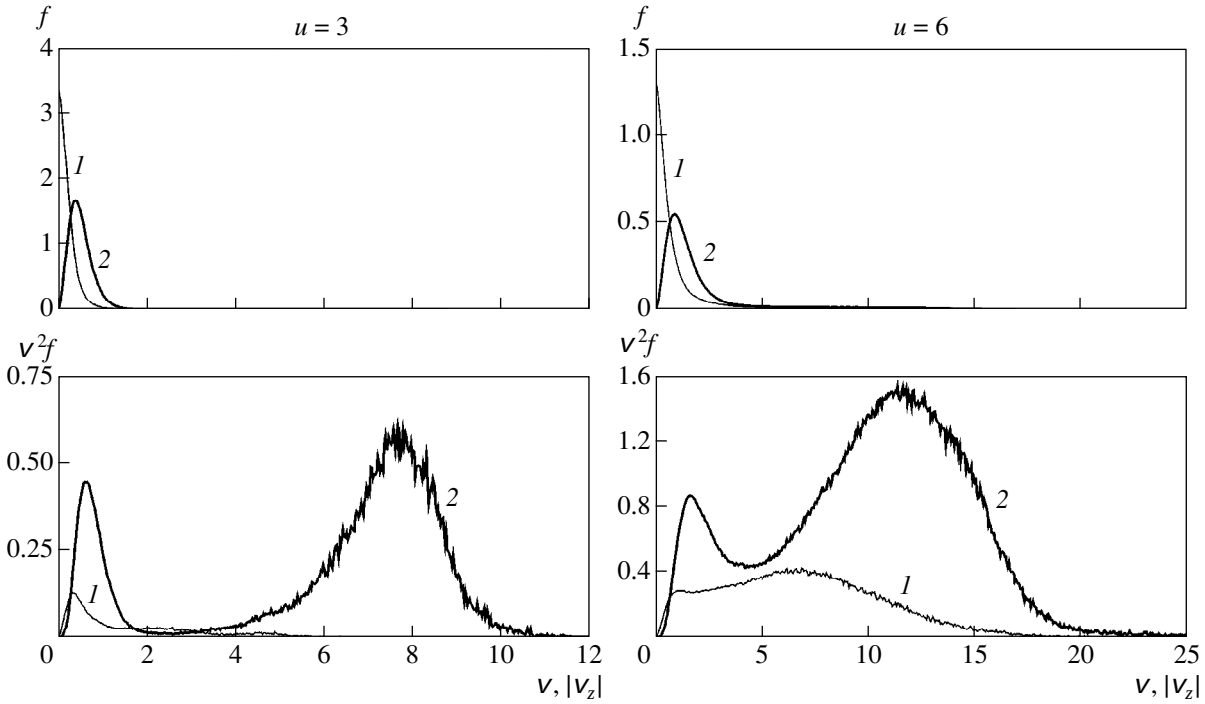

Fig. 8. Ion distribution $f(v)$ over the absolute value of the velocity and the velocity distribution $v^2 f(v)$ of the ion kinetic energy (curves *2*) and the related distributions $f(v_z)$ and $v_z^2 f(v_z)$ over the absolute value of the velocity component v_z (curves *1*) downstream of the shock front for the incident plasma flow velocities $u = 3$ and 6.

lation of the shock front and the related reduction in the effective velocity of the plasma flow onto the front. From the ion distribution over v_z, we can also see that, in the case of a CSW with $u = 3$, the degree of anisotropy in the distribution function decreases only slightly on the time scales under consideration and that isotropization is pronounced only in the range of low velocities corresponding to the main ion flow, which is not reflected from the shock front. In the case of a CSW with $u = 6$, isotropization is highly pronounced; in agreement with [9], the rate at which the ion distribution function becomes isotropic is highest in the low-velocity range.

The main simulation results characterizing the plasma state downstream of the shock front are summarized in the table, which presents the values of the following parameters:

the computed Alfvén–Mach number defined as $M_A = x_F/t + u$, where x_F is the coordinate of the shock front at the time $t = 15$;

the average magnetic field $\bar{B}_z$ in the region $x_1 < x < x_2$ downstream of the shock front (or the compression ratio downstream of the front);

the distribution of the plasma internal energy downstream of the shock front over different degrees of freedom: the electron thermal energy W_e, the ion thermal energies $W_{i\perp}$ in the *x*- and *y*-directions, the ion thermal energy W_{iz} in the *z*-direction, and the energy $W_B = \int_{x_1}^{x_2}\left(\frac{B^2}{2} - \frac{\bar{B}_z^2}{2}\right)dx$ of the magnetic field oscillations downstream of the front;

the ion velocity v_m corresponding to the median kinetic energy (i.e., the velocity dividing the area under the curve $v^2 f(v)$ into two halves); and

the ratio of the squared median velocity v_m to the squared mean ion thermal velocity v_{Ti}^2.

A comparison of the data listed in the table and the results of our one-dimensional modeling [6] shows

Table

u	M_A	$\bar{B}_z$	W_e, %	$W_{i\perp}$, %	W_{iz}, %	W_B, %	v_m	v_m^2/v_{Ti}^2
3	4.36	3.18	75.4	22.4	1.9	0.3	7.2	29
6	8.17	3.72	51.3	35.5	12.5	0.7	11	7.3

that, in the case of a CSW with $u = 3$, one- and two-dimensional computations give approximately the same values of the global parameters of the plasma downstream of the shock front. However, the results of one- and two-dimensional simulations of a CSW with $u = 6$ are noticeably different. In two-dimensional modeling, the values of M_A and $\bar{B}_z$ are close to those determined by the shock adiabat with $\gamma = 5/3$. This result is a consequence of the fact that the ion distribution function becomes much more isotropic: the energy W_{iz} of the ion thermal motion in the z-direction becomes comparable with the energies $W_{i\perp}/2$ of the thermal motion in the x- and y-directions. As in one-dimensional simulations, in the case of a two-dimensional CSW with $u = 6$, ion heating is responsible for about one-half of the plasma thermal energy. In both one- and two-dimensional models, the energy W_B of the magnetic field oscillations (including those excited downstream of the shock front) contribute only slightly to the plasma internal energy, regardless of the CSW velocity u. Like in one-dimensional simulations, the ion spectrum for supercritical CSWs is enriched with "superthermal" particles. This conclusion can be drawn from the values of the ratio v_m^2 / v_{Ti}^2, although the median velocity $v_m = 11$ in the case of a CSW with $u = 6$ is somewhat lower than that in the one-dimensional problem ($v_m = 13$).

5. CONCLUSION

We have shown that two-dimensional effects play a minor role in the formation of CSWs with low Alfvén–Mach numbers ($M_A < 5$), so that such CSWs can be described using a one-dimensional model [6]. In the range of higher Mach numbers, the onset of instabilities and two-dimensional effects in the (x, z) plane play a fairly important role, especially inside the CSW front, where the plasma density and magnetic field are perturbed so strongly that the generated x- and y-components of the magnetic field are comparable in amplitude with the perturbations of the B_z component. In the case of CSWs with high Mach numbers, two-dimensional effects cause the ion distribution function to become more isotropic downstream of the shock front and slightly reduce the energy of the reflected ions. As in the one-dimensional problem, ion heating is primarily governed by the ions that are reflected from the shock front and whose velocities downstream of the front are far above the ion thermal velocities.

ACKNOWLEDGMENTS

We are grateful to V.B. Yakubov for fruitful discussions. This research was made possible in part by Award no. RP2-158 of the US Civilian Research and Development Foundation for the Independent States of the Former Soviet Union (CRDF).

REFERENCES

1. D. Biskamp, Nucl. Fusion **13**, 719 (1973).
2. Yu. A. Berezin and V. A. Vshivkov, Fiz. Plazmy **3**, 365 (1977) [Sov. J. Plasma Phys. **3**, 207 (1977)].
3. M. M. Leroy, D. Winske, C. C. Goodrich, *et al.*, J. Geophys. Res. **87**, 5081 (1982).
4. V. P. Bashurin, S. F. Garanin, and A. I. Golubev, Vopr. At. Nauki Tekh., Ser.: Metody Programmy Chisl. Resheniya Zadach Mat. Fiz., No. 2, 21 (1983).
5. S. F. Garanin and A. I. Golubev, Vopr. At. Nauki Tekh., Ser.: Teor. Prikl. Fiz., No. 1, 18 (1985).
6. S. F. Garanin, A. I. Golubev, and N. A. Ismailova, in *Proceedings of 25th EPS Conference on Controlled Fusion and Plasma Physics, Prague, 1998* [ECA **22C**, 149 (1998)].
7. V. A. Thomas, J. Geophys. Res. **94** (A9), 12009 (1989).
8. P. H. Yoon, Phys. Fluids B **4**, 3627 (1992).
9. S. F. Garanin and S. D. Kuznetsov, in *Proceedings of 25th EPS Conference on Controlled Fusion and Plasma Physics, Prague, 1998* [ECA **22C**, 161 (1998)].
10. A. M. Buĭko, G. I. Volkov, S. F. Garanin, *et al.*, Dokl. Akad. Nauk **334**, 323 (1995) [Phys. Dokl. **40**, 459 (1995)].
11. O. M. Burenkov, S. F. Garanin, A. N. Demin, *et al.*, Fiz. Plazmy **23**, 203 (1997) [Plasma Phys. Rep. **23**, 183 (1997)].
12. Yu. A. Berezin and M. P. Fedoruk, *Modeling of Nonsteady Plasma Processes* (Nauka, Novosibirsk, 1993).

Translated by G. V. Shepekina

Plasma Physics Reports, Vol. 26, No. 5, 2000, pp. 405–408. Translated from Fizika Plazmy, Vol. 26, No. 5, 2000, pp. 434–438.

PLASMA DYNAMICS

Efficiency of Laser Energy Input into a Hohlraum through a Hole

I. G. Lebo*, V. V. Nikishin, V. B. Rozanov*, and V. F. Tishkin****

**Lebedev Institute of Physics, Russian Academy of Sciences, Leninskiĭ pr. 53, Moscow, 117924 Russia*

***Institute of Mathematical Modeling, Russian Academy of Sciences, Miusskaya pl. 4a, Moscow, 125047 Russia*

Received June 25, 1999

Abstract—Results are presented from the two-dimensional numerical simulations of laser energy input into a hohlraum through a hole. This problem is of interest for ICF research, specifically, for optimization of laser microtarget design. The optimum relations are found between the hole size and the effective laser spot radius under conditions close to those of present-day ICF experiments. © *2000 MAIK "Nauka/Interperiodica".*

1. INTRODUCTION

The promising concept of microtargets intended for ICF research assumes that a laser beam is input into a hohlraum through a hole. Among such microtargets, there are indirect-drive [1, 2], inverse-corona [3, 4], and laser greenhouse [5, 6] targets, as well as targets with an internal energy input (for a long-wavelength laser driver) [7]. In principle, laser input into the interior cavity of the target can enhance the efficiency of the interaction of radiation with a plasma; increase the energy fraction deposited directly in the fuel; and prevent the outer layers of the target shell from expansion, thus increasing the pressure on the inner layers. The laser energy input into the hohlraum can be efficiently converted into X-ray and electron heat fluxes. This results in equalizing the pressure on the nonevaporated layers of the target shell that move toward the center; thus, the homogeneity of fuel compression increases. These advantages of the internal input of laser energy into a target can be realized only if the hole area is much less than the total area of the outer shell.

In this paper, we analyze the efficiency of laser energy input into a hohlraum through a hole. When radiation passes through the hole, its wall evaporates, which decreases the fraction of the energy penetrating into the hohlraum (see, e.g., [8, 9]). Ultimately, this can result in a complete screening and absorption of most of the laser radiation outside the hohlraum. Based on two-dimensional numerical calculations, we have obtained the optimum relations between the hole size and the effective laser spot radius.

In modeling the heating and compression of spherical laser targets, the Lagrangian method is traditionally used to calculate gas-dynamic flows (see, e.g., [10]). However, the use of the Lagrangian method to model targets with an internal input of laser energy encounters great difficulties because Lagrangian cells of the shell turn out to be strongly deformed near the boundary of the hole and the internal plasma outflows through this hole [11]. To model the above processes, we used the NUTCY two-dimensional Eulerian code in cylindrical coordinates r and z [12].

2. BRIEF DESCRIPTION OF THE NUTCY CODE

The NUTCY two-dimensional Eulerian code in cylindrical coordinates is designed to solve the set of equations of gas dynamics, nonlinear heat conduction, and laser-radiation transport along the z direction:

$$\frac{\partial \rho}{\partial t} + \frac{1}{r}\frac{\partial r\rho u}{\partial r} + \frac{\partial \rho w}{\partial z} = 0,$$

$$\frac{\partial \rho u}{\partial t} + \frac{1}{r}\frac{\partial r\rho u^2}{\partial r} + \frac{\partial \rho uw}{\partial z} + \frac{\partial p}{\partial r} = 0,$$

$$\frac{\partial \rho w}{\partial t} + \frac{1}{r}\frac{\partial r\rho uw}{\partial r} + \frac{\partial \rho uw}{\partial z} + \frac{\partial p}{\partial z} = 0, \qquad (1)$$

$$\frac{\partial e}{\partial t} + \frac{1}{r}\frac{\partial ru(e+p)}{\partial r} + \frac{\partial (e+p)w}{\partial z} = -\mathrm{div}\,\mathbf{q}_T - \mathrm{div}\,\mathbf{q}_L,$$

$$e = \rho\left(\varepsilon + \frac{u^2 + w^2}{2}\right), \quad p = (\gamma - 1)\varepsilon\rho.$$

Here, q_T is the heat flux. The velocity $\mathbf{V}$ has a radial and z component: u and w, respectively. The problem was solved in the one-temperature approximation; i.e., only the electron heat conduction was taken into consideration, $\mathbf{q}_T = -\kappa \mathrm{grad} T$, where κ is the electron thermal conductivity and $q_L(r, z, t)$ is the intensity of laser radiation. It was assumed that radiation propagates in the z direction. The calculations were performed in the region $0 < r < R$ and $0 < z < L$.

The set of equations (1) was solved by "splitting" the problem into subproblems corresponding to different physical process. To solve the gas-dynamic equations (the continuity equation, the Euler equations for two velocity components, and the energy conservation equation with no account of the heat or laser radiation transports), we used explicit nonlinear conservative quasi-monotonic difference schemes with a higher

1063-780X/00/2605-0405$20.00

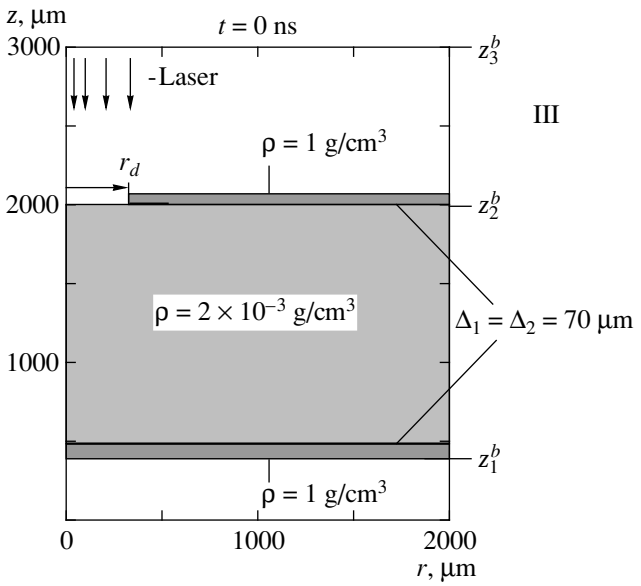

Fig. 1. Schematic of the target: z_1^b is the lower boundary of the first condensed shell, z_2^b is the lower boundary of the upper condensed shell, and z_3^b is the boundary of the calculation region.

order approximation, as in the NUT program [13]. To solve the heat-transport equation, we used implicit difference schemes. The heat-transport equations

$$C_v\rho\frac{\partial T}{\partial t} = \frac{\partial}{r\partial r}\left(\kappa r\frac{\partial T}{\partial r}\right) + \frac{\partial}{\partial z}\left(\kappa\frac{\partial T}{\partial z}\right) + \frac{\partial q}{\partial z}, \qquad \frac{\partial q(z, r, t)}{\partial z} = -\chi_{las}q, \tag{2}$$

were solved by the sweep method separately in each direction. In calculations, we used the Spitzer–Braginskii formula for the electron heat conductivity, $\kappa = \kappa_0 T^{2.5}$ [14].

3. FORMULATION OF THE PROBLEM AND RESULTS OF SIMULATIONS

The parameters of the problem were chosen to be close to those achievable in present-day experiments. We considered the following problem (see Fig. 1). A cylindrical region with a radius of 2000 μm and 3000 μm in height was divided into five domains. In domain I ($0 \le z \le 400$ μm), the mass density was taken to be $\rho = 10^{-5}$ g/cm^3; in domain II ($400 \le z \le 470$ μm), we set $\rho = 1$ g/cm^3; and in domain III ($470 \le z \le 2000$ μm), we set $\rho = 2 \times 10^{-3}$. The third domain modeled a low-density absorber with a mass density lower than the critical mass density for laser radiation at a wavelength of 0.35 μm (for the third harmonic of a neodymium laser and a plasma produced from polyethylene, the critical mass density is equal to $\rho_c = 3.07 \times 10^{-2}$ g/cm^3). In domain IV ($2000 \le z \le 2070$ μm), we set $\rho = 1$ g/cm^3. This domain had a hole with radius $r_d = 50$ μm on the axis. Domain V corresponded to a low-density plasma ($\rho = 10^{-5}$ g/cm^3). The above structure modeled a region in the vicinity of one hole in a laser-greenhouse spherical target. A laser pulse with an energy of 3 kJ, a duration of 1 ns, and a right-triangle waveform entered the target from above. The radiation intensity had a Gaussian transverse profile $\propto \exp(-(r/r_f)^2)$ with $r_f = 250$ μm. The hole radius r_d was a variable parameter.

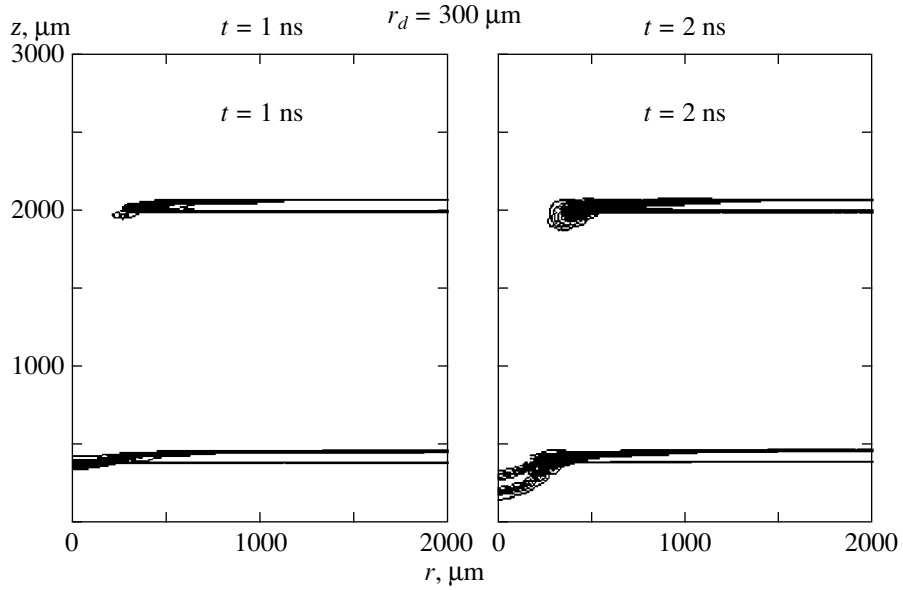

Fig. 2. Version 2 ($r_d = 300$ μm): density contours at $t = 1$ and 2 ns.

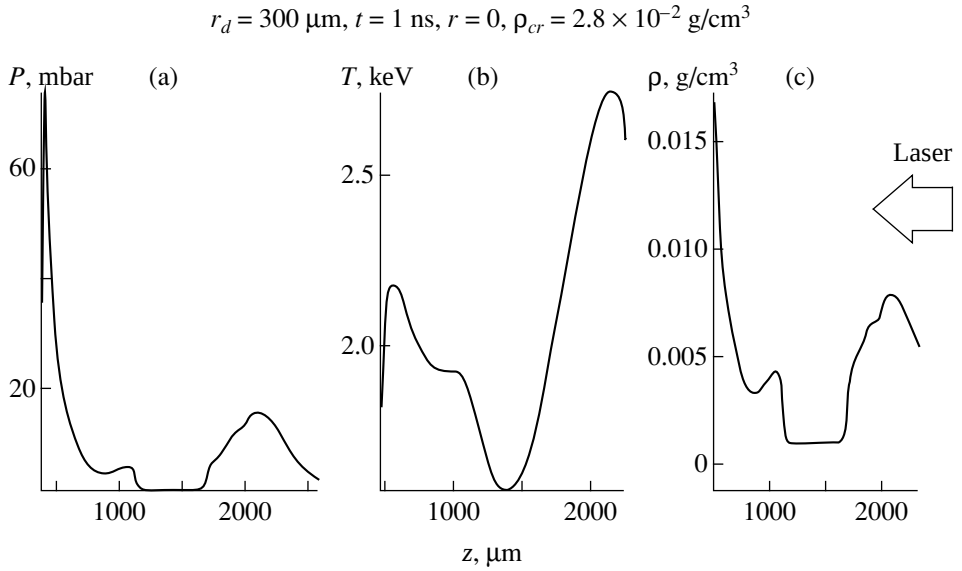

Fig. 3. Version 2: longitudinal profiles of (a) pressure, (b) temperature, and (c) mass density at t = 1 ns.

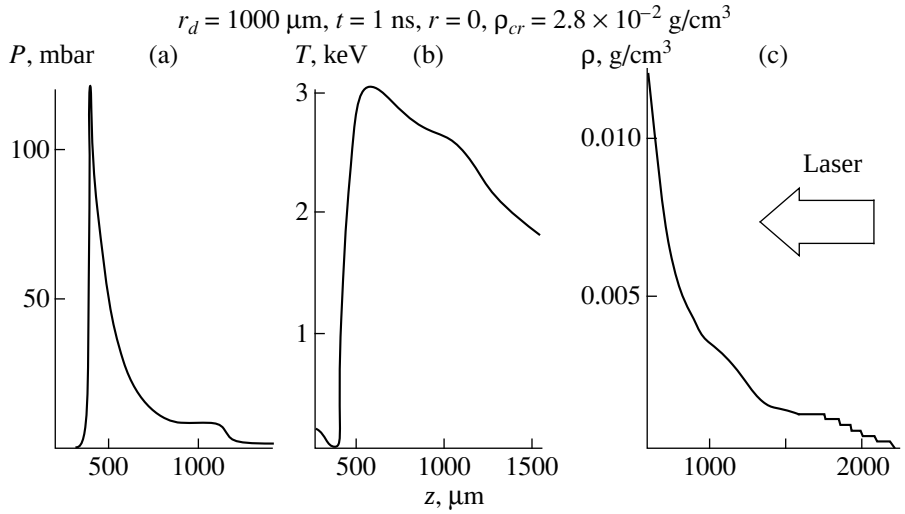

Fig. 4. Version 5 (r_d = 1000 μm): longitudinal profiles of (a) pressure, (b) temperature, and (c) mass density at t = 1 ns.

The results of calculations were compared with those for r_d = 1000 μm (in fact, the latter corresponded to the absence of an upper cover). We examined the efficiency of radiation input into the hole for various values of the ratio r_d/r_f. Figure 2 shows the contour plots of the target mass density at t = 1 and 2 ns for r_d = 300 μm. It is seen that, by t = 2 ns, the material of the inner target shell began to move. Figure 3 shows the longitudinal profiles of the pressure p, temperature T, and mass density ρ on the axis at 1 ns for the same hole radius. It is seen that, along with the density maximum at z < 500 μm (the inner target shell), a density peak arises at z = 2000 μm. This is a consequence of the evaporation of the hole-wall material. As a result, the temperature in the region around $z \sim 2000$ μm increases (Fig. 3b) and the efficiency of energy transfer deep into the target decreases. Thus, the inner target appears to be screened. For r_d = 1000 μm, this effect is absent (Fig. 4) and laser radiation penetrates deep into the target to z = 600 μm. To determine how the energy loss due to screening depends on the r_d/r_f ratio, we calculated the total energy contents in domains I, II, III, and IV. By the energy input in the hohlraum (E_{in}), we mean the sum of the energies in domains I, II, and III. By the energy transferred to the inner target, E_{I}, we mean the energy in domain I [note that, during the target heating, the inner shell almost completely shifts into domain I (Fig. 2)]. Figure 5a shows the time behavior of E_{in} for

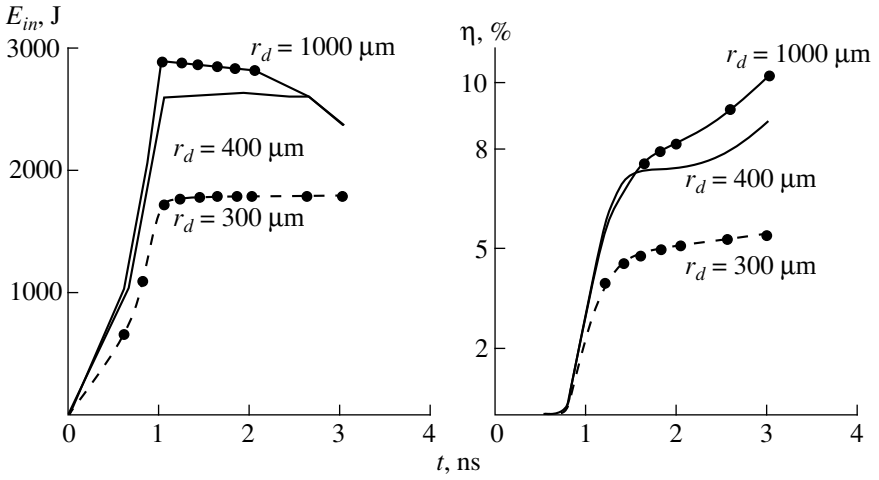

Fig. 5. Time behavior of (a) energy input into the hohlraum and (b) hydrodynamic efficiency for different values of the hole radius r_d.

r_d = 300, 400, and 1000 μm. It is seen that, for r_d/r_f = 1.6, the energy input into the target is close to that in the case of direct irradiation. By hydrodynamic efficiency, we mean the ratio $\eta = E_I/E_{in}$. Figure 5b shows the time behavior of η for the above values of the hole radius. It is seen that, for $r_d/r_f = 1.6$, the hydrodynamic efficiency is close to that of direct-irradiation targets.

4. CONCLUSION

The results obtained show that, for the hydrodynamic efficiency of the targets under consideration to be comparable with that of direct-heating targets, the hole radius should be 1.5–1.6 times larger than the laser spot radius. If this ratio is decreased to 1.0–1.2, then the energy loss increases almost twofold. In principle, if the outer shell is made of a high-Z material, the time during which the hole is filled with the plasma increases. However, for a correct modeling of such a problem, the radiation transport in a plasma must be incorporated into the model. This problem will be considered in a separate paper.

ACKNOWLEDGMENTS

We thank S.Yu. Gus'kov and N.V. Zmitrenko for fruitful discussions of the results obtained.

REFERENCES

1. W. J. Hogan, Fusion Eng. Des. **9**, 401 (1989).
2. C. Nakai, S. Kahalas, and L. Rudakov, Nucl. Fusion **30**, 1779 (1990).
3. A. V. Bessarab, G. V. Dolgoleva, A. I. Zaretskiĭ, *et al.*, Dokl. Akad. Nauk SSSR **282**, 857 (1985) [Sov. Phys. Doklady **30**, 478 (1985)].
4. A. V. Bessarab, V. A. Gaĭdash, G. V. Dolgoleva, *et al.*, Zh. Éksp. Teor. Fiz. **102**, 1800 (1992) [Sov. Phys. JETP **75**, 970 (1992)].
5. S. Yu. Gus'kov, N. V. Zmitrenko, and V. B. Rozanov, Zh. Éksp. Teor. Fiz. **108**, 548 (1995) [JETP **81**, 296 (1995)].
6. I. G. Lebo, I. V. Popov, V. B. Rozanov, and V. F. Tishkin, Kvantovaya Électron. (Moscow) **22**, 1257 (1995) [Quantum Electron. **25**, 1226 (1995)].
7. N. G. Basov, I. G. Lebo, V. B. Rozanov, *et al.*, Kvantovaya Électron. (Moscow) **25**, 327 (1998) [Quantum Electron. **28**, 316 (1998)].
8. A. V. Bessarab, S. G. Garanin, G. A. Kirilov, *et al.*, Phys. Rev. E **54**, 5612 (1996).
9. S. Yu. Gus'kov, V. V. Demchenko, I. G. Lebo, and V. B. Rozanov, J. Russ. Laser Res. **19**, 397 (1998).
10. I. G. Lebo, I. V. Popov, V. B. Rozanov, *et al.*, J. Russ. Laser Res. **15**, 136 (1994).
11. V. A. Gasilov, S. Yu. Gus'kov, A. Yu. Krukovskii, *et al.*, J. Russ. Laser Res. **18**, 515 (1997).
12. I. G. Lebo, V. V. Nikishin, V. B. Rozanov, and V. F. Tishkin, in *Proceedings of 6th International Workshop on Physics of Compressible Turbulent Mixing, Marseille, 1997*, p. 312.
13. I. V. Popov, V. F. Tishkin, V. V. Nikishin, *et al.*, in *Proceedings of 23rd Conference on Laser Interaction with Matter, Oxford, 1994* [Inst. Phys. Conf. Ser., No. 140, 43 (1995)].
14. S. I. Braginskii, in *Reviews of Plasma Physics*, Ed. by M. A. Leontovich (Gosatomizdat, Moscow, 1963; Consultants Bureau, New York, 1965), Vol. 1.

Translated by N. F. Larionova

Plasma Physics Reports, Vol. 26, No. 5, 2000, pp. 409–414. Translated from Fizika Plazmy, Vol. 26, No. 5, 2000, pp. 439–444.

PLASMA DYNAMICS

Analytic Study of Electron Flows with a Virtual Cathode

A. E. Dubinov

All-Russia Research Institute of Experimental Physics, Russian Federal Nuclear Center, Sarov, Nizhni Novgorod oblast, 607188 Russia

Received June 17, 1999; in final form, November 10, 1999

Abstract—The formation of a virtual cathode is studied with one-dimensional analytic self-consistent dynamic models describing the pulsed injection of an electron beam into equipotential regions: a half-space or a plane-parallel gap. © *2000 MAIK "Nauka/Interperiodica".*

1. INTRODUCTION

It is well known that, if the current of an electron beam injected into an equipotential cavity is above a certain level, then the beam space charge creates a potential barrier that prevents further electron injection into the cavity, so that some of the electrons are reflected from the potential barrier back to the injection plane. A reflection point characterized by an infinite (in the hydrodynamic approximation) electron density is referred to as a virtual cathode (VC). A VC is unsteady in nature: its periodic displacements and oscillations of its total electric charge give rise to high-power electromagnetic (mostly, microwave) radiation.

At present, it is impossible to describe the electron and wave properties of an electron flow in the presence of a VC by taking a rigorous analytic approach, because the existing mathematical methods fail when the flow velocity is multivalued. Consequently, theoretical studies of systems with a VC are being carried out mainly via computer modeling.

However, in some cases, the problem of the formation of a VC can be investigated self-consistently using simple analytic models that are limited to plane-parallel geometry and allow the formation of a VC to be traced self-consistently throughout the initial stage, even over a certain time interval after the flow velocity becomes non-single-valued.

Here, we consider self-consistent analytic models describing the above processes when an electron beam is injected into a half-space or a plane-parallel equipotential gap.

2. MODELS OF THE FORMATION OF A VC DURING THE INJECTION OF AN ELECTRON BEAM INTO A HALF-SPACE

We consider the injection of a monoenergetic electron beam into a half-space bounded by a metal plane $z = 0$. We are not interested whether the electron beam is injected through a metal grid or a metal foil (both transparent to electrons), in which case a positive image charge is induced in the grid, or whether the electron inflow into the half-space is stimulated by, e.g., an intense flux of X-ray photons knocking the electrons out of the metal surface (and thus giving rise to an unneutralized positive ion charge at the surface of the photoemitter). In both cases, the positive charge at each instant of time is exactly equal to the total charge of the beam electrons. Neglecting the positive charge (as was done, e.g., in [1]) makes the problem physically meaningless.

Let the flux density of the electrons emitted from the surface $z = 0$ at the time $t = 0$ be $N\,[\mathrm{cm}^{-2}\,\mathrm{s}^{-1}] = N(t)$. By the time t, the total space charge of the emitted electrons per unit area of the surface is equal to

$$Q = -e\int_0^t N(\tau)d\tau \qquad (1)$$

so that the related positive surface charge is $|Q|$. Consequently, according to [2–4], the electrons injected during the time interval from τ to $\tau + d\tau$ are affected by the electric field $E(\tau)$, whose magnitude is only governed by the charge of the electrons emitted by the time τ, so that we have

$$E(\tau) = 4\pi e\int_0^\tau N(\tau)d\tau. \qquad (2)$$

Relationship (2) is valid up to the time at which one of the injected electron layers overtakes a layer of the electrons that were emitted earlier (an exact expression for this time will be obtained below). For the particular case of an electron pulse with a step density profile $N(t) = N_0\Theta(t)$, where $\Theta(t)$ is the Heaviside step function of unit height, we obtain

$$E(\tau) = 4\pi e N_0\tau. \qquad (3)$$

1063-780X/00/2605-0409$20.00

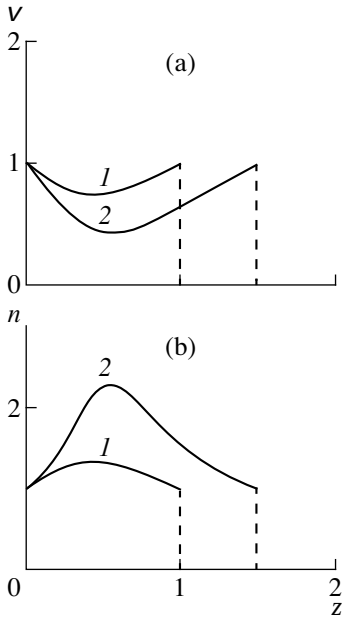

Fig. 1. Instantaneous profiles of (a) the velocity and (b) density at $t = (1)$ 1 and (2) 1.5 in the case of beam injection into a half-space.

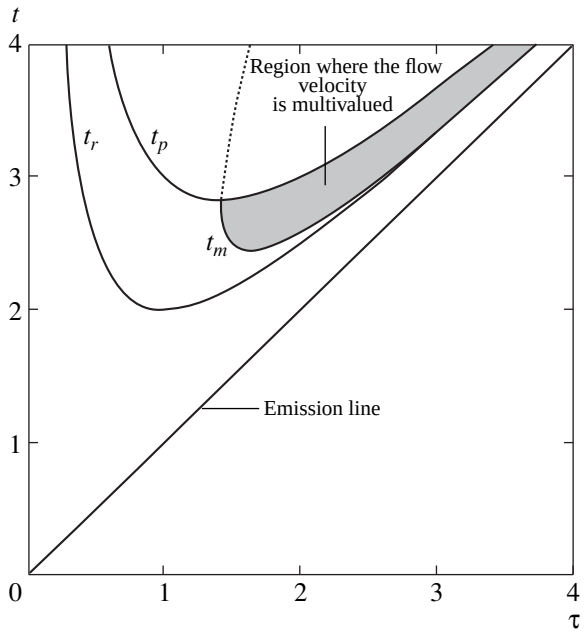

Fig. 2. Phase diagram of a beam injected into a half-space in the (t, τ) plane.

so that, in Lagrangian variables (t, τ), the electron motion is described by the equation

$$\frac{\partial^2}{\partial t^2} z(t, \tau) = -\frac{e}{m} E(\tau) = -\frac{4\pi e^2 N_0}{m} \tau \qquad (4)$$

with the initial conditions

$$z(\tau, \tau) = 0, \quad \dot{z}(\tau, \tau) = v_0. \qquad (5)$$

We introduce the dimensionless units by normalizing the time variables to $\tau' = mv_0/4\pi e^2 N_0$, the length to $v_0\tau'$, the velocity to v_0, the electron density to N_0, the electric field to $mv_0/e\tau'$, and the potential to mv_0^2/e. In dimensionless form, equation (4) with initial conditions (5) becomes

$$\frac{\partial^2}{\partial t^2} z(t, \tau) = -\tau, \quad z(\tau, \tau) = 0, \quad \dot{z}(\tau, \tau) = 1. \qquad (6)$$

The problem as formulated is easy to solve:

$$v(t, \tau) = 1 + \tau^2 - t\tau, \qquad (7)$$

$$z(t, \tau) = t - \tau + t\tau^2 - t^2\tau/2 - \tau^3/2. \qquad (8)$$

In Figs. 1a and 1b, respectively, we plot profiles of the electron velocity $v(z)$ and electron density $n(z)$ calculated from (7) and (8), and the electron trajectories in the (z, t) plane are plotted in Fig. 2.

The times t_r at which different electron layers are reflected from the potential barrier ($v = 0$) are defined as

$$t_r = \tau + \frac{1}{\tau}, \qquad (9)$$

and the time t_p at which the electrons return to the injection plane can be found from the equation $z(t_p, \tau) = 0$ [see (8)]. This equation has two roots,

$$t_p = \tau, \quad t_p = \tau + \frac{2}{\tau}. \qquad (10)$$

The first root corresponds to the time of electron injection, and the second root is the time at which the electrons return to the injection plane $z = 0$.

Let us determine the time at which the electron flow velocity becomes non-single-valued, i.e., when equality (3) fails to hold. In the region in which the flow velocity is single-valued, we have

$$\frac{\partial}{\partial \tau} z(t, \tau) < 0. \qquad (11)$$

This condition holds for

$$t_m < \tau\left(2 - \sqrt{1 - \frac{2}{\tau^2}}\right) \quad \text{and} \quad t_m > \tau\left(2 + \sqrt{1 - \frac{2}{\tau^2}}\right). \qquad (12)$$

Relationships (9), (10), and (12) determine the states of the electron flow; the boundaries between different states in the (t, τ) plane are displayed in Fig. 3.

Solutions similar to (7) and (8) can also be derived for the relativistic case [3]

$$v(t, \tau) = \frac{\varsigma}{\sqrt{1 + \beta_0^2 \varsigma^2}}, \quad (13)$$

$$z(t, \tau) = \frac{\gamma_0 - \sqrt{1 + \beta_0^2 \varsigma^2}}{(\gamma_0 - 1)} \tau, \quad (14)$$

where

$$\varsigma(t, \tau) = \gamma_0 - \tau(\gamma_0 - 1)(t - \tau)\beta_0^2 \quad (15)$$

and β_0 and γ_0 are the normalized velocity and Lorentz factor of the injected electrons.

It is also of interest to study the dynamics of the electrons injected into a half-space with allowance for the energy spread of the injected beam. Let us assume that the surface density of the electrons injected through the surface $z = 0$ (or emitted from this surface) at the time $t = 0$ is N [cm^{-2}] and that the electron distribution function $f(W_0)$ in terms of the kinetic energy $W_0 = mv^2/2$ is normalized to N so as to satisfy the condition

$$\int_0^\infty f(W_0) dW_0 = N. \quad (16)$$

The total electric charge of the emitted electrons per unit area is $Q = -eN$, the related positive surface charge being $|Q|$. The electric field acting on the electrons with the energy W_0 is

$$E(W_0) = 4\pi e \int_{W_0}^\infty f(W) dW. \quad (17)$$

The electron motion in the electric field (17) is described by the relationships

$$v(W_0, t) = \sqrt{\frac{2W_0}{m}} - \frac{eE(W_0)}{m} t, \quad (18)$$

$$z(W_0, t) = \sqrt{\frac{2W_0}{m}} t - \frac{eE(W_0)}{2m} t^2. \quad (19)$$

For the specific case of a rectangular distribution function, which is assumed to be nonzero within the interval $\{W_{0\,\min}; W_{0\,\max}\}$ (Fig. 4), relationships (18) and (19) can be rewritten as

$$v(W_0, t) = \sqrt{\frac{2W_0}{m}} - \frac{4\pi e^2 N}{m} \frac{W_{0\,\max} - W_0}{W_{0\,\max} - W_{0\,\min}} t, \quad (20)$$

$$z(W_0, t) = \sqrt{\frac{2W_0}{m}} t - \frac{2\pi e^2 N}{m} \frac{W_{0\,\max} - W_0}{W_{0\,\max} - W_{0\,\min}} t^2. \quad (21)$$

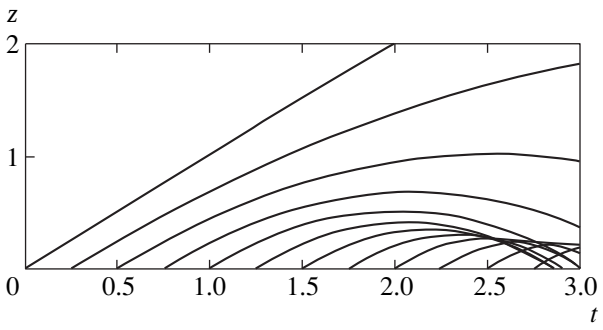

Fig. 3. Electron trajectories in the (z, t) plane in the case of long-time injection of a beam into a half-space.

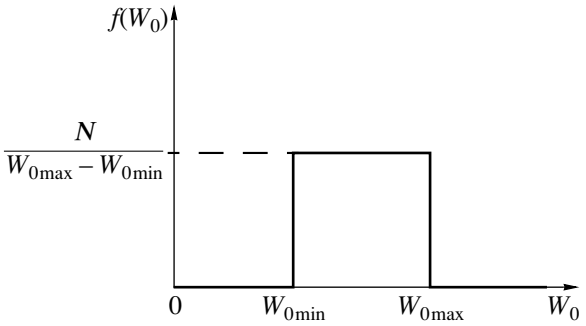

Fig. 4. Electron energy distribution in the case of instantaneous injection of a beam into a half-space.

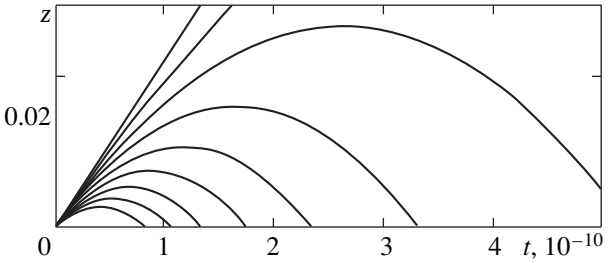

Fig. 5. Electron trajectories in the (z, t) plane in the case of instantaneous injection of a beam into a half-space.

Figure 5 illustrates the electron trajectories in the (z, t) plane that were calculated from formulas (20) and (21) with $W_{0\,\max} = 150$ keV and $W_{0\,\min} = 50$ keV.

The time t_r at which the electrons are reflected and the time t_p at which they return to the emitting surface are

$$t_r(W_0) = \sqrt{\frac{2W_0}{m}} \frac{m}{4\pi e^2 N} \frac{W_{0\,\max} - W_{0\,\min}}{W_{0\,\max} - W_0}, \quad t_p = 2t_r. \quad (22)$$

Note that, in the case of instantaneous emission, in which we are interested here, the electron flow velocity can never be non-single-valued, because the condition $\partial z/\partial W_0 > 0$ always holds.

It is noteworthy that the models of electron injection into a half-space that were treated in this section imply the absence of transit particles, because all of the injected electrons will inevitably (sooner or later) return to the injection plane.

3. MODEL OF THE FORMATION OF A VC DURING ELECTRON INJECTION INTO A PLANE EQUIPOTENTIAL GAP

Now, we consider the dynamics of an electron flow in a plane equipotential gap. To the best of the author's knowledge, Ignatov and Rukhadze [5] were the first to study the problem as formulated. Because of the serious mathematical difficulties, they solved the problem of the formation of a VC using the particle simulation technique. However, the initial stage of the formation of a VC in a plane gap may be treated analytically and some of the parameters characterizing the formation process may be evaluated exactly, as will be done in this section. Of course, this circumstance does not make the results obtained in [5] any less important, because our analytic approach is valid only for a finite time interval and cannot be used to describe the modulation of the currents of transit and reflected electrons (see below).

The dynamics of the electron flow in a plane equipotential gap differs markedly from that of electrons injected into a half-space (see Section 2). The most important difference is the presence of transit electrons, which appear because the electron flow induces a positive charge not only in the emitter but also in the other electrode (collector). We describe the initial stage of formation of a VC in a plane equipotential gap using the model that was developed in [6–8] and that (unlike the model proposed in [2–4]) makes it possible to follow the evolution of the process over a certain time interval after the flow velocity becomes non-single-valued.

We consider an electron beam injected through a thin conducting foil (or grid) into a plane equipotential gap. We assume that the gap is wide enough for the front of the electron flow not to reach the opposite conducting surface during the injection; the corresponding condition will be refined below.

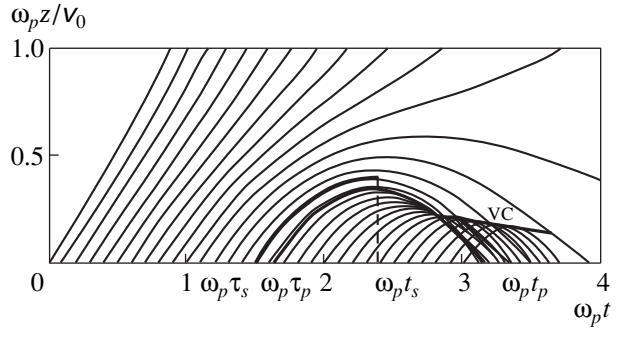

Fig. 6. Electron trajectories in the (z, t) plane in the case of long-time injection of a beam into a plane equipotential gap.

Let $t = 0$ be the initial time of electron injection in a strong guide magnetic field, the density and velocity of the injected electrons being n and v, respectively. In Lagrangian variables, the equation of electron motion in the flow, the continuity equation, and the equation for the electric field can be written as

$$\frac{\partial v(t,\tau)}{\partial t} = -\frac{e}{m}E(t,\tau), \tag{23}$$

$$\frac{\partial n(t,\tau)}{\partial t} + \frac{\partial}{\partial z(t,\tau)}[n(t,\tau)v(t,\tau)] = 0, \tag{24}$$

$$\frac{\partial E(t,\tau)}{\partial t} = -4\pi e n(t,\tau), \tag{25}$$

where τ is the time of injection of an electron layer. We eliminate $n(t, \tau)$ and $E(t, \tau)$ from these equations and use the relationship $\partial/\partial z = v^{-1}\partial/\partial t$ to arrive at the basic model equation

$$2v\ddot{v} - \dot{v}\dot{v} = 0. \tag{26}$$

The Cauchy problem for equation (26) supplemented with the boundary conditions

$$v(t,\tau)|_{t=\tau} = v_0, \tag{27}$$

$$\dot{v}(t,\tau)|_{t=\tau} = -\omega_p^2 v_0 \tau, \tag{28}$$

$$\ddot{v}(t,\tau)|_{t=\tau} = \omega_p^2 v_0 \tag{29}$$

at the injection plane can be readily integrated by quadratures:

$$\dot{\xi} = -\frac{2}{\sqrt{3}}\omega_p\sqrt{|\xi|^{3/2}\operatorname{sgn}\xi + \frac{3}{4}\omega_p^2\tau^2 - 1} \qquad (\xi = v/v_0). \tag{30}$$

Before proceeding to an analysis of the dynamics of an electron flow using integral (30), we determine the time interval over which our model is valid. Recall that, in Poukey and Rostoker's model [2], the electric field was taken to be of the form (2), which is valid up to the time at which the electron flow velocity becomes non-single-valued (i.e., a VC starts to form). In contrast, our model, which is based on the equations for an electron flow and the field equation (25), is self-consistent and makes it possible to treat longer time intervals in comparison with those in the model of [2–4].

We assume that the gap is wide enough so that the electrons reflected from the VC return to the injection plane before the transit electrons reach the opposite electrode. In this case, our model is valid up to the time at which the front of the flow of the reflected electrons reaches the injection plane, because the electron losses from the gap cannot be incorporated into boundary

conditions (28) and (29). This time can be determined by equating dv/dt to zero and the velocity v to v_0:

$$t_p = \tau_p \frac{\sqrt{3}}{\omega_p}\int_0^1 \frac{d\xi}{\sqrt{\xi^{3/2}+1}} \quad (31)$$

with

$$\tau_p = \sqrt{\frac{2}{3}}\frac{2}{\omega_p}. \quad (32)$$

Numerically, the times in (31) and (32) can be estimated as

$$t_p \approx 3.10\omega_p^{-1}, \quad \tau_p \approx 1.63\omega_p^{-1}. \quad (33)$$

The electron trajectories in the (z, t) plane that were calculated from our model are illustrated in Fig. 6, in which one of the heavy curves shows the trajectory of the electrons injected at the time $\tau = \tau_p$. It is also an easy matter to estimate the distance that the front ($\tau = 0$) of the electron flow passes by the time t_p:

$$d_f \approx 9.31\frac{v_0}{\omega_p}. \quad (34)$$

This implies that the condition $L > d_f$ (where L is the gap width) is necessary in order for the time interval over which our model is valid to be the longest.

The bounce frequency of the electrons in the potential well between the emitting cathode and the VC can be estimated as

$$\omega_0 = \frac{\pi}{t_p - \tau_p} \approx 2.14\omega_p. \quad (35)$$

Of course, the bounce cycle times are different for different electron layers. Consequently, by the bounce frequency of the electrons in the potential well, we mean a characteristic frequency close to the mean bounce frequency measured experimentally from the emission spectra.

Let us estimate the time required for a VC to form. The time at which an electron layer injected at the time τ will stop can be found from the condition $\xi(t, \tau) = 0$. Then, we determine which of the electron layers will be the first to stop. To do this, we must find the extremum (minimum) of the function defined implicitly through the equation $\xi(t, \tau) = 0$ from the condition $dt/d\tau = 0$. Performing the required manipulations, we find that the electron layer that will stop the first is injected at the instant τ_s that satisfies the transcendental equation

$$\frac{3^{3/2}\omega_p\tau_s}{8}\int_0^1 \frac{d\xi}{\left(\xi^{3/2}+\frac{3}{4}\omega_p^2\tau_s^2-1\right)^{3/2}} = 1. \quad (36)$$

The instant t_s at which this layer stops is

$$t_s = \tau_s + \frac{\sqrt{3}}{2\omega_p}\int_0^1 \frac{d\xi}{\sqrt{\xi^{3/2}+\frac{3}{4}\omega_p^2\tau_s^2-1}}. \quad (37)$$

Numerical estimates give

$$t_s \approx 2.35\omega_p^{-1}, \quad \tau_s \approx 1.49\omega_p^{-1}. \quad (38)$$

The time t_s governs the temporal scale on which a VC forms. Another heavy curve in Fig. 6 shows the trajectory of the electrons injected at the time $\tau = \tau_s$.

4. CONCLUSION

We have analyzed some self-consistent one-dimensional models describing the dynamics of an electron flow. The results obtained can be summarized as follows.

In studying the dynamics of an electron beam injected into a half-space, we have considered the two cases: long-time injection of a monoenergetic electron beam and instantaneous injection of a beam with a prescribed electron energy spectrum. In both cases, all of the injected electrons return to the injection plane. In the first case, a VC appears in the electron flow; moreover, at the time at which the VC starts to form, the electron flow velocity becomes non-single-valued, thereby limiting the applicability range of our model. In the second case, the reflected electrons come back to the injection plane as a laminar flow, so that the flow velocity always remains single-valued.

We have constructed a simple self-consistent analytic model of the initial stage of the formation of a VC in a plane-parallel equipotential gap. Analyzing this model allowed us to determine the temporal scale on which the VC forms. Unlike the models developed in Section 2, which can be applied only up to the time at which the electron flow velocity becomes non-single-valued, the applicability range of the self-consistent model is broader but it is limited by the fact that the electron losses in the injection plane are impossible to incorporate. The model makes it possible not only to study the processes that occur before the formation of a VC but also to trace its time evolution and estimate the bounce cycle frequency of the electrons in the potential well between the emitting cathode and the VC.

The results obtained may prove useful for developing high-power microwave oscillators operating with a VC [7–10], collective ion accelerators in systems with a VC [11], and generators of high-power pulses of soft X radiation in reflecting systems [12].

ACKNOWLEDGMENTS

I am grateful to Prof. A.A. Rukhadze for bringing paper [5] to my attention.

REFERENCES

1. N. D. Naumov, Dokl. Akad. Nauk **359**, 323 (1998) [Dokl. Phys. **43**, 154 (1998)].
2. J. W. Poukey and N. Rostoker, Plasma Phys. **13**, 897 (1971).
3. E. Hantzsche, Beitr. Plasmaphys. **15** (4), 157 (1975).
4. E. Hantzsche, Beitr. Plasmaphys. **17** (4), 253 (1977).
5. A. M. Ignatov and A. A. Rukhadze, Kratk. Soobshch. Fiz. **11**, 13 (1977).
6. V. D. Selemir, A. E. Dubinov, and N. V. Stepanov, Preprint No. 25-93, VNIIÉF (All-Russia Research Institute of Experimental Physics, Arzamas-16, 1993).
7. B. V. Alyokhin, A. E. Dubinov, V. D. Selemir, *et al.*, IEEE Trans. Plasma Sci. **945**, 945 (1994).
8. V. D. Selemir, B. V. Alekhin, V. E. Vatrunin, *et al.*, Fiz. Plazmy **20**, 689 (1994) [Plasma Phys. Rep. **20**, 621 (1994)].
9. A. A. Rukhadze, S. D. Stolbetsov, and V. P. Tarakanov, Radiotekh. Élektron. (Moscow) **37**, 385 (1992).
10. A. E. Dubinov and V. D. Selemir, Zarubezhnaya Radioélektron., No. 4, 54 (1995).
11. Ya. B. Faĭnberg, in *Proceedings of Conference on Nuclear-Physics Research Dedicated to the 50th Anniversary of Nuclear Fission in the USSR, Moscow, 1983* (TsNIIatominform, Moscow, 1983), Part 1, p. 222.
12. T. W. L. Sanford, J. A. Halbleib, G. Cooperstein, and B. V. Weber, IEEE Trans. Nucl. Sci. **42**, 1902 (1995).

Translated by O. E. Khadin

Plasma Physics Reports, Vol. 26, No. 5, 2000, pp. 415–423. Translated from Fizika Plazmy, Vol. 26, No. 5, 2000, pp. 445–454.

DUSTY PLASMA

Ordered Dusty Structures in the Plasma of an RF Electrodeless Gas Discharge

A. V. Zobnin*, A. P. Nefedov*, V. A. Sinel'shchikov*, O. A. Sinkevich, A. D. Usachev*, V. S. Filinov*, and V. E. Fortov***

**High Energy Density Research Center, Associated Institute for High Temperatures, Russian Academy of Sciences, Izhorskaya ul. 13/19, Moscow, 127412 Russia*

***Moscow Power Engineering Institute (Technical University), ul. Krasnokazarmennaya 17, Moscow, 111250 Russia*

Received July 2, 1999

Abstract—Results are presented from the experimental studies and numerical simulations of the behavior of dust grains in the plasma of an inductive RF discharge. The experiments were carried out with neon at a pressure of 25–500 Pa and with 1.87-μm melamine formaldehyde grains. The discharge was excited by a ring inductor supplied from a generator operating at a 100-MHz frequency. The effective dust-grain interaction potential used in numerical simulations involved the spatial dependence of the grain charge on the plasma floating potential, grain-interaction anisotropy resulting from the focusing of the drift ion current by the negatively charged grains, and specific features of the shielding of the dust grains by the plasma electrons and ions recombining both in the plasma bulk and on the grain surface. The results of Monte Carlo simulations show that the dust grains form specific filament structures observed experimentally in the plasma of an inductive electrodeless discharge.

1. INTRODUCTION

The properties of a dusty plasma and, first of all, the conditions for the formation of ordered charged-grain structures (so-called plasma crystals) were experimentally studied mainly near the electrodes of an RF capacitive discharge [1–7], in the thermal plasma [8, 9], and in the standing strata of a glow discharge [10–12]. The dust grain levitation and the formation of ordered dusty structures in the low-pressure plasma of an inductive RF discharge were first reported in [13].

In order to confine and suspend charged dust grains, it is necessary to create a potential well. The potential wells produced in different types of discharges differ significantly from each other; however, in every case, their formation is governed by the charge-particle fluxes on the wall of the discharge tube or the electrodes of a gas-discharge device. In an electrode gas discharge, there is an external electrostatic field and an external dc current. The combined action of the external electric field and the electrostatic field of the tube wall on the charged dust grains makes it possible to balance out the gravity force, so that the grain is suspended. In a stratified glow discharge, a spatial structure is formed in which the plasma parameters change periodically (with a characteristic scale length of several centimeters) along the plasma column. At the head of the stratum, the electric field can attain 10–15 V/cm, whereas, outside this region, the field is weak (~1 V/cm). The maximum of the electron density is shifted toward the anode with respect to the field maximum. The electron energy distribution is bimodal. The second maximum is predominant in the stratum head, and its center is close to the excitation potential of the neutral-gas atoms. Because of the high floating potential of the discharge-tube wall, the stratum potential is two-dimensional: the axis–wall potential difference in the stratum head attains 20–30 V. If the discharge tube is in the upright position, the grains with a sufficiently large charge and relatively small mass can be suspended in this potential well; the strong radial electric field prevents the grains from depositing on the wall of the discharge tube. In an asymmetric RF capacitive discharge, the period-averaged constant voltage in the sheath near one of the electrodes is nonzero due to the self-biasing effect [14]; this results in the formation of a potential well in which the dust grains can be suspended.

In an electrodeless RF gas discharge, both the external dc current and external electrostatic field are absent. In this case, an important role is played by the electrostatic fields that originate due to the violation of plasma electric neutrality caused by the different diffusivities and mobilities of the electrons and ions. The spatial distribution of the plasma parameters in the central region of an electrodeless RF discharge is more uniform than in a glow discharge with strata. The formation of a potential well in an electrodeless RF discharge is determined by both the volume processes in the plasma and recombination and adsorption of charges on the discharge-tube wall.

1063-780X/00/2605-0415$20.00

2. DESCRIPTION OF THE SETUP AND RESULTS OF EXPERIMENTS

In this study, as in [13], the plasma was produced in a glass tube 27 mm in diameter and more than 20 cm long. The tube was in the upright position (Fig. 1). An RF voltage generator with a power up to 10 W operated at the 100-MHz frequency. The power deposited in the discharge through an annular inductor was about several watts. The position of the discharge tube in the inductor could be varied. The working gas was neon at a pressure P from 25 to 500 Pa. When the generator was switched on, a luminous plasma region filled the entire tube cross section. The size of the plasma formation along the tube depended on the gas pressure and the generator power and could vary from several centimeters to the entire length of the tube. The dust grains were injected into the plasma by shaking a metal container positioned on the upper end of the tube. The bottom of the container was made of a small-cell metal grid. We used monodisperse grains of melamine formaldehyde 1.87 ± 0.05 μm in diameter. Since the density of the grain substance was 1.5 g/cm^3, the grain mass was 5.1×10^{-6} μg. The diagnostic facility was the same as in [12, 13]. A striplike, 25-mm-wide and ~200-μm-thick (in the waist) laser beam produced by a diode laser operating at the 670-nm wavelength passed through the plasma. The laser beam could be displaced in both the vertical and horizontal direction, and the beam plane could be rotated. This allowed us to observe different cross sections of the plasma volume. The dust grains were observed in scattered laser radiation with the use of a CCD array, and the produced images were recorded by a videotape recorder.

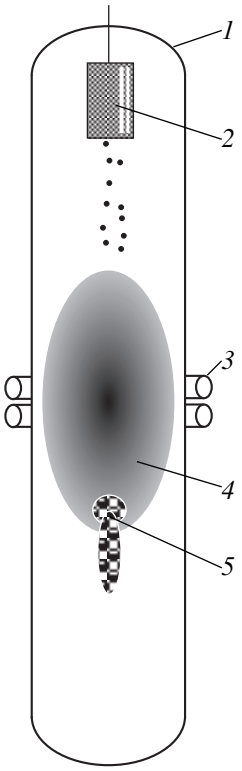

Fig. 1. Schematic of the experimental device: (*1*) discharge tube, (*2*) grain container, (*3*) inductor, (*4*) plasma formation, (*5*) region where the structures produced from monodisperse grains were observed.

In this paper, the first attempt is made to describe the levitation of dust grains in an electrodeless RF discharge; therefore, the theoretical approach we will use further does not pretend to completely describe the behavior of grains under the conditions in question. Our main purpose is to choose an appropriate model of a potential well and describe the most characteristic properties of the dust behavior. Hence, for numerical simulations, it is natural to choose the experimental conditions under which stable steady structures without grain oscillations are observed. From this standpoint, the most appropriate neon-pressure range is from 30 to 80 Pa and the most appropriate structures are those presented in Figs. 2 and 3. The levitation of monodisperse grains was observed only in the peripheral region of the discharge (Fig. 1), namely, at the low boundary of the plasma formation in the transient region between the luminous plasma core and neutral gas. In the center of the discharge, the levitation of grains was not observed. When the grains were injected from above, they deviated toward the tube wall, bent around the plasma core, and then approached again the tube axis in the region where the plasma emission intensity decreased substantially. As the deposited power increased, the vertical size of the plasma volume increased; i.e., the boundaries of the luminous region shifted upward and downward and, correspondingly, the region occupied by the grains shifted downward as a whole. In this case, the structure formed of grains remained unchanged as it moved downward along with the discharge boundary until it reached the bottom of the discharge tube. The structures presented in Figs. 2 and 3 were obtained by injecting the grains into the plasma at a fixed pressure. It is seen that the dust cluster together to form filaments extended in the upright direction. As is seen from Fig. 2, the number of filaments in the structure decreases toward the discharge periphery. The number of grains confined in such structures is limited from above. When the filament reaches a certain length that depends on the pressure, the structure ceases to capture new grains; i.e., saturation occurs. New grains either remain uncaptured or they force out other grains and occupy their place. As the pressure increases, the longitudinal size of the structure and the distance between grains decrease (Fig. 2) and the structure itself extends in the transverse direction (Fig. 3).

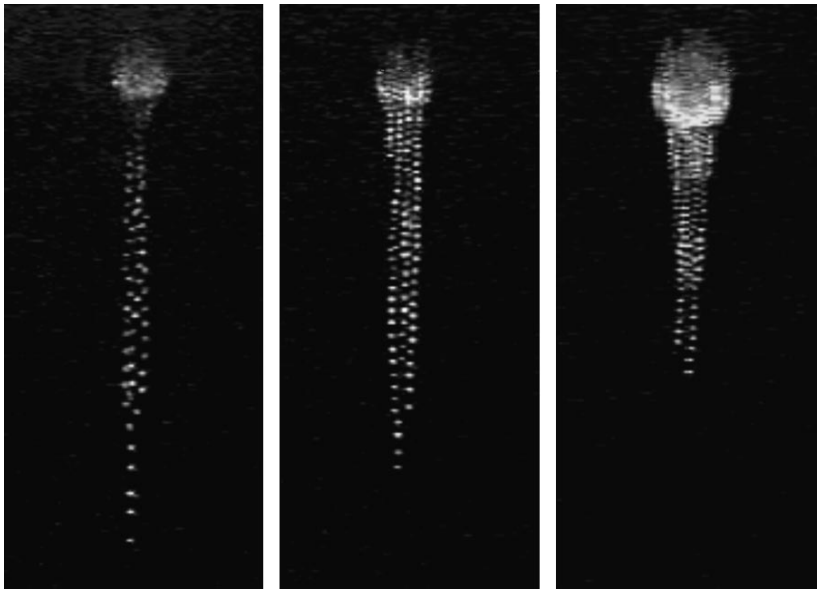

Fig. 2. Structures formed in neon at different pressures. The fragment dimensions are 17×7.4 mm.

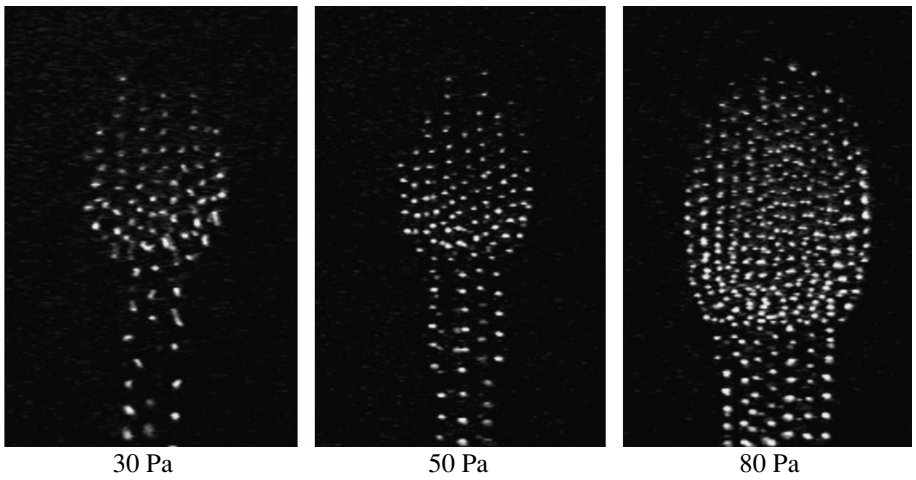

Fig. 3. The image of the upper region of the structures obtained at different neon pressures. The fragment dimensions are 5.2×3.4 mm.

3. ANALYSIS OF THE CONDITIONS FOR FORMATION OF A POTENTIAL WELL FOR DUST GRAINS

In order to determine the shape of a potential well formed in an electrodeless RF discharge, it is necessary to find the distribution of the amplitude of the heating RF field and the densities and temperatures of the plasma electrons and ions. This problem contains a natural small parameter, namely, the ratio of the difference between the ion and electron densities to the electron density $(n_i - n_e)/n_e \ll 1$. Therefore, in the first approximation, the plasma can be assumed quasineutral ($n_i = n_e$). In this case, the spatial distribution of both the heating RF electric field and the electron density can be found from Maxwell's equations and the balance equation for the number of electrons with allowance for ambipolar diffusion, electron-impact ionization, and the boundary conditions for the electric field and electrons. Knowing the spatial distribution of electrons, we can find the distribution of the electrostatic field by solving Poisson's equation, in which we take into account the difference between the density distributions of electrons and ions over the plasma volume. The obtained distribution of the electrostatic field determines the configuration of

the potential well in the plasma without dust grains. Accurate calculations of the plasma parameters of an inductive RF discharge were carried out in [15].

It is should be kept in mind that the presence of charged grains in the potential well (especially when their number is large) can change the initial well configuration. However, when calculating the formation of a dusty structure in the given electrostatic field produced by a positively charged plasma and negatively charged discharge-tube wall, the distortion of the initial well configuration can be neglected in the first approximation. In order to perform numerical simulations of the structures formed by charged dust grains, we need appropriate analytical expressions adequately describing the physical properties of the well potential. The region where the plasma quasineutrality is violated can be approximately described as an electric-charge double layer with thickness l_q. We assume that the positive space charge is mainly located on a surface whose shape is close to an elongated ellipsoid of revolution. To find the space charge located on the ellipsoid surface, it is necessary to take into account its Debye shielding by the plasma electrons and ions on the characteristic spatial scale on the order of l_q. The total effective positive charge of the ellipsoid surface can be found from the relationship $Q(\sigma_m) \approx 8\pi\varepsilon_0 a k_B T_e(\sigma_m)\exp(-l_q/r_D)/e$, where ε_0 is the permittivity of vacuum, a is the characteristic size of the ellipsoid (the half-distance between foci), r_D is the Debye radius, σ_m is the coordinate of the ellipsoid surface in elliptic coordinates, e is the electron charge, and T_e is the electron temperature. From the physical considerations and estimates made for our experimental conditions, it follows that $l_q/r_D > 1$. The potential field of a conducting charged ellipsoid of revolution can be expressed in terms of elementary functions [16]

$$\tilde{\varphi}(\mathbf{r}) = \frac{Q(\sigma_m)}{8\pi\varepsilon_0 a}\ln\left(\frac{\sigma(\mathbf{r})+1}{\sigma(\mathbf{r})-1}\right), \quad (1)$$

where $Q(\sigma_m)$ is the effective charge of an ellipsoid with the parameter σ_m (with allowance for charge shielding), $\sigma(\mathbf{r}) = (r_1 + r_2)/2a$, and r_1 and r_2 are the distances of an arbitrary point with coordinates (x, y, z) from the ellipsoid foci $(0, 0, -a)$ and $(0, 0, a)$.

Note that (1) describes the potential field outside a positively charged elliptic plasma object produced in an inductive RF discharge. However, inside this object, the model potential (1) turns to infinity logarithmically. Therefore, the model potential should be corrected. For this purpose, we introduce the characteristic function $\tilde{\chi}(\mathbf{r}) = (1 - \exp(-[(1-\sigma(r))/\sigma_m]))$, which vanishes on the centerline of the ellipsoid, between its foci. The resulting potential has the form $\varphi_1(\mathbf{r}) = \tilde{\varphi}(\mathbf{r})\tilde{\chi}(\mathbf{r})$. Another important factor is that the tube wall is negatively charged, because it is at the floating plasma potential. To analyze the behavior of the electric potential near the tube wall quantitatively, it is necessary to consider the structure of the sheath near a nonemitting wall [17]. The thickness l_W of this sheath can be estimated as $l_W \simeq \max(l_e, r_D)$, where l_e is the electron mean free path and r_D is the Debye radius corresponding to the plasma parameters near the wall ($l_W/R < 1$), where R is the radius of the discharge tube. It should be taken into account that, in an electron sheath of length r_b, the electron temperature varies from $T_e(\mathbf{r})$ inside the plasma to the equilibrium value $T_e(R) = T_a = T_W$, ($T_e(\mathbf{r}) > T_a$) on the tube wall. The small value of the ratio $r_b/R \simeq l_e/(R\sqrt{\delta}) \ll 1$, where δ is the coefficient of inelastic energy loss, and the azimuthal uniformity of the tube-wall charge allow us to evaluate the shape of the potential well far from the wall and approximate it by the simple expression $\varphi_2(\mathbf{r}) = \varphi_W(z)\chi_r(\mathbf{r}_p)$ [18], where $\chi_r(\mathbf{r}_p) = -(r_p/R)^{3/2}$ and $r_p = (x^2 + y^2)^{1/2}$ is the length of the radius vector in the (x, y) plane. Here, $\varphi_W(z)$ accounts for the variations in the potential of the tube wall along the z-axis; this potential is approximated by the dependence [18] $\varphi_W(z) = \varphi_\infty + \Delta\varphi/(1 + (z/d_W)^2)$, where d_W is the characteristic length of variations in the wall potential along the z-axis, φ_∞ is the wall potential at $|z| \gg d_W$, and $\Delta\varphi = \varphi_W(0) - \varphi_\infty$. Thus, the electric field of the well, which is determined by the combined action of the electric field produced by the discharge-tube wall, $\varphi_2(z)$, and the field of a positively charged plasma core (1) is

$$\varphi(\mathbf{r}) = \varphi_1(\mathbf{r}) + \varphi_2(\mathbf{r}). \quad (2)$$

Particular values of the parameters entering into the formulas presented will be chosen below, when considering the results of numerical simulation.

4. GRAIN CHARGE AND MECHANISMS FOR THE INTERACTION BETWEEN GRAINS

In order to study the interaction between the dust grains and the formation of ordered structures, it is necessary to know the mechanisms for the grain charging and the nature of forces acting on the grains. At present, several physical mechanisms governing both the balance between gravitational and electric forces acting on suspended grains and the interaction between them are discussed in the literature. As was noted above, the electric force acting on a grain is found by solving Poisson's equation with allowance for the spatial distributions of electrons and ions generated by an RF field, as well as the distribution of dust grains, whose charge depends, in turn, on the local floating potential. Since this self-consistent problem is too complicated, it is convenient to separate out a force responsible for the interaction between dust grains and consider the plasma to be a background. The density of plasma electrons and ions is three orders of magnitude higher than the grain number density; therefore, the plasma–grain interaction can be modeled by introducing an effective

dust-grain interaction potential, which can be found by averaging over the electron and ion positions. Thus, the dust-grain subsystem is open and can exchange the charge and energy with the gas-discharge plasma. Further, we will follow the approach developed in [18] and assume that the grain charge $Q(\mathbf{r})$ is a given function of spatial coordinates and, according to the commonly accepted views [19–21], is proportional to the plasma floating potential

$$Q(\mathbf{r}) \equiv eZ_p = C\phi_t(\mathbf{r}), \tag{3}$$

where $C \simeq 4\pi\varepsilon_0 R_p$ is the coefficient on the order of the dust-grain capacitance, R_p is the grain radius, and $\phi_t(\mathbf{r})$ is the floating plasma potential depending on spatial coordinates. In this case, the seed potential of the interaction between two dust grains has the form

$$V(\mathbf{r}_1, \mathbf{r}_2) = \frac{1}{4\pi\varepsilon_0}\frac{Q(\mathbf{r}_1)Q(\mathbf{r}_2)}{|\mathbf{r}_1 - \mathbf{r}_2|}. \tag{4}$$

In addition to the partial shielding of the grain charge by the plasma electrons and ions, which interact strongly with the dust grains, a very important factor is the appearance of regions with increased free-ion concentration. These regions are produced due to the focusing action of the large negative charge of dust grains on the ion drift current in the plasma. The regions with increased ion density downstream of the dust grains were considered, e.g., in [22, 23], in which Poisson's equation was solved and the ion–neutral collisions and charge exchange processes were taken into account by the Monte Carlo method. In those papers, the characteristics of the point positive charge equivalent to the ion cloud were also calculated and the distance between this charge and the dust grain was found. According to [22], the equivalent positive charge can attain one-third of the grain charge and the equivalent charge–grain distance d is less than or on the order of the Debye radius. Usually, the average distance $\langle r \rangle$ between the dust grains in the gas-discharge plasma is larger than the Debye radius r_D and, according to [22], is larger than d.

In spite of the absence of the external direct electric current in an electrodeless RF discharge, there are always ion currents caused by diffusion and ion motion in the electrostatic field E_s: $j_i = e(\mu_i E_s n_i - D_i \nabla n_i) = -eD_a \nabla n_i$, where μ, D_i, and D_a are the ion mobility, diffusivity, and ambipolar diffusivity, respectively. The ion currents in the plasma core and at the periphery differ in magnitude and direction. Thus, in the central region of the discharge, the radial current $j_{ir} = -eD_a dn_e/dr$ is dominant, whereas on the periphery, the current flows mainly in the axial direction $j_{iz} = -eD_a dn_e/dz$. Their averaged ratio can be estimated by using the relationship $j_{iz}/j_{ir} \approx T_e^{\text{in}} R/T_e^{\text{ex}} a$. Here, R is the radius of the discharge tube and T_e^{in} and T_e^{ex} are the temperatures inside and outside the plasma formation, respectively [17].

It is also of importance that, under the conditions in question, the ratio of the drift ion velocity to the thermal velocity is on the order of unity, $v_i/\sqrt{8k_B T_i/\pi m_i} \simeq T_e l_i/T_i R \simeq 1$, where l_i is the ion mean free path [17]. In this case, the shielding cloud of positive ions can be asymmetric around the dust-grain center. The asymmetry of the distribution of the positive-charge cloud leads to the origination of a virtual dipole with the dipole moment $\zeta eZ_p r_D$, where $\zeta \leq 1$ is the dimensionless parameter. Note that the asymmetry of the positive-charge cloud depends on the position of the dust grain. Anisotropic polarization of the background plasma can affect different processes. For example, when the dust grain enters the region occupied by the plasma from above, its charge changes due to the change in the local floating potential; the positive charge of the ion cloud surrounding the dust grain also changes. As a result, the effective charge of the system consisting of a negatively charged dust grain and a positive ion cloud changes. If the change in the effective charge proceeds sufficiently rapidly, the dust grain flows around the positively charged plasma region. Such behavior of dust grains was observed in the experiment: a fraction of the grains falling from the container was forced out toward the discharge-tube wall when approaching the luminous region and flow around the central region of the discharge. The polarization of the plasma containing dust grains can lead to the capture of other dust grains if their average kinetic energy is not too large. It is the interaction anisotropy that can cause the ordering of dust grains and formation of spatial or linear crystal-like structures [18]. It follows from the aforesaid that, in order to correctly describe the interaction between dust grains, it is necessary to introduce the effective potentials taking into account the above effects.

5. EFFECTIVE DUST-GRAIN INTERACTION POTENTIAL

The shielding of dust grains by the plasma, the influence of the electron and ion fluxes, and recombination processes on the grain surface were taken into account in [6]. It was shown that, at small distances, the pair potential of interaction $\tilde{\varphi}(\mathbf{r}_1, \mathbf{r}_2)$ is shielded by the Debye exponential law and, at distances on the order of several Debye lengths, it is inversely proportional to the squared distance between the grains. Based on the results of numerical calculations [6, 22, 24, 25] and introducing an effective positive point charge Q_+ that takes into account the presence of regions with an increased ion density, we can use the following approximation for the effective pair potential $U(\mathbf{r}_{12})$ of the

interaction between dust grains located at the distance $\mathbf{r}_{12}$ from each other:

$$U(\mathbf{r}_i, \mathbf{r}_j) = \frac{1}{4\pi\varepsilon_0}\frac{Q_s(\mathbf{r}_i)Q_s(\mathbf{r}_j)}{|\mathbf{r}_i - \mathbf{r}_j|}\exp\left(-\frac{|\mathbf{r}_i - \mathbf{r}_j|}{r_D}\right)$$
$$+ (1 - D(|\mathbf{r}_i - \mathbf{r}_j|))\frac{\tilde{A}}{|\mathbf{r}_i - \mathbf{r}_j|^2} + \frac{P^i Q_s^j - P^j Q_s^i}{|\mathbf{r}_i - \mathbf{r}_j|^2}$$
$$\times (1 - \tilde{D}(|\mathbf{r}_i - \mathbf{r}_j|)) \qquad (5)$$
$$+ \frac{\sigma^i Q_s^j + \sigma^j Q_s^i - 3P^i P^j + Q_+^1 Q_+^2 d^2\cos(\theta_{ij})}{|\mathbf{r}_i - \mathbf{r}_j|^3}$$
$$\times (1 - \tilde{D}(|\mathbf{r}_i - \mathbf{r}_j|)).$$

Here, $\mathbf{r}_i$ and $\mathbf{r}_j$ are the radius vectors of the ith and jth grains; $\mathbf{r}_{ij} = \mathbf{r}_j - \mathbf{r}_i$;

$$Q_s^l = Q_s(\mathbf{r}_l) = \int_V \rho(\mathbf{r}_l, \tilde{\mathbf{r}}_1)d\tilde{\mathbf{r}}_1 = Q_-(\mathbf{r}_l) + Q_+(\mathbf{r}_l + d\mathbf{e}_l^+)$$

is the excessive negative charge of the dipole formed by the negatively charged dust grain and the effective positive point charge;

$$P^l = P(\mathbf{r}_l) = \int_V |\tilde{\mathbf{r}}_1|\cos(\theta)\rho(\mathbf{r}_l, \tilde{\mathbf{r}}_1)d\tilde{\mathbf{r}}_1$$
$$= dQ_+(\mathbf{r}_l + d\mathbf{e}_l^+)\cos(\theta_l)$$

is the dipole moment; θ_i is the angle between the vector $\mathbf{r}_{ij}$ and the unit vector $\mathbf{e}_i^+$ directed from the negatively charged ith dust grain to the equivalent point positive charge of its ion cloud; θ_{ij} is the angle between the vectors $\mathbf{e}_i^+$ and $\mathbf{e}_j^+$;

$$\sigma^l = \sigma(\mathbf{r}_l) = \int_V |\tilde{\mathbf{r}}_1|^2((3\cos^2(\theta) - 1)/2)\rho(\mathbf{r}_l, \tilde{\mathbf{r}}_1)d\tilde{\mathbf{r}}_1$$
$$= d^2 Q_+(\mathbf{r}_l + d\mathbf{e}_l^+)((3\cos^2(\theta_d) - 1)/2)$$

is the quadrupole moment; $\tilde{D}(|\mathbf{r}_{ij}|)$ and $D(|\mathbf{r}_{ij}|)$ are the fitting functions, which, under our conditions, change from unity to zero over a distance equal to one and two Debye radii, respectively; and $\tilde{A}$ is the fitting constant. The direction of the unit vector $\mathbf{e}^+$ coincides with the direction of the local electric field in the potential well. In this model, the dependence of the Debye radius on spatial coordinates is neglected. This dependence will be analyzed in a future study.

It is convenient to choose the Debye radius as a unit length. Then, we have

$$\beta U(\mathbf{r}_i, \mathbf{r}_j) = \frac{\beta e^2}{4\pi\varepsilon_0}\frac{Z_s(\mathbf{r}_i)Z_s(\mathbf{r}_j)}{r_D}\left\{\frac{\exp(-|\mathbf{r}_{ij}|)}{|\mathbf{r}_{ij}|} + [1 - D(|\mathbf{r}_{ij}|)]\frac{\tilde{A}}{|\mathbf{r}_{ij}|^2}\right.$$
$$+ \frac{d[Z_+(\mathbf{r}_i)/Z_s(\mathbf{r}_i)\cos(\theta_i) - Z_+(\mathbf{r}_j)/Z_s(\mathbf{r}_j)\cos(\theta_j)]}{|\mathbf{r}_{ij}|^2}(1 - \tilde{D}(|\mathbf{r}_{ij}|)) \qquad (6)$$
$$\left. + \frac{d^2\left[\frac{Z_+(\mathbf{r}_i)}{Z_s(\mathbf{r}_i)}\frac{3\cos^2(\theta_i) - 1}{2} + \frac{Z_+(\mathbf{r}_j)}{Z_s(\mathbf{r}_j)}\frac{3\cos^2(\theta_j) - 1}{2} - \frac{Z_+(\mathbf{r}_i)Z_+(\mathbf{r}_j)}{Z_s(\mathbf{r}_i)Z_s(\mathbf{r}_j)}(3\cos(\theta_i)\cos(\theta_j) - \cos\theta_{ij})\right]}{|\mathbf{r}_{ij}|^3}(1 - \tilde{D}(|\mathbf{r}_{ij}|))\right\},$$

where $\beta = 1/k_B T_p$, $k_B T_p$ is the energy temperature of the dust grains: and $Z(\mathbf{r}_i)$ is a charge expressed in terms of the electron charge $Q(\mathbf{r}_i) = Z(\mathbf{r}_i)e$. The distances are normalized to the Debye radius r_D (for simple estimates, it can be written in the form $r_D^2 = kT_g/4\pi e^2(n_e + n_i)$, where T_g is the gas temperature).

The Coulomb coupling parameter can be represented as

$$\Gamma(\mathbf{r}_i, \mathbf{r}_j) = \frac{\beta e^2}{4\pi\varepsilon_0}\frac{Z_s(\mathbf{r}_i)Z_s(\mathbf{r}_j)}{r_D} \approx \Gamma = Z_p^2 e^2/4\pi\varepsilon_0 k_B T_p r_D$$

or

$$\Gamma = \gamma_p\langle r\rangle/r_D.$$

Here, $\gamma_p = Z_p^2 e^2/4\pi\varepsilon_0 k_B T_p\langle r\rangle$ is the nonideality parameter, Z_p is the characteristic grain charge, and $\langle r\rangle = (4\pi n_p/3)^{-1/3}$ is the average distance between grains.

Note once again that potential (6) takes into account a number of physical factors affecting the interaction of dust grains in the plasma. First, we include the spatial dependence of the grain charge on the floating potential. Second, the first and second terms describing the spherically symmetric part of the interaction involve

the shielding of the dust grains by the plasma electrons and ions, which strongly interact with grains. The third and fourth terms in (6) describe the anisotropic interaction of dust grains, which results from focusing of the ion current by the highly charged dust grains. For the dust grains positioned one above the other, the sum of the third and fourth terms in the expression for the effective potential becomes negative (the grains attract each other). If the grains are positioned in the horizontal plane, the above sum is positive and the grains are repelled from each other. The fitting function $\tilde{D}$ also takes into account the destruction of the ion clouds when the dust grains approach each other at a distance on the order of the Debye radius. A dust grain can be suspended if its weight is balanced out by the electrostatic field of the potential well, which acts on both the negatively charged dust grain and the equivalent positive charge of the surrounding ion cloud.

6. NUMERICAL SIMULATION

To carry out numerical simulations of ordered structures, it is necessary to specify the dependence of the grain charge and effective charge of the surrounding ion cloud on spatial coordinates. As a first approximation, we assume that the negative charge of the dust grains is proportional to the floating potential of the discharge-tube wall; i.e., it is a function of the vertical coordinate of the dust grain only, namely, $\phi_t(\mathbf{r}) = \varphi_W(z)$ [see (3)]. As was done in [18], we assume that the effective charge of the ion cloud is proportional to the dust-grain charge. As was mentioned above, in the general case, the relationship between the negative charge of the dust grain and positive charge of the shielding cloud can be different due to the difference between recombination processes in the plasma-production region and at small distances from the discharge-tube wall, where the wall-sheath processes play an important role. In our model, this difference was not taken into account. Finally, the charge dependence on spatial coordinates was taken in the form

$$Z_-(\mathbf{r}) = Z_p\phi_z,$$

$$Z_+(\mathbf{r}) = -\alpha Z_-(\mathbf{r}),$$

$$\phi_z = \varphi_W(z)/\varphi_W(0),$$

where the coefficient α accounts for the difference between the effective charge of the ion cloud and the dust-grain charge ($\alpha < 1$). Returning to the interaction of dust grains with the potential well described by (2), we note that the potential energy (normalized to the energy temperature of dust grains k_BT_p) of the interaction of the ith grain with the electrostatic field of the potential well created by an inductive discharge is described by the expression

$$\beta V(\mathbf{r}_i) = \beta e[\varphi(\mathbf{r}_i)Z_-(\mathbf{r}_i) + \varphi(\mathbf{r}_i + d\mathbf{e}_i^+)Z_+(\mathbf{r}_i + d\mathbf{e}_i^+)]. \quad (7)$$

Numerical simulations of the plasma with dust grains were carried out by the standard Monte Carlo method [26]. A finite number N of grains was placed in a cell of size L. It was convenient to measure the cell size L in terms of the Debye radius r_D, which was about 0.5 mm under the experimental conditions. Taking into account the performance of the available computers and restricting ourselves to a reasonable computation time, the number of grains was chosen to be $N = 300$–1000. Accordingly, the linear size of the Monte Carlo cell holding the characteristic dusty structure was chosen to be $L = 80r_D \approx 4$ cm, which approximately corresponds to the experimental conditions. Note that the linear size and the number of dust grains used in numerical calculations were less than those in the experiment; this substantially reduces the requirements for computer power and decreases the computation time to about ten hours. The dust grains were suspended in a potential well described by (7). Parameters Q, a, and σ_m estimated for our experimental conditions were 3×10^2e, $8r_D$, and 2, respectively. The parameters of the potential corresponding to the force with which the tube wall acted on the grains were taken to be $\varphi_\infty = 8$ V, $\Delta\varphi = 8$ V, and $d_W = 14r_D$. Gravity acted on the grains along the z-axis.

The interaction between dust grains is determined by (6). In calculations, the quantities $T_p = 300$°C, $Z_p = 3 \times 10^3$, Γ, and L were fixed, whereas the parameters d and $|Z_+(\mathbf{r}_i)/Z_s(\mathbf{r}_i)| = |\alpha/(\alpha - 1)|$ varied from $0.5r_D$ to $2r_D$ and from 0.01 to 0.5, respectively. According to the results of [22], this corresponded to the conditions of a 20- to 200-Pa-pressure gas discharge. From the physical standpoint, the change in the absolute value of the parameter $Z_+(\mathbf{r}_i)/Z_s(\mathbf{r}_i)$ is equivalent to the change in the neutral-gas pressure; for example, the increase in the neutral-gas pressure decreases the mean free path of ions and prevents them from focusing downstream of the dust grains. Figure 4 compares potential (6) to the Coulomb and Debye potentials, as well as the Debye potential approaching the asymptote r^{-2} at large distances. For convenience, the ratios of these potentials to the Coulomb potential are presented on the logarithmic scale. Thus, the Coulomb potential in Fig. 4 is presented by the zero-ordinate horizontal line, whereas the Debye potential corresponds to the linear dependence. All of the repelling potentials are substantially weaker than the Coulomb potential.

7. DISCUSSION

Let us consider the results of Monte Carlo simulations. The total uncompensated dipole charge $Z_s(\mathbf{r})$ as a function of height is shown in Fig. 5. The vertical axis shows the coordinate along the discharge-tube axis (the total length is equal to the size of the Monte Carlo cell). The center of the plasma ellipsoid generated by an RF discharge is positioned at the $0.9L$ height. As the distance from the center of the plasma ellipsoid decreases,

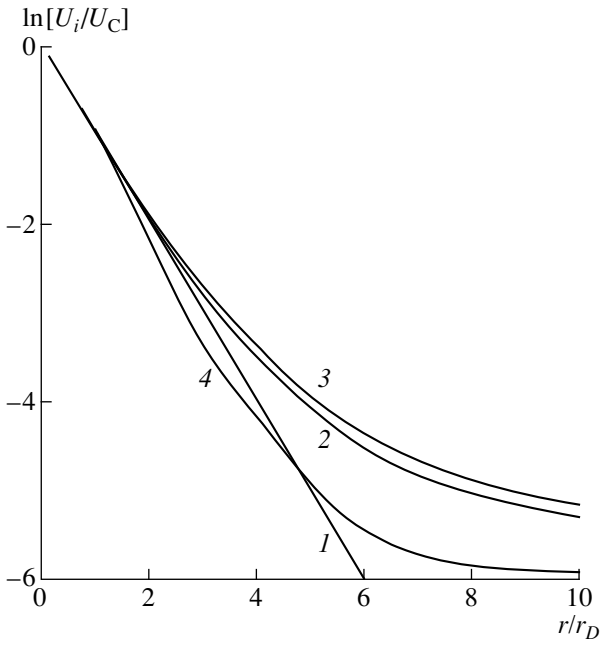

Fig. 4. Logarithm of the ratio of the dust-grain interaction potential U_i to the Coulomb potential U_C: (*1*) Debye potential, (*2*) Debye potential approaching the asymptote r^{-2} at large distances, and (*3*, *4*) upper and lower values the potential (6) takes when the angle θ varies from 0 to π for $d = 0.8r_D$ and $Z_+(\mathbf{r}_i)/Z_s(\mathbf{r}_i) \approx -0.1$.

the total charge $Z_s(\mathbf{r}_i)$ of the system consisting of a negatively charged grain and positive ion cloud increases in magnitude. In spite of the attraction to the plasma ellipsoid, a significant number of dust grains are located in the region of the RF discharge where the plasma potential is smaller in magnitude and changes rather gradually. Calculations show that the change in the pressure or, analogously, in the ratio $Z_+(\mathbf{r}_i)/Z_s(\mathbf{r}_i)$ affects the distribution only slightly. Figure 6 presents the axial vertical cross section of the calculated dusty structure. The figure size is equal to the size of the Monte Carlo cell. The horizontal axis in Fig. 6 shows the distance across the discharge tube. The point 0.5 *L* corresponds to the discharge-tube axis. The scale division 0.1 corresponds to approximately $8r_D$, or 4 mm. As was noted above, the physical reason for the formation of a linear structure is the focusing action of the negatively charged dust grains on the ion current, which leads to the production of clouds with increased ion density between grains. As a result, an additional attraction occurs between the dust grains along the discharge axis against the background of a spherically symmetric effective repelling potential. At the same time, in the horizontal plane, there is additional repelling.

The data presented confirm the conclusion about the predominant location of grains in the region of the potential well where the repelling energy is minimum. The appearance of individual, very long filament structures is energetically advantageous not only because of the dipole attraction in the linear structures, but also because of the presence of the non-Coulomb additive to the Coulomb force (this effect was discussed in [18]). This additive is directed oppositely to the gradient of the charge $Q(\mathbf{r})$ (in our case, outward from the center of the plasma ellipsoid).

Note also that, as the pressure increases, the Debye radius decreases and the effective focusing of the ion current by the negatively charged dust grains becomes weaker. This results in a decrease in the dipole moment determining the dust-grain interaction potential in the model in question. As a result, the increase in the pres-

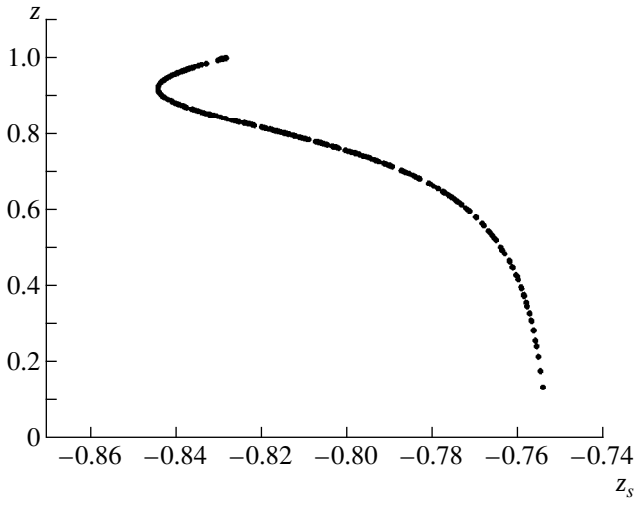

Fig. 5. The quantity Z_s in terms of $3 \times 10^3 e$ as a function of height for $d = 0.8r_D$ and $Z_+(\mathbf{r}_i)/Z_s(\mathbf{r}_i) \approx -0.1$.

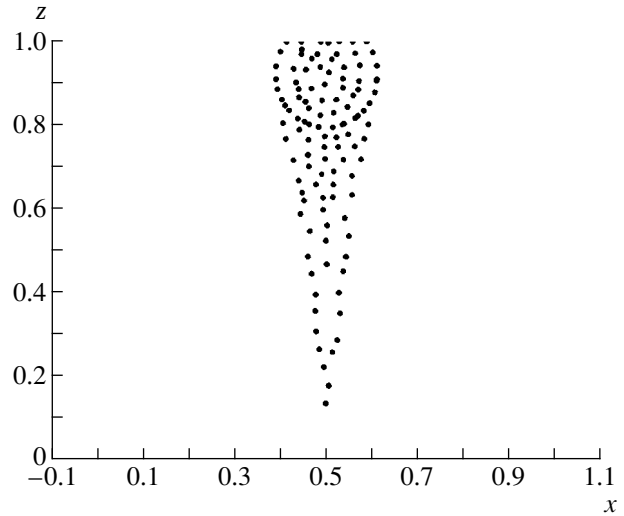

Fig. 6. Vertical cross section of a dusty structure for $d = 0.8r_D$ and $Z_+(\mathbf{r}_i)/Z_s(\mathbf{r}_i) \approx -0.1$.

sure leads to a decrease in the size of linear grain structures and the number of grains in them. This is in qualitative agreement with the experimental results.

8. CONCLUSION

We have carried out experimental and theoretical studies of the physical mechanisms for dust-grain levitation and the formation of ordered grain structures in the plasma of an inductive RF discharge. The plasma was produced in neon at a pressure of 25–500 Pa. The melamine formaldehyde grains were 1.87 μm in diameter. An effective dust-grain interaction potential is proposed. The potential takes into account the spatial dependence of the grain charge on the plasma floating potential and the interaction anisotropy resulting from the focusing of the drift ion current by the negatively charged grains. We have performed Monte Carlo simulations of the ordered structures produced in the dusty plasma. The results of simulations allowed us to explain the specific features of the formation of filament grain structures in the plasma of an electrodeless inductive discharge. The results are in qualitative agreement with the experiments.

ACKNOWLEDGMENTS

We thank Yu.V. Gerasimov for assistance in experiments. This work was supported by the Russian Foundation for Basic Research, project no. 97-02-16572.

REFERENCES

1. J. H. Chu and I. Lin, Phys. Rev. Lett. **72**, 4009 (1994).
2. H. Thomas, G. E. Morfill, V. Demmel, *et al.*, Phys. Rev. Lett. **73**, 652 (1994).
3. A. Melzer, T. Trottenberg, and A. Piel, Phys. Lett. A **191**, 301 (1994).
4. J. B. Pieper and J. Goree, Phys. Rev. Lett. **77**, 3137 (1996).
5. A. Melzer, A. Homann, and A. Piel, Phys. Rev. E **53**, 2757 (1996).
6. J. E. Daugherty, M. D. Kilgore, R. K. Porteous, and D. B. Graves, J. Appl. Phys. **72**, 3934 (1992).
7. Y. Hayashi and K. Tachibana, Jpn. J. Appl. Phys. **33**, L804 (1994).
8. V. E. Fortov, A. P. Nefedov, O. F. Petrov, *et al.*, Phys. Lett. A **219**, 89 (1996).
9. V. E. Fortov, V. S. Filinov, A. P. Nefedov, *et al.*, Zh. Éksp. Teor. Fiz. **111**, 889 (1997) [JETP **84**, 489 (1997)].
10. V. E. Fortov, A. P. Nefedov, V. M. Torchinsky, *et al.*, Pis'ma Zh. Éksp. Teor. Fiz. **64**, 86 (1996) [JETP Lett. **64**, 92 (1996)].
11. V. E. Fortov, A. P. Nefedov, V. M. Torchinsky, *et al.*, Phys. Lett. A **229**, 317 (1997).
12. A. M. Lipaev, V. I. Molotkov, A. P. Nefedov, *et al.*, Zh. Éksp. Teor. Fiz. **112**, 2030 (1997) [JETP **85**, 1110 (1997)].
13. Yu. V. Gerasimov, A. P. Nefedov, V. A. Sinel'shchikov, and V. E. Fortov, Pis'ma Zh. Tekh. Fiz. **24** (19), 62 (1998) [Tech. Phys. Lett. **24**, 774 (1998)].
14. Yu. P. Raĭzer, M. N. Shneĭder, and N. A. Yatsenko, *RF Capacitive Discharge* (Nauka, Moscow, 1995).
15. U. Kortshagen, I. Pukropski, and L. D. Tsendin, Phys. Rev. E **51**, 6063 (1995).
16. L. D. Landau and E. M. Lifshitz, *Electrodynamics of Continuous Media* (Nauka, Moscow, 1970; Pergamon, Oxford, 1960).
17. O. A. Sinkevich and I. P. Stakhanov, *Plasma Physics* (Vysshaya Shkola, Moscow, 1991).
18. O. M. Belotserkovskiĭ, I. E. Zakharov, A. M. Nefedov, *et al.*, Zh. Éksp. Teor. Fiz. **115**, 819 (1999) [JETP **88**, 449 (1999)].
19. H. M. Thomas and G. E. Morfill, Nature (London) **379**, 806 (1996).
20. V. N. Tsytovich, Usp. Fiz. Nauk **167**, 57 (1997) [Phys. Usp. **40**, 53 (1997)].
21. A. P. Nefedov, O. F. Petrov, and V. E. Fortov, Usp. Fiz. Nauk **167**, 1215 (1997) [Phys. Usp. **40**, 1163 (1997)].
22. V. A. Schweigert, I. V. Schweigert, A. Melzer, *et al.*, Phys. Rev. E **54**, 4155 (1996).
23. I. V. Schweigert, V. A. Schweigert, V. M. Bedanov, *et al.*, Zh. Éksp. Teor. Fiz. **114**, 1672 (1998) [JETP **87**, 905 (1998)].
24. F. Melandso and J. Goree, Phys. Rev. E **52**, 5312 (1995).
25. F. Melandso and J. Goree, J. Vac. Sci. Technol. A **14**, 511 (1996).
26. V. M. Zamalin, G. E. Norman, and V. S. Filinov, *Monte Carlo Method in Statistical Thermodynamics* (Nauka, Moscow, 1977).

Translated by A. D. Smirnova[†]

[†] Deceased.

Plasma Physics Reports, Vol. 26, No. 5, 2000, pp. 424–427. Translated from Fizika Plazmy, Vol. 26, No. 5, 2000, pp. 455–458.

DUSTY PLASMA

Electrostatic Structures in a Plasma and BGK Screening

K. V. Chukbar

Russian Research Centre Kurchatov Institute, pl. Kurchatova 1, Moscow, 123182 Russia

Received May 20, 1999; in final form, August 11, 1999

Abstract—It is shown that the electrostatic attraction between two likely charged plane plates in a plasma can appear due to the formation of "holes" in the phase space of the electrons or ions. The possibility of extending the theory of this effect to the three-dimensional case of a plasma with point dust grains is discussed. *© 2000 MAIK "Nauka/Interperiodica".*

One of the main theoretical problems in the physics of dusty plasmas is that of explaining the experimentally observed mutual attraction between dust grains. Although, in plasmalike media, dust grains, as a rule, behave as probes at a negative floating (on the order of $\sim T_e$) plasma potential (or, in some cases, positive potential), they nevertheless form quite regular and stable crystalline structures [1–3]. Real dusty plasmas are rather complicated systems characterized by a diversity of dynamic interaction processes, which involve plasma particles of each species: due to the permanent bombardment of solid-state grains by electrons and ions, the charge, energy, momentum, etc. are continuously exchanged between the grains and plasma particles. Due to their complexity, dusty plasmas are the subject of significant research efforts aimed at developing more theoretical models (in addition to the many models that have already been constructed) for studying all possible attraction mechanisms (see [1–3]). However, the starting point in constructing each of these models is the assertion that taking into account only electrostatic forces is insufficient to build up a realistic theory, because describing the electrostatic interaction of likely charged "test" dust grains within the approximation of Debye screening should inevitably result in their repulsion. A somewhat different approach was developed in [4–8] and subsequent studies, which were devoted to the questions of how the steady ion flows that may arise in the plasma affect the classical screening (in which case the relevant mechanisms could not be regarded as being "static").

Although the starting assertion adopted in most papers has a solid physical foundation, it seems to be somewhat erroneous. In this paper, we focus on the possibility that the structures of likely charged test grains coupled exclusively through electrostatic forces can, in principle, form via unconventional screening mechanisms in a dusty plasma. Our analysis reveals that such dust-grain structures possess some interesting properties, which should be observed in experiments. Unfortunately, the author succeeded in rigorously justifying the proposed physical picture of the formation of electrostatic structures only in the one-dimensional case. Although this case may also be investigated experimentally, the one-dimensional character of the problem introduces additional difficulties in establishing an agreement between the proposed model picture and the realistic one. On the other hand, these obstacles do not seem to be insurmountable (see below); moreover, from the methodological standpoint, it is important that conventional approaches that do not possess any three-dimensional properties do not ensure a complete analysis of a real situation.

We consider the interaction of two infinite plane plates having the same surface charge density σ and located at $x = \pm a$. In this case, the spatial distribution of the electrostatic potential is determined by the equation [9, 10]

$$\frac{d^2\varphi}{dx^2} + 4\pi\rho(\varphi) = -4\pi\sigma(\delta(x-a) + \delta(x+a)), \quad (1)$$

where ρ is the charge density of the screening cloud, which is induced as a result of the response of the plasma components to the perturbing action of the external charges (in the case at hand, plates) in the plasma. This charge density is found from the assumption that the steady-state velocity distribution functions of the plasma electrons and ions are $f_\alpha(m_\alpha v^2/2 + e_\alpha\varphi)$,

$$\rho(\varphi) = \sum_{\alpha = e, i} e_\alpha n_\alpha \left(\int f_\alpha dv - 1\right). \quad (2)$$

In the linear approximation, for low values of φ and for Maxwellian distributions, formula (2) passes over to the classical Debye expression $-ne^2\varphi(1/T_e + z_i/T_i)$.

Note that, in this model formulation of the problem, the plates are assumed to be transparent to electrons and ions; more precisely, the plates interact with plasma particles only through the electric field. Each of the attempts to incorporate other (nonelectrostatic) forces fails to extend the model to a non-one-dimensional case, because the physical motion of plasma electrons and ions, which is also affected primarily by

1063-780X/00/2605-0424$20.00 © 2000 MAIK "Nauka/Interperiodica"

the electric fields of the grains, is, at the same time, much less sensitive to a solid-state point grain than to a plate.

The most general solution to equation (1) can easily be written in quadratures, in which case the charges in the form of plane plates do not affect the spatial distribution of $\varphi(x)$ but are responsible for the electric field jumps at the plate positions, $[d\varphi/dx]_-^+ = -4\pi\sigma$. To better understand the problems associated with the above arguments that likely charged particles will inevitably repulse each other, it is only necessary to analyze the properties of the quadrature expressions and there is no need to write out the relevant integrals. To do this, it is sufficient to know the general features of the behavior of the solution in coordinate space (Fig. 1) and (simultaneously) in the phase plane of equation (1) (Fig. 2). For definiteness, we choose $\sigma > 0$ (the sign of the external charges is unimportant in our problem). Since equation (1) without allowance for external charges is invariant under the transformation $x \longrightarrow -x$, the phase portrait of this equation is symmetric about the axis $\varphi' = 0$ but not about the axis $\varphi = 0$, by virtue of the fact that, in the general case, $\rho(\varphi) \neq -\rho(-\varphi)$.

We can immediately see that, for any single-valued continuous function $\rho(\varphi)$ (it is, in fact, suffice to require that the function be integrable) satisfying, in the general (nonlinear and non-Maxwellian) case, the quite permissive restrictions $\rho(0) = 0$ (the plasma is quasineutral far from the plates) and $\operatorname{sign}\rho = -\operatorname{sign}\varphi$ (the functions f_α are monotonically decreasing functions of their arguments; otherwise, we cannot speak about the screening and the situation under analysis is unstable; see [10]), the point $x = -a$ in Fig. 1 (in which the potential profile is symmetric about the axis $x = 0$) corresponds to a certain point φ_0 (dependent of σ and a) of the transition from the upper branch $\varphi' = s(\varphi)$ of the separatrix to a phase trajectory inside the region bounded by the separatrix $\varphi' = \pm s(\varphi)$ in Fig. 2 (the point $x = a$ corresponds to the transition back to the lower branch of the separatrix). In other words, the electric field $|d\varphi/dx|$ on the outer surfaces of the plates is always stronger than that on the inner surfaces; i.e., in the model at hand, the electrostatic interaction inevitably results in the repulsion of the plates. The question of whether the electrostatic interaction will always result in the repulsion of likely charged point grains in three-dimensional geometry appears to be unanswered.

Nevertheless, in contrast to the above considerations and to the "theorem" we have just proved, the relation between the electric fields on the outer and inner surfaces of the plates can be reversed. For this purpose, the function $\rho(\varphi)$ should be chosen to be different over different spatial intervals: $(-\infty, -a)$, $(-a, a)$, and (a, ∞); i.e., this function, being "globally" continuous, should take on different values at $\varphi \neq \varphi_0$ within these intervals. In this case, first, the separatrices are different for different portions of the phase trajectories of equation (1) and, second, the transitions at the point φ_0 can result in

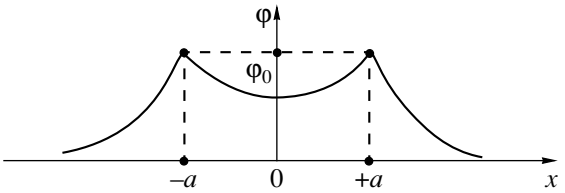

Fig. 1. Solution to (1) in coordinate space.

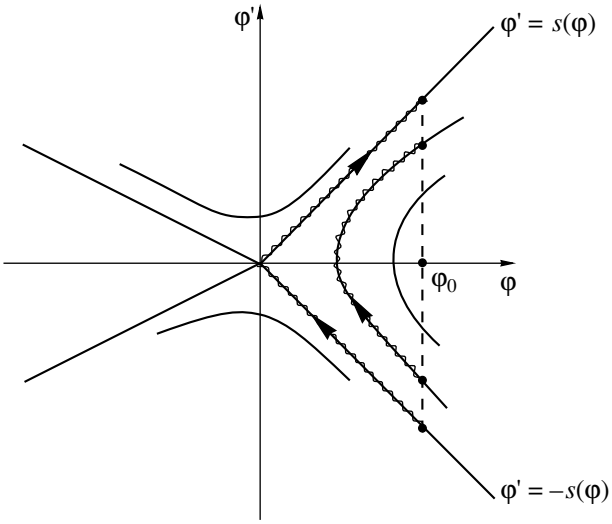

Fig. 2. Phase portrait of equation (1) with the separatrix $s(\varphi) \equiv \sqrt{\int_0^\varphi 8\pi|\rho(\phi)|\,d\phi}$.

an increase in $|\varphi'|$, so that the trajectory remains inside the desired region (φ, φ') if the spatial distribution of the charge density of the screening cloud between the plates is such that the curve $\varphi' = -s(\varphi)$ between the plates lies below that in the external region.

In fact, from the time of the classical paper by Bernstein *et al.* [11], it has been well known that the plasma may exhibit nearly arbitrary self-consistent steady-state (or running at a constant velocity) potential distributions, referred to as Bernstein–Green–Kruskal (BGK) waves: it is always possible to choose the distribution functions f_α that ensure that the charge density $\rho(\varphi)$ satisfies the homogeneous (without the right-hand side) equation (1) for an arbitrary (hand-drawn) function $\varphi(x)$. Such freedom stems from the fact that the electrons and ions that may be trapped in the regions of potential humps and wells, respectively, do not contribute to the plasma charge outside these regions. As a result, the distribution function f_α of each plasma component turns out to be different in different spatial regions, in which case the solution can be constructed from piecewise functions. Unfortunately, the reverse problem of determining the distribution functions f_α in (2) from the desired charge density ρ [as is the case

with the solution of equation (1)] is justified mathematically only within one-dimensional geometry, in which we are working here; nevertheless, this circumstance stands as an additional argument in favor of the choice of our model. However, the phenomenon in question does not possess these specific features (see below).

We can easily see that the external charges, which manifest themselves only in the boundary conditions at $x = \pm a$, do not restrict the freedom in the choice of distribution functions. This indicates that it is possible to "construct" a steady plasma state in which the values of $|\varphi'|$ at the inner surfaces of the plates will be higher than those at the outer surfaces (the questions of whether this state is stable and how it is established as time elapses go beyond the scope of our paper, which is aimed merely at discussing the possibility for this state to exist). This plasma state can be called the "BGK screening state."

On the other hand, the physical situation under analysis is rather nontrivial. For the likely charged plates to attract one another, it is necessary to ensure an opposite plasma charge between the plates in excess of the charge ρ of a single plasma cloud. However, such a plasma charge cannot be ensured at the expense of the electron (in the case $\sigma > 0$) or ion (in the opposite case) trapping because, in the region between the planes, the potential $\varphi(x)$ exhibits a hump rather than a well (Fig. 1). However, we can open up another possibility: the cloud charge ρ can be changed in the desired manner through the deficiency of the plasma particles of another species (it is the two-component nature of the plasma that is responsible for freedom in choosing the distribution functions in the case of BGK screening [11]). In other words, we speak about a so-called hole in the phase space of the ions (see, e.g., [11, 12]). In fact, the ions that come from $\pm\infty$ are successively reflected from the potential barriers (Fig. 1), thereby giving rise to the plasma charge $\rho(\varphi)$, so that only a certain fraction of the ions can overcome the potential barriers and enter the well region between them. If, initially, the well region is free of trapped positive ions (i.e., those with energies $m_i v^2/2 + e_i\varphi < e_i\varphi_0$) or contains a smaller number of positive ions in comparison with that at the points with the same electric potential outside the system of two plates, then the well region will be negatively charged because of the incomplete neutralization of the plasma electron component between the plates.

Now, we are left with an example of the above possible situation in which $|\varphi'(-a + 0)| > |\varphi'(-a - 0)|$ (according to [11], the number of such examples is infinite). Performing fairly simple manipulations, we can reduce the problem to that of the existence of a positive quantity $\tilde{\varphi} < \varphi_0$ satisfying the condition

$$\int_{\tilde{\varphi}}^{\varphi_0} -\rho_{in}(\phi)d\phi > \int_0^{\varphi_0} -\rho_{out}(\phi)d\phi, \qquad (3)$$

where ρ_{out} and ρ_{in} (which take on the same value at $\varphi = \varphi_0$) are the charge densities of the screening cloud outside the system of two plates and in the region between them, respectively. (Recall that the potential ρ_0 at the charged plates should be determined self-consistently from the complete solution to equation (1). In our approach, fixing this potential at the prescribed values of σ and ρ corresponds to fixing a certain value of a; however, this circumstance is unimportant for the effect under analysis.) The simplest example obeying condition (3) is that in which the velocity distribution functions of the electrons and ions are both Maxwellian with the temperatures $T_i \ll T_e \longrightarrow \infty$ and no ions are trapped in the region $(-a, a)$. In this example, the screening is governed exclusively by the ions, and, for low values of φ, we have

$$\rho_{out} = e_i n_i\left(\exp\left(-\frac{e_i\varphi}{T_i}\right) - 1\right) \approx -n_i\frac{e_i\varphi}{T_i},$$

$$\rho_{in} = e_i n_i\left(\exp\left(-\frac{e_i\varphi}{T_i}\right)\mathrm{erfc}\sqrt{\frac{e_i(\varphi_0 - \varphi)}{T_i}} - 1\right)$$

$$\approx -n_i\left(\frac{e_i\varphi}{T_i} + \sqrt{\frac{2e_i(\varphi_0 - \varphi)}{\pi T_i}}\right)$$

(in the case of BGK screening, the requirement $\rho(0) = 0$ should not necessarily be satisfied in the region between the plates), which obviously indicates that condition (3) holds.

Recall that the simple one-dimensional model we have examined cannot be automatically extended to plasmas that contain point dust grains and are described in three-dimensional geometry. One (but not the most important) reason is the lack of relevant rigorous mathematical formulas. The main problem is that, in three-dimensional plasma configurations, the potential wells, which naturally form between the charged test planes, should be prepared in a certain way. On the other hand, it is the holes (rather than the trapping regions) in the phase spaces of the electrons and ions that make the BGK regime easy to realize, because, in the case of nonuniform potential distributions in non-one-dimensional plasma configurations, the dominant role is played by the scattering processes, which hinder particle trapping but prevent the particle trajectories from passing through certain regions in phase spaces. Generally, in six-dimensional ($2 \times 3 = 6$) phase spaces, the holes not only may exist but may also be stable [12].

Thus, we have shown that the mutual attraction of likely charged test grains and, accordingly, the formation of regular crystalline structures in dusty plasmas may, in principle, be explained in terms of unconventional screening mechanisms. However, in this model, crystalline structures have to be composed of the initial external charged grains and the "holes" that appear in the plasma and whose charge is opposite to the grain charge. Presumably, the most serious obstacle to the

achieving the BGK regime is the plasma collisionality, which is unfavorable for the existence of piecewise distribution functions. The main qualitative (and somewhat surprising) distinguishing feature of the proposed attraction mechanism is that the plasma should contain particles whose charge coincides in sign with the charge of the test dust grains. In the example we have analyzed, the sign of the surface charge density was chosen arbitrarily: the proposed mechanism is insensitive to this sign and applies equally well to ions and electrons, in contrast to the flow-related screening mechanism mentioned above [4–8], in which the key role is played by directed ion motion at reasonable velocities. Moreover, it is the electron holes that may be observed in present-day dusty plasma experiments, because most of them are carried out with negatively charged dust grains.

ACKNOWLEDGMENTS

I am grateful to A.S. Kingsep and V.N. Tsytovich, who from time to time directed my attention to dusty plasma, and to V.P. Pastukhov for fruitful discussions. This work was supported in part by the Ministry of Science of the Russian Federation (under the program "Fundamental Problems of Nonlinear Dynamics") and INTAS (grant no. 21, 1998).

REFERENCES

1. V. N. Tsytovich, Usp. Fiz. Nauk **167**, 57 (1997) [Phys. Usp. **40**, 57 (1997)].
2. A. M. Ignatov, Fiz. Plazmy **24**, 731 (1998) [Plasma Phys. Rep. **24**, 677 (1998)].
3. A. P. Nefedov, O. F. Petrov, and S. A. Khrapak, Fiz. Plazmy **24**, 1109 (1998) [Plasma Phys. Rep. **24**, 1037 (1998)].
4. S. V. Vladimirov and M. Nambu, Phys. Rev. E **52**, R2172 (1995).
5. M. Nambu, S. V. Vladimirov, and P. K. Shukla, Phys. Lett. A **203**, 40 (1995).
6. S. V. Vladimirov and O. Ishihara, Phys. Plasmas **3**, 444 (1996).
7. F. Melanso and J. Goree, Phys. Rev. E **52**, 5312 (1995).
8. V. A. Schweigert, I. V. Schweigert, A. Meltzer, *et al.*, Phys. Rev. E **54**, 4155 (1996).
9. D. A. Frank-Kamenetskiĭ, *Course on Plasma Physics* (Atomizdat, Moscow, 1968), Chap. 1.
10. A. F. Alexandrov, L. S. Bogdankevich, and A. A. Rukhadze, *Principles of Plasma Electrodynamics* (Vysshaya Shkola, Moscow, 1988; Springer-Verlag, Berlin, 1984).
11. I. B. Bernstein, J. M. Green, and M. D. Kruskal, Phys. Rev. **108**, 546 (1957).
12. V. I. Petviashvili and V. V. Yan'kov, in *Reviews of Plasma Physics*, Ed. by M. A. Leontovich and B. B. Kadomtsev (Énergoatomizdat, Moscow, 1985; Consultants Bureau, New York, 1990), Vol. 14.

Translated by G. V. Shepekina

Plasma Physics Reports, Vol. 26, No. 5, 2000, pp. 428–438. Translated from Fizika Plazmy, Vol. 26, No. 5, 2000, pp. 459–469.

NONLINEAR PHENOMENA

Qualitative Models of the Enhanced-Rate Propagation of a Magnetic Field in a Plasma due to the Hall Effect

A. B. Kukushkin and K. V. Cherepanov

Russian Research Centre Kurchatov Institute, pl. Kurchatova 1, Moscow, 123182 Russia

Received May 20, 1999

Abstract—Two qualitative electron magnetohydrodynamic models are developed of an enhanced-rate (in comparison with ordinary diffusion) propagation of a magnetic field in a plasma due to the Hall effect. The first model is based on a simple hydrodynamic approach, which in particular makes it possible to reproduce some familiar results. The second model provides an exact analytic description of the main global parameters of the enhanced-rate propagation of a magnetic field in an isothermal inhomogeneous plasma: the front velocity of the magnetic field and the effective front width. © *2000 MAIK "Nauka/Interperiodica".*

1. INTRODUCTION

The Hall effect in plasmas [1, 2], which is governed by the freezing of a magnetic field in the electron component and, accordingly, by transport of the magnetic field with the electron current velocity, results in an enhanced-rate propagation of the magnetic field, whereas the current flows along the plasma density gradient (to follow the development of this problem, see reviews and papers [3–14]). The electron density can be nonuniform both at the plasma boundary (at the electrode surface) and in the plasma interior. The main mechanism for the rapid penetration of a magnetic field into a plasma is the "braking" of the magnetic field (which is carried by the electric current) at the positive gradient of the electron density. As a result, the magnetic field is "scattered" in the direction orthogonal to the direction of the electron current. This phenomenon has a substantial impact on the dynamics of the field and electron component treated in the electron magnetohydrodynamic (EMHD) theory and on the plasma dynamics treated in a more general MHD approximation. In particular, the rapid penetration of a magnetic field due to the Hall effect plays a key role in the formation of a highly inhomogeneous noncylindrical current sheath in Filippov's plasma focus (PF) discharges. This is confirmed by the good agreement (see [12]) between the experimental data obtained by Orlov *et al.* on the LV-2 device [15] and the results of two-dimensional numerical simulations carried out by Vikhrev and Zabajdullin [11].

In accordance with the hypothesis advanced by Kukushkin and Rantsev-Kartinov [18], the Hall effect plays a particularly important role [16, 17] in the formation of a closed heterogeneous spheromak-like magnetic configuration (SLMC) by the self-magnetic field of Filippov's PF. An analysis of the experimental results of [15] performed by Kukushkin *et al.* [16, 17] provides evidence for the formation of an SLMC with a substantial stored energy. An important feature of the formation of an SLMC in a PF discharge is the possibility of further increasing the stored energy via the compression of the plasma inside the SLMC by the residual magnetic field of the PF. In a hybrid Z–θ pinch that is formed at the major axis of an SLMC, the plasma energy density is substantially (several orders of magnitude) higher than that in experiments on building up force-free spheromak configurations [19] (with the help of an artificially produced poloidal field) and on confining the spheromak plasma in a special chamber of the "flux conserver" type (see, e.g., [20]).

Here, we develop two qualitative models of an enhanced-rate (in comparison with ordinary diffusion) propagation of the magnetic field in a plasma due to the Hall effect. The first model, which develops the "hydrodynamic" approach proposed by Kukushkin [21], makes it possible not only to reproduce some familiar results of EMHD theory, such as the propagation of a magnetic field along the anode surface in a homogeneous plasma (Section 2.1) and the penetration of a magnetic field into a plasma with a step (Section 2.2) density profile and with a density profile increasing monotonically (Section 2.3) in the direction of the current velocity, but also to derive scalings for a plasma with a nonmonotonic density profile in the EMHD model (Section 2.3) and for the initial stage of the plasma displacement from the anode in MHD theory (Section 2.4). The second model provides exact analytic expressions for the main global parameters of the enhanced-rate propagation of a magnetic field in an isothermal inhomogeneous plasma: the front velocity of the magnetic field (Section 3.1) and the effective front thickness (Section 3.2).

1063-780X/00/2605-0428$20.00

2. "HYDRODYNAMIC" MODEL OF THE ENHANCED-RATE PROPAGATION OF A MAGNETIC FIELD IN A PLASMA

2.1. Enhanced-Rate Propagation of a Magnetic Field along the Anode

In EMHD theory (in which the ion velocity is equal, by definition, to $V_i = 0$), the enhanced-rate propagation of a magnetic field along the anode surface due to the Hall effect can be described by a simple qualitative model proposed by Kukushkin [21], which is based on the qualitative solution to the EMHD equations for an isothermal plasma (Fig. 1),

$$\frac{\partial \mathbf{H}}{\partial t} = -\mathbf{curl}(D_\sigma \mathrm{rot}\,\mathbf{H}) + \mathbf{curl}[\mathbf{V}_e, \mathbf{H}], \quad (1)$$

$$\mathbf{V}_e = -\frac{c}{4\pi ne}\mathbf{curl}\mathbf{H}, \quad (2)$$

with the following initial and boundary conditions: the magnetic field $\mathbf{H} = (0, -H_0, 0)$ at $t = 0$ is nonzero only in the region $X < 0$ and the anode occupies the region $Z < 0$. The EMHD model is based on the following qualitative considerations. A magnetic field diffusely penetrating into the plasma gives rise to a density gradient on the diffusion scale length $\Delta x_{\mathrm{dif}}(t)$. By virtue of the freezing of the magnetic field in the electron plasma component, the plasma density gradient–driven electron current with density $j_z = (c/4\pi)(\mathbf{curl}\,\mathbf{H})_Z = (c/4\pi)(\partial H_y/\partial x)$ carries the magnetic field with a current velocity $V_{eZ} = -j_z/ne$ toward the anode. Near the anode surface, where a high (formally, infinitely high) electron density (and, accordingly, infinitely high electron conductivity) prevents the magnetic field from penetrating into the anode, the electron current changes direction and starts to flow with a velocity $V_{eX}(t) \approx cH_0/4\pi ne\Delta x_{\mathrm{dif}}(t)$ along the anode surface, thus carrying the magnetic field with a velocity $\omega_e\tau_{ei}$ times higher than the diffusion velocity. From these considerations, we easily arrive at the following results:

$$\Delta z_{\mathrm{eff}} \sim \Delta x_{\mathrm{dif}} = \sqrt{2D_\sigma t}, \quad (3)$$

$$\Delta x_{\mathrm{eff}} \sim \sqrt{2D_{\mathrm{eff}}\, t}, \quad (4)$$

$$D_{\mathrm{eff}} = (\omega_e\tau_{ei})^2 D_\sigma, \quad (5)$$

where

$$D_\sigma = \frac{c^2}{4\pi\sigma}, \quad (6)$$

τ_{ei} is the electron–ion (e–i) collision frequency, ω_e is the electron gyrofrequency, σ is the plasma conductivity, and D_σ is the magnetic field diffusion coefficient in a plasma.

The qualitative model proposed in [21] reproduces the above formula for D_{eff}, which was derived earlier by Gordeev *et al.* [9] from an exact analytic (actually, one-dimensional) analysis of the magnetic field propagation in a narrow layer along the anode (the applicability range of the equations used in [9] was then analyzed in detail by Chukbar [10]). The results obtained in [9], which apply to the propagation of a magnetic field in a plasma in a narrow layer along the anode, were later confirmed by the results of two-dimensional numerical simulations [11], which are valid not only in the anode region but also over the entire plasma volume.

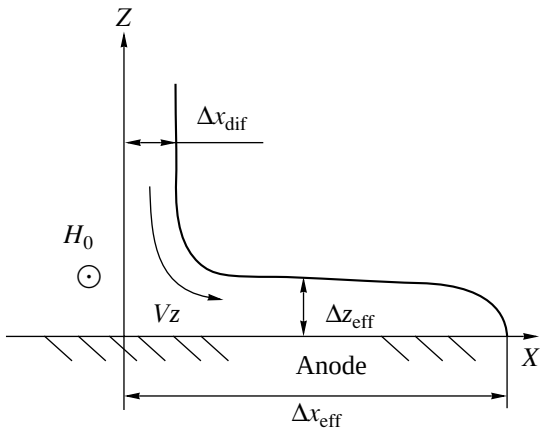

Fig. 1. A graphical illustration of the mechanism for enhanced-rate propagation of a magnetic field along the anode surface.

2.2. Propagation of a Magnetic Field along the Boundary between Two Media in the EMHD Model

We consider the propagation of a magnetic field along the boundary between two media with different densities, n_1 and n_2, of free electrons (see the left part of Fig. 2). This is the problem of the magnetic field propagation along the anode surface generalized to the case in which the magnetic field can penetrate into the anode. We consider the simplest case of an isothermal plasma (the method described below can also be used to treat the problem in the case of a nonisothermal plasma).

We consider the magnetic field distribution such that, for $n_2 > n_1$, the electron motion is as shown in the right part of Fig. 2. The motion of the magnetic field front is governed by the current velocities in the first (V_{e1}) and second (V_{e2}) media. If the second medium were an anode with infinite conductivity, then, by the time t, the magnetic field in the first medium would propagate over the distance $\Delta x_{\mathrm{eff}}^{(1)} \sim \sqrt{2D_{\mathrm{eff}}^{(1)} t}$. However, since the conductivity of the second medium is finite, the electrons in the second medium move in the direction opposite to that of the electron motion in the first medium, causing the magnetic field front to propagate backward through the distance $\Delta x_{\mathrm{eff}}^{(2)} \sim \sqrt{2D_{\mathrm{eff}}^{(2)} t}$.

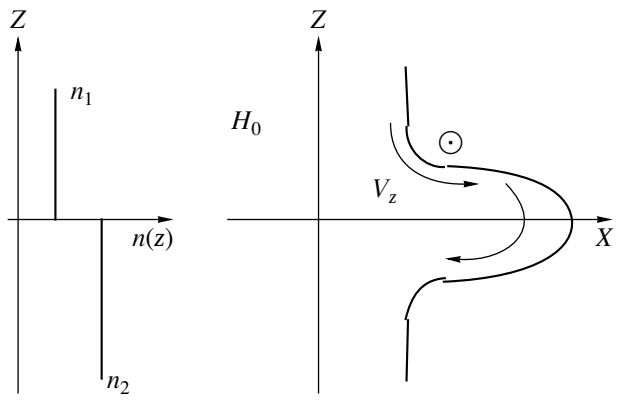

Fig. 2. A graphical illustration of the mechanism for enhanced-rate propagation of a magnetic field along the boundary between two media with different densities of free electrons (on the left). The shape of the field front profile at a certain time is displayed on the right. The arrows show the direction of the electron current.

Consequently, the distance through which the field front propagates along the boundary between the two media with the same temperatures can be estimated as the difference

$$\Delta x_{\text{eff}} \sim \sqrt{2D_{\text{eff}}^{(1)}t} - \sqrt{2D_{\text{eff}}^{(2)}t}. \quad (7)$$

With allowance for (5) and (6), we obtain

$$\Delta x_{\text{eff}}^{(1,2)} \sim \frac{cH_0}{4\pi e}\frac{n_2 - n_1}{n_2 n_1}\sqrt{\frac{t}{2D_\sigma}} = \sqrt{2D_{\text{eff}}^{(1,2)}t}, \quad (8)$$

where

$$\sqrt{D_{\text{eff}}^{(1,2)}} \equiv \sqrt{D_{\text{eff}}^{(1)}} - \sqrt{D_{\text{eff}}^{(2)}}, \quad (9)$$

and, as a result, arrive at

$$D_{\text{eff}}^{(1,2)} \sim \left(\frac{\sigma H_0^2}{ec}\frac{n_2 - n_1}{n_2 n_1}\right)^2 D_\sigma. \quad (10)$$

In the limit $n_2 \longrightarrow \infty$, formula (10) passes over to (5).

Expression (10) coincides with the relevant expression that was obtained by Vikhrev and Zabajdullin [11,13] using the model that they developed and successfully tested numerically. Note that, in [11, 13], expression (10) was derived for the more general case of media with different conductivities.

2.3. Propagation of a Magnetic Field in a Plasma with a Finite Current-Aligned Density Gradient in the EMHD Model

We consider the dynamic problem of a magnetic field transport by the electric current in a plasma with a small electron-density gradient of fixed sign along the magnetic field front, assuming the plasma temperature to be constant. The results we will obtain from solving this model problem will allow us to derive a qualitative formula describing the motion of the magnetic field front in a plasma with a small density gradient of arbitrary sign, which is regarded as a small density perturbation.

The evolutionary equation for the magnetic field has the form

$$\frac{\partial H}{\partial t} = D_\sigma\left(\frac{\partial^2 H}{\partial x^2} + \frac{\partial^2 H}{\partial z^2}\right) - \frac{\partial}{\partial x}(HV_x) - \frac{\partial}{\partial z}(HV_z), \quad (11)$$

where the velocities V_x and V_z depend on the plasma density $n(z)$.

Neglecting diffusion along the magnetic field front, i.e., imposing the condition

$$\frac{\partial^2 H}{\partial x^2} \gg \frac{\partial^2 H}{\partial z^2}, \quad (12)$$

we reduce the initial equation to

$$\frac{\partial H}{\partial t} = D_\sigma\frac{\partial^2 H}{\partial x^2} - \frac{\partial}{\partial x}(HV_x) - \frac{\partial}{\partial z}(HV_z). \quad (13)$$

In the case n = const, equation (13) automatically goes over to a standard one-dimensional equation for the magnetic field diffusion (with the boundary conditions presented in Section 2.1). The diffusive penetration of the field $H^{(0)}$ into a plasma gives rise to a plasma current with the density

$$j_z = -enV_Z^{(0)} = \frac{c}{4\pi}\frac{\partial H^{(0)}}{\partial x} \approx -en\omega_e\tau_{ei}\frac{\partial \Delta x_{\text{dif}}}{\partial t}. \quad (14)$$

where the superscript in the velocity refers to the unperturbed plasma density. Since, in the case at hand, $\partial H/\partial x = 0$, we have $V_x^{(0)} = 0$.

Now, we turn to a plasma in which the density is nonuniform in the direction of the current (i.e., along the Z-axis). We seek the electron current velocity in the form $V_x = V_x^{(0)} + V_x^{(1)}$. Assuming that the density perturbation affects the field dynamics only slightly, we arrive at the relationship

$$\frac{\partial}{\partial x}(HV_X^{(1)}) \sim -\frac{\partial}{\partial z}(HV_Z^{(0)}), \quad (15)$$

which implies that the perturbed current with the velocity $V_x^{(1)}$ is driven exclusively by the plasma density gradient $\partial n/\partial z \neq 0$. Here, we also assume that the transport of the magnetic field by the current causes the "tongue" to extend in the x direction (see Fig. 2) more rapidly than in the case of ordinary diffusion. Then, equation (13) splits into the conventional diffusion equation and equation (15), which describes the magnetic field transport at the electron current velocity. With allowance for (14), we obtain the estimate for $V_x^{(1)}$ and, accordingly,

for the velocity of the magnetic field front motion driven by the density gradient $\partial n/\partial z$,

$$\dot{x} \equiv V_X^{(1)} \approx -V_Z^{(0)} \frac{\partial \ln n}{\partial z} \Delta x_{\rm dif} \approx \omega_e \tau_{ei} D_\sigma \frac{\partial \ln n}{\partial z}, \qquad (16)$$

in which case the field front penetrates the distance

$$\Delta x_{\rm eff}^{(1)} = \int_0^t V_X^{(1)}(z, t')dt' = \omega_e \tau_{ei} \frac{\partial \ln n}{\partial z} D_\sigma t. \qquad (17)$$

With allowance for the front motion driven by ordinary diffusion, we obtain

$$\Delta x_{\rm eff} \approx \Delta x_{dif} \left(1 + \varepsilon \omega_e \tau_{ei} \Delta x_{\rm dif} \frac{\partial \ln n}{\partial z}\right). \qquad (18)$$

The qualitative method used to derive (18) implies that the numerical coefficient ε is of order unity.

Estimate (16) agrees with the results of analytically solving the problem of the penetration of a magnetic field into a plasma whose density increases in the direction of the electron current [6, 7].

To analyze the case in which the electron current substantially changes its direction, i.e., the problem of how the propagation direction of the magnetic field changes in the presence of a localized electron density perturbation (this process may be called the "scattering" of the magnetic field by a localized electron density perturbation), we can apply estimate (16) to a local change in the propagation direction of the magnetic field due to $(\mathbf{j}_e, \partial n/\partial \mathbf{r}) \neq 0$. In this way, it is necessary to transform formula (16) to the frame of reference in which the Z-axis is oriented in the local direction of the vector $\mathbf{j}_e$, so that the magnetic field is scattered through a small angle with respect to this vector. The coordinates of the magnetic field front in the new frame and in the laboratory frame are related by

$$\frac{\partial x}{\partial t} = \frac{\partial \tilde{x}}{\partial t}\cos\alpha - \frac{\partial \tilde{z}}{\partial t}\sin\alpha + \sqrt{\frac{D_\sigma}{2t}}, \qquad (19)$$

$$\sin\alpha = \left|\frac{\partial x}{\partial z}\right| \left[1 + \left(\frac{\partial x}{\partial z}\right)^2\right]^{-1/2}, \quad \cos\alpha = \left[1 + \left(\frac{\partial x}{\partial z}\right)^2\right]^{-1/2},$$

where α is the angle between the tangent to the front at the point at which the new coordinates $(\tilde{Z}, \tilde{X})$ are introduced and the Z-axis (see Fig. 3). With allowance for the relationships

$$\left.\begin{aligned} \frac{\partial \tilde{z}}{\partial t} \approx \frac{c}{4\pi n e} \frac{H_0}{\Delta \tilde{x}_{\rm dif}} = \omega_e \tau_{ei} D_\sigma \sqrt{\frac{1}{2D_\sigma t}} \\ \frac{\partial \tilde{x}}{\partial t} \approx \omega_e \tau_{ei} D_\sigma \frac{\partial \ln n}{\partial z} \cos\alpha \end{aligned}\right\}, \qquad (20)$$

which hold in the new frame, we obtain the following equation, which describes the motion of the magnetic field front $x = x(z, t)$ and is linear in x:

$$\frac{\partial x}{\partial t} + \left|\frac{\partial x}{\partial z}\right| \omega_e \tau_{ei} \sqrt{\frac{D_\sigma}{2t}} = \omega_e \tau_{ei} D_\sigma \frac{\partial \ln n}{\partial z} + \sqrt{\frac{D_\sigma}{2t}}, \qquad (21)$$

where the e–i collision frequency $\tau_{ei} = \tau_{ei}(z)$ depends implicitly on z through the plasma density $n(z)$. Equation (21) has the solution

$$\begin{aligned} x = \omega_e \tau_{ei} \frac{\partial \ln n}{\partial z} D_\sigma t + \sqrt{2D_\sigma t} \\ + f\left(\int_{Z_0}^{Z} \frac{dz'}{\omega_e \tau_{ei}(z')} - \sqrt{2D_\sigma t}\right). \end{aligned} \qquad (22)$$

Here, the first term accounts for the contribution of the nonuniform plasma density; the second terms incorporates the contribution of the ordinary diffusion; and the third term describes the transport of the initially perturbed magnetic field front, which is specified through the equation $x(z)|_{t=0} = f\left(\int_{Z_0}^{Z} \frac{dz'}{\omega_e \tau_{ei}(z')}\right)$, by an electron current with the current velocity V_z.

This result generalizes formula (18) (and the corresponding limit of the exact solution obtained by Kingsep *et al.* [7]) to the case of an alternating-sign density gradient $\partial n/\partial z$. Formula (22) describes not only the extension of the tongue in the direction of ordinary diffusion (which results in a faster penetration of the mag-

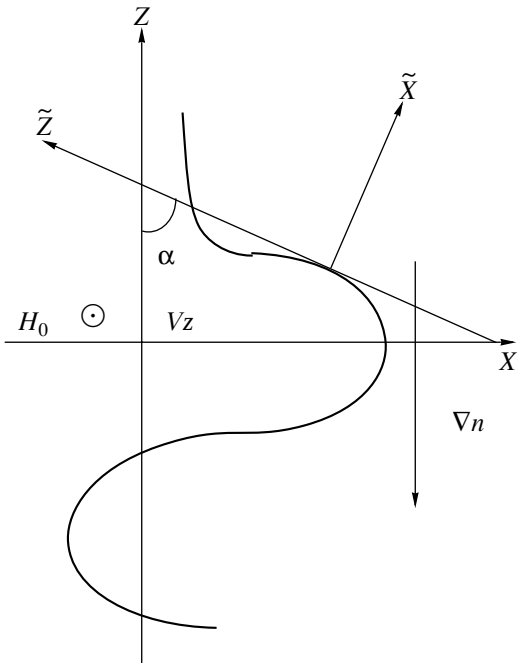

Fig. 3. A schematic representation of the transition from the initial (laboratory) frame to the local frame with the $\tilde{Z}$-axis oriented along the electron current. The arrow indicates the initial direction of the electron density gradient.

netic field into a plasma) but also the appearance of a similar new "tongue," which is stretched in the opposite direction and in which the background magnetic field is reduced (Fig. 3). Formula (22) agrees with the numerical results obtained by Zabajdullin and Vikhrev [14], who simulated the propagation of a magnetic field in a plasma with an alternating-sign density gradient along the current velocity. Also, formula (22) is in qualitative agreement with the results obtained by Chukbar and Yan'kov [8] for the case of a steady-state density profile varying periodically in the direction of the current velocity. Chukbar and Yan'kov [8] showed that, in a steady state, the current flows along snakelike lines, in which case the plasma electric conductivity is $(\omega_e\tau_{ei})^2$ times higher.

The above derivation of the formula describing the evolution of the magnetic field front in a plasma with a small density gradient can be generalized to the case in which the plasma density gradient is arbitrary but the magnetic field diffusion in the direction perpendicular to the field front is still incompletely incorporated. If we take into account the fact that, as the direction of the velocity vector of the electron current at the magnetic field front changes, the absolute value of the velocity vector decreases with time according to the "diffusion" law $(V_z^{(0)}(t))^2 = V_x^2 + V_z^2$, then the velocity component orthogonal to the initial magnetic field front can be estimated as

$$V_x(t) \sim V_z^{(0)}(t)\sin\varphi,$$

$$V_x(t) \approx \Delta x_{\text{dif}} V_z(t)\frac{\partial \ln n}{\partial z}, \quad \tan\varphi = \Delta x_{\text{dif}}\frac{\partial \ln n}{\partial z},$$

where φ is the angle by which the direction of the current velocity changes. This velocity component can be rewritten as

$$V_x(t) \approx V_z^{(0)}\frac{\partial \ln n}{\partial z}\frac{1}{\sqrt{1+\left(\Delta x_{\text{dif}}\dfrac{\partial \ln n}{\partial z}\right)^2}}, \qquad (23)$$

so that the evolution of the magnetic field front is described by the equation

$$x_0 = \omega_e\tau_{ei}\left(\frac{\partial \ln n}{\partial z}\right)^{-1}\left(\sqrt{1+D_\sigma t\left(\frac{\partial \ln n}{\partial z}\right)^2}-1\right). \qquad (24)$$

This result agrees qualitatively with the formula

$$x_0 = \frac{1}{2}\omega_e\tau_{ei}D_\sigma t\frac{n_0}{n(z)}\frac{\partial \ln n}{\partial z}\Big/\left(1+\frac{\partial \ln n}{\partial z}\sqrt{D_\sigma t}\right) \qquad (25)$$

(where n_0 is the unperturbed plasma density), which was deduced by Zabajdullin [22] from the results of two-dimensional numerical simulations. The above formulas reflect the fact that the transition between two limiting regimes of the enhanced-rate propagation of a magnetic field in a plasma due to the Hall effect—specifically, the regime in which the magnetic field propagates as a wave (see [7]) and the regime of diffusive penetration (see [9])—can be described qualitatively by the parameter

$$\mu = \sqrt{D_\sigma t}\frac{\partial \ln n}{\partial z}. \qquad (26)$$

Although formulas (24) and (25) are insufficiently accurate for describing the dynamics of the magnetic field front (see Section 3.2 below), they are simple and illustrative and provide a better insight into the transition between different regimes of the enhanced-rate propagation of a magnetic field in a plasma due to the Hall effect.

2.4 Enhanced-Rate Propagation of a Magnetic Field in a Plasma along the Anode Surface with Allowance for Finite Ion Inertia: Plasma Displacement from the Anode

Now, we consider how the enhanced-rate propagation of a magnetic field affects the dynamics of plasma ions (this corresponds to the disruption of the ion's immobility in the sense that ion inertia is taken into account). An understanding of this problem requires solving two-fluid MHD equations (see, e.g., [2, 3, 5, 23, 24]).

For equal constant electron and ion temperatures, $T_e = T_i = T$ = const [24, 25], and for a magnetic field pressure much higher than the plasma pressure, $H^2/8\pi \gg p$ (the latter condition is valid, in particular, in the initial stages of high-current gas discharges, such as *Z*-pinch discharges and PF discharges), the Euler equation and continuity equation take the familiar form

$$\left.\begin{aligned}\rho\frac{d\mathbf{u}}{dt} &= -\nabla\frac{H^2}{8\pi}+\frac{1}{4\pi}(\mathbf{H}\nabla)\mathbf{H}\\ \frac{\partial\rho}{\partial t}+\operatorname{div}(\rho\mathbf{u}) &= 0\end{aligned}\right\},$$

where the plasma density ρ and plasma velocity $\mathbf{u}$ are determined by $\rho = m_e n_e + m_i n_i$ and $\mathbf{u} = \dfrac{m_e n_e \mathbf{V}_e + m_i n_i \mathbf{V}_i}{\rho}$, respectively.

For the magnetic field $\mathbf{H} = (0, -H_0, 0)$ and plasma velocity $\mathbf{u} = (u_x, 0, u_z)$ the second term on the right-hand side of the Euler equation vanishes, in which case we have

$$\left.\begin{aligned}\rho\frac{du_x}{dt} &= -\frac{\partial}{\partial x}\frac{H^2}{8\pi}\\ \rho\frac{du_z}{dt} &= -\frac{\partial}{\partial z}\frac{H^2}{8\pi}\end{aligned}\right\}. \qquad (27)$$

Using the approach proposed by Kukushkin [21], we can find the scaling describing the plasma displacement from the anode in the above-mentioned initial dis-

charge stage, in which the plasma compression is insignificant and we can set the plasma density to be constant, $\rho = \rho_0 = \text{const}$. Since, near the anode surface, the magnetic field falls off from H_0 to zero along the X-axis (Fig. 1), we have $\partial H/\partial x \approx -H_0/\Delta x_{\text{eff}}$ and, analogously, $\partial H/\partial z \approx -H_0/\Delta z_{\text{dif}}$ (see Section 2.1), which yields

$$\frac{du_x}{dt} \approx \frac{2H_0}{8\pi\rho_0}\frac{2H}{\Delta x_{\text{eff}}} = \frac{H_0^2}{4\pi\rho_0\sqrt{2D_{\text{eff}}\,t}}.$$

We integrate this equation over t to obtain

$$u_x \approx \frac{H_0^2}{2\pi\rho_0\omega_e\tau_{ei}}\sqrt{\frac{t}{2D_\sigma}}, \tag{28}$$

$$u_z \approx \frac{H_0^2}{2\pi\rho_0}\sqrt{\frac{t}{2D_\sigma}}. \tag{29}$$

A comparison between (28) and (29) gives

$$u_z \simeq (\omega_e\tau_{ei})u_x. \tag{30}$$

Consequently, in the initial stage, the velocity u_z at which the plasma is displaced from the anode is $\omega_e\tau_{ei}$ times higher than the velocity at which the plasma is "dragged" along the anode surface. Thus, we can conclude that the efficiency with which the plasma is displaced from the anode surface because of the magnetic field penetration into the anode region is much higher than the efficiency with which the plasma is dragged by the field.

The perturbed plasma density near the anode can be estimated in an analogous manner from the continuity equation in which the plasma density is sought in the form $\rho(t) \approx \rho_0(1 + \delta(t))$ with $\delta(t) \ll 1$. In the initial stage of the plasma displacement from the anode surface ($t \ll 1/\omega_e\omega_i\tau_{ei}$), the plasma density evolves according to the law

$$\rho(t) \approx \rho_0(1 - \omega_e\tau_{ei}\omega_i t). \tag{31}$$

3. GLOBAL PARAMETERS OF THE MAGNETIC FIELD PROPAGATION IN A PLASMA

We consider a two-dimensional problem of the propagation of a magnetic field in an isothermal plasma in the EMHD model. We assume that at the initial time $t = 0$, the magnetic field $\mathbf{H} = (0, -H_0, 0)$ occupies the region $x < 0$ in a plasma with density $n = n(z)$. With allowance for (2), equation (11), which describes the magnetic field dynamics, becomes

$$\frac{\partial H}{\partial t} = D_\sigma\left(\frac{\partial^2 H}{\partial x^2} + \frac{\partial^2 H}{\partial z^2}\right) - \frac{cH}{4\pi e}\frac{\partial H}{\partial x}\frac{\partial}{\partial z}\left(\frac{1}{n}\right). \tag{32}$$

When the plasma density gradient along the magnetic field front in a plasma is small, we can neglect magnetic field diffusion in the Z direction, in which case, with allowance for the inequality $\frac{\partial^2 H}{\partial x^2} \gg \frac{\partial^2 H}{\partial z^2}$, equation (32) can be simplified to

$$\frac{\partial H}{\partial t} = D_\sigma\frac{\partial^2 H}{\partial x^2} - \frac{cH}{4\pi e}\frac{\partial H}{\partial x}\frac{\partial}{\partial z}\left(\frac{1}{n}\right). \tag{33}$$

This equation has an exact analytic solution [7] describing the propagation of the magnetic field in a plasma in the form of a wave,

$$H = \frac{H_0}{e^{\frac{x-ut}{\lambda}} + 1}, \tag{34}$$

where the front width is characterized by the parameter

$$\lambda = \left[\frac{\sigma H_0}{2ec}\frac{\partial}{\partial z}\left(\frac{1}{n}\right)\right]^{-1} \tag{35}$$

and the front velocity is

$$u = -\frac{cH_0}{8\pi e}\frac{\partial}{\partial z}\left(\frac{1}{n}\right). \tag{36}$$

In a plasma with an arbitrary density gradient, equation (32) cannot be solved analytically, meaning only numerical results have been obtained [11, 13, 14, 22]. However, it turns out that such global parameters of the magnetic field dynamics as the depth of the penetration of a magnetic field into a plasma and the effective width of the magnetic field front can be described analytically.

3.1. Velocity of the Enhanced-Rate Penetration of a Magnetic Field into a Plasma and the Penetration Depth

We start by imposing the conditions (Fig. 4)

$$H(z, x, t)|_{x\to-\infty} = H_0, \quad H(z, x, t)|_{x\to+\infty} = 0, \quad \left.\frac{\partial H}{\partial x}\right|_{x\to+\infty} = 0 \tag{37}$$

and introducing the effective penetration depth x_0,

$$\int_{-\infty}^{+\infty}(H(x, z, t) - H_0 h(x_0 - x)) = 0, \tag{38}$$

where $h(x)$ is a step function of unit height.

As will be shown below, definition (38) correlates reasonably well with the solutions to equation (33) and with the results obtained for the case of a steep density gradient. Definition (38) and conditions (37) will enable us to derive a closed differential equation for the penetration depth of the magnetic field into a plasma.

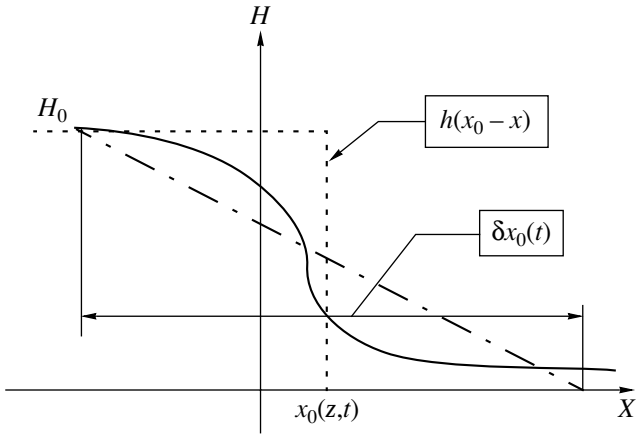

Fig. 4. A comparison of the position of the front of the propagating magnetic field (dashed lines) with the instantaneous magnetic field profile (solid curve). The linear approximation of the field front profile (dashed-and-dotted line) and the characteristic front width are shown schematically.

We differentiate (38) with respect to time, take into account (37), and perform simple manipulations to obtain

$$\frac{\partial x_0(z,t)}{\partial t} = D_\sigma \frac{\partial^2 x_0(z,t)}{\partial z^2} - \frac{cH_0}{8\pi e}\frac{\partial}{\partial z}\left(\frac{1}{n(z)}\right). \quad (39)$$

Equation (39) with the initial condition $x(z, t = 0) = 0$ has the solution

$$x_0(z,t) = -\frac{cH_0}{16\pi e}\int_{-\infty}^{\infty}\int_0^t \frac{\partial}{\partial \xi}\left(\frac{1}{n(\xi)}\right)\frac{e^{-\frac{(z-\xi)^2}{4D_\sigma(t-\tau)}}}{\sqrt{\pi D_\sigma (t-\tau)}} d\tau d\xi. \quad (40)$$

Taking the time derivative of (39), we find that the field front velocity, defined as $u \equiv u_x = \partial x_0/\partial t$, satisfies the equation

$$\frac{\partial u(z,t)}{\partial t} = D_\sigma \frac{\partial^2 u(z,t)}{\partial z^2}. \quad (41)$$

Assuming that, at the initial instant, the magnetic field does not diffuse in the z-direction $\left(\frac{\partial^2 H}{\partial x^2} \gg \frac{\partial^2 H}{\partial z^2}\right.$ and $\left.\frac{\partial^2 x_0(z,t)}{\partial z^2}\bigg|_{t=0} = 0\right)$, we determine the front velocity at $t = 0$:

$$u(z,0) = -\frac{cH_0}{8\pi e}\frac{\partial}{\partial z}\left(\frac{1}{n(z)}\right). \quad (42)$$

The solution to equation (41) with the initial condition (42) is

$$u(z,t) = -\frac{cH_0}{16\pi e\sqrt{\pi D_\sigma t}}\int_{-\infty}^{\infty}\frac{\partial}{\partial \xi}\left(\frac{1}{n(\xi)}\right)e^{-\frac{(z-\xi)^2}{4D_\sigma t}} d\xi. \quad (43)$$

The same solution can also be derived by differentiating expression (40) with respect to time.

This solution generalizes the results obtained previously for the penetration depth of the magnetic field and the propagation velocity of the magnetic field front in plasmas with small [7] and infinitely large [9, 11, 13] density gradients. In fact, in the first case, we have

$$u = -\frac{cH_0}{16\pi e\sqrt{\pi D_\sigma t}}\int_{-\infty}^{\infty}\frac{\partial}{\partial \xi}\left(\frac{1}{n(\xi)}\right)e^{-\frac{(z-\xi)^2}{4D_\sigma t}} d\xi$$

$$= -\frac{cH_0}{8\pi e\sqrt{\pi D_\sigma t}}\int_{-\infty}^{+\infty}\frac{z-\xi}{4D_\sigma t}\frac{1}{n(\xi)}e^{-\frac{(z-\xi)^2}{4D_\sigma t}} d\xi.$$

Changing the variable $y = z - \xi$ and taking into account the relationship $\frac{1}{n(z-y)} \approx \frac{1}{n(z)} - \frac{1}{n^2(z)}\frac{\partial n}{\partial z}(z-y)$, which is valid for a plasma with a small density gradient, we arrive at expression (36). For a jump in the plasma density (Fig. 2), we have

$$\frac{\partial}{\partial \xi}\frac{1}{n} = -\frac{n_2 - n_1}{n_1 n_2}\delta(\xi),$$

which yields

$$x_0(z,t) = -\frac{cH_0}{16\pi e D_\sigma}\frac{n_2 - n_1}{n_1 n_2} \times \left\{\sqrt{4D_\sigma t}\, e^{-\frac{z^2}{4D_\sigma}} - z\sqrt{\pi}\left[1 - \mathrm{erf}\left(\frac{|z|}{\sqrt{4D_\sigma t}}\right)\right]\right\}, \quad (44)$$

where $\mathrm{erf}(x)$ is the error function. At the point $z = 0$, we obtain

$$x_0(t) = \frac{cH_0}{16\pi e D_\sigma}\frac{n_2 - n_1}{n_1 n_2}\sqrt{D_\sigma t} = \frac{\sigma H_0}{2ec}\frac{n_2 - n_1}{n_1 n_2}\sqrt{D_\sigma t}, \quad (45)$$

thereby determining the effective diffusion coefficient for the magnetic field,

$$D_{\mathrm{eff}} = \left(\frac{\sigma H_0}{2ec}\frac{n_2 - n_1}{n_1 n_2}\right)^2 D_\sigma, \quad (46)$$

which was evaluated earlier by Vikhrev and Zabajdullin [11, 13].

If the plasma density increases gradually from n_1 to n_2 over a finite distance, then, as $t \longrightarrow \infty$ ($4/D_\sigma t \gg \xi^2$),

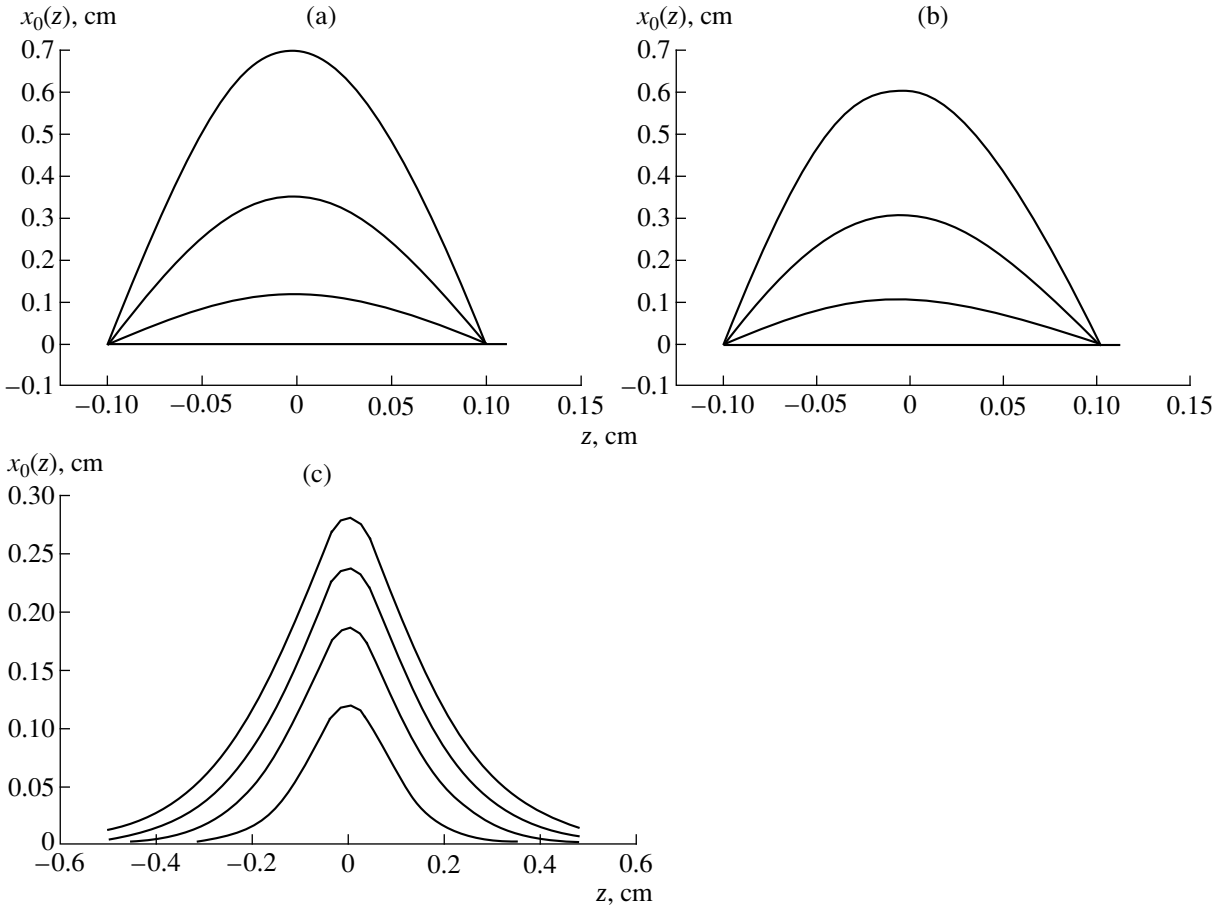

Fig. 5. A comparison between the spatial profiles of the magnetic field front at different times $\left(t = \frac{n}{4} \times 10^{-7}\ \text{s}, n = 1, \ldots, 4\right)$. Profiles (a) and (b) are computed from the approximate formulas (24) and (25), respectively, and profile (c) is calculated from the exact formula (40). The plasma density profile used in simulations is specified as $n(z) = n_0(1 + 1/2\delta(1 - \sin(\pi z/L)))$ for $|z| < L/2$ and $n = 0$ for $|z| \geq L/2$. Here, $n_0 = 1.0 \times 10^{17}$ cm^{-3}, $L = 0.2$ cm, the relative jump in the density is $\delta = 0.1$, the electron temperature is $T_e = 5$ eV, the initial magnetic field is $H_0 = 1.0 \times 10^4$ G, $D_\sigma = 3.7 \times 10^5$ cm^2/s, and $\omega_e\tau_{ei} = 33.5$.

the front velocity will approach the value

$$u = -\frac{cH_0}{16\pi e\sqrt{\pi D_\sigma t}}\frac{n_2 - n_1}{n_2 n_1}. \tag{47}$$

Numerical integration of expression (40) shows that the approximate formulas (24) and (25) are insufficiently accurate, because the magnetic field diffusion in the direction perpendicular to the instantaneous magnetic field front is incompletely incorporated (Fig. 5).

3.2. Front Width

In order to describe the front width δx_0, it is expedient to define it as

$$H_0(\delta x_0(z, t))^2 = \alpha\int_{-\infty}^{\infty}(x - x_0)[H(x, z, t) - H_0 h(x_0 - x)]dx. \tag{48}$$

It is convenient to choose the proportionality coefficient α by replacing the function $H(x, z, t)$ in formula (48) with its linear approximation (Fig. 4). As a result, we approximately obtain $\alpha = 6$.

As an example, we can use definition (48) taken with the exact field magnitude (34) corresponding to a small density gradient as an adequate characteristic front width, in which case we have $\delta x_0 = \pi\lambda$.

To transform (48), we apply the same mathematical procedure as in the previous section. As a result, we arrive at the differential equation for the front width,

$$\frac{1}{\alpha}\frac{\partial(\delta x_0)^2}{\partial t} = \frac{1}{\alpha}\frac{\partial^2(\delta x_0)^2}{\partial z^2} + D_\sigma\left[1 + \left(\frac{\partial x_0}{\partial z}\right)^2\right] + \frac{c}{4\pi enH_0}\frac{\partial \ln n}{\partial z}\int_{-\infty}^{\infty}(x - x_0)H\frac{\partial H(x, z, t)}{\partial x}dx, \tag{49}$$

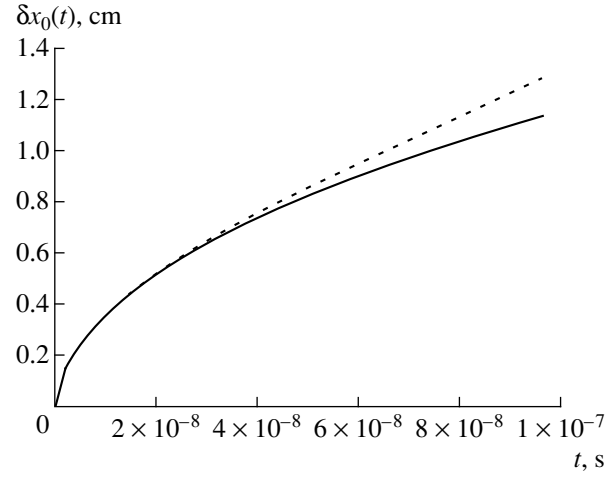

Fig. 6. Time evolution of the front width at the point $z = 0$ in the case of a periodically varying density profile $n(z) = n_0(1 + 1/2\delta(1 - \sin(\pi z/L)))$. The remaining parameters, namely, n_0, L, δ, T_e, and H_0, are the same as in Fig. 5, the initial front width being $q = 0$. The dashed curve reflects the time evolution computed from the approximate formula (54).

with the initial condition

$$H_0(\delta x_0)^2 = \alpha \int_{-\infty}^{\infty} x[H(x, z, t = 0) - H_0 h(-x)]dx. \quad (50)$$

The derivative $\partial x_0/\partial z$ can be found from (40).

Approximating the magnetic field profile in the last term of equation (49) by a linear function, we can readily see that, under the conditions $(L/\delta x_0)\omega_e\tau_{ei} \gg 1$ (where L is the spatial scale on which the plasma density varies) and $\omega_e\tau_{ei} \gg 1$ (which is characteristic of the enhanced-rate propagation problem under discussion), this term may be neglected. Interestingly, with the exact solution (34), the last term in equation (49) exactly equals zero.

Inserting expression (40) for $x_0(z, t)$ into (49) yields the equation

$$\frac{1}{\alpha}\frac{\partial(\delta x_0)^2}{\partial t} \simeq D_\sigma \frac{1}{\alpha}\frac{\partial^2(\delta x_0)^2}{\partial z^2} + D_\sigma \Bigg[1 + \frac{1}{4}(\omega_e\tau_{ei}D_\sigma)^2 \Bigg(\int_{-\infty}^{\infty}\int_{0}^{t} \frac{\partial^2}{\partial\xi^2}\Big(\frac{n_0}{n(\xi)}\Big) \frac{e^{-\frac{(z-\xi)^2}{4D_\sigma t}}}{\sqrt{4\pi D_\sigma \tau}} d\tau d\xi \Bigg)^2 \Bigg]. \quad (51)$$

With allowance for (50), the solution to this equation can be written as

$$(\delta x_0(z, t))^2/\alpha = D_\sigma t + \frac{1}{\sqrt{4\pi D_\sigma t}} \int_{-\infty}^{+\infty} q(\xi) e^{-\frac{(z-\xi)^2}{4D_\sigma t}} d\xi + D_\sigma \int_{0}^{t}\int_{-\infty}^{+\infty} g^2(\xi, \tau) \frac{e^{-\frac{(z-\xi)^2}{4D_\sigma(t-\tau)}}}{\sqrt{4\pi D_\sigma(t-\tau)}} d\xi d\tau, \quad (52)$$

where

$$g(z, t) \equiv \frac{\partial x_0}{\partial z} = \frac{1}{2}\omega_e\tau_{ei}D_\sigma \times \int_{-\infty}^{\infty}\int_{0}^{t} \frac{\partial^2}{\partial\xi^2}\Big(\frac{n_0}{n(\xi)}\Big) \frac{e^{-\frac{(z-\xi)^2}{4D_\sigma t}}}{\sqrt{4\pi D_\sigma t}} d\tau d\xi \quad (53)$$

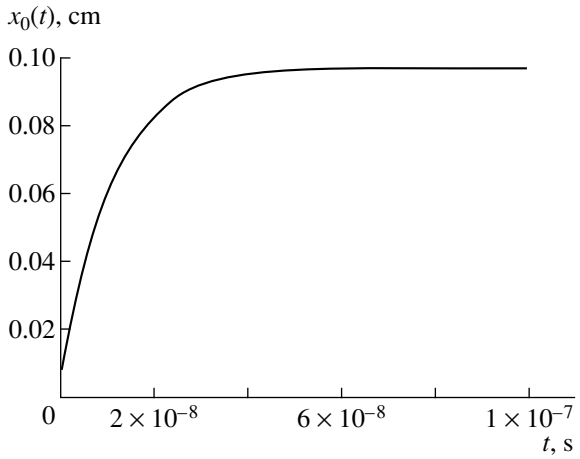

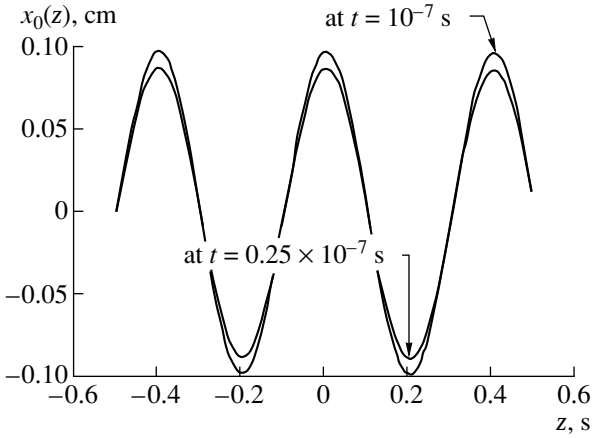

Fig. 7. Time evolution of the effective magnetic field front (40) at the fixed point $z = 0$ in the case of a plasma with a periodically varying density (on the left) and spatial profiles of the field front at two different times (on the right) for the same parameters as in Fig. 6.

and the quantity $q(z) \equiv (\delta x_0(z))^2/\alpha|_{t=0}$ accounts for the contribution of the initial thickness of the magnetic field front.

If the second derivative $\partial^2/\partial z^2[n_0/n(z)]$ varies more gradually than $\exp\left(-\frac{z^2}{4D_\sigma t}\right)$ (at least over the distance between $z - \sqrt{12D_\sigma t}$ and $z + \sqrt{12D_\sigma t}$), then, in expressions (52) and (53), we can take the density-dependent functions outside the integrals. For q = const, we obtain from (52) and (53)

$$\delta x_0(z, t) = \alpha\sqrt{\frac{q}{\alpha} + \left\{1 + \left[\frac{1}{6}(\omega_e\tau_{ei})D_\sigma t\frac{\partial^2}{\partial z^2}\left(\frac{n_0}{n(z)}\right)\right]^2\right\}D_\sigma t}. \quad (54)$$

The condition for the function $\partial^2/\partial z^2[n_0/n(z)]$ to gradually vary yields

$$\left|\frac{\partial^2}{\partial z^2}\left(\frac{n_0}{n(z \pm \sqrt{12D_\sigma t})}\right) - \frac{\partial^2}{\partial z^2}\left(\frac{n_0}{n(z)}\right)\right| \ll 1. \quad (55)$$

This inequality determines the time interval over which expression (54) is valid.

Numerical simulations with formula (52) and its approximate version (54) show that, in the initial stage, the approximate expression (54) gives quite exact (up to three significant digits) results (see Fig. 6).

It is of interest to consider the case of a plasma whose density varies periodically in space. Our simulations carried out with formula (40) show that, in such a plasma, the shape of the field front profile changes markedly only over a finite time interval and then remains essentially unchanged (Fig. 7). Of course, this does not indicate that the magnetic field stops penetrating: the field front becomes thicker by an amount δx_0, which is determined from (52), (53), or (54).

4. CONCLUSION

We have developed two qualitatively different EMHD models of an enhanced-rate (in comparison with ordinary diffusion) propagation of a magnetic field in a plasma due to the Hall effect. The first model is based on a simple hydrodynamic approach, which, in our opinion, has permitted considerable insights into the role of the Hall effect in a plasma. In particular, this model makes it possible to reproduce some familiar theoretical results and may prove useful for clarifying the role of the Hall effect without turning to simplified models, which are inevitably used in rigorous analytic analyses.

In contrast, the second model endeavors to provide an exact analytic description of the representative parameters of the magnetic field propagation. In the case of an enhanced-rate propagation of the magnetic field in an isothermal inhomogeneous plasma, these are the effective velocity of the magnetic field front and the effective front width. The results obtained with this model make it possible to check the accuracy of the simple formulas—in particular, formula (25), derived by Zabajdullin [22], and formula (24), obtained in Section 2—that describe a transition from the regime of diffusive penetration [9] to the regime in which the magnetic field propagates as a wave [7].

ACKNOWLEDGMENTS

We are grateful to O.Z. Zabajdullin and K.V. Chukbar for a helpful discussion of the manuscript.

REFERENCES

1. A. I. Morozov and A. P. Shubin, Zh. Éksp. Teor. Fiz. **46**, 710 (1964) [Sov. Phys. JETP **19**, 484 (1964)].
2. A. I. Morozov and L. S. Solov'ev, in *Reviews of Plasma Physics*, Ed. by M. A. Leontovich (Atomizdat, Moscow, 1974; Consultants Bureau, New York, 1980), Vol. 8.
3. A. S. Kingsep, K. V. Chukbar, and V. V. Yan'kov, in *Reviews of Plasma Physics*, Ed. by B. B. Kadomtsev (Énergoizdat, Moscow, 1987; Consultants Bureau, New York, 1990), Vol. 16.
4. V. V. Vikhrev and K. G. Gureev, Nucl. Fusion **17**, 291 (1977).
5. V. V. Vikhrev and S. I. Braginskii, in *Reviews of Plasma Physics*, Ed. by M. A. Leontovich (Atomizdat, Moscow, 1980; Consultants Bureau, New York, 1986), Vol. 10.
6. A. S. Kingsep, L. I. Rudakov, and K. V. Chukbar, Dokl. Akad. Nauk SSSR, Fiz. **262**, 1131 (1982) [Sov. Phys. Doklady **27**, 140 (1982)].
7. A. S. Kingsep, Yu. V. Mokhov, and K. V. Chukbar, Fiz. Plazmy **10**, 854 (1984) [Sov. J. Plasma Phys. **10**, 495 (1984)].
8. K. V. Chukbar and V. V. Yan'kov, Zh. Tekh. Fiz. **58**, 2130 (1988) [Sov. Phys. Tech. Phys. **33**, 1293 (1988)].
9. A. V. Gordeev, A. V. Grechikha, and Ya. L. Kalda, Fiz. Plazmy **16**, 95 (1990) [Sov. J. Plasma Phys. **16**, 55 (1990)].
10. K. V. Chukbar, Zh. Éksp. Teor. Fiz. **109**, 1335 (1996) [JETP **82**, 719 (1996)].
11. V. V. Vikhrev and O. Z. Zabaĭdullin, in *Proceedings of 3rd International Conference on Dense Z-Pinches, London, 1993* (AIP, New York, 1993), Ed. by M. Haines and A. Knight [AIP Conf. Proc. **299**, 165 (1993)].
12. V. V. Vikhrev, O. Z. Zabaĭdullin, and A. R. Terent'ev, Fiz. Plazmy **21**, 23 (1995) [Plasma Phys. Rep. **21**, 20 (1995)].
13. V. V. Vikhrev and O. Z. Zabaĭdullin, Fiz. Plazmy **20**, 968 (1994) [Plasma Phys. Rep. **20**, 867 (1994)].
14. O. Z. Zabaĭdullin and V. V. Vikhrev, Phys. Plasmas **3**, 2248 (1996).
15. M. M. Orlov, A. R. Terent'ev, and V. A. Khrabrov, Fiz. Plazmy **11**, 1517 (1985) [Sov. J. Plasma Phys. **11**, 876 (1985)]; Fiz. Plazmy **11**, 1268 (1985) [Sov. J. Plasma Phys. **11**, 727 (1985)].
16. A. B. Kukushkin, V. A. Rantsev-Kartinov, and A. R. Terentiev, Fusion Technol. **32**, 83 (1997).

17. A. B. Kukushkin, V. A. Rantsev-Kartinov, A. R. Terentiev, and K. V. Cherepanov, in *Proceedings of 4th International Conference on Dense Z-Pinches, Vancouver, 1997* (AIP, New York, 1997), Ed. by N. R. Pereira, J. Davis, and P. E. Pulsifer [AIP Conf. Proc. **409**, 381 (1997)].

18. A. B. Kukushkin, V. A. Rantsev-Kartinov, Preprint No. IAE 5646/6 (RRC Kurchatov Institute, Moscow, 1993).

19. J. B. Taylor, Phys. Rev. Lett. **33**, 139 (1974); Rev. Mod. Phys. **58**, 741 (1986).

20. T. R. Jarboe, Plasma Phys. Controlled Fusion **36**, 945 (1994).

21. A. B. Kukushkin, in *Proceedings of 3rd International Conference on Dense Z-Pinches, London, 1993* (AIP, New York, 1993), Ed. by M. Haines and A. Knight [AIP Conf. Proc. **299**, 154 (1993)].

22. O. Z. Zabaĭdullin, Preprint No. 5828/6 (RRC Kurchatov Institute, Moscow, 1994).

23. V. E. Golant, A. P. Zhilinskiĭ, and I. E. Sakharov, *Fundamentals of Plasma Physics* (Atomizdat, Moscow, 1977; Wiley, New York, 1980).

24. V. S. Imshennik and N. A. Bobrova, *Dynamics of Collisional Plasmas* (Énergoatomizdat, Moscow, 1997).

25. V. F. D'yachenko and V. S. Imshennik, in *Reviews of Plasma Physics*, Ed. by M. A. Leontovich (Atomizdat, Moscow, 1967; Consultants Bureau, New York, 1970), Vol. 5.

Translated by O. E. Khadin

Plasma Physics Reports, Vol. 26, No. 5, 2000, pp. 439–445. Translated from Fizika Plazmy, Vol. 26, No. 5, 2000, pp. 470–477.

PLASMA KINETICS

The Two and Three Most Representative Ionization State Approximations for Impurity Description in Coronal Plasmas

V. I. Gervids[1] and D. Kh. Morozov[2, 3]

[1]*Moscow Engineering Physics Institute (Technical University), Kashirskoe sh. 31, Moscow, 115409 Russia*
[2]*Instituto de Ciencias Nucleares, UNAM, A.P. 70-543, 04510, Mexico D.F., Mexico*
[3]*Institute for Nuclear Fusion, Russian Research Centre Kurchatov Institute, pl. Akademika Kurchatova 1, Moscow, 123182 Russia*

Received July 2, 1999; in final form, October 21, 1999

Abstract—Based on the analytical study of the solutions to the coronal balance equations, as well as on the numerical results, it is shown that, in many cases of practical interest, it is possible to describe the impurity ionization state with acceptable accuracy by only the two or three most representative ionization states. Reduced models for light impurities and strongly ionized heavy impurities in coronal hydrogen plasmas are proposed. The models make it possible to obtain analytical results for many cases as well as to significantly reduce computation time. In these approximations, simple equations determining the dynamics of impurity distributions over ionization states are derived. *© 2000 MAIK "Nauka/Interperiodica".*

1. INTRODUCTION

The theory of radiative impurities in hydrogen plasmas is applied for edge and divertor plasmas in thermonuclear devices as well as in astrophysics for interstellar and intergalactic clouds, stellar atmospheres, and solar prominences (see, e.g., reviews [1–3]). It is well known that radiative impurities are sometimes able to change the plasma dynamics qualitatively, which leads to the appearance of new types of equilibria and linear and nonlinear waves and significantly changes the stability criteria. However, one needs an extremely cumbersome set of equations describing each ionization state separately for a full impurity description. Thus, for carbon, which is the main impurity in tokamak plasmas, seven ionization states must be described, from neutrals to fully ionized ions. Obviously, it is impossible to get any qualitative results with analytical calculations in this way. Numerical solution of a set of partial differential equations for each ionization state is an extremely time-consuming procedure. Thus, in order to minimize the computation time, as well as to elaborate analytical models, some reduced descriptions of impurity ionization states are being developed.

If the electron temperature is not too high, $T_e \leq$ 100 eV, such that the impurity is not too deeply ionized and, respectively, the principal quantum number $n \geq 3$, then relatively heavy impurities with $Z > 20$ exist in coronal plasmas as collections of a large number of neighboring ionization states. The properties of these states change slowly with the transition from one state to another. Table 1 shows ionization energies for different ionization states of iron as an example. One can see that only one transition from Fe^{+7} to Fe^{+8} leads to an increase in the ionization energy by a factor of 1.5. For all other transitions, the increase in the ionization energy does not exceed 10–20%.

As shown in [4, 5], under these conditions, the real impurity distribution over ionization states may be approximated by a Gaussian function. An impurity charge averaged over the ionization state distribution and the width of the Gaussian peak are defined by simple equations.

Under the same temperature conditions, light impurities with $Z < 10$ and $n \leq 2$ exist in coronal plasmas in the form of two or three neighboring ionization states with significantly different properties. Table 2 shows ionization energies for carbon ionization states as an example.

It is easily seen that, in this case, the Gaussian representation fails, because the difference in ionization energies is on the order of the energy itself or larger. However, this fact makes it possible to simplify the problem. Under these conditions, the ratios between the ionization and recombination rates for ions with charges nearest to the charge of the most representative ions are significantly larger than for more distant ionization states. Thus, the concentrations of ions with charges nearest to the charge of the most representative ones are significantly higher (see Section 2).

To our knowledge, Galushkin *et al.* [6] were the first to propose the two or three ionization state approximations. This approach was used for investigations of thermal instabilities in radiative plasmas [7–9]. How-

1063-780X/00/2605-0439$20.00

Table 1

Ion	Fe^{+6}	Fe^{+7}	Fe^{+8}	Fe^{+9}	Fe^{+10}	Fe^{+11}	Fe^{+12}
ΔE_{ion}, eV	133	163	248	279	309	349	380

Table 2

Ion	C^{+0}	C^{+1}	C^{+2}	C^{+3}	C^{+4}	C^{+5}
ΔE_{ion}, eV	11	24	48	64	392	490

ever, it was not well founded and its validity limits were not defined properly.

The purpose of this work is to set the foundation and to develop reduced dynamic models for impurities existing mainly as ionization states with a relatively small amount of electrons in hydrogen coronal plasmas. The model is valid not only for light impurities but also for heavy impurities under high temperatures, for instance, near the plasma column axis of tokamaks.

Simplifications related to the "space" parts of models, like developing one-dimensional or diffusion approximations, are beyond our interest. In this paper, we investigate only the simplifications determined by the structure of coronal balance equations and properties of ionization–recombination processes reducing problems to the two or three most representative ion approximations.

The paper is organized as follows. In Section 2, the validity conditions of the two- and three-ion approximations are examined based on analytic estimations and numerical results. In Section 3, the set of equations describing impurities in two- and three-ion approximations are derived. The most important results are summarized in the Conclusion.

2. VALIDITY CONDITIONS FOR THE TWO AND THREE MOST REPRESENTATIVE IONIZATION STATE APPROXIMATIONS

Without going into detail, the impurity dynamics is described by a set of equations with the following structure:

$$\frac{\partial f_z}{\partial t} + \mathrm{div}(f_z v_z) = \sum_{z'} \alpha_{zz'} f_{z'} - \beta_z f_z, \qquad (1)$$

where f_z is the density, momentum, or energy; $\alpha_{zz'}$ is the transition rate from state z' to state z; β_z is the transition rate from the state z to any other state; and v_z is the transport velocity of f_z.

Below, we will use a coronal model. This model describes impurities perfectly in the plasma core, as well as in the edge tokamak plasmas, under almost any experimental conditions.

We note that, within the coronal model, calculations of the excited level populations and the relative concentrations of ionization states are independent problems, because, within this model, the total concentration of ions is practically equal to their concentration in the ground state.[1] This fact significantly simplifies many calculations, for instance, calculations of the line radiative losses—the most important part of radiative losses under many experimental conditions. In this case, one can calculate separately radiative losses for every ionization state, find the distribution over ionization states, and then summarize radiative losses over all states taking into account their relative concentrations.

When calculating the impurity distribution over ionization states in a coronal model, the right-hand side of (1) may be simplified:

$$\frac{\partial n_z}{\partial t} + \mathrm{div}(n_z v_z) = n_e(J_{z-1} n_{z-1} + R_{z+1} n_{z+1} - n_z(J_z + R_z)). \qquad (2)$$

Here, n_e is the electron density and $I_z = \langle v\sigma_z^{\mathrm{ion}} \rangle$ and $R_z = \langle v\sigma_z^{\mathrm{rec}} \rangle$ are the ionization and recombination rates, respectively, for ions with charge z.

Equating the left-hand side of (2) to zero, i.e., neglecting the time derivative and transport processes, we obtain the following steady-state solution to the set of coronal balance equations:

$$y_{z_0} = 1/N,$$

$$N = \sum_{k=1}^{z_0} \prod_{m=1}^{k} \frac{R_{z_0-m+1}}{I_{z_0-m}} + 1 + \sum_{k=1}^{Z-z_0} \prod_{m=1}^{k} \frac{I_{z_0+m-1}}{R_{z_0+m}},$$

$$y_{z_0-k} = y_{z_0} \prod_{m=1}^{k} \frac{R_{z_0-m+1}}{I_{z_0-m}}, \quad k = 1, 2, \ldots, z_0, \qquad (3)$$

$$y_{z_0+k} = y_{z_0} \prod_{m=1}^{k} \frac{I_{z_0+m-1}}{R_{z_0+m}}, \quad k = 1, 2, \ldots, Z - z_0,$$

[1] In this paper, we do not take into account effects that lead to violation of the coronal model, for instance, the effects related to metastable states. These effects are well known (see, e.g., [10]).

$$\sum_{z=1}^{Z} y_z = 1.$$

Here, $y_z = n_z / \sum_{k=0}^{Z} n_k$ is the relative concentration of ions with electric charge z; Z is the atomic impurity number; and z_0 is the charge of the most representative ion, i.e., the ion with the largest relative concentration. For the coronal equilibrium, the most representative ion charge may be found without calculating all of the concentrations ($0 \le z \le Z$) but by solving the inequalities

$$\frac{R_{z_0}}{I_{z_0-1}} < 1 < \frac{R_{z_0+1}}{I_{z_0}},$$

which can be replaced by the approximate equalities

$$\frac{R_{z_0}}{I_{z_0-1}} \approx 1, \quad \frac{R_{z_0+1}}{I_{z_0}} \approx 1.$$

From the expressions above for y_{z_0-k} and y_{z_0+k} and the approximate equalities determining z_0 and omitting "shell" factors containing such parameters as electron numbers in the outer shell, its principal quantum number, and vacation number, we find

$$\frac{y_{z_0-2}}{y_{z_0-1}} \propto \left(\frac{\Delta E(z_0-2)}{\Delta E(z_0-1)}\right)^3 \exp\left(-\frac{\Delta E(z_0-1) - \Delta E(z_0-2)}{T_e}\right),$$

$$\frac{y_{z_0+2}}{y_{z_0+1}} \propto \left(\frac{\Delta E(z_0)}{\Delta E(z_0+1)}\right)^3 \exp\left(-\frac{\Delta E(z_0+1) - \Delta E(z_0)}{T_e}\right).$$

These relations show that, in the three most representative ion approximation, the concentrations of ions with charges $z_0 - 2$ and $z_0 + 2$ are significantly smaller than the concentrations of ions with charges $z_0 - 1$, z_0, and $z_0 + 1$ and may be omitted. This means that the approximation is valid if the following inequalities are satisfied:

$$\frac{\Delta E(z_0-1) - \Delta E(z_0-2)}{T_e} \gg 1,$$

$$\frac{\Delta E(z_0+1) - \Delta E(z_0)}{T_e} \gg 1.$$

The computations (some of these results are represented below) show that, from a practical point of view, it is sufficient to satisfy the weaker inequalities

$$\frac{\Delta E(z_0-1) - \Delta E(z_0-2)}{T_e} > 1,$$

$$\frac{\Delta E(z_0+1) - \Delta E(z_0)}{T_e} > 1.$$

The results of calculating relative ionization state concentrations, ion charges averaged over ionization state distributions $\langle z \rangle = \sum_{k=0}^{Z} k y_k$, and line radiation intensities for light impurities are presented below. It should be noted that relative ionization state concentrations and radiation intensities of individual ionization states have been calculated in most of the earlier papers; however, they were not presented directly because the authors mainly concentrated on practically used integral parameters.

We used the calculation method described in [6] using the most updated and accurate data for ionization energies, transition energies, and oscillator strengths from [11]. Photorecombination was calculated taking into account electron capture into excited states. Dielectronic recombination was calculated with the modified Burgess's expression [12] and corrections to the electron density. Line radiation intensities calculated here are in good agreement with the results of Post *et al.* [13], Breton *et al.* [14], Tarter *et al.* [15], and other authors.

Beryllium is an interesting case because it was used as a material for divertor plates in JET experiments [16]. Our calculations show that only three or less ionization states with relative concentrations $y_z > 0.01$ may exist simultaneously in plasmas.

The most important impurities for fusion experiments are carbon (Fig. 1) and nitrogen (Fig. 2). One can see from Fig. 1 that, for 7 eV < T_e < 10 eV, four ionization states exist simultaneously. However, even in this temperature range, the relative concentration of the less representative (inside these four states) ionization states does not exceed 6%. Qualitatively, the ionization state distribution for nitrogen looks like that for carbon. The temperature range in which more than three ionization states exist is slightly broader and is shifted toward high temperatures: 12 eV < T_e < 20 eV.

One can see from the results presented above that impurities in plasmas may be described with the two- or three-ion approximation in a wide temperature range with an appropriate accuracy. This is possible at least for processes with characteristic times longer than the relaxation time of the impurity distribution functions over the ionization states. The validity conditions for these approximations are the inequalities represented above; i.e., the ratio of the difference between ionization energies of the neighboring states to the electron temperature must be larger than or on the order of the electron temperature.

We note again that these approximations are valid for strongly ionized heavy impurities. Thus, for iron, it is accurate enough if $T_e > 2$ keV.

In order to test the accuracy of the three most representative ion approximation, we calculated the ion charge averaged over the ionization state distribution, $\langle z \rangle$ (Fig. 3), and the total line radiation intensity for nitrogen (Fig. 4) taking into account all ionization states and using the three-ion approximation. One can see from Fig. 3 that the two curves do not coincide only

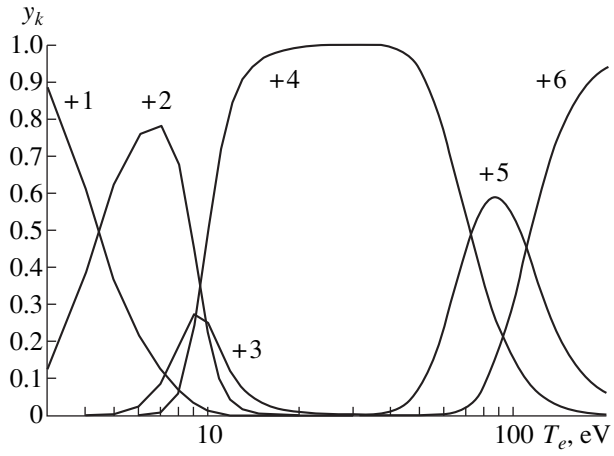

Fig. 1. Relative concentrations of carbon ions for the coronal equilibrium vs. the electron temperature. The numerals near the curves show the ion charge.

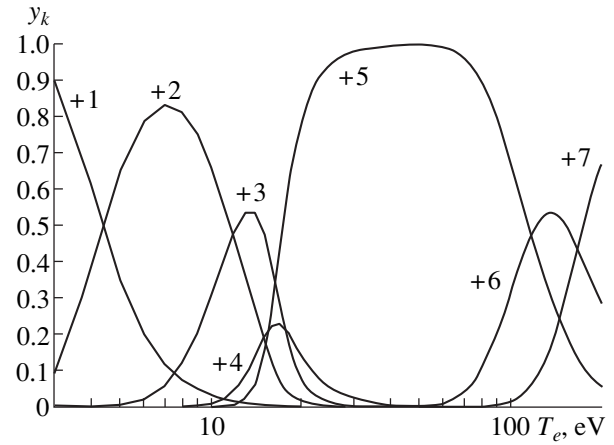

Fig. 2. Same as in Fig. 1, but for nitrogen.

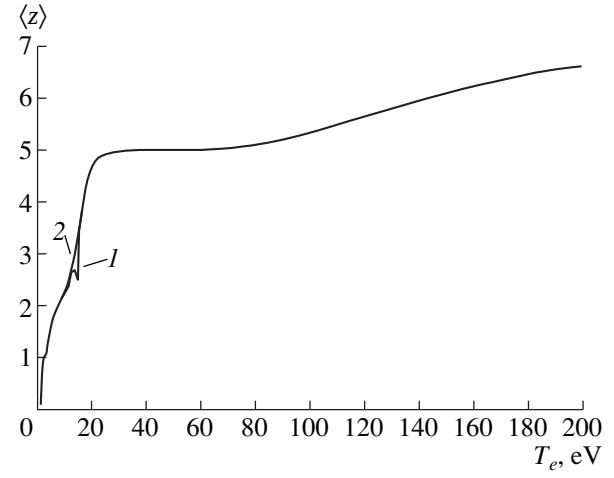

Fig. 3. The nitrogen ion charge averaged over ionization states for the coronal equilibrium. Curve *1* is calculated with the three-ion approximation, and curve *2* is calculated taking into account all of the ionization states.

within a narrow temperature range 12 eV < T_e < 15 eV. The difference does not exceed 20%.

The difference in line radiation intensities calculated in two different ways is observed in three ranges near 17, 50, and 90 eV.

In the region around 17 eV, the three-ion approximation does not take into account strongly radiating lithium-like ions. Their concentration for such low temperatures is small; however, the contribution to the total radiation is noticeable. For temperatures near 50 eV, the lithium-like ion concentration is small due to the high value of the temperature and the three-ion approximation again does not take it into account. For the temperature region around 90 eV, the three-ion approximation does not take into account helium-like ions. However, for all three ranges, the difference between the accurate and the three ion curves does not exceed 5–15%.

From the results demonstrated above, one can see that the two and three most representative ion approximations describe impurities with enough accuracy, at least for slow processes. Now, we have to evaluate the spreading of the distribution for the fast processes. Let us assume that the electron temperature increases rapidly. Due to the exponential dependence of the ionization rates on the temperature, the ionization rates of the weakly ionized ionization states increase more than those of highly ionized states, whose ionization energies are higher. Thus, under the total shift of the maximum toward higher temperatures, the width of the peak will not increase significantly during a relaxation process. A steep decrease in the temperature may be considered in a similar way. Thus, the proposed approximations are also valid for fast electron temperature changes.

3. MHD EQUATIONS FOR THE TWO AND THREE MOST REPRESENTATIVE ION APPROXIMATIONS

As shown by Rozhansky *et al.* [17], in the zero approximation, the impurity velocity is determined by the main plasma parameters and does not depend on the ion charge. The perpendicular velocity is determined mainly by the $\mathbf{E} \times \mathbf{B}$ drift, and its velocity does not depend on the ion charge,

$$\mathbf{u}_\perp = \frac{c}{B^2}\mathbf{E} \times \mathbf{B}. \tag{4}$$

Here, c is the speed of light and $\mathbf{E}$ and $\mathbf{B}$ are the electric and magnetic fields, respectively.

The parallel velocity is described by the equation

$$m_I \frac{d(n_z u_{z\|})}{dt} = -\frac{\partial n_z T_i}{\partial l} - C_z m_i n_e \nu_{iz}(u_{z\|} - u_{i\|}) + zen_z E_\| + n_z z^2 \left(\alpha_z \frac{\partial T_e}{\partial l} + \beta_z \frac{\partial T_i}{\partial l}\right) + S_z. \tag{5}$$

Here, m_I is the impurity ion mass; n_z and $u_{z\|}$ are the concentration and parallel velocity of ions with charge z, respectively; T_i is the ion temperature; $u_{i\|}$ is the main plasma parallel velocity; l is the coordinate along the field line; C_z is a constant taking into account a possible anomaly of the main plasma–impurity collisions; $\nu_{iz} = \frac{4\sqrt{2\pi}e^4\Lambda z^2 n_z}{3\sqrt{m_i}T_i^{3/2}}$ is the impurity–main plasma collision frequency; α_z and β_z are the numerical factors in the electron and ion thermal forces, respectively; and S_z is the parallel momentum source associated with the ionization and recombination processes. We assume that the main plasma ion temperature T_i is equal to the impurity temperature T_I. This assumption is valid for many applications. First of all, we can neglect the inertia in comparison with the thermal force. The impurity velocity usually does not significantly exceed the impurity thermal speed. Thus, the ratio of the inertial term to the thermal force term may be estimated as

$$m_I\frac{d(n_z u_{z\|})}{dt}\Big/\left(z^2 n_z\left(\alpha_z\frac{\partial T_e}{\partial l}+\beta_z\frac{\partial T_i}{\partial l}\right)\right)\approx\frac{1}{(\alpha_z+\beta_z)z^2}. \quad (6)$$

We put here $T_e \approx T_i$. For estimates, one can put $\alpha_z + \beta_z \approx 3$. For light impurities, ratio (6) is significantly smaller than unity if $z \geq 2$. Thus, this inequality is satisfied if the temperature is high enough. For $T_e \gg T_i$, this inequality is even stronger.

It is clear that the first term on the right-hand side of (5) is also smaller than the thermal force term by the factor $(\alpha_z + \beta_z)z^2$ if the difference in spatial scales on which the density and temperature vary is not too large. We neglect this term, as well as the last one, because the Coulomb collision frequency is usually significantly larger than the ionization and recombination rates. The electrostatic potential usually does not exceed the value T_e/e. In this case, the ratio of the parallel electric force to the thermal force is on the order of $1/(\alpha_z + \beta_z)z$ and is also small. Finally, we obtain

$$u_{z\|} = u_{i\|} + \frac{1}{C_z\sqrt{2}m_i\nu_{ii}}\frac{\partial}{\partial l}(\alpha_z T_e + \beta_z T_i). \quad (7)$$

Thus, in the zero approximation, the parallel and perpendicular velocities of the impurity ions with charge z may be expressed in terms of the main plasma parameters and do not depend on the ion charge.

If we know the impurity velocity $\mathbf{u}_I$, it is easy to derive equations for the ionization state concentrations. Introducing the relative concentrations

$$y_z = n_z/n_I, \quad y_z + y_{z+1} = 1 \quad (8)$$

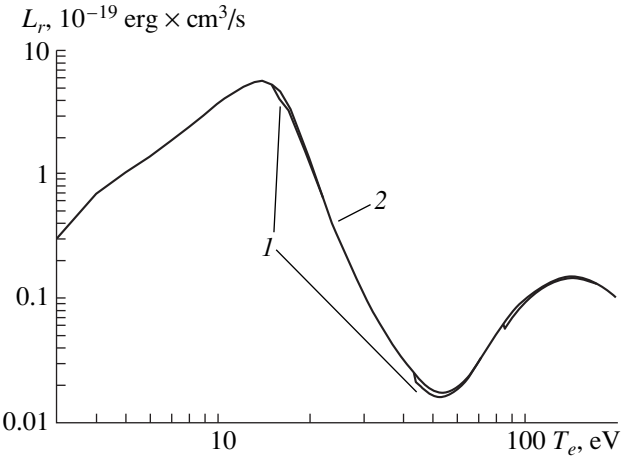

Fig. 4. Total radiative losses of nitrogen normalized to the impurity and electron concentrations. Curve *1* corresponds to the three-ion approximation, and curve *2* corresponds to calculations using all of the ionization states.

in the two-ion approximation, from the discontinuity equation and the normalization condition (8), we obtain

$$\frac{\partial y_z}{\partial t} + \mathbf{u}_I\cdot\nabla y_z = n_e[R_{z+1} - (J_z + R_{z+1})y_z]. \quad (9)$$

It might seem that equation (9) is sufficient for our purposes. However, even though we know that the most representative ions are the ions with charges z and $z + 1$, the values of these charges are known only for the case of the coronal equilibrium. Moreover, the value of z may change in a discrete way. Thus, it is more convenient to pass over to a continuous variable (the charge averaged over ionization states),

$$\langle z\rangle = zy_z + (z+1)y_{z+1} = z + 1 - y_z. \quad (10)$$

As a result, we obtain

$$\frac{\partial\langle z\rangle}{\partial t} + \mathbf{u}_I\cdot\nabla\langle z\rangle = -\nu_z(\langle z\rangle - z_*). \quad (11)$$

Here, $\nu_z = n_e(J_z + R_{z+1})$ and $z_* = z + 1 - \frac{R_{z+1}}{J_z + R_{z+1}}$ is the averaged equilibrium charge under the given electron temperature. The accuracy of calculations with (11) may be increased due to the fact that $z_*(T_e)$ was calculated in many papers taking into account all of the ionization states (see, e.g., [10, 13]). The value ν_z may be calculated easily with a model of an averaged ion [18]. In order to increase the accuracy of calculations and calculate the distribution over ionization states using (8) and (10), we should know the value of z. In the two most representative ion approximation (two-ion approximation), the quantity $\langle z\rangle$ always satisfies the condition $z < \langle z\rangle < z + 1$. Thus, the value of z is simply equal to the integer part of $\langle z\rangle$.

The two-ion approximation is attractive due to its simplicity and validity for analytic calculations. For instance, it gives good results for examinations of the thermal stability in radiative plasmas. However, as follows from the results of Section 1, the temperature ranges in which this approximation is valid are separated by ranges in which the validity conditions are violated.

More accurate results that are valid for a wide range of electron temperatures may be obtained with the approximation of the three most representative ions (three-ion approximation). In this approximation, the states with charges $z-1$, z, and $z+1$ are taken into account. The normalization condition gives

$$y_{z-1} + y_z + y_{z+1} = 1, \tag{12}$$

and the averaged charge takes the form

$$\langle z\rangle = z + 1 - y_z - 2y_{z-1}. \tag{13}$$

Taking into account (12), we can write two equations

$$\frac{\partial y_z}{\partial t} + \mathbf{u}_I \cdot \nabla y_z = n_e[R_{z+1} - (J_z + R_z + R_{z+1})y_z + (J_{z-1} - R_{z+1})y_{z-1}], \tag{14}$$

$$\frac{\partial y_{z-1}}{\partial t} + \mathbf{u}_I \cdot \nabla y_{z-1} = n_e[y_z R_z - y_{z-1}J_{z-1}]. \tag{15}$$

Using the continuous variable $\langle z\rangle$, we obtain a set of two symmetric equations

$$\left(\frac{\partial}{\partial t} + \mathbf{u}_I \cdot \nabla\right) y_{z-1} = -\nu_{z-1}\left[(y_{z-1} - y^*_{z-1}) + A_1(\langle z\rangle - z_*)\right],$$
$$\left(\frac{\partial}{\partial t} + \mathbf{u}_I \cdot \nabla\right)\langle z\rangle = -\nu_z\left[(\langle z\rangle - z_*) + A_2(y_{z-1} - y^*_{z-1})\right]. \tag{16}$$

Here, $\nu_{z-1} = n_e(J_{z-1} + 2R_z)$; $\nu_z = n_e(R_{z+1} + J_z - R_z)$; $A_1 = \dfrac{R_z}{\nu_{z-1}} n_e$; $A_2 = \dfrac{2J_z + R_{z+1} - J_{z-1} - 2R_z}{\nu_z} n_e$; and the quantities z_* and y^*_{z-1} are defined under the condition of the coronal equilibrium by the expressions

$$z_* = \frac{J_{z-1}J_z - R_zR_{z+1} + z(J_{z-1}J_z + J_{z-1}R_{z+1} + R_zR_{z+1})}{J_{z-1}J_z + J_{z-1}R_{z+1} + R_zR_{z+1}}, \tag{17a}$$

$$y^*_{z-1} = \frac{R_zR_{z+1}}{J_{z-1}J_z + J_{z-1}R_{z+1} + R_zR_{z+1}}. \tag{17b}$$

As noted above, we do not need to use these expressions, because the values of z_* and y^*_{z-1} were calculated in many papers with account for all of the ionization states. Here, the constants of elementary processes may be calculated using the averaged ion model.

In the three-ion approximation, it is not as easy to calculate z as in the two-ion approximation. This value may lay within one of the two intervals, $z-1 < \langle z\rangle < z$ or $z < \langle z\rangle < z+1$, and one can obtain a wrong value by simply taking an integer part of $\langle z\rangle$. It follows from (13) that, for the given $\langle z\rangle$ and $0 \le y_{z-1} \le 1$, there exists only one value of z satisfying this equation. Indeed, let us suppose that there is another value, $z' = z \pm 1$, satisfying this equation at another value of $y_z = y'_z$. Substitution of z' and y'_z yields

$$z = \langle z\rangle - 1 \pm 1 + y'_z + 2y_{z-1}. \tag{18}$$

Subtracting (13) from (18), we obtain

$$y_z - y'_z = \pm 1. \tag{19}$$

Taking into account the normalization condition, this equation may be satisfied only if $y_{z-1} = 0$, $y_z = 1$, or $y'_z = 1$. However, in this case, $z = \langle z\rangle$. For other cases, there exists only one value of z satisfying (13) at any value of y_z and it may be obtained as an integer of the expression $z_1 = \langle z\rangle + 2y_{z-1}$.

Two different effects compete in (11) and (16). The higher the velocity of impurity transport from the plasma region with the given temperature to the region with another temperature, the larger the distance at which the impurities "remember" their initial states. The transport is determined by the terms on the left-hand sides of (11) and (16) that are proportional to the velocity. The larger the inverse relaxation time ν_z on the right-hand side of the equations, the faster impurities "forget" their initial states and achieve equilibrium values. The relation between these velocities changes in a wide range and is determined by the specific conditions of the problem. Let us estimate these parameters for tokamak divertor conditions.

Estimates for ν_z are given in [9]. They depend on the temperature and, for the divertor plasma, lie in the interval $\nu_z \approx 10^2$–10^3 s^{-1}. The deviation of $\langle z\rangle$ from the equilibrium value for light impurities does not exceed a few units. The fastest displacement of an impurity in the direction perpendicular to the divertor plate occurs due to the $\mathbf{E}\times\mathbf{B}$ drift [16], when the perpendicular electric field may attain the value of $T_e/(e\rho_p)$ in certain divertor regions. Here, ρ_p is the deuteron Larmor radius in the poloidal magnetic field (see, e.g., [19]). In this case, the impurity velocity perpendicular to the divertor plate may be estimated as $V_I \approx 10^4$–10^5 cm/s and the convective term is significantly larger than the relaxation term, which is proportional to ν_z. If such a strong electric field does not exist and the impurity transport is

determined by the anomalous Bohm-type diffusion or thermal force at characteristic spatial scales on the order of 1–10 cm, the transport velocity is one or two orders of magnitude lower. Under these conditions, the convective and relaxation terms are of the same order of magnitude. The conditions under which the relaxation term dominates and impurities are in equilibrium are hardly probable in divertor plasmas. However, such conditions may occur in some other cases.

4. CONCLUSION

The validity of the two and three parameter models (the two and three most representative ions) is well founded for the dynamics of plasmas with radiative impurities.

It is shown that the two main representative ions (two-ion approximation) successfully describe light impurities for practically all temperature ranges, except for some narrow intervals. The more accurate three-ion approximation for light impurities is valid for all temperature ranges of practical interest within an accuracy of 10–15%.

For the two-ion and three-ion approximations, the dynamic equations for the charge averaged over ionization states and charge distribution over ionization states are derived. In the two-ion approximation, they are reduced to one equation for an impurity ion charge averaged over ionization states. This approach provides the possibility to considerably decrease the computational time as well as to obtain analytical results.

The models proposed are also applicable for describing strongly ionized heavy impurities under thermonuclear temperatures.

ACKNOWLEDGMENTS

This work was supported by the grants DGAPA IN117498 and 27974-E CONACyT, Mexico.

REFERENCES

1. B. Lipshults, J. Nucl. Materials **145–147**, 15 (1987).
2. B. Meerson, Rev. Modern Phys. **68**, 215 (1996).
3. D. Kh. Morozov and J. J. E. Herrera, Fiz. Plazmy **24**, 379 (1998) [Plasma Phys. Rep. **24**, 347 (1998)].
4. V. V. Ivanov, A. B. Kukushkin, and V. S. Lisitsa, Fiz. Plazmy **13**, 1341 (1987) [Sov. J. Plasma Phys. **13**, 774 (1987)].
5. A. B. Arutunov, S. I. Krasheninnikov, and D. Yu. Prokhorov, Fiz. Plazmy **17**, 1150 (1991) [Sov. J. Plasma Phys. **17**, 668 (1991)].
6. Yu. I. Galushkin, V. I. Gervids, and V. I. Kogan, in *Proceedings of VI International Conference on Plasma Physics and Controlled Nuclear Fusion Research, Madison, 1971*, Vol. 2, p. 407.
7. S. I. Krasheninnikov, D. Kh. Morozov, D. J. Sigmar, *et al.*, Contrib. Plasma Phys. **36**, 271 (1996).
8. D. Kh. Morozov and J. J. E. Herrera, in *Proceedings of Joint 1998 International Congress on Plasma Physics and 25th EPS Conference on Controlled Fusion and Plasma Physics, Prague, 1998*, Vol. 22C, p. 1892.
9. D. Kh. Morozov, J. J. E. Herrera, and V. I. Gervids, Contrib. Plasma Phys. **38**, 278 (1998).
10. V. I. Gervids, A. G. Zhidkov, V. S. Marchenko, and S. I. Yakovlenko, in *Reviews of Plasma Physics*, Ed. by M. A. Leontovich and B. B. Kadomtsev (Énergoatomizdat, Moscow, 1982; Consultants Bureau, New York, 1984), Vol. 12.
11. D. A. Verner, E. M. Verner, and G. J. Ferland, Atomic Data Nucl. Data Tables **64**, 1 (1996).
12. A. Burges, Astrophys. J. **141**, 1588 (1965).
13. D. E. Post, R. V. Jensen, C. B. Tarter, *et al.*, Atomic Data Nucl. Data Tables **20**, 397 (1977).
14. C. Breton, C. De Michelis, and M. Mattioli, Nucl. Fusion **16**, 891 (1976).
15. C. B. Tarter, J. Quant. Spectrosc. Radiat. Transfer **17**, 531 (1977).
16. S. Clement, D. Campbell, S. K. Erents, *et al.*, in *Proceedings of 17th EPS Conference on Controlled Fusion and Plasma Heating, Amsterdam, 1990*, Vol. 14B, p. 1373.
17. V. A. Rozhansky, D. Kh. Morozov, and J. J. E. Herrera, in *Proceedings of 26th EPS Conference on Controlled Fusion and Plasma Physics, Maastricht, 1999* [ECA **23J**, 1277 (1999)].
18. R. V. Jensen, D. E. Post, W. H. Grasberger, *et al.*, Nucl. Fusion **17**, 1187 (1977).
19. T. D. Ronglien, G. D. Porter, and D. D. Riutov, J. Nucl. Mat. **266–269**, 654 (1999).

Translated by the authors

Plasma Physics Reports, Vol. 26, No. 5, 2000, pp. 446–455. Translated from Fizika Plazmy, Vol. 26, No. 5, 2000, pp. 478–487.

ELEMENTARY PROCESSES IN PLASMA

Analysis of the Differential Cross Section for Ionization of a Hydrogen Atom by Fast Electrons in a Uniform Electric Field

V. I. Krylov and V. V. Pivkin

Institute of General Physics, Russian Academy of Sciences, ul. Vavilova 38, Moscow, 117942 Russia
Khabarovsk State Pedagogical University, ul. Karla Marksa 68, Khabarovsk, 680000 Russia

Received December 24, 1998; in final form, August 6, 1999

Abstract—The differential cross section for ionization of a hydrogen atom by fast electrons in an external uniform electric field is calculated using the nonrelativistic Born approximation. It is shown that the cross section obtained can differ substantially from a similar ionization cross section of an isolated atom in the angular distribution of secondary electrons in momentum space, oscillation terms, and magnitude. © *2000 MAIK "Nauka/Interperiodica".*

1. INTRODUCTION

The collisions of electrons with atoms and ions in an external uniform quasi-steady electric field can differ significantly from collisions with an isolated atom even when the external electric field is far below the atomic field. This is explained by the interference and the change in the time the electrons stay in the vicinity of the scattering atom while they are reflected from the potential barrier of the external electric field. These effects come into play if the distance between the atomic nucleus and the reflection point of the electrons and the mean time the electrons stay in this region are shorter than the spatial and temporal scales of the problem.

This case was considered in [1, 2], where, in particular, the differential cross section for ionization of a hydrogen atom by fast electrons in a uniform electric field was calculated using the nonrelativistic Born approximation. When calculating the cross section, the asymptotes of the wave functions of the final electron states were taken in the form of standing waves (along the external electric field) in the region between the atom nucleus and the reflection point of the electrons and in the form of progressive waves in the region where reflection points were absent [1].

Evidently, such wave functions describe the density of the electron current in a weakly ionized gas in an external electric field or in a plasma region with a linear size on the order of the Debye radius where a sufficiently strong electric field exists.

Since mathematical expressions for the atom-ionization cross sections obtained in [1, 2] are rather cumbersome and their interpretation raises certain difficulties, only a preliminary and qualitative analysis of the expressions was performed in those papers.

In this paper, a more detailed quantitative study of the cross section under consideration is carried out using numerical methods. The numerical results show (as was predicted in [2]) that, under certain conditions, the cross section for ionization of a hydrogen atom by fast electrons in a uniform electric field can be substantially larger than a similar ionization cross section of an isolated atom, as well as that of an atom in a uniform electric field, calculated from asymptotes of the wave functions of the final electron states that have the form of standing waves (along the uniform field) at infinity [3, 4] (such functions were used to describe the final states of photoelectrons in [5, 6]) and which are thus inapplicable for describing the density of the electron current with a nonzero longitudinal component.

The cross section in question also differs markedly from the cross section [7] corresponding to the probability of ionization of a hydrogen atom by an electron in an oscillating uniform electric field (in the limiting case of zero frequency). Note that, in [7], the interference of electrons in the course of their reflection from the potential barrier of the external electric field was not taken into consideration when choosing the form of the wave functions.

2. FORMULATION OF THE PROBLEM, BASIC EQUATIONS

As in [1, 2], we assume that, in a half-space, there is a uniform time-independent electric field $\boldsymbol{\varepsilon}$ normal to the boundary of the half-space.

We assume that the z-axis of the Cartesian coordinate system x, y, and z is antiparallel to the field direction ($\boldsymbol{\varepsilon} : \boldsymbol{\varepsilon} = (0, 0, -\varepsilon)$) and a hydrogen-atom nucleus is positioned at the point (0, 0, 0), at a distance L from the boundary of the region occupied by the field. It is con-

1063-780X/00/2605-0446$20.00

venient to set the potential of the uniform electric field at this point to be equal to zero.

Let a monoenergetic flow of primary electrons accelerated by the electric field fall from the boundary onto a hydrogen atom, causing its ionization.

Keeping in mind that the differential cross section will be calculated in the Born approximation, the wave function for the initial state of a primary electron, constructed from the asymptotes of the Airy functions, can be written in the form

$$\psi_{\chi} = \frac{A_{\chi}}{S^{1/4}}\exp\left\{i\left[\frac{2}{3}\frac{\chi_z}{|\chi_z|}S^{3/2} + \mathbf{k}_{\perp}\mathbf{r}\right]\right\}, \quad (1)$$

where A_{χ} is the normalization constant determining the flow density, $S = \frac{z}{l} + \frac{E_z}{e\varepsilon l}$, $l = \left(\frac{\hbar^2}{2m_e e\varepsilon}\right)^{1/3}$; m_e and $-e$ are the mass and charge of an electron, $E_z = \frac{\hbar^2\chi_z^2}{2m_e} + e\varepsilon L$ is the electron longitudinal energy, and the wave vector $\boldsymbol{\chi} = (\mathbf{k}_{\perp}, \chi_z)$ determines the electron momentum $\hbar\boldsymbol{\chi}$ at the field boundary.

Functions (1) also describe the final states of both primary and secondary (which left the atom) electrons, provided that

$$E_z > e\varepsilon L \quad (2)$$

and the normalization constant A_{χ} enters the expression for the number of states referred to the volume element $d^3\boldsymbol{\chi}$ of the $\boldsymbol{\chi}$-space [1–4].

If the longitudinal electron energy in the final state is less than $e\varepsilon L$ ($E_z < e\varepsilon L$), then, according to the considerations given in the Introduction, in the Born approximation, the electron motion along the field between the reflection point ($z_r = -E_z/e\varepsilon$) and the atom nucleus must be described everywhere by a finite and real Airy function decreasing exponentially at $z < z_r$ (see, e.g., [8]). At the same time, in the half-space $z > 0$, the longitudinal component of the electron flow density in the uniform electric field obviously must differ from zero and, consequently, the wave-function asymptote in this half-space must take form (1) and correspond to a progressive wave (see [1] for details).

If the inequalities

$$e\varepsilon l \ll E_z \ll e\varepsilon L, \quad (3)$$

hold, we can neglect the interaction between the electrons and atom nucleus and use the asymptotes of Airy functions. Thus, the wave function $\psi_{\mathbf{k}}$ for the classically permitted region of motion can be written in the following form [1]:

$$\psi_{\mathbf{k}} = \frac{A_{\mathbf{k}}}{S^{1/4}}\exp(i\mathbf{k}_{\perp}\mathbf{r})\begin{cases}\sin\left(\frac{2}{3}S^{3/2} + \alpha_1\right) & \text{for } z_r < z < 0\\ \exp\left(i\left[\frac{2}{3}S^{3/2} + \alpha_2\right]\right) & \text{for } z > 0,\end{cases} \quad (4)$$

where the phases α_1 and α_2 (α_{a1} and α_{a2} for the atomic electron) should be regarded as fitting parameters that, presumably, are close to $\pi/4$; $A_{\mathbf{k}}$ is the normalization constant related to the number of electron states $dn_{\mathbf{k}}$ referred to the element volume $d\mathbf{k}^3$ of the $\mathbf{k}$-space by the equation $dn_{\mathbf{k}} = (|k_z|l/8\pi^3|A_{\mathbf{k}}|^2)d^3\mathbf{k}$; and $\mathbf{k} = (\mathbf{k}_{\perp}, \sqrt{2m_e E_z}/\hbar)$ is the local wave vector determining the electron momentum in the vicinity of the nucleus. Assuming that a low (compared to the atomic field) external uniform electric field switches on adiabatically slowly, the state of the atom electron is described by the wave function ψ_0 of an isolated atom: $\psi_0 = (\pi a^3)^{-1/2}\exp(-r_a/a)$, where $\mathbf{r}_a$ is the radius vector of the atom electron and $a = \hbar^2/(m_e e^2)$. Because of a rapid decrease of this function at $r_a \gg a$, it is sufficient to use $\psi_{\mathbf{k}}$ in the matrix element in the classically permitted region only, i.e., to use it in form (4) when conditions (3) are satisfied (note that the latter provide the inequality $|z_r| \gg a$ required for the condition $\varepsilon \ll |e|/a^2$ to be fulfilled). Using (1) and (4) for the wave functions of the initial and final electron states, we obtain the following expression for the differential cross section $d\sigma$ for ionization of a hydrogen atom by fast electrons in a uniform electric field (in atomic units):

$$d\sigma = \frac{2}{\pi^2}\frac{kk_a^2}{k_0}|T|^2 d\mathrm{o}\, d\mathrm{o}_a\, dk_a, \quad (5)$$

where $\mathbf{k}_0$ and $\mathbf{k}$ are the wave vectors of the initial and final states of the primary electron, respectively. Here, we assume that $\mathbf{k}_0$ lies in the xz plane, $\mathbf{k}_a$ is the wave vector of the final state of the atomic electron, $k^2 = k_0^2 - k_a^2 - 1$; $d\mathrm{o} = \sin\theta d\theta d\varphi$ and $d\mathrm{o}_a = \sin\theta_a d\theta_a d\varphi_a$. In [1, 2], the angles θ, φ, φ_a, and θ_a were defined as follows: θ is the angle between the z-axis and the vector $\mathbf{k}$, φ is the angle between $\mathbf{k}_{0\perp}$ and $\mathbf{k}_{\perp}$, θ_a is the angle between the z-axis and $\mathbf{k}_a$, and φ_a is the angle between $\mathbf{k}_{0\perp}$ and $\mathbf{k}_{a\perp}$. The expression for T takes a different form depending on the relation between k_z, k_{az}, and εL.

If the inequalities $\varepsilon^{2/3} \ll k_z^2/2$ and $k_{az}^2/2 \ll \varepsilon L$ corresponding to (3) are satisfied, then we have

$$T = \frac{1}{2}R_{-}[q_{+}(1 + Q_{-}^2)]^{-2}\exp[-i(\gamma_1 - \gamma_{a1})]$$

$$-\frac{1}{2}M_-[q_-(1+\lambda_-^2)]^{-2}\exp[i(\gamma_1+\gamma_{a1})]$$

$$-\frac{1}{2}R_+[q_+(1+Q_+^2)]^{-2}\exp[-i(\gamma_1+\gamma_{a1})]$$

$$-\frac{1}{2}M_+[q_-(1+\lambda_+^2)]^{-2}\exp[i(\gamma_1-\gamma_{a1})]$$

$$+2D[q_+(1+Q_+^2)]^{-2}\exp[-i(\gamma_2+\gamma_{a2})]$$

$$-h_+P_-(1+w_-^2)^{-2}\exp(-i\gamma_{a2})$$

$$-\frac{i}{2}h_-[P_-(1+w_-^2)^{-2}\exp(i\gamma_{a1})-P_+(1+w_+^2)^{-2}\exp(-i\gamma_{a1})],$$

where

$$\mathbf{q}_\pm = \mathbf{k}_\pm - \mathbf{k}_0, \quad \mathbf{k}_\pm = (\mathbf{k}_\perp, \pm\sqrt{2E_z}),$$

$$\mathbf{k}_{a\pm} = (\mathbf{k}_{a\perp}, \pm\sqrt{2E_{az}}), \quad \mathbf{Q}_\pm = \mathbf{q}_+ + \mathbf{k}_{a\pm},$$

$$\boldsymbol{\lambda}_\pm = \mathbf{q}_- + \mathbf{k}_{a\pm}, \quad \mathbf{w}_\pm = (\mathbf{q}_\perp + \mathbf{k}_{a\perp}, iq_\perp \pm k_{az}),$$

$$R_\pm = 1 + \frac{iQ_{\pm z}}{2\sqrt{1+Q_\perp^2}}\left(3+\frac{Q_{\pm z}^2}{1+Q_\perp^2}\right),$$

$$M_\pm = 1 + \frac{i\lambda_{\pm z}}{2\sqrt{1+\lambda_\perp^2}}\left(3+\frac{\lambda_{\pm z}^2}{1+\lambda_\perp^2}\right),$$

$$P_\pm = 1 + \frac{iw_{\pm z}}{2\sqrt{1+w_\perp^2}}\left(3+\frac{w_{\pm z}^2}{1+w_\perp^2}\right),$$

$$D = 1 - \frac{iQ_{+z}}{2\sqrt{1+Q_\perp^2}}\left(3+\frac{Q_{+z}^2}{1+Q_\perp^2}\right),$$

$$h_\pm = \left[e^{-i\gamma_2} - \frac{i}{2}e^{-i\gamma_1}\right]\frac{q_\perp \pm iq_{+z}}{q_\perp q_+^2} + \frac{i}{2}\frac{q_\perp \pm iq_{-z}}{q_\perp q_-^2}e^{i\gamma_1},$$

$$\gamma_{1,2} = \alpha_{1,2} + |k_z|^3/3\varepsilon, \quad \gamma_{a1,2} = \alpha_{a1,2} + |k_{az}|^3/3\varepsilon.$$

When $\varepsilon^{2/3} \ll k_{az}^2/2 \ll \varepsilon L < k_z^2/2$, we have

$$T = [q_+(1+Q_+^2)]^{-2}(iR_+e^{-i\gamma_{a1}} + 2De^{-i\gamma_{a2}}) - i[q_+(1+Q_-^2)]^{-2}R_-e^{i\gamma_{a1}}.$$

When $\varepsilon^{2/3} \ll k_z^2/2 \ll \varepsilon L < k_{az}^2/2$, T takes the form

$$T = i[q_+(1+Q_+^2)]^{-2}(R_+e^{-i\gamma_1} + 2iDe^{-i\gamma_2}) - iM_-[q_-(1+\lambda_+^2)]^{-2}R_-e^{i\gamma_1} + h_-P_+(1+w_+^2)^{-2} - h_+P_-(1+w_-^2)^{-2}.$$

Finally, when $k_z^2/2,\ k_{az}^2/2 > \varepsilon L$, we have

$$T = 4[q_+(1+Q_+^2)]^{-2}. \tag{6}$$

When $q_+^2 \gg k_a^2 \gg 1$, formula (5) with T in form (6) is similar to the expression for the differential cross section $d\sigma_0$ for ionization of an isolated hydrogen atom by fast electrons which was obtained by Massey and Mohr (see, e.g., [8]) with allowance for the interaction of the secondary electron with the atom nucleus:

$$d\sigma_0 = \frac{2^6 k k_{a+}[Q_+^2 - k_{a+}^2 + (k_{a+}^2+1)(\mathbf{q}_+\mathbf{k}_{a+}/q_+k_{a+})^2]}{\pi k_0 q_+^2[1+Q_+^2]^4[(q_+ + k_{a+})^2+1][(q_+ - k_{a+})^2+1](1-e^{-2\pi/k_{a+}})} \times \exp\left(-\frac{2}{k_{a+}}\arctan\frac{2k_{a+}}{q_+^2 - k_{a+}^2 + 1}\right)d\sigma d\sigma_a dk_{a+}. \tag{7}$$

Expressions (5) and (6) make sense if $k^2 \gg k_a^2 \gg 1$; here, the first inequality allows us to ignore the exchange effects, whereas the second one ensures the applicability of the Born approximation. We note that, according to the choice of the wave functions for the final electron states, we have $\theta, \theta_a \in (0, \pi/2)$ if $k_{az}^2/2$, $k_z^2/2 \ll \varepsilon L$ and $\theta_a, \theta \in (0, \pi)$ if $k_z^2/2,\ k_{az}^2/2 > \varepsilon L$.

The most significant distinction of the cross section $d\sigma$ from $d\sigma_0$ and from the similar cross sections obtained in [3, 4] is that the denominator in $d\sigma$ contains the quantity $q_\perp$, which, under certain conditions, can vanish and, consequently, $d\sigma/d\sigma_0$ can be much greater than unity. The numerical analysis of the above expressions confirms the previous results obtained in [2].

3. NUMERICAL ANALYSIS OF CROSS SECTIONS

The cross section $d\sigma$ is analyzed numerically by representing the functions $F = d\sigma/d\sigma d\sigma_a dk_a$ in the form of surfaces constructed on the planes with coordinates corresponding to the parameters entering the formula for $d\sigma$.

We note that the angles θ, φ, θ_a, and φ_a used in [1, 2], which are convenient for determining the applicability conditions for mathematical expressions defining T,

are not quite suitable from the physical standpoint for analyzing $d\sigma$ for the purpose of comparing it with the ionization cross section $d\sigma_0$ of an isolated atom. For this reason, instead of θ and θ_a, we introduce the angles θ_n and θ_{an} between $\mathbf{k}_0$ and the vectors $\mathbf{k}$ and $\mathbf{k}_a$. Also, instead of φ and φ_a, we introduce the angles φ_n and φ_{an} between the vector $\mathbf{i}_n = [\mathbf{j}, \mathbf{n}]$ (here, $\mathbf{n} = \mathbf{k}_0/k_0$ and $\mathbf{j}$ is the unit vector in the direction along the y-axis) and projections of the vectors $\mathbf{k}$ and $\mathbf{k}_a$ onto the plane formed by the vectors $\mathbf{i}_n$ and $\mathbf{j}$ (such coordinates are usually employed when considering particle collisions).

The quantities $\mathbf{k}_\pm$, $\mathbf{q}_\pm$, and $\mathbf{k}_{a\pm}$, which determine T, are expressed through the chosen angles as follows:

$$k_x = k(\cos\theta_0\sin\theta_n\cos\varphi_n + \sin\theta_0\cos\theta_n),$$

$$k_y = k\sin\theta_n\sin\varphi_n,$$

$$k_{z\pm} = \pm k(\cos\theta_0\cos\theta_n - \sin\theta_0\sin\theta_n\cos\varphi_n),$$

$$q_x = k(\cos\theta_0\sin\theta_n\cos\varphi_n + \sin\theta_0\cos\theta_n) - k_0\sin\theta_0,$$

$$q_y = k\sin\theta_n\sin\varphi_n,$$

$$q_{z\pm} = \pm k(\cos\theta_0\cos\theta_n - \sin\theta_0\sin\theta_n\cos\varphi_n) - k_0\cos\theta_0,$$

$$k_{ax} = k_a(\cos\theta_0\sin\theta_{an}\cos\varphi_{an} + \sin\theta_0\cos\theta_{an}),$$

$$k_{ay} = k_a\sin\theta_{an}\sin\varphi_{an},$$

$$k_{az\pm} = \pm k_a(\cos\theta_0\cos\theta_{an} - \sin\theta_0\sin\theta_{an}\cos\varphi_{an}),$$

where θ_0 is the angle between the vector $\mathbf{k}_0$ and the z-axis.

To study the behavior of the functions F and $F_0 = d\sigma_0/dod\mathrm{o}_a dk_a$ (which will be compared with F), we created a program that allowed us to set the numerical values for various parameters of the function under study and visualize the surfaces in any pair of the parameters on the computer display.

The program was written so that the points of the calculated surface had some additional properties. By placing the mouse cursor on the calculated surface, we could trace the coordinates of the cursor point. We could introduce the coordinates of an arbitrary point into the parameter list in order to examine how the surface in the vicinity of the point depends on the other parameters. The program also could seek the function maximums in given domains on the plane where the function was defined.

When changing one function to another, the preset parameters were kept unchanged, which allowed us to compare different functions at the same parameters. We note that the program was written in C^{++} permitting the use of complex numbers.

For the numerical analysis, we set $\varepsilon = 0.01$ and $L = 10^4$. We begin the analysis of the function F with the case $k_a = 10$, $k = 50$, and $k_0 = 51$ (according to the applicability conditions for the expressions obtained for $d\sigma$ and $d\sigma_0$). First, we set the phases α_1, α_2, α_{a1}, and α_{a2} to be equal to $0.78 \approx \pi/4$ (the angles are given in radians).

The analysis of the surfaces $F(\theta_n, \theta_0)$, $F(\theta_{an}, \theta_0)$, $F(\theta_0, \varphi_{an})$, and $F(\theta_0, \varphi_n)$ at the given values of the parameters (the first two surfaces are presented in Fig. 1, whereas the latter two almost coincide with the second function; the white strips on the coordinate planes show the regions in which the obtained formulas are inapplicable; the indexes n are omitted) shows that the main maximums of the functions $F(\theta_n, \varphi_n)$ and $F(\theta_{an}, \varphi_{an})$ take maximum values at $\theta_0 = 1.2818$, $\theta_{an} = 1.2911$, and $\varphi_{an} = 3.1424$ for the first surface and $\theta_n = 0.0877$ and $\varphi_n = 0.0014$ for the second surface.

Figure 2 shows these surfaces and their fragments of the function $F(\theta_{an}, \varphi_{an})$ in the intervals (1.289, 1.292) and (3.12, 3.16) of the angles θ_{an} and φ_{an}, respectively, and for the function $F(\theta_n, \varphi_n)$ in the intervals (0.11596, 0.116) and (–0.14, 0.14) of the angles θ_n and φ_n, respectively.

It follows from this figure that the fragments of the function $F(\theta_{an}, \varphi_{an})$ have an oscillatory structure and vary from 0.121 to 0.898 with a period of 0.01 (along φ_a). The oscillation amplitude of the function $F(\theta_n, \varphi_n)$ is substantially smaller near its main maximum, approximately equal to 0.9, whereas for the maximum of about 0.043 the amplitude of variations of the function $F(\theta_n, \varphi_n)$ is 0.016.

In order to compare this cross section with a similar ionization cross section for an isolated atom, Fig. 3 illustrates the surfaces of $F_0(\theta_n, \varphi_n)$ and $F_0(\theta_{an}, \varphi_{an})$ calculated for the same values of k_a, k, ε, and L and for $\theta_n = 0.1961$, $\varphi_n = 0$, $\theta_{an} = 1.3742$, and $\varphi_{an} = \pi$. These parameters correspond to the highest maximums of the calculated functions, which are approximately equal to 0.014, i.e., more than one order of magnitude lower than the highest maximums of $F(\theta_n, \varphi_n)$ and $F(\theta_{an}, \varphi_{an})$. The value of the angle $\theta_0 = 0.2818$ for the surfaces $F(\theta_n, \varphi_n)$ and $F(\theta_{an}, \varphi_{an})$ presented in Fig. 2 corresponds to the case when the momentums of the electrons incident on the atom are directed almost perpendicular to the vector $\boldsymbol{\varepsilon}$.

In this case, the other characteristic values of the angle θ_0 are 0 (when the momentums of the primary electrons in their initial states are antiparallel to $\boldsymbol{\varepsilon}$) and 0.2891 (when the primary electrons move in the transverse direction to $\mathbf{k}_0$ given by $\theta_0 = 1.2818$).

Figures 4 and 5 show the surfaces $F(\theta_n, \varphi_n)$ and $F(\theta_{an}, \varphi_{an})$ and their fragments corresponding to these values of the angle θ_0. For each case, we chose the values of the parameters θ_n, φ_n, θ_{an}, and φ_{an} that corresponded to the highest maximums of the functions $F(\theta_n, \varphi_n)$ and $F(\theta_{an}, \varphi_{an})$.

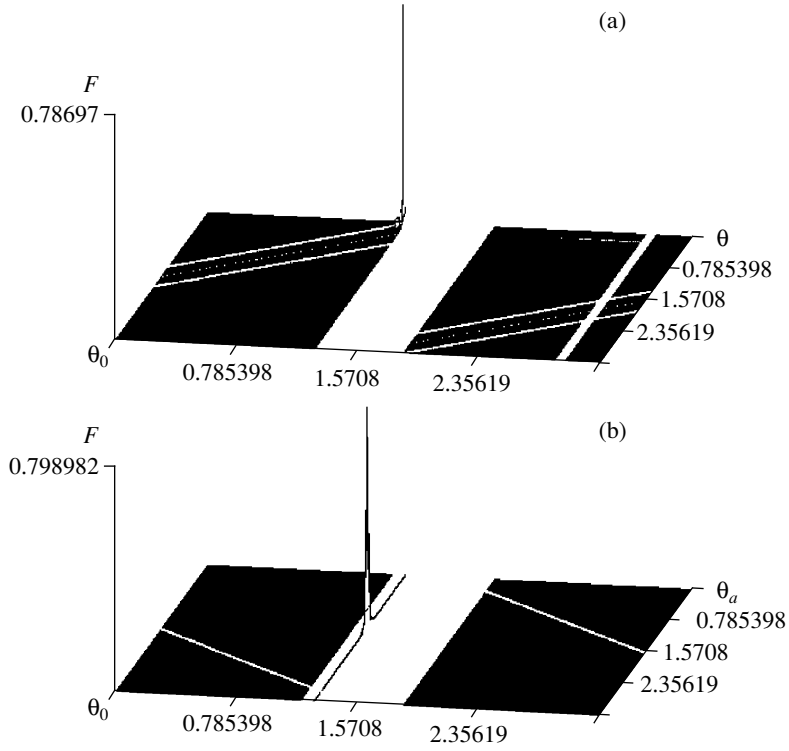

Fig. 1. Functions $F(\theta_n, \theta_0)$, and $F(\theta_{an}, \theta_0)$ calculated for $k_a = 10$ and $k = 50$ and illustrating the existence of maximums at (a) $\theta_0 = 1.2818$ and $\theta_n = 0.0877$ and (b) $\theta_{an} = 1.2911$ (the index n at θ_n and θ_{an} is omitted).

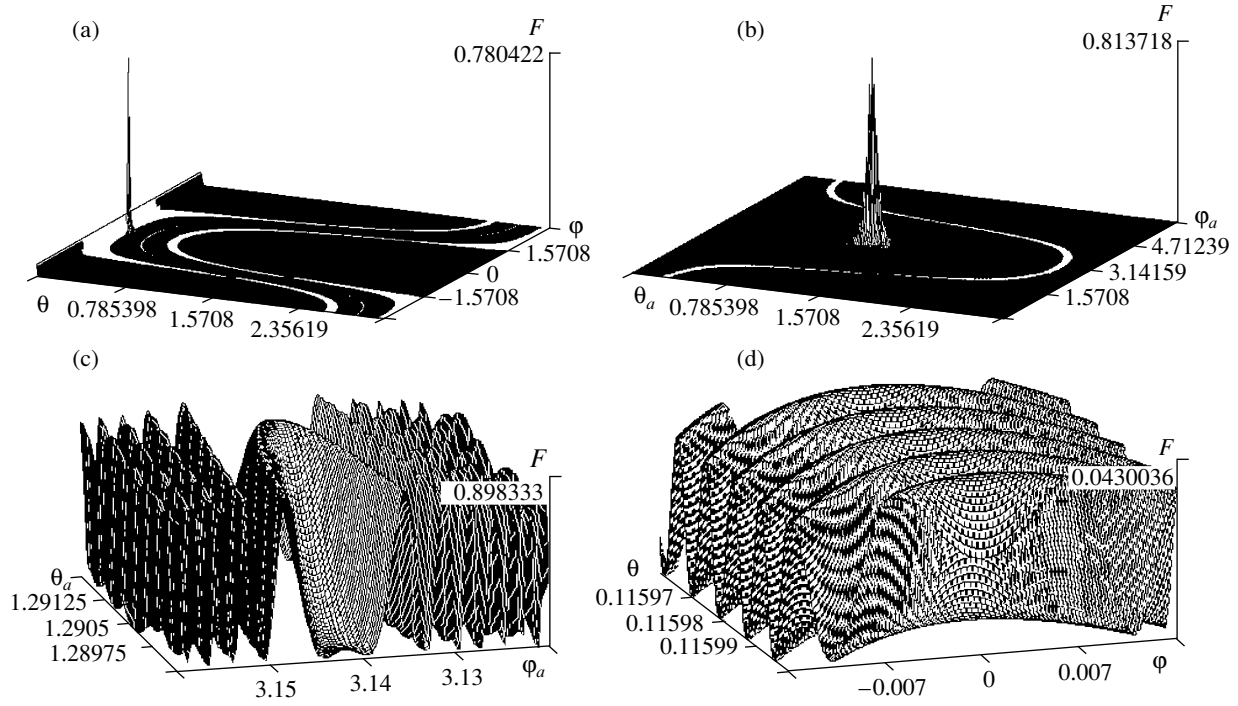

Fig. 2. Functions $F(\theta_n, \varphi_n)$ and $F(\theta_{an}, \varphi_{an})$ and their fragments calculated for $k_a = 10$, $k = 50$, and $\theta_0 = 1.2818$: (a) $F(\theta_n, \varphi_n)$ for $\theta_{an} = 1.2911$ and $\varphi_{an} = 3.1424$; (b) $F(\theta_{an}, \varphi_{an})$ for $\theta_n = 0.0877$ and $\varphi_n = 0.0014$; (c) $F(\theta_{an}, \varphi_{an})$ varying from 0.121 to 0.898 in the intervals (1.289, 1.292) and (3.12, 3.16) of the angles θ_{an} and φ_{an}, respectively; and (d) $F(\theta_n, \varphi_n)$ varying from 0.027 to 0.043 in the intervals (0.11596, 0.116) and (–0.014, 0.014) of the angles θ_n and φ_n, respectively (the index n at θ_n, θ_{an}, φ_n, and φ_{an} is omitted).

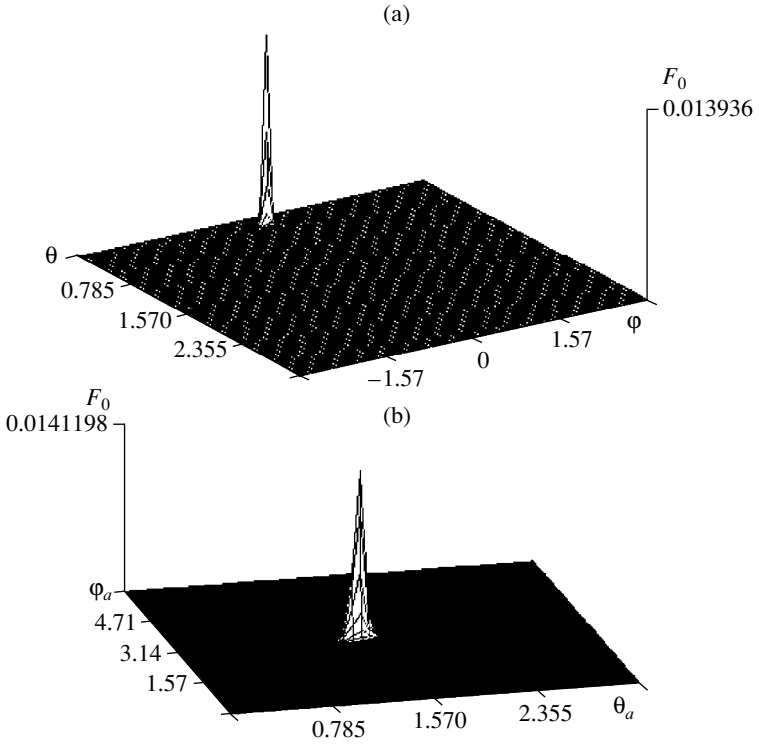

Fig. 3. Surfaces $F_0(\theta_n, \varphi_n)$ and $F_0(\theta_{an}, \varphi_{an})$ calculated for $k_a = 10$ and $k = 50$: (a) $F_0(\theta_n, \varphi_n)$ for $\theta_{an} = 1.3742$ and $\varphi_{an} = \pi$; (b) $F_0(\theta_{an}, \varphi_{an})$ for $\theta_n = 0.1961$ and $\varphi_n = 0$ (the index n at θ_n, θ_{an}, φ_n, and φ_{an} is omitted).

Thus, for the surfaces shown in Fig. 4, we set $\theta_n = 0.0006$, $\varphi_n = 0.0014$, $\theta_{an} = 0.005$, and $\varphi_{an} = 3.1418$; for $\theta_0 = 0.2891$, we used the following values of these parameters: $\theta_n = 0$, $\varphi_n = 0.377$, $\theta_{an} = 0.26$, and $\varphi_{an} = 3.1444$. It easily seen from the shape of the surfaces shown in these figures that the functions $F(\theta_n, \varphi_n)$ and especially $F(\theta_{an}, \varphi_{an})$ depend strongly on the angle θ_0, whereas both $F_0(\theta_n, \varphi_n)$ and $F_0(\theta_{an}, \varphi_{an})$ are independent of θ_0 (which follows from general considerations and directly from the calculation of the surfaces F_0).

From the fragment of the function $F(\theta_{an}, \varphi_{an})$ (Fig. 4) calculated in the intervals $(0, 0.014)$ and $(0, 2\pi)$ of the angles θ_{an} and φ_{an}, respectively, one can see that this function is almost independent of φ_{an} and oscillates between 0.12 to 0.58 with a period of about 0.003 along θ_{an}.

The function $F(\theta_n, \varphi_n)$ also depends weakly on φ_n, but unlike $F(\theta_{an}, \varphi_{an})$, it does not oscillate at sufficiently large values corresponding to the conditions $\varepsilon^{2/3} \ll E_{az} \ll \varepsilon L < E_z$. This is explained by the form of the expression for T, which contains no oscillatory terms dependent on k_z when $\varepsilon L < E_z$.

The function $F(\theta_{an}, \varphi_{an})$ for $\theta_0 = 0.289$ has an oscillatory structure, which is seen from its fragment presented in Fig. 5 for the intervals $(0.255, 0.265)$ and $(3.11, 3.17)$ of the angles θ_{an} and φ_{an}, respectively. However, the structure of this surface is more intricate in comparison with the previous case, because this function depends on φ_{an}. The function $F(\theta_n, \varphi_n)$, shown in the same figure, depends weakly on φ_n, which is illustrated by its fragment for $\theta_n \in (0, 0.01\pi)$ and $\varphi_n \in (-\pi, \pi)$. The maximum values of these functions are close to 0.58, which is one order of magnitude higher than the maximum values of the function $F_0(\theta_n, \varphi_n)$, $F_0(\theta_{an}, \varphi_{an})$.

To examine the cross section under the condition

$$\varepsilon^{2/3} \ll E_z \ll \varepsilon L < E_{az}, \tag{8}$$

we considered the functions $F(k, k_a)$, $F(\theta_{an}, k_a)$, $F(\varphi_{an}, k_a)$, and $F(\theta_0, k_a)$ presented in Fig. 6. The analysis of these functions showed that, for $\theta_0 = 1.2818$, $k_a = 15.44$, and $k = 49.6$, in the planes (θ_n, φ_n) and $(\theta_{an}, \varphi_{an})$ there exist fairly large domains corresponding to inequalities (8) and, for the angles $\theta_n = 0.2762$, $\varphi_n = 0.0001$, $\theta_{an} = 1.2692$, and $\varphi_{an} = 3.1416$, the functions $F(\theta_{an}, \varphi_{an})$ and $F(\theta_n, \varphi_n)$ are peaked, the maximums being 176474.53 and 176990.13, respectively. These surfaces are shown in Fig. 7 together with the functions $F_0(\theta_n, \varphi_n)$ and $F_0(\theta_{an}, \varphi_{an})$, which attain maximums approximately equal to 0.0032 at the same values of k and k_a and $\theta_{an} = 1.2692$, $\varphi_{an} = 3.14189$, $\theta_n = 0.3016$, and $\varphi_n = 0.0014$.

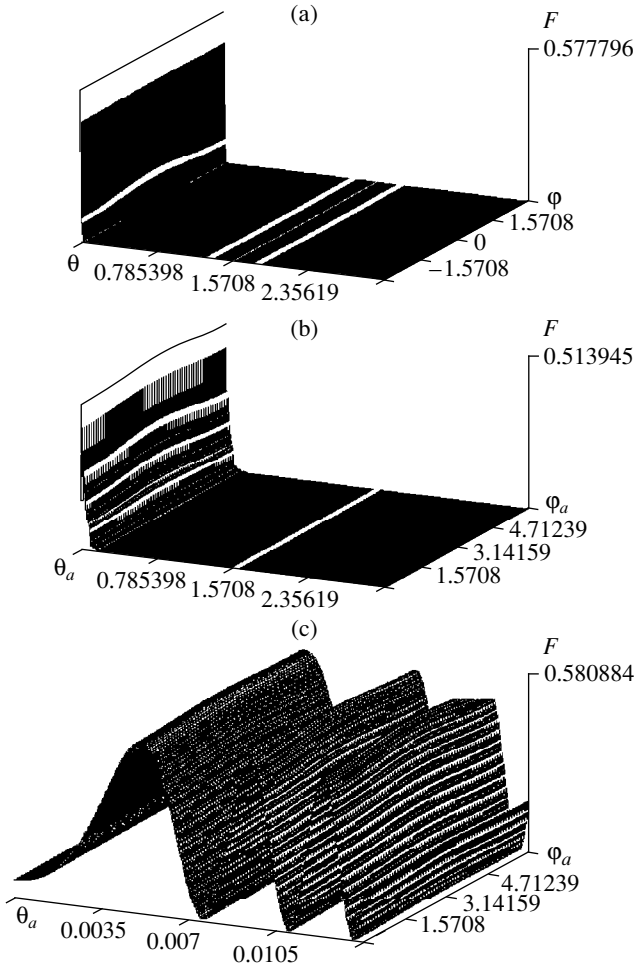

Fig. 4. Surfaces (a) $F(\theta_n, \varphi_n)$ and (b) $F(\theta_{an}, \varphi_{an})$: calculated for $\theta_0 = 0$ corresponding to the longitudinal (antiparallel to ε) direction of the primary electrons incident on the atom for $k_a = 10$ and $k = 50$; (c) the fragment of $F(\theta_{an}, \varphi_{an}) \in (0.12, 0.58)$ for $\theta_{an} \in (0, 0.014)$ (the difference between the maxima of the function and its fragment is due to different numbers of the points per unit area of the coordinate planes; the index n at θ_n, θ_{an}, φ_n, and φ_{an} is omitted).

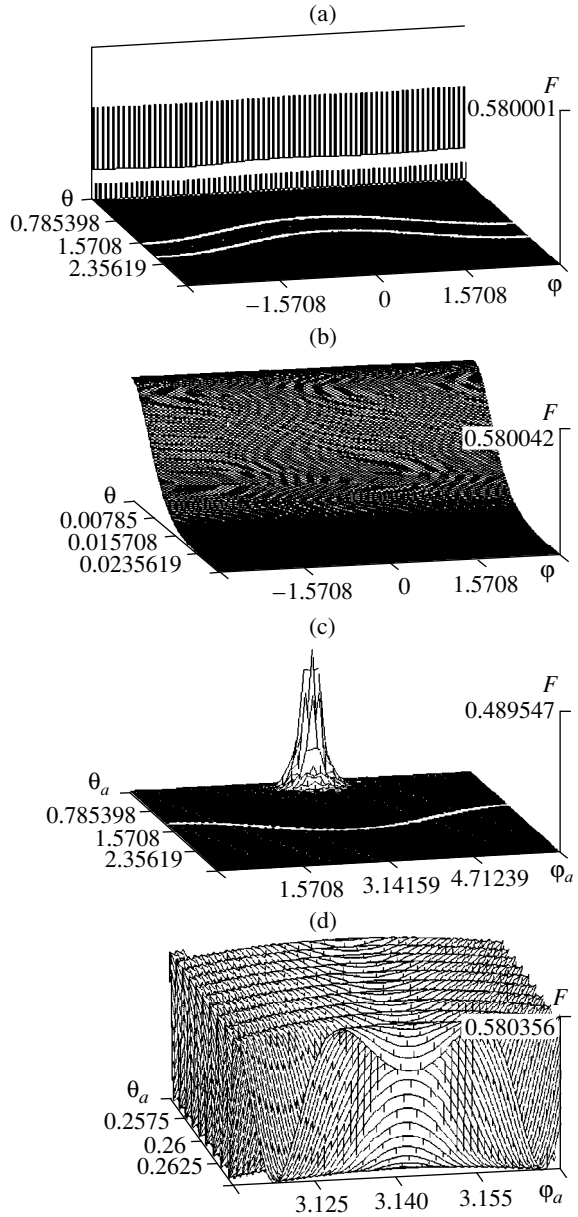

Fig. 5. Surfaces (a) $F(\theta_n, \varphi_n)$ and (c) $F(\theta_{an}, \varphi_{an})$ and their fragments calculated for $\theta_0 = 0.289$, $k_a = 10$, and $k = 50$: (b) $F(\theta_n, \varphi_n)$ for $\theta_n \in (0, 0.01\pi)$ and $\varphi_n \in (-\pi, \pi)$ and (d) $F(\theta_{an}, \varphi_{an})$ for $\theta_{an} \in (0.255, 0.265)$ and $\varphi_{an} \in (3.11, 3.17)$; $F(\theta_{an}, \varphi_{an}) \in (0.12, 0.58)$ (the index n at θ_n, θ_{an}, φ_n, and φ_{an} is omitted).

We note a general feature of the functions in question that follows from the shape of the surfaces considered above. The values of the angles θ_{an} at which the functions $F(\theta_{an}, \varphi_{an})$ and $F_0(\theta_{an}, \varphi_{an})$ attain their maximums are close to each other and the values of φ_{an} for both functions are close to π. Also almost coincident are the angles θ_{an} and θ_0 corresponding to the maximum value of the function $F(\theta_{an}, \varphi_{an})$. This means that, when a hydrogen atom is ionized by fast electrons in a uniform electric field, it is most likely that the secondary electron leaving the atom moves in the direction antiparallel to $\boldsymbol{\varepsilon}$. In other words, we can expect that the cross section for ionization of a hydrogen atom by electrons will increase significantly if a uniform electric field is antiparallel to the momentum of the electrons that leave the atom in the absence of a field ($\boldsymbol{\varepsilon} = 0$) with maximum probability. We should note that, in the model presented here, this effect is not related to the tunnel "extraction" of an electron from an atom due to an external field, because we do not consider the influence of the external field on the atomic electron in the ground state.

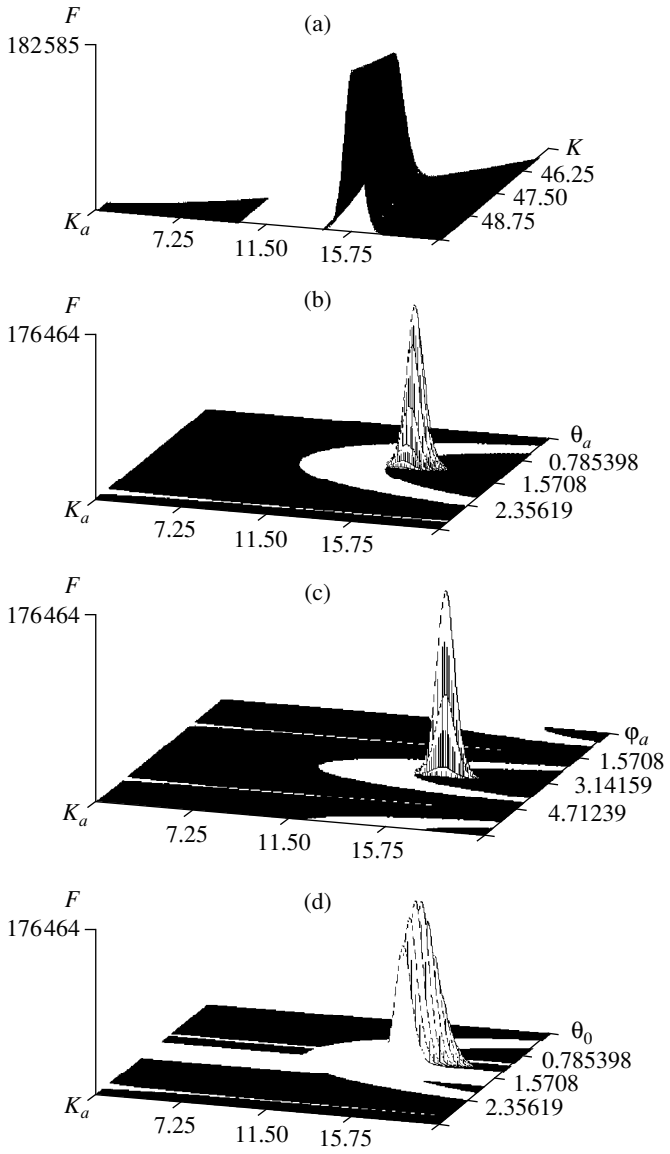

Fig. 6. Surfaces $F(k, k_a)$, $F(\theta_{an}, k_a)$, $F(\varphi_{an}, k_a)$, and $F(\theta_0, k_a)$ illustrating the existence of the maxima and corresponding to inequalities (8) for (a) $k_a = 15.44$ and $k = 49.6$, (b) $\theta_{an} = 1.2692$, (c) $\varphi_{an} = 3.1416$, and (d) $\theta_0 = 1.2818$ (the index n at θ_{an} and φ_{an} is omitted).

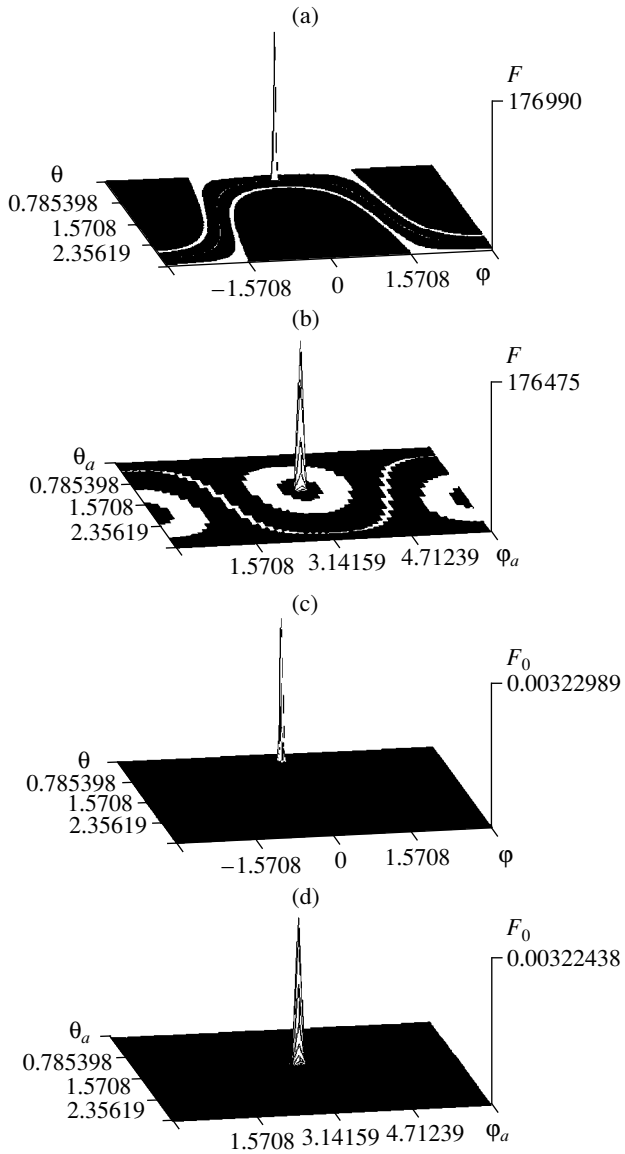

Fig. 7. Surfaces $F(\theta_n, \varphi_n)$, $F(\theta_{an}, \varphi_{an})$, $F_0(\theta_n, \varphi_n)$, and $F_0(\theta_{an}, \varphi_{an})$ for $\theta_0 = 1.2818$, $k_a = 15.44$, and $k = 49.6$: (a) $F(\theta_n, \varphi_n)$ for $\theta_{an} = 1.2692$ and $\varphi_{an} = 3.1416$, (b) $F(\theta_{an}, \varphi_{an})$ for $\theta_n = 0.2762$ and $\varphi_n = 0.0001$, (c) $F_0(\theta_n, \varphi_n)$ for $\theta_{an} = 1.2692$ and $\varphi_{an} = 3.1419$, and (d) $F_0(\theta_{an}, \varphi_{an})$ for $\theta_n = 0.3016$ and $\varphi_n = 0.0014$ (the index n at θ_n, θ_{an}, φ_n, and φ_{an} is omitted).

Let us examine the dependence of the cross section on the phases α_1, α_2, α_{a1}, and α_{a2}.

Figure 8 shows the functions $F(\alpha_{a1}, \alpha_{a2})$ and $F(\alpha_1, \alpha_2)$ corresponding to the surfaces $F(\theta_n, \varphi_n)$ and $F(\theta_{an}, \varphi_{an})$ presented in Figs. 2, 5, and 7.

It is seen from Fig. 8 that, if the conditions $\varepsilon^{2/3} \ll E_{az}$ and $E_z \ll \varepsilon L$ are satisfied, then the values of the functions $F(\alpha_1, \alpha_2)$ and $F(\alpha_{a1}, \alpha_{a2})$ lie in the intervals (0.066, 1.5234) and (0.0002, 1.409), respectively.

If the inequalities $\varepsilon^{2/3} \ll E_{az} \ll \varepsilon L < E_z$ are satisfied, then the values of the function $F(\alpha_{1a}, \alpha_{a2})$ lie in the interval (0.002, 0.909). If the inequalities $\varepsilon^{2/3} \ll E_z \ll \varepsilon L < E_{az}$ are satisfied, then the function $F(\alpha_1, \alpha_2)$ varies from 176426.36 to 176507.14.

Hence, the cross section under consideration can depend strongly on the parameters α_1, α_2, α_{a1}, and α_{a2}. However, if it is considerably greater than the cross section for ionization of an isolated hydrogen atom by

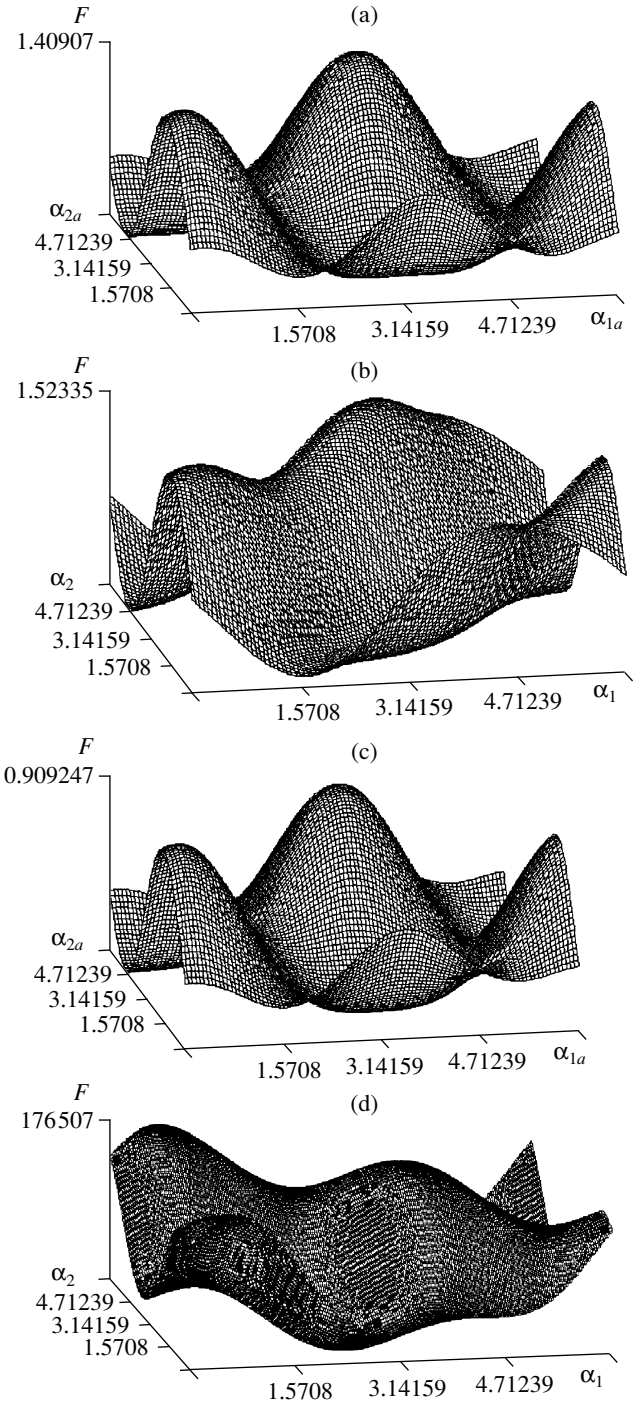

Fig. 8. Functions $F(\alpha_{a1}, \alpha_{a2})$ and $F(\alpha_1, \alpha_2)$: (a) $F(\alpha_{a1}, \alpha_{a2})$ and (b) $F(\alpha_1, \alpha_2)$ calculated for θ_n, θ_{an}, φ_n, and φ_{an} corresponding to Fig. 2 and inequalities $\varepsilon^{2/3} \ll E_{az}, E_z \ll \varepsilon L$, $0.0002 \le F(\alpha_{a1}, \alpha_{a2}) \le 1.41$, $0.066 \le F(\alpha_1, \alpha_2) \le 1.52$; (c) $F(\alpha_{a1}, \alpha_{a2})$ calculated for θ_n, θ_{an}, φ_n, and φ_{an} corresponding to Fig. 5 and inequalities $\varepsilon^{2/3} \ll E_{az} \ll \varepsilon L < E_z$, $0.002 \le F(\alpha_{a1}, \alpha_{a2}) \le 0.909$; and (d) $F(\alpha_1, \alpha_2)$ calculated for θ_n, θ_{an}, φ_n, and φ_{an} corresponding to Fig. 7 and inequalities $\varepsilon^{2/3} \ll E_z \ll \varepsilon L < E_{az}$, $176426.36 \le F(\alpha_1, \alpha_2) \le 176507.14$.

electrons, its relative variations [corresponding to the variations in the phases α_1, α_2, α_{a1}, and α_{a2} in the intervals $(0, 2\pi)$] are much smaller than unity and the specific values of the phases are of no importance.

Note also that the cross section can increase significantly under the condition $E_{az}, E_z \ll \varepsilon L$ if, for example, $\varepsilon = 0.001$ and $1 < k_a^2 \ll k^2 < 400$. In this case, the cross section is almost independent of the parameters α_1, α_2, α_{a1}, and α_{a2}.

4. CONCLUSION

It is expected from the above considerations that the differential cross section for ionization of a hydrogen atom by fast electrons in an external uniform electric field can differ significantly from a similar ionization cross section of an isolated atom in both the angular dependence and magnitude. The most pronounced increase in the cross section is expected if the atom is ionized by electrons with momentums directed almost perpendicularly to the uniform electric field, while the momentums of the electrons leaving the atom are antiparallel to this field.

The cross section under consideration contains oscillation terms whose periods depend on the longitudinal energy of both primary and secondary electrons. The anisotropy that appears in the cross section is due to the uniform electric field.

The physical explanation for these effects is the redistribution (in comparison with the case $\varepsilon = 0$) of the mean electron density when the electrons are reflected from the potential barrier of the external electric field.

In ionized gases, these effects should appear when the distance between the scattering-atom nucleus and the point of the electron reflection from the potential barrier of the uniform electric field is shorter than the mean distance between ions or gas atoms: $E \ll e\varepsilon n^{-1/3}$ (here, n is the density) and the mean time $\tau \sim \sqrt{m_e E}/e\varepsilon$ needed for the electrons to pass over this distance is much shorter than the characteristic time of the process under study. Assuming $E = 1$ eV and $n = 10^{12}$ cm^{-3}, we obtain $\varepsilon \gg 10^4$ V/cm and $\tau < 10^{-11}$. Hence, it is expected that, if a gas with a density of 10^{12} cm^{-3} is in an alternating electric field with frequency $\omega < 10^{12}$ s^{-1} and amplitude on the order of 10^2 kV/cm, the above effects should come into play.

ACKNOWLEDGMENTS

We thank A. A. Rukhadze and O. V. Kudrevatova for discussion of the results obtained. This work was supported by the Council of the Federal Program "Government Support of the Integration between Higher Education and Basic Research for 1997–2000" (under the subprogram "K0560FTsP Integration").

REFERENCES

1. V. I. Krylov, Kratk. Soobshch. Fiz., Nos. 7–8, 90 (1995).
2. V. I. Krylov, Kratk. Soobshch. Fiz., Nos. 9–10, 83 (1996).
3. V. I. Krylov, Pis'ma Zh. Tekh. Fiz. **16** (23), 60 (1995) [Tech. Phys. Lett. **16**, 189 (1995)].
4. V. I. Krylov, Kratk. Soobshch. Fiz., Nos. 1–2, 37 (1992).
5. V. D. Kondratovich and V. N. Ostrovskiĭ, Zh. Éksp. Teor. Fiz. **79**, 395 (1980) [Sov. Phys. JETP **52**, 198 (1980)].
6. I. I. Fabrikant, Zh. Éksp. Teor. Fiz. **83**, 1675 (1982) [Sov. Phys. JETP **56**, 967 (1982)].
7. O. V. Kudrevatova, Prikl. Fiz., Nos. 3–4, 83 (1995).
8. L. D. Landau and E. M. Lifshitz, *Quantum Mechanics: Non-Relativistic Theory* (Nauka, Moscow, 1974; Pergamon, Oxford, 1977).

Translated by N. F. Larionova

Plasma Physics Reports, Vol. 26, No. 5, 2000, pp. 456–461. Translated from Fizika Plazmy, Vol. 26, No. 5, 2000, pp. 488–493.

LOW-TEMPERATURE PLASMA

Numerical Investigation of a Microwave Discharge Driven by the H_{10}-Type Wave

N. Zh. Kaĭryev, É. B. Kulumbaev, and V. M. Lelevkin

Kyrgyz–Russian Slavic University, Bishkek, 720000 Kyrgyzstan

Received February 4, 1999; in final form, April 26, 1999

Abstract—A two-dimensional numerical model is proposed for studying a steady microwave discharge driven by the H_{10}-type wave. The parameters of a discharge in nitrogen at atmospheric pressure are calculated. The results obtained agree qualitatively with the experimental data. *© 2000 MAIK "Nauka/Interperiodica".*

1. INTRODUCTION

Microwave plasmatrons having unique parameters and capable of producing a spectrally pure plasma at elevated pressures are widely used in plasma chemistry [1, 2]. In order to successfully apply plasmatrons in various technological units, it is necessary to know how the external controlled generator parameters affect the plasma characteristics. Because of the nonlinear interaction between a plasma and an electromagnetic field, solving the problem at hand theoretically runs into serious difficulties. So far, the mechanism for the formation of a microwave discharge has been analyzed qualitatively [3] and the techniques for investigating radial plasmatrons in a quasi-two-dimensional approximation [2], the method of equivalent schemes [1, 4], and the channel models for plasma generators based on the H_{10}-type [2, 5] wave have been developed.

Here, we present a two-dimensional numerical model of a microwave discharge driven by the H_{10}-type wave. We calculate the parameters of a discharge in nitrogen at atmospheric pressure when the electromagnetic power is launched either into one end or symmetrically into opposite ends of the waveguide. We compare the results obtained with the experimental data [4].

2. MODEL

We consider a steady microwave discharge in a cylindrical quartz tube of radius R installed perpendicularly to the wide walls of a rectangular waveguide of cross section $a \times b$ (Fig. 1). The discharge is maintained via dissipation of the electromagnetic energy of a TE-wave with the field components $\mathbf{E}(0; E_y = E; 0)\exp(i\omega t - ikz)$ and $\mathbf{B}(B_x; 0; B_z)\exp(i\omega t - ikz)$. The wave is launched into the waveguide, is partially reflected from the discharge plasma, and partially penetrates into the plasma. The steady burning regime of a discharge is ensured by heat removal to the walls of the discharge tube via thermal conduction. We assume that the discharge plasma is immobile and is in local thermodynamic equilibrium and that the discharge parameters change insignificantly along the electric field vector.

2.1. Equations

The microwave discharge parameters are described by the energy balance equation and wave equation,

$$\frac{\partial}{\partial x}\left(\lambda\frac{\partial T}{\partial x}\right) + \frac{\partial}{\partial z}\left(\lambda\frac{\partial T}{\partial z}\right) + \frac{1}{2}\sigma|E|^2 = 0, \qquad (1)$$

$$\frac{\partial^2 E}{\partial x^2} + \frac{\partial^2 E}{\partial z^2} + \frac{\omega^2}{c^2}\left(\varepsilon - i\frac{\sigma}{\omega\varepsilon_0}\right)E = 0, \qquad (2)$$

and the magnetic field components are determined from the Maxwell equations

$$B_x = -\frac{i}{\omega}\frac{\partial E}{\partial z}, \quad B_z = \frac{i}{\omega}\frac{\partial E}{\partial x}.$$

Here, T is the temperature, λ is the thermal conductivity, $\varepsilon = 1 - \sigma/\varepsilon_0\nu_e$ is the plasma permittivity, $\sigma = e^2 n_e \nu_e / m_e(\omega^2 + \nu_e^2)$ is the electric conductivity, ν_e is the electron collision frequency, n_e is the electron density, e and m_e are the charge and mass of an electron, $k =$

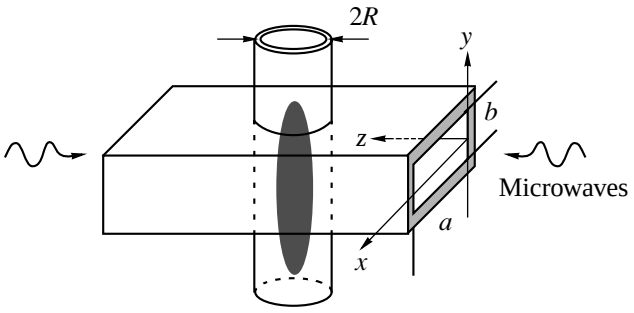

Fig. 1. Schematic of a microwave discharge driven by the H_{10}-type wave in a rectangular waveguide.

1063-780X/00/2605-0456$20.00 © 2000 MAIK "Nauka/Interperiodica"

$\sqrt{(\omega/c)^2 - (\pi/a)^2}$ is the longitudinal wavenumber, c is the speed of light, and ε_0 is the dielectric constant.

2.2. Boundary Conditions

The computation region for the temperature is bounded by the "cold" walls of the discharge tube:

$$T(x, z) = T_R = 300 \text{ K for } z^2 + (x - a/2)^2 = R^2.$$

The electric field is computed in the rectangular region ($0 \le x \le a/2$, $-L \le z \le L$) with the boundary conditions

$$E = 0 \text{ (perfectly conducting waveguide walls)}$$

$$\text{at } x = 0 \quad \partial E/\partial x = 0,$$

$$\partial T/\partial x = 0 \text{ (symmetry conditions) at } x = a/2; \qquad (3)$$

$$\frac{\partial E}{\partial z} - ikE = -2ikE_I \exp(-ikz)\sin(\pi x/a) \text{ at } z = -L;$$

$$\frac{\partial E}{\partial z} + ikE = 0 \quad \text{at } z = L.$$

These boundary conditions correspond to a solution to equation (2) for a waveguide with $\sigma = 0$ and $\varepsilon = 1$ and the boundary conditions

$$E = [E_I \exp(-ikz) + E_R \exp(ikz)]\sin(\pi x/a)$$

$$\text{at } z = -L, \qquad (4)$$

$$E = E_T \exp(-ikz)\sin(\pi x/\alpha) \text{ at } z = L,$$

where E_I, E_R, and E_T are the field amplitudes of the incident, reflected, and penetrating waves of the H_{10} type (the dimensions a and b are chosen so that the fundamental H_{10}-mode penetrates into the waveguide, whereas the higher modes, which are captured numerically in the discharge region, are completely damped before they reach the boundaries $z = \pm L$).

When the microwave power is launched symmetrically into opposite ends of the waveguide, the boundary conditions for the computation region $-L \le z \le 0$ are

$$\partial E/\partial z = 0, \quad \partial T/\partial z = 0 \text{ at } z = 0.$$

2.3. Method of Solution

We solved equations (1) and (2) with the boundary conditions numerically using the finite-difference scheme on a rectangular nonuniform grid. The equations were discretized by the control volume method [6]. The discrete analogues of the equations were solved iteratively with the help of the sweep method along the z-axis.

The technique for solving equation (2) is governed by the numerical implementation of the boundary conditions (3). Since the wave equation determines the electric field amplitude to within an arbitrary constant complex factor, we replaced the first condition in (3) by

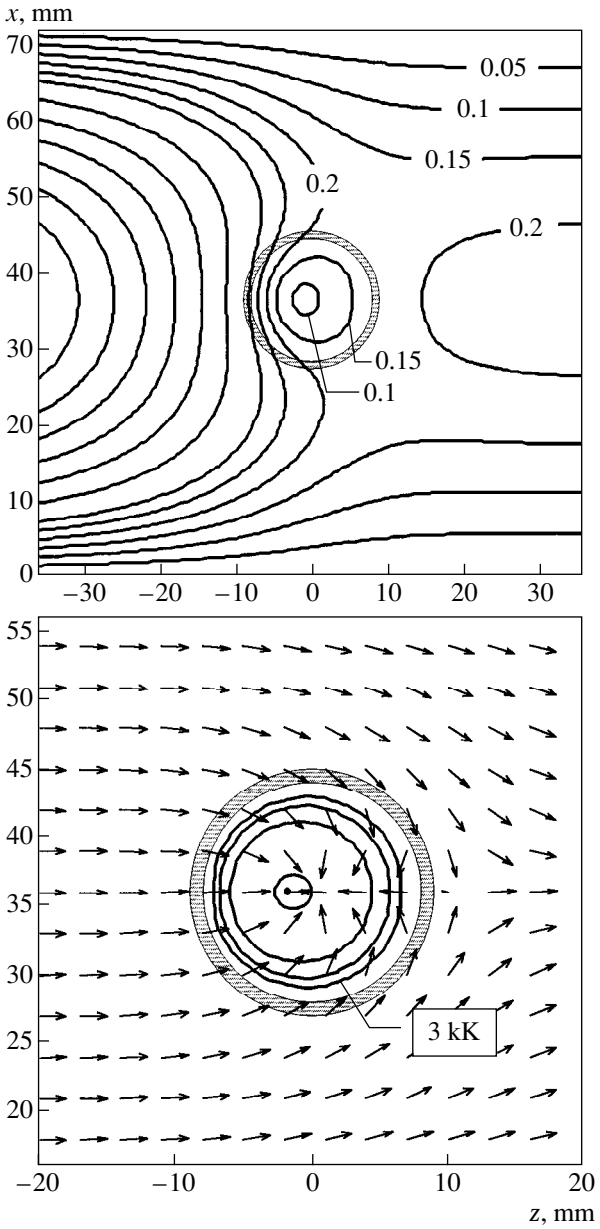

Fig. 2. Electric field distribution $E(x, z)/E_{max}$ (with E_{max} = 0.63 kV/cm), Poynting vector field, and temperature distribution (adjacent isotherms represent the change in the temperature by 1 kK) in a microwave discharge with an electromagnetic power P_I = 1.5 kW launched into one end of the waveguide. The discharge-tube walls are hatched.

$\tilde{E} = \sin(\pi x/a)$ at $z = -L$, taking into account the condition at the right boundary iteratively. The solution obtained, $\tilde{E}(x, z)$, was scaled, $E(x, z) = K_E \tilde{E}(x, z)$, using the coefficient K_E, which was computed either from the power of the incident wave,

$$P_I = \frac{kE_I^2}{4\mu_0\omega}ab, \quad K_E = E_I/\tilde{E}(a/2, -L),$$

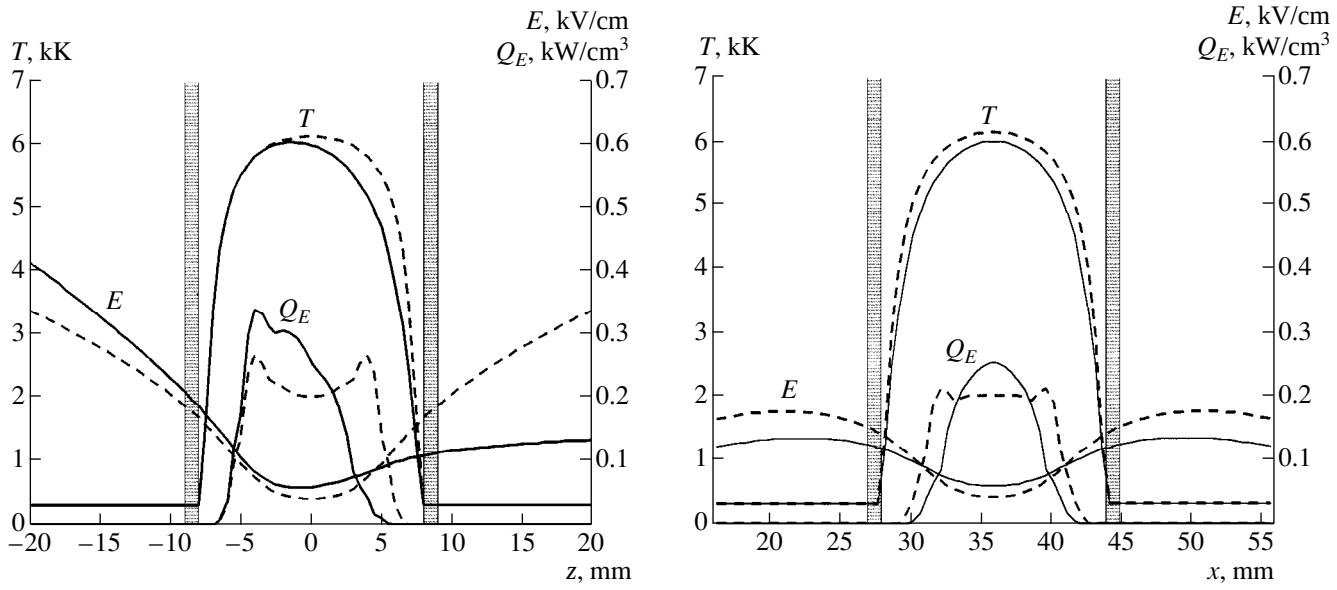

Fig. 3. Profiles of the electric field strength, temperature, and specific power ($Q_E = \sigma E^2/2$) dissipated in the plasma of a microwave discharge with an electromagnetic power $P_I = 1.5$ kW launched into one end (solid curves) and into opposite ends (dashed curves) of the waveguide. The dielectric-tube walls are hatched.

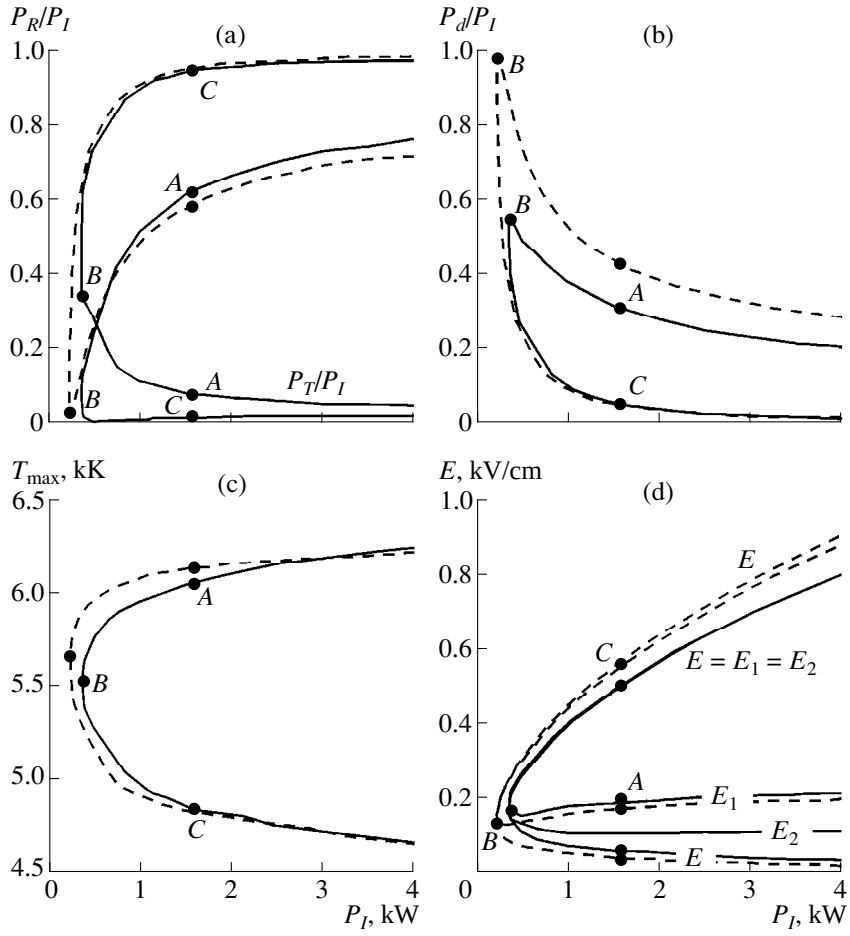

Fig. 4. (a) Reflection and penetration coefficients, (b) absorption coefficient of the microwave power, (c) maximum temperature, and (d) electric field strength in a microwave discharge with a wave launched into one end (solid curves) and into opposite ends (dashed curves) of the waveguide. E is the extremum strength, $E_1 = E(a/2, -R)$, and $E_2 = E(a/2, R)$.

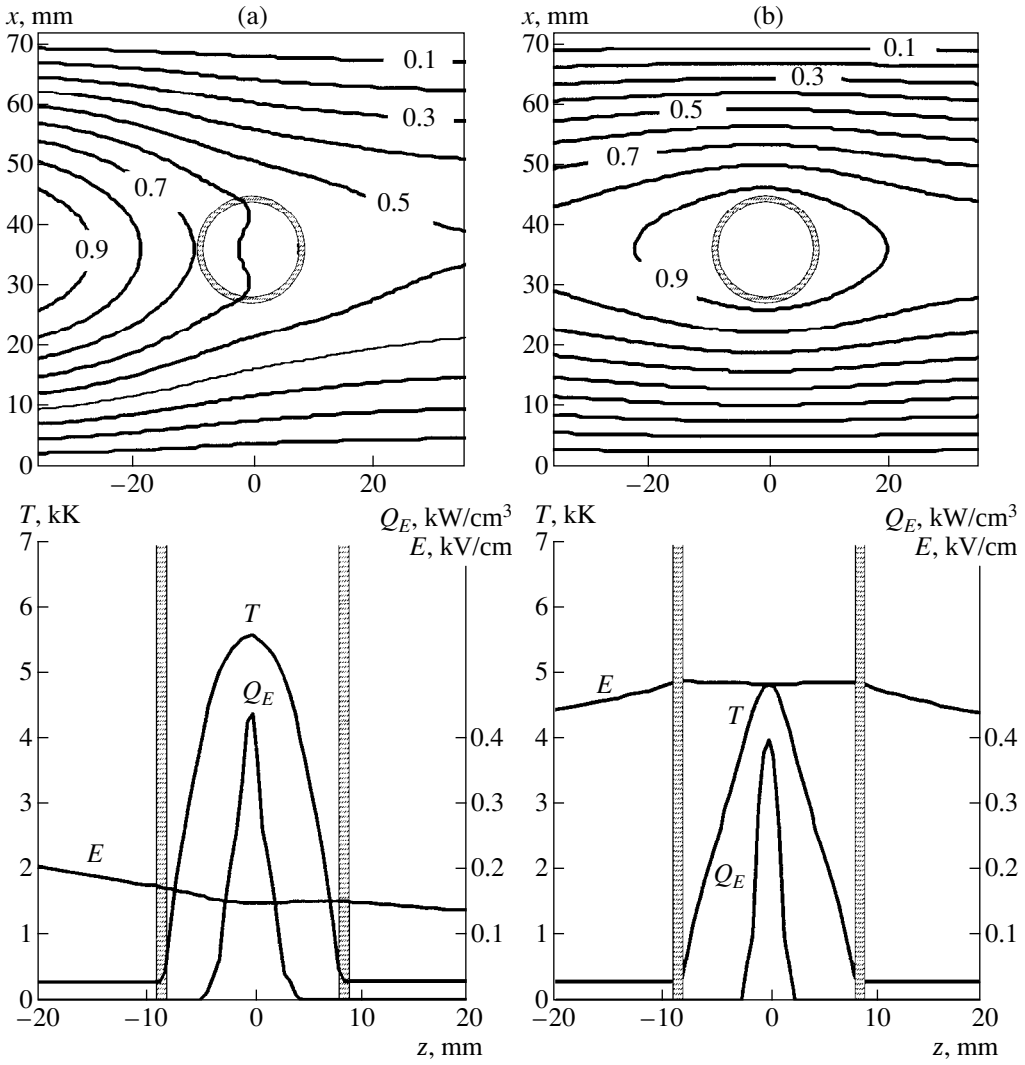

Fig. 5. Distributions of the electric field strength, temperature, and specific power ($Q_E = \sigma E^2/2$) dissipated in the plasma of a microwave discharge with a wave launched into one end of the waveguide in (a) transient and (b) unstable regimes. The dielectric-tube walls are hatched.

or from the power dissipated in the discharge plasma,

$$P_d = b\iint_S \frac{1}{2}\sigma|E|^2 dxdz, \quad K_E = \sqrt{P_d/\tilde{P}_d},$$

where S is the cross-sectional area of the quartz tube. The amplitudes E_I, E_R, and E_T were calculated from relationships (4).

3. RESULTS

We calculated the parameters of a microwave discharge in nitrogen at atmospheric pressure under the following experimental conditions [4]: a = 72 mm, b = 34 mm, $\omega/2\pi$ = 2.4 GHz, R = 8 mm, and P_I = 1.5 kW. The rate constants for a nitrogen plasma at atmospheric pressure were taken from [3, 7]. The electron density was found by evaluating the equilibrium plasma content, and the temperature dependence of the electron collision frequency was determined from the electric conductivity σ_0 at $\omega = 0$: $\nu_e = e^2 n_e/m_e\sigma_0$.

3.1. Wave Launched into One End of the Waveguide

We consider an electromagnetic wave incident on the plasma in a cylindrical channel with dielectric walls in a rectangular waveguide. Because of the interaction of a plasma with an electromagnetic field, the isolines of $|\mathbf{E}|$ are closely spaced inside the discharge front (Fig. 2). The region where the electromagnetic field energy is dissipated serves as a "sink" for the Poynting vector $(\mathbf{E}\times\mathbf{B}^* + \mathbf{E}^*\times\mathbf{B})/4\mu_0$ (where the asterisk stands

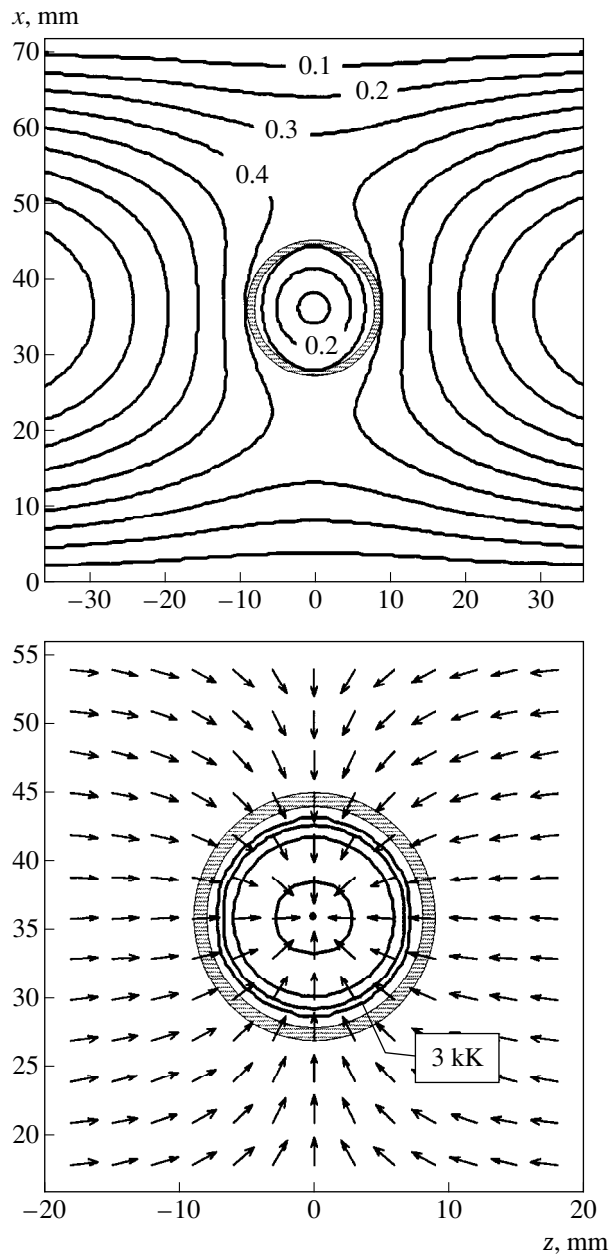

Fig. 6. The electric field distribution $E(x, z)/E_{max}$ (with E_{max} = 0.47 kV/cm), Poynting vector field, and temperature distribution (adjacent isotherms represent the change in the temperature by 1 kK) in a microwave discharge with an electromagnetic power P_I = 1.5 kW launched into opposite ends of the waveguide. The dielectric-tube walls are hatched.

for complex conjugation), which is directed toward the plasma center and results in the appearance of two singular points (a nodal point and a saddle point) on the *z*-axis. The skin layer is ring-shaped, the skin effect being most pronounced on the side of the incident wave. Behind the saddle point, the vector of the density flux of electromagnetic energy becomes solenoidal and the electric field grows. The electromagnetic power dissipation (P_d = 0.46 kW) causes intense plasma heating in the discharge front. The distribution of isotherms (T_{max} = 6046 K) is asymmetric: they are shifted toward the incident wave (Figs. 2, 3). A fraction of the electromagnetic field energy is reflected from the plasma (P_R = 0.89 kW), while the remaining fraction penetrates into the plasma (P_T = 0.15 kW). In the *x*-direction (Fig. 3), the temperature is highest at the channel axis, whereas the electric field is weakest at the axis and strongest near the walls.

The results obtained agree qualitatively with the experimental data [4]: $T_{max} = (6200 \pm 300)$ K and $P_R \approx P_T \approx 0.38$ kW, the threshold power being 0.6 kW. Presumably, discrepancies with the experimental data may be attributed to the conversion of the incident wave into a coaxial wave between the discharge plasma and the metal tubes that screen the plasma outside the waveguide and also to the azimuthal rotation of a gas inside the channel [4].

3.2. Burning Regimes

According to the results obtained (Fig. 4), a microwave discharge may burn in the (*A*) stable, (*B*) transient, and (*C*) unstable regimes, which agrees with the experiment [1–3]. As in [3], we determined the stability of a discharge against temperature fluctuations. The *stable* regime is characterized by a relatively high plasma temperature, large fractions of the dissipated and reflected electromagnetic power, a weaker electric field, and a lower power of the electromagnetic field penetrating into the plasma. The dimensions of the skin layer are much smaller than those of the discharge. In the *transient* regime, the relative fraction of the electromagnetic wave energy dissipated in the plasma is maximum (P_d/P_I = 0.55), while the fraction of the reflected energy is minimum (Fig. 4). The skin effect in the electric field is less pronounced (Fig. 5). The temperature distribution $T(x, z)$ (T_{max} = 5580 K) and the distribution of the heat source (i.e., of the dissipated power, which is described by the dissipative term in the energy balance equation) in the discharge plasma are almost symmetric. The discharge burns at a minimum threshold power of 0.37 kW of the electromagnetic field launched into the plasma (Fig. 4). In the *unstable* regime, the electric field *E* is higher and the temperature *T* is lower than those in the other regimes: the related isotherms are circular, the temperature being highest at the channel axis (Fig. 5).

3.3. Wave Launched into Opposite Ends of the Waveguide

When electromagnetic waves are launched into opposite ends of the waveguide, the electric field distribution and the Poynting vector field are both symmetric with one nodal point (Fig. 6). The isotherms are nearly circular, the temperature being maximum (T_{max} =

6136 K) on the channel axis. The isolines of the electric field strength in the discharge plasma are ellipses stretched in the *x*-direction (Figs. 3, 6). For an electromagnetic power of 1.5 kW launched into the plasma, the fractions of the dissipated and reflected powers are 0.65 and 0.85 kW, respectively. In comparison with the case of a wave launched into one end of the waveguide, the threshold power is somewhat lower (0.23 kW), while the maximum temperature is higher (5645 K) and the absorption coefficient is larger ($P_d/P_I \approx 1$) in the transient regime (see Fig. 4). This agrees with the estimates made in [1, 2].

3.4. Discharge Tube with a Larger Radius

In a discharge tube with a radius $R = 16$ mm, the distributions of the plasma parameters and electromagnetic field do not change qualitatively. When an electromagnetic wave is launched into one end of the waveguide, the temperature distribution is more asymmetric and a larger fraction of microwave power is reflected. Accordingly, the fraction of the power dissipated in the discharge, the fraction of the power penetrating into the plasma, the maximum temperature, and the electric field strength in a discharge are all lower. When electromagnetic waves are launched into opposite ends of the waveguide, the isotherms inside the discharge plasma are ellipses stretched in the *z*-direction, the temperature being maximum at two points that lie on the symmetry axis and are shifted toward the channel walls. The remaining parameters change in the same manner as those in the case of a wave launched into one end of the waveguide.

4. CONCLUSION

Our simulations of a microwave discharge driven by the H_{10}-type wave have revealed a qualitative agreement between the results of two-dimensional computations and the experimental data, the existence of stable and unstable (against temperature fluctuations) burning regimes of discharges (the absorption coefficient of the electromagnetic field power being optimum in the transient regime), and the possibility of achieving a nonmonotonic temperature distribution in the discharge plasma.

For the description of a microwave discharge to be adequate to experiment, it is necessary to take into account the conversion of the incident electromagnetic wave and gas-dynamic processes and simulate the discharge using a three-dimensional model.

REFERENCES

1. *Microwave Plasma Sources: Physics, Technology, and Applications*, Ed. by V. M. Batenin, I. I. Klimovskiĭ, G. V. Lysov, and V. N. Troitskiĭ (Énergoatomizdat, Moscow, 1988).
2. *RF and Microwave Plasmatrons*, Ed. by S. V. Dresvin, A. A. Bobrov, V. M. Lelevkin, *et al.* (Nauka, Novosibirsk, 1992), Vol. 6.
3. Yu. P. Raizer, *Gas Discharge Physics* (Springer-Verlag, Berlin, 1991).
4. L. M. Baltin, V. M. Batenin, I. I. Devyatkin, *et al.*, Teplofiz. Vys. Temp. **9**, 1105 (1971); Élektron. Tekh., Ser. 1: Élektronika SVCh, No. 1, 26 (1972).
5. A. A. Bobrov, O. V. Kudrevatova, G. V. Lysov, and E. A. Petrov, Élektron. Tekh., Ser. 1: Élektronika SVCh, No. 5, 45 (1979).
6. S. Patankar, *Numerical Heat Transfer and Fluid Flow* (McGraw-Hill, New York, 1980; Énergoatomizdat, Moscow, 1984).
7. *Theory of Electric Arcs*, Ed. by V. S. Éngel'sht, V. Ts. Gurovich, G. A. Desyatkov, *et al.* (Nauka, Novosibirsk, 1990), Vol. 1.

Translated by G. V. Shepekina

Plasma Physics Reports, Vol. 26, No. 5, 2000, pp. 462–464. Translated from Fizika Plazmy, Vol. 26, No. 5, 2000, pp. 494–496.

BRIEF COMMUNICATIONS

Theory of Nondiffusive Penetration of a Magnetic Field into a Conducting Medium

V. Yu. Zaburdaev

Russian Research Centre Kurchatov Institute, pl. Kurchatova 1, Moscow, 123182 Russia

Received July 8, 1999

Abstract—The penetration of a current and, accordingly, a magnetic field into the plasma of pulsed systems characterized by short temporal and spatial scales can be investigated in electron magnetohydrodynamics. A study is made of the rapid penetration of the magnetic field of an injected high-current ion beam into a plasma. *© 2000 MAIK "Nauka/Interperiodica".*

This work is a continuation of studies devoted to the rapid penetration of a magnetic field into a plasma or plasmalike media. An investigation of this phenomenon in the electron magnetohydrodynamic (EMHD) model revealed many interesting processes that were not captured with the help of the classical theory of the skin effect. Among the works on this problem, we should mention an important paper by Kingsep *et al.* [1], in which it was predicted that the magnetic field could penetrate into the plasma in the form of a nonlinear constant-amplitude wave moving at a constant velocity.

Our purpose here is to study the characteristic behavior of the magnetic field of a high-current charged-particle beam injected into a plasma. The short temporal and spatial scales of the problem, τ and a, allow us to apply the EMHD approach [1], which is valid under the conditions

$$\omega_{pe}, \omega_{He} \gg \tau^{-1} \gg \omega_{pi}, \omega_{Hi}, \tag{1}$$

$$c/\omega_{pi}, \rho_{Hi} \gg a \gg c/\omega_{pe}, \rho_{He}, \tag{2}$$

$$v_{Te}, v_{Ae} \gg j/ne \gg c_s, v_A, \tag{3}$$

where

$$\omega_{H\alpha} = Z_\alpha eB/m_\alpha c, \quad \omega_{p\alpha}^2 = 4\pi n Z_\alpha^2 e^2/m_\alpha,$$

$$c_s = (ZT_e/MA)^{1/2}, \quad v_A = B/\sqrt{4\pi n_i MA}.$$

The beam can be modeled merely by the external current j_b, because the mechanical component of the beam-particle generalized momentum dominates over its field component, $|\mathbf{p}| \gg \left|\frac{Ze}{c}\mathbf{A}\right|$ (or, in other words, the Larmor radius of the beam electrons substantially exceeds the spatial scale a). Analogously, we can neglect the friction between the beam and plasma particles in comparison with the Ohmic resistance, because the effective Coulomb collision frequency is proportional to $E_b^{-3/2}$, where E_b is the energy of the beam particles. Under conditions (1)–(3), the plasma ion velocity is much lower than the plasma electron velocity, so that the plasma ions can be assumed to be immobile.

The geometry of the problem is illustrated in Fig. 1. The z-axis is directed along the external current $z \parallel \mathbf{j}_b$; the plasma occupies the half-space $0 < z < a$; and the system is uniform along the y-axis, $\partial/\partial y \equiv 0$. At the initial time $t = 0$, the reverse current in the plasma completely neutralizes the external (beam-driven) current and $\mathbf{B} \equiv 0$. Outside the plasma, at any instant, we have $\mathbf{B} = \mathbf{B}_0$, where $\mathbf{B}_0$ is the self-magnetic field of the beam. Under the assumptions adopted, the ion and electron beams can be treated in the same manner; we should only keep in mind that, in the case of an electron beam, the beam current flows in the direction opposite to that of the beam.

We start with the set of equations

$$\mathbf{curl}\mathbf{E} = -\frac{1}{c}\frac{\partial \mathbf{B}}{\partial t},$$

$$\mathbf{curl}\mathbf{B} = \frac{4\pi}{c}(\mathbf{j} + \mathbf{j}_b),$$

$$\mathbf{j} = -en_e\mathbf{v}_e$$

and the equation of electron motion

$$m\frac{d\mathbf{v}_e}{dt} = -e\mathbf{E} - \frac{1}{n_e}\nabla p_e - \frac{e}{c}[\mathbf{v}_e\mathbf{B}] + \frac{e}{\sigma}\mathbf{j}.$$

Assuming, for simplicity, that n = const and σ = const and performing the necessary manipulations, we obtain

$$\frac{\partial}{\partial t}\left(\mathbf{curl}\mathbf{v}_e - \frac{e}{mc}\mathbf{B}\right) = \mathbf{curl}\left[\mathbf{v}_e, \mathbf{curl}\mathbf{v}_e - \frac{e}{mc}\mathbf{B}\right] - \frac{ce}{4\pi m\sigma}\Delta\mathbf{B} - \frac{e}{m\sigma}\mathbf{curl}\,\mathbf{j}_b, \tag{4}$$

1063-780X/00/2605-0462$20.00 © 2000 MAIK "Nauka/Interperiodica"

$$\mathbf{v}_e = \frac{\mathbf{j}_b}{ne} - \frac{c}{4\pi}\mathbf{curlB}. \quad (5)$$

We should point out the following important property of equation (4). In the limit of infinitely high conductivity, equation (4) passes over to the familiar frozen-in equation in which the frozen-in quantity is the curl of the generalized plasma-electron momentum $\mathbf{P} = \mathbf{p} - \frac{e}{c}\mathbf{A}$.

The problem of the transport of a magnetic field by an external current was solved by Kingsep *et al.* [2] without allowance for electron inertia. The physical model they developed can be outlined as follows. The magnetic field penetration is described by the dynamic equation

$$\frac{\partial B}{\partial t} + v\frac{\partial B}{\partial z} = D\frac{\partial^2 B}{\partial z^2}, \quad v = j_b/ne, \qquad D = \frac{c^2}{4\pi\sigma}, \quad B = B_y. \quad (6)$$

In the initial stage, when the profile of B is steep, the magnetic field penetrates into a plasma due to diffusion. In later stages, when the profile of B becomes sufficiently smooth, the magnetic field becomes frozen in the current-carrying electrons and is transported by them. The magnetic field enters the plasma through the boundary $z = 0$ with the velocity $v = j/ne$. The exact solution to equation (6) is

$$B = \frac{B_0}{2}\left(\exp\frac{vz}{D}\operatorname{erfc}\frac{z+vt}{2\sqrt{Dt}} + \operatorname{erfc}\frac{z-vt}{2\sqrt{Dt}}\right). \quad (7)$$

As a result of the competition between diffusion and the linear transport of the magnetic field out of the plasma, the steady-state magnetic-field profile

$$B = B_0\exp\frac{v}{D}(z-a)$$

is established at the boundary $z = a$ (Fig. 2).

In our problem, we take into account electron inertia, insert (5) into (4), and perform simple but rather laborious manipulations to obtain the following one-dimensional equation, describing this physical model:

$$\frac{\partial}{\partial t}\left(B - \frac{c^2}{\omega_{pe}^2}\frac{\partial^2 B}{\partial z^2}\right) + v\frac{\partial}{\partial z}\left(B - \frac{c^2}{\omega_{pe}^2}\frac{\partial^2 B}{\partial z^2}\right) = D\frac{\partial^2 B}{\partial z^2}, \quad (8)$$

$$B(z, 0) = B_0\theta(-z), \quad (9)$$

$$B = B_y,\ v = j_b/ne,\ a^2 = c^2/\omega_{pe}^2,\ D = \frac{c^2}{4\pi\sigma}.$$

Following [2], we neglect the effects at the beam boundary; i.e., we omit the term $\mathbf{curl}\frac{\mathbf{j}_b}{\sigma}$, which accounts for the magnetic field generation.

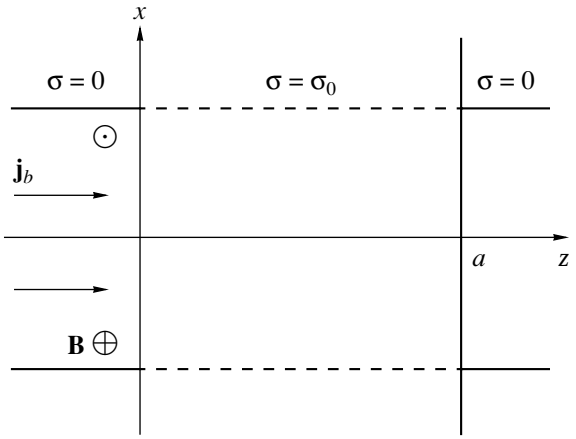

Fig. 1. Geometry of the problem.

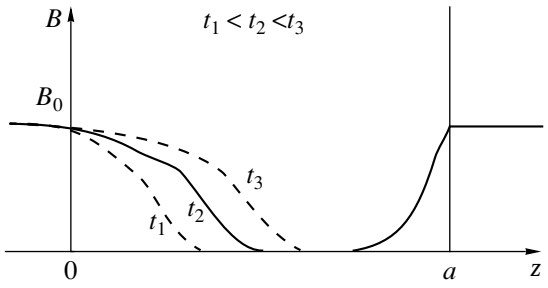

Fig. 2. Penetration of a magnetic field into the plasma without allowance for electron inertia.

Taking the Fourier transformation of (8) in the z-coordinate, we arrive at a linear differential equation. This equation can be easily integrated to yield the time dependence of the Fourier transformed magnetic field. With allowance for the initial conditions, we can represent the exact solution to equation (8) in terms of the Fourier integral,

$$B(z, t) = B_0\left[\frac{1}{2} - \frac{1}{2\pi}\int_{-\infty}^{+\infty}\frac{\sin(k(z-vt))}{k}\exp\left(-\frac{Dtk^2}{1+a^2k^2}\right)dk\right]. \quad (10)$$

The specific form of both the initial condition (9) and equation (8) allows us to follow the penetration of the initial jump (9) in the magnetic field into a plasma using the Lax method, i.e., expanding the solution into a series in functions with different smoothness [3]. To do this, we represent the exact solution (10) as the sum of discontinuous and smooth functions, $B = B_{sing} + B_{con}$. As the discontinuous function B_{sing}, we adopt $B_{sing} = \varphi(z, t)\theta(S(z, t))$, where $\theta(x)$ is the Heaviside step function. We substitute B_{sing} into equation (8) and collect the factors in the generalized functions $\theta(S(z, t))$, $\delta(S(z, t))$, $\delta'(S(z, t))$, and $\delta''(S(z, t))$. If we succeed in finding the

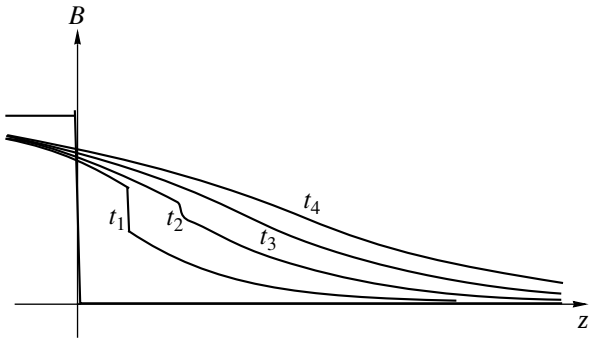

Fig. 3. Penetration of a magnetic field into the plasma with allowance for electron inertia.

functions $\varphi(z, t)$ and $S(z, t)$ with which to force the factors in the delta function and its derivatives to zero, then we could state that the remaining function B_{con} would be at least continuous. The desired functions $\varphi(z, t)$ and $S(z, t)$ satisfy the equations

$$S_t' + vS_x' = 0, \tag{11}$$

$$\varphi_t + \varphi_x = -\frac{D}{a^2}\varphi. \tag{12}$$

Equation (11) implies that $S = f(x - vt)$. Equation (12) can be integrated by the method of characteristics. With allowance for the fact that, at $t = 0$, the function B_{sing} should satisfy the initial condition (9), we obtain the final expression for B_{sing}:

$$B_{\text{sing}} = B_0\theta(vt - z)e^{-\frac{D}{a^2}t}. \tag{13}$$

Analyzing (13), we can see that the initial discontinuity (9) propagates with the current velocity v and is exponentially damped as time elapses. The diffusion acts to reduce the jump rather than smooth the profile. Applying the same procedure, we can show that the remaining function $B_{\text{con}} = B - B_{\text{sing}}$ is infinitely differentiable. Of course, the solutions obtained and the boundary conditions are discontinuous because we work in the EMHD theory. In reality, the magnetic field changes sharply on a spatial scale of about c/ω_{pe}. On infinitely long time scales, the discontinuity disappears and the magnetic field profile becomes smooth, in which case neglecting the highest derivative in equation (8) yields equation (6). The time evolution of the solution is illustrated in Fig. 3.

Thus, in our problem, unlike in the nonlinear problems treated by Gordeev *et al.* [4, 5] with allowance for electron inertia, no small-scale solitons are generated: we deal with a discontinuity (rather than a soliton) that appears on a spatial scale of about c/ω_{pe} and is exponentially damped with time. The effective distance over which the jump propagates is equal to $l_{\text{eff}} \approx \frac{4\pi\sigma}{\omega_{pe}^2}\frac{j_b}{ne} = \frac{j_b}{ne\nu_{ei}}$.

ACKNOWLEDGMENTS

I am grateful to A.S. Kingsep for his guidance and support throughout the work and to K.V. Chukbar and V.V. Below for valuable discussions. This work was supported in part by the Russian Foundation for Basic Research (project no. 99-2-16659), the program of the Ministry of Science and Technology of the Russian Federation "Problems of Nonlinear Dynamics," and INTAS (grant no. 21-1998).

REFERENCES

1. A. S. Kingsep, Yu. V. Mokhov, and K. V. Chukbar, Fiz. Plazmy **10**, 854 (1984) [Sov. J. Plasma Phys. **10**, 495 (1984)].
2. A. S. Kingsep, L. I. Rudakov, and K. V. Chukbar, Dokl. Akad. Nauk SSSR **262**, 1131 (1982) [Sov. Phys. Doklady **27**, 140 (1982)].
3. R. Courant, *Partielle Differentialgleichungen* (Gottingen, 1932; Mir, Moscow, 1964).
4. A. V. Gordeev, A. S. Kingsep, and L. I. Rudakov, Phys. Rep. **243**, 221 (1984).
5. A. V. Gordeev, A. S. Kingsep, and L. I. Rudakov, Phys. Rep. **243**, 233 (1984).

Translated by I. A. Kalabalyk